Heinrich Heine
Universität
Düsseldorf

Synthesis of metal-organic framework@polymer monolithic composites for water sorption based adsorption heat transformation applications

Inaugural-Dissertation

zur Erlangung des Doktorgrades
der Mathematisch-Naturwissenschaftlichen Fakultät
der Heinrich-Heine-Universität Düsseldorf

vorgelegt von
Emrah Hastürk
aus Istanbul

Düsseldorf, November 2019

aus dem Institut für Anorganische Chemie und Strukturchemie I
der Heinrich-Heine-Universität Düsseldorf

Gedruckt mit der Genehmigung der
Mathematisch-Naturwissenschaftlichen Fakultät der
Heinrich-Heine-Universität Düsseldorf

Referent: Prof. Dr. Christoph Janiak
Korreferent: Prof. Dr. Christian Ganter

Tag der mündlichen Prüfung: 19.12.2019

Die vorliegende Arbeit wurde im Rahmen des Projekts „Optimierung von neuartigen Materialien für zyklische Adsorptionsprozesse“ (kurz: OPTIMAT-Projekt) in der Zeit von Oktober 2015 bis November 2019 an der Heinrich-Heine-Universität Düsseldorf im Institut für Anorganische Chemie und Strukturchemie I im Arbeitskreis von Prof. Dr. Christoph Janiak angefertigt. Teilnehmende Verbundprojektpartner waren das Fraunhofer-Institut für Solare Energiesysteme (ISE), DencoHappel GmbH (später FläktGroup) und die Heinrich-Heine-Universität Düsseldorf (HHU Düsseldorf).

Eidesstattliche Erklärung

Ich versichere an Eides statt, dass die Dissertation von mir selbstständig und ohne unzulässige fremde Hilfe unter der Beachtung der „Grundsätze zur Sicherung guter wissenschaftlicher Praxis“ an der Heinrich-Heine-Universität Düsseldorf erstellt worden ist. Die aus fremden Quellen direkt oder indirekt übernommenen Gedanken sind als solche kenntlich gemacht. Die Arbeit wurde bisher weder im Inland noch im Ausland in gleicher oder ähnlicher Form einer anderen Prüfungsbehörde vorgelegt. Es wurden keine früheren erfolglosen Promotionsversuche unternommen.

………………………………… …………………………………

Ort, Datum **Unterschrift**

Danksagung

Ich bedanke mich herzlich bei Herrn Prof. Dr. C. Janiak, der mir die Möglichkeit gegeben hat meine Dissertation in seinem Arbeitskreis anzufertigen und für die dabei gewährten wissenschaftlichen Freiräume. Für das Korrekturlesen von Manuskripten und für die Zusammenarbeit bei den Publikationen bin ich ihm sehr verbunden und auch für die Gelegenheiten, dass ich an vielen wissenschaftlichen Tagungen und Konferenzen teilnehmen konnte.

Bei Herrn Prof. Dr. Christian Ganter bedanke ich mich für die Übernahme des Zweitgutachtens.

Ich danke meinen Bachelor- bzw. Master-Studenten Burhan Topalli, Moritz Steinert und Jens Tappen für die gute Zusammenarbeit.

Mein besonderer Dank gilt Annette Ricken, Dietmar Frunzke, Birgit Tommes, Marcell Demandt. sowie Frau Schäfer und Jutta Bourgeois für die Unterstützung bei allen organisatorischen Fragen.

Natürlich möchte ich mich auch bei allen, die mir bei Messungen und anderen Aufbauten geholfen haben, bedanken. Für die analytischen Untersuchungen sind dies Birgit Tommes, Anna Kautz, Alexander Nuhnen, Simon Millan, Anna Goldman, Alexa Schmitz, Dennis Dietrich, Sandra Nießing, Carsten Schlüsener und Bastian Moll.

Ein ganz besonderer Dank gilt meinen Bürokollegen Niels Tannert, Annika Herbst, Ilka Simon, Simon-Patrick Höfert, Vasily Gvilava, Christian Jansen, Alex Spieß, Serkan Gökpinar und Karsten Klauke.

Desweiteren möchte ich mich ganz besonders bei Niels Tannert, Carsten Schlüsener, Serkan Gökpinar, Julian Quodbach und Tobie Matemb Ma Ntep für die enge Zusammenarbeit danken.

Abschließend danke ich meiner Familie, die mir viel Verständnis gezeigt und mich ständig unterstützt hat.

Publication list

E. Hastürk, S.-J. Ernst, C. Janiak,
Recent advances in adsorption heat transformation focusing on the development of adsorbent materials.
Curr. Opinion Chem. Eng. 24 (2019) 26–36. DOI: 10.1016/j.coche.2018.12.011

E. Hastürk, C. Schlüsener, J. Quodbach, Christoph Janiak,
Shaping of metal-organic frameworks into mechanically stable monoliths with poly(vinyl alcohol) by phase separation technique.
Micropor. Mesopor. Mater. 280 (2019) 277–287. DOI: 10.1016/j.micromeso.2019.02.011

E. Hastürk, S.-P. Höfert, B. Topalli, C. Schlüsener, Christoph Janiak,
Shaping of MOFs via freeze-casting method with hydrophilic polymers and their effect on textural properties.
Micropor. Mesopor. Mater. (Akzeptiert).

N. Tannert, S. Gökpinar**, E. Hastürk**, S. Nießing, C. Janiak,
Microwave-assisted dry-gel conversion-a new sustainable route for the rapid synthesis of metal-organic frameworks with solvent re-use.
Dalton Trans. 47 (2018) 9850–9860. DOI: 10.1039/C8DT02029A

S. Millan, B. Gil-Hernández, **E. Hastürk**, A. Schmitz, C. Janiak,
A 2D zinc coordination polymer built from the mono-deprotonated 4,4‘-azobis(3,5-dimethyl-1H-pyrazole) ligand.
Z. Anorg. Allg. Chem. 644 (2018) 1311–1316. DOI: 10.1002/zaac.201800286

T.J.M. Ma Ntep, H. Reinsch, B. Moll, **E. Hastürk**, S. Gökpinar, H. Breitzke, C. Schlüsener, L. Schmolke, G. Buntkowsky, C. Janiak,
Realizing the potential of acetylenedicarboxylate by functionalization to halofumarate in Zr^{IV}-metal-organic frameworks.
Chem. Eur. J. 24 (2018) 14048–14053. DOI: 10.1002/chem.201802838

S. Gökpinar, S.-J. Ernst, **E. Hastürk**, M. Möllers, I. El Aita, R. Wiedey, N. Tannert, S. Nießing, S. Abdpour, A. Schmitz, J. Quodbach, G. Füldner, S. Henninger, C. Janiak,
Air-con metal-organic frameworks in binder composites for water adsorption heat transformation systems.
Ind. Eng. Chem. Res. (Akzeptiert), DOI: 10.1021/acs.iecr.9b04394

P.K. Tsobnang, **E. Hastürk**, D. Fröhlich, E. Wenger, P. Durand, J.L. Ngolui, C. Lecomte, C. Janiak.
Water Vapor Single-Gas Selectivity via Flexibility of Three Potential Materials for Autonomous Indoor Humidity Control.
Cryst. Growth Des. 19 (2019) 2869–2880. DOI: 10.1021/acs.cgd.9b00097

T.J.M. Ma Ntep, H. Reinsch, P.P.C. Hügenell, S.-J. Ernst, **E. Hastürk**, C. Janiak,
Designing a new aluminium muconate metal–organic framework (MIL-53-muc) as a methanol adsorbent for sub-zero temperature heat transformation applications.
J. Mater. Chem. A 7 (2019) 24973–24981. DOI: 10.1039/C9TA07465A

Kurze Zusammenfassung

Die Arbeit beginnt mit einem Überblick zu neuen Entwicklungen bei adsorptiven Wärmetransformations-Prozessen mit dem Fokus auf der Entwicklung bei den Adsorbentien. Die Adsorptionswärme-Transformation (englisch: adsorption heat transformation, AHT) basiert auf der zyklischen Ad- und Desorption eines Arbeitsmediums in einem porösen Material. Wenn das Arbeitsfluid durch das aktive leere Sorptionsmaterial zur Verdampfung gebracht wird, wird die erforderliche Verdampfungswärme in thermisch angetriebenen Adsorptionskältemaschinen zu einer nützlichen Kühlung. Die Antriebswärme regeneriert das leere Sorptionsmaterial durch Desorption des Arbeitsmediums. Die Adsorptionswärme in dem Sorptionsmaterial und die Kondensationswärme des Arbeitsfluids können in dem Adsorptionswärmepumpen-Modus verwendet werden. Somit trägt die Adsorptionswärme-Umwandlung zu energiesparenden Technologien bei. Die Adsorbensentwicklung spielt eine entscheidende Rolle für die Verbesserung der AHT-Technologien. Neben Kieselgel und Zeolithen als Adsorbensmaterialien, die bisher in den handelsüblichen AHT-Geräten eingesetzt werden, haben in den letzten Jahren vor allem metallorganische Gerüste (englisch: metal-organic frameworks, MOFs) Beachtung gefunden. Kompositmaterialien aus Salzen mit Kieselgelen, Zeolithen und MOFs sowie Aktivkohlen wurden ebenfalls untersucht, um zu AHT-Technologien beizutragen. Die Reduzierung der Installations- / Produktionskosten und die Steigerung der Effizienz von AHT-Geräten müssen erreicht werden, um die Verbreitung von AHT zu erhöhen.

Vor dem Hintergrund der möglichen Anwendung von MOFs in AHT-Technologien wurden Formgebungsverfahren von MOFs mit Polymeren als monolithische Verbundwerkstoffe untersucht. Es wurde dabei beobachtet, dass sich die Polymer-Kompatibilität jedes MOFs je nach Formgebungsmethode ändert. Zwei verschiedene Methoden wurden systematisch zur Formgebung von MOFs untersucht.

In der ersten Methode (siehe Kapitel 3.1) wurden die MOFs Alfum und MIL-101(Cr) zum ersten Mal unter Verwendung einer Phasentrennungstechnik erfolgreich in hydrophilen Polyvinylalkohol (PVA)-Monolithen eingebettet. Die Vakuumtrocknung hat sich als die bevorzugte Trocknungsmethode zur Herstellung sauberer PVA-Monolithe im Vergleich zur überkritischen und Gefriertrocknung erwiesen, um die monolithische Form zu erhalten und eine Schrumpfung zu verhindern. Unterschiedliche Beladungsmengen von MOFs ergaben ähnliche erwartete massengewichtete Sorptionseigenschaften, die auf die Reproduzierbarkeit dieser Methode hinweisen. Interessanterweise sind Porenvolumen und Wasserbeladung der Alfum@PVA-Monolithe höher als der erwartete Wert. Das zusätzliche Porenvolumen und damit eine höhere Aufnahme in die Wassersorption wurde auf die Bildung von Mesoporen aus Grenzflächenhohlräumen zwischen Alfum und PVA zurückgeführt. Dies wird durch die t-Plot-Methode unterstützt, die nur die Beibehaltung der 30-70 % des Alfum-Mikroporenvolumens

anzeigt. Dieses Phänomen wurde nur bei Alfum@PVA-Monolithen beobachtet, nicht bei MIL-101(Cr)@PVA-Monolithen.

MOF@PVA-Monolithe mit 33 Gew.% bis 80 Gew.% MOF konnten unter Beibehaltung der MOF-Sorptionseigenschaften erhalten werden. Bis zu 83 % der BET-Oberfläche und 84 % der Wasseradsorption des reinen MOFs im MIL-101(Cr)@PVA-Monolith wurden erreicht. Alfum@PVA-Monolith zeigten noch bessere Ergebnisse mit bis zu 95 % der erwarteten BET-Oberfläche und 120 % der erwarteten Wasserdampfaufnahme. Unter den drei in dieser Arbeit verwendeten PVAs zeigte das mittelmolekulare PVA2 die Fähigkeit, als geeigneteres Polymer im Vergleich zum niedermolekularen PVA3 und zum hochmolekularen PVA1 zu fungieren.

Mechanische Stabilitätstests von Alfum@PVA-Monolithen zeigten maximale Stabilität für 65 Gew.% Alfum beladenen Monolithen, während höhere und niedrigere MOF-Beladungen zu weniger mechanisch stabilen Monolithen führten. Darüber hinaus zeigten reine PVA-Monolithen vor allem plastisches und elastisches Verhalten, wobei die Monolithe mit 50 und 65 Gew.% Alfum leichte plastische Eigenschaften und hohe Verformungsbeständigkeit aufwiesen. Für die Monolithen mit 50 und 65 Gew.% Alfum können Spannungen bis zu 0.12 N/m^2, d.h. bis zu einer Kraft von 63 N, mit einer geringeren Dehnung (< 0.2 %) gegenüber den PVA-Monolithen aufgebracht werden.

In der zweiten Methode (siehe Kapitel 3.2) wurde die Gefriergusstechnik verwendet, um die MOFs Alfum, MIL-160(Al) und MIL-101(Cr) mit den hydrophilen Polymeren PAA, PAANa, PEG, PEI, PVA(88), PVA(98) und PVP zu formen. Das Gefriergussverfahren wurde zunächst anhand Alfum und PVA optimiert und die optimierten Bedingungen später auf die Herstellung der anderen MOF@Polymer-Monolithe angewendet. Es wurde beobachtet, dass ein höheres Molekulargewicht des PVA-Polymers zu geringerer Blockierung der Poren des MOF im Monolith führt. Auch mit einem erhöhten MOF-Gehalt im Monolithen wurde eine bessere Porenzugänglichkeit erreicht.

Das Gefrieren mit Flüssigstickstoff und die anschließende Gefriertrocknung (englisch: liquid nitrogen and freeze-drying, LNFD) wurde in dieser Arbeit als optimierte Methode zur schnellen und einfachen Monolithbildung unter Beibehaltung der strukturellen Eigenschaften der MOFs bestimmt. 21 verschiedene monolithische Verbundwerkstoffe wurden bis zu 80 Gew.% Beladung von MOFs hergestellt und erstmals konnte im Gefriergussverfahren eine nahezu vernachlässigbare Porenblockierung der eingebetteten MOFs nachgewiesen werden. Monolithe aus Alfum und MIL-160(Al) mit PVA und PVP ergaben die besten Ergebnisse hinsichtlich BET-Oberfläche und Porenvolumen unter den Monolithen aus Alfum@Polymer und MIL-160(Al)@Polymer. Mit Ausnahme von PEI und PEG ergaben andere Polymere im Alfum@Polymer-Monolith sehr gute Ergebnisse bis zu 114 % der erwarteten Wasserbeladung bei $p \cdot p_0^{-1} = 0.35$. Zusätzlich betrug die Wasserbeladung von MIL-160(Al) 80@PAA, PVA(98), PVA(88)4 und PVP etwa 100 % des erwarteten Wertes bei $p \cdot p_0^{-1} = 0.20$. Alle

MIL-101(Cr)@Polymer-Monolithe ergaben über 85 % der erwarteten BET-Oberfläche und 90 % des erwarteten Porenvolumens, ausgenommen MIL-101(Cr)@PEI mit 47 % der erwarteten BET-Oberfläche und 52 % des erwarteten Porenvolumens. Ein weiteres bemerkenswertes Ergebnis ist die hydrophile Verschiebung der MOF@Poylmer-Verbundwerkstoffe, die am Ausgangspunkt der S-förmigen Wassersorptionsisotherme der entsprechenden MOFs beobachtet wurde. Dieser Bereich liegt für Alfum@Polymer-Monolith bei $p \cdot p_0^{-1} \leq 0.15$, für MIL-160(Al)@Polymer-Monolith bei $p \cdot p_0^{-1} \leq 0.05$ und für MIL-101(Cr)@Polymer-Monolith bei $p \cdot p_0^{-1} \leq 0.4$. Beispielsweise zeigten die MIL-101(Cr)@Polymer-Monolithe eine Wasseraufnahme von bis zu 330 % der berechneten Werte im Relativdruck von 0.4, was auf eine hydrophile Verschiebung der gebildeten Monolithen im Vergleich zum reinen MIL-101(Cr) hinweist.

Eine starke Porenblockierung in den Monolithen von Al-MOFs mit PEI ist das Ergebnis einer deutlichen Wechselwirkung zwischen MOF und Polymer, die in den IR-Spektren beobachtet wurde. Die in-situ-Vernetzung unterhalb des Gefrierpunktes (Kryo-Polymerisation) führte keiner zu einer Verbesserung der Sorptionseigenschaften der Verbundwerkstoffe.

Im Gegensatz zum Gefriergussverfahren spielt das Molekulargewicht eine entscheidende Rolle für die Sorptionseigenschaften von Verbundwerkstoffen, die durch in-situ-PVA-Vernetzung hergestellt werden.

Zusätzlich zu den oben genannten Formgebungsmethoden wurde die Einbettung von Alfum in das R,F-xerogel mit bis zu 57 % Beladung und einer Porenzugänglichkeit von 89 % erfolgreich durchgeführt. Die Kryo-Polymerisationstechnik, bei der PEI chemisch vernetzt wurde, konnte zur Herstellung von MOF@PEI-Monolithen eingesetzt werden. Allerdings wurden die vorbereiteten Komposite mit 81, 66 und 51 Gew.% MOF nicht als Monolith erhalten. Nur mit 36 Gew.% MOF war es möglich, einen Monolithen zu erhalten, jedoch mit einer geringen Porenzugänglichkeit von 11 %.

Short summary

The work begins with an overview of new developments in adsorptive heat transformation processes with a focus on the development of adsorbents. The adsorption heat transformation (AHT) is based on the cyclic ad- and desorption of a working medium in a porous material. As the working fluid vaporized by the active empty sorption material, the required heat of vaporization in thermally driven adsorption chillers becomes a useful cooling. The driving heat regenerates the empty sorption material by desorption of the working medium. The adsorption heat in the sorption material and the condensation heat of the working fluid can be used in the adsorption heat pump mode. Thus, the adsorption heat conversion contributes to energy-saving technologies. The adsorbent development plays a decisive role for the improvement of the AHT technologies. In addition to silica gel and zeolites as adsorbent materials, which have hitherto been used in commercially available AHT devices, metal-organic frameworks (MOFs) in particular have attracted attention in recent years. Composite materials from salts with silica gels, zeolites and MOFs as well as activated carbons were also investigated to contribute to AHT technologies. The reduction of installation/production costs and the increase in the efficiency of AHT devices must be achieved in order to increase the widespread use of AHT.

Against the background of the possible application of MOFs in AHT technologies, shaping processes of MOFs with polymers as monolithic composite materials were investigated. It was observed that the polymer compatibility of each MOF changes according to the shaping method. Two different methods for shaping MOFs were systematically investigated.

In the first method (see section 3.1 for details), MOFs Alfum and MIL-101(Cr) were successfully embedded for the first-time in hydrophilic polyvinyl alcohol (PVA) monoliths using a phase-separation technique. Vacuum drying has proven to be the preferred drying method for producing neat PVA monoliths compared to supercritical and freeze-drying in order to retain the monolith shape and avoid shrinkage. Different loading amounts of MOFs resulted in similar expected sorption properties indicating the reproducibility of this method. Interestingly, the pore volume and water loading of Alfum@PVA monoliths are higher than the expected value. The additional pore volume and accordingly higher uptake in water sorption were attributed to the formation of mesopores from interfacial voids between Alfum and PVA. This is supported by t-plot method, which only indicates the retention of 30-70% of the Alfum-micropore volume. This phenomenon was only observed with Alfum@PVA monoliths not with MIL-101(Cr)@PVA monoliths.

MOF@PVA monoliths with 33 wt% to 80 wt% MOF could be obtained while maintaining sorption properties of MOFs. Up to 83% of the BET surface area and 84% of the water adsorption of neat MOFs in the MIL-101(Cr)@PVA monolith was achieved. Alfum@PVA monoliths showed better results with up to 95% of expected BET surface area and 120% of expected water vapor uptake. Among three PVA used in this work, medium-molecular weight

PVA2 showed ability to act as a more suitable polymer compared to the low-molecular weight PVA3 and the high-molecular weight PVA1.

Mechanical stability tests of Alfum@PVA monoliths showed maximum stability for 65 wt% Alfum loaded monolith, whereas higher and lower MOF loading resulted in mechanically less stable monoliths. In addition, neat PVA monoliths showed a primarily plastic and elastic behavior, however, the monoliths with 50 and 65 wt% Alfum exhibited slightly plastic properties and a high resistance against deformation. For the monoliths with 50 and 65 wt% Alfum, stresses up to 0.12 N/m^2, i.e. up to a force of 63 N can be applied together with a lower strain (< 0.2%) compared to the PVA monoliths.

In the second method (see section 3.2 for details) the freeze-casting technique was used to form the MOFs Alfum, MIL-160(Al) and MIL-101(Cr) together with hydrophilic polymers PAA, PAANa, PEG, PEI, PVA(88), PVA(98) and PVP. The freeze-casting method was initially optimized with Alfum and PVA, and the resulting conditions later applied to the preparation of the other MOF@polymer monoliths. It was observed that the higher the molecular weight of the polymer PVA, the less the pores of the MOF are blocked in the monolith. With an increased MOF content in the monolith a better pore accessibility was achieved.

Freezing with liquid nitrogen and subsequent freeze-drying (LNFD) was determined in this work as the optimized method for rapid and easy monolith formation with retention of the textural properties of the MOFs. 21 different monolithic composites were prepared up to 80 wt% loading of MOFs and it was shown for the first time in the freeze-casting method almost negligible pore blocking of the embedded MOFs. Monoliths of Alfum and MIL-160(Al) with PVA and PVP gave the best results in terms of BET surface area and pore volume among the Alfum@polymer and MIL-160(Al)@polymer monoliths. With the exception of PEI and PEG, other polymers in Alfum@polymer monolith provided very good results up to 114% of the calculated water loading at $p \cdot p_0^{-1} = 0.35$. In addition, water loading of MIL-160(Al)80@PAA, PVA(98), PVA(88)4 and PVP was about 100% of the expected value at $p \cdot p_0^{-1} = 0.20$. All MIL-101(Cr)@polymer monoliths resulted over 85% and 90% of the calculated BET surface area and pore volume, respectively, excluding MIL-101(Cr)@PEI with 47% of the calculated S(BET) and 52% of the calculated V(pore). Another remarkable result is the hydrophilic shift in the MOF@poylmer composites observed at the starting point of the S-shaped water sorption isotherm of the corresponding MOFs. This range is for Alfum@polymer monolith $p \cdot p_0^{-1} \leq 0.15$, for MIL-160(Al)@polymer monolith $p \cdot p_0^{-1} \leq 0.05$ and for MIL-101(Cr)@polymer monolith $p \cdot p_0^{-1} \leq 0.4$. For example, MIL-101(Cr)@polymer monoliths showed a water uptake of up to 330% in the relative pressure of 0.4, indicating a hydrophilic shift of the formed monoliths compared to pure MIL-101(Cr).

A strong pore blocking in the monoliths of Al-MOFs with PEI is a result of a clear interaction between MOF and polymer observed in the IR spectra. In-situ cross-linking below the freezing point (cryopolymerization) did not lead to an improvement in the sorption properties of the composites. In contrast to the freeze-casting method, the molecular weight plays a critical role on the sorption properties of the composites fabricated by in-situ PVA cross-linking.

Other shaping processes were also examined in the section “unpublished results” (see section 4 for details). In addition to the shaping method mentioned above, the embedding of Alfum in a R,F-xerogel was also successfully prepared for loads of up to 57% with a pore accessibility of 89%. The cryopolymerization technique, in which PEI was chemically cross-linked, was also used to produce the MOF@PEI monolith. However, the prepared composite material was not obtained as a monolith with 81 wt%, 66 wt% and 51 wt% MOF. It was only possible to obtain a monolith with 36 wt% MOF, but the pore accessibility was only 11%.

List of abbreviations and symbols

Acac	Acetylacetone
Alfum	Aluminum fumarate
AHT	Adsorption heat transformation
BDC	1,4-Benzenedicarboxylate
BET	Brunauer-Emmett-Teller
DMF	*N,N'*-Dimethylformamide
DMSO	Dimethyl sulfoxide
EDX	Energy dispersive X-ray spectroscopy
EtOH	Ethanol
h	Hour(s)
IR	Infrared spectroscopy
IUPAC	International Union of Pure and Applied Chemistry
K	Kelvin
mg	(Milli)gram
MIL	Matériaux de l'Institut Lavoisier
min	Minute(s)
mL	Milliliter(s)
(m)mol	(Milli)mol, unit of amount of substance (1 mol $\hat{=}$ $6.022 \cdot 10^{23}$ particles)
MOF	Metal-organic framework
NLDFT	Nonlocal density functional theory
nm	Nanometer(s)
NMR	Nuclear Magnetic resonance
p	Pressure
PAA	Polyacrylic acid
PAANa	Sodium polyacrylate
PEG	Polyethylene glycol
PEI	Polyethylene imine
PVA	Polyvinyl alcohol
PVA1	Polyvinyl alcohol with an average M_w = 124 – 186 kDa, 99% hydrolyzed
PVA2	Polyvinyl alcohol with an average M_w = 125 kDa, 98% hydrolyzed
PVA3	Polyvinyl alcohol with an average M_w = 22 kDa, 97.5 – 99.5% hydrolyzed
PVA(98)	Polyvinyl alcohol with an average M_w of 125 kDa and 98% hydrolyzed
PVA(88)1	Polyvinyl alcohol with an average M_w of 10 - 26 kDa and 86-89% hydrolyzed
PVA(88)2	Polyvinyl alcohol with an average M_w of 31 kDa and 88% hydrolyzed
PVA(88)3	Polyvinyl alcohol with an average M_w of 67 kDa and 88% hydrolyzed
PVA(88)4	polyvinyl alcohol with an average M_w of 130 kDa and 88% hydrolyzed

PVA(88)5	Polyvinyl alcohol with an average M_w of 205 kDa and 88% hydrolyzed
PVP	Polyvinyl pyrrolidone
(P)XRD	(Powder) X-ray diffraction
Q_{ads}	Heat of adsorption
Q_{con}	Heat of condensation
Q_{des}	Heat of desorption
Q_{ev}	Heat of evaporation
QSDFT	Quench solid density functional theory
rt	Room temperature
R,F-xerogel	Resorcinol-formaldehyde based xerogel
SBU	Secondary building unit
SEM	Scanning electron microscopy
TGA	Thermogravimetric analysis
TMAOH	Tetramethylammonium hydroxide
wt%	Weight percentage (weight%)

Table of contents

1 Introduction

Section 1.1 contains the introduction of this dissertation in the form of a minireview, which was published in an international journal. The introduction is self-contained with a separate list of references.

1.1 Recent advances in adsorption heat transformation focusing on the development of adsorbent materials

Emrah Hastürk, Sebastian-Johannes Ernst, Christoph Janiak

Curr. Opin. Chem. Eng. 24 (2019) 26–36
DOI: 10.1016/j.coche.2018.12.011
Impact factor 2018: 4.463

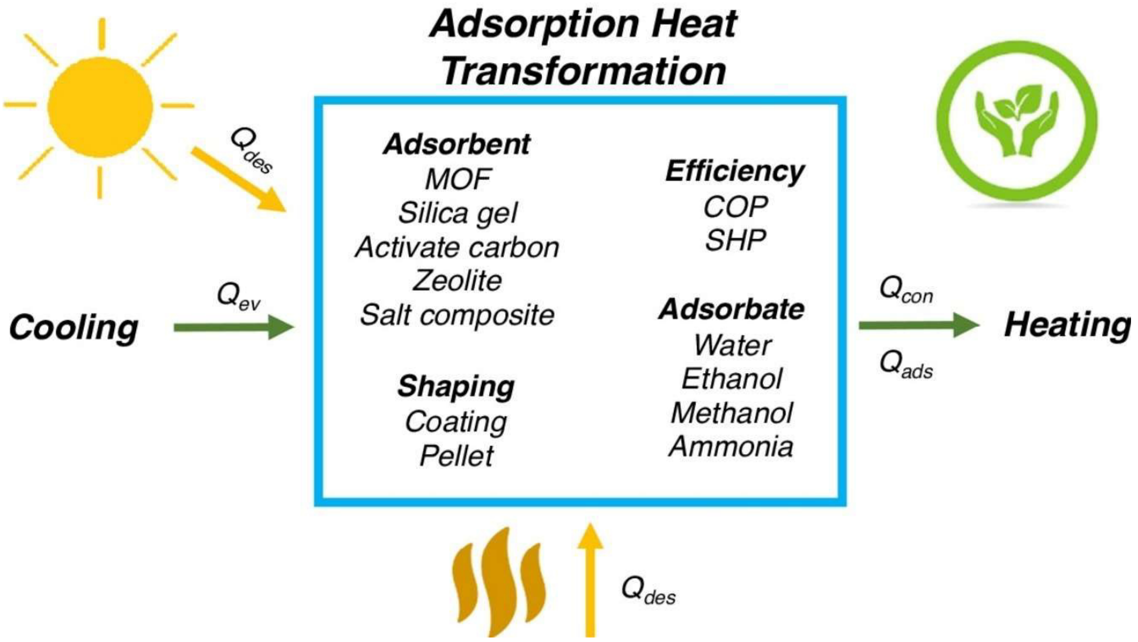

Graphical abstract

Abstract:

Adsorption heat transformation (AHT) is an environmentally friendly energy saving process applied for air conditioning purposes, that is, either for cooling (including also ice making and refrigeration), or heating. AHT is based on the cycling ad- and desorption of a working fluid in a porous material. When the working fluid is driven to evaporation by the active empty sorbent material the required heat of evaporation translates into useful cooling in thermally driven

adsorption chillers. Driving heat regenerates the empty sorbent material through desorption of the working fluid. The heat of adsorption in the sorbent material and the heat of condensation of the working fluid can be used in the adsorption heat-pumping mode. Thus, adsorption heat transformation contributes to energy saving technologies. Adsorbent development plays a critical role for the improvement of AHT technologies. Besides silica gel and zeolites as adsorbent materials, which are up to now used in the commercially available AHT devices; especially metal-organic frameworks (MOFs) are getting more attentions in recent years. Composite materials from salts with silica gels, zeolites and MOFs as well as activated carbons have also been researched to contribute to AHT technologies. Reduction of installation/production cost and enhancement of the efficiency of AHT devices need to be achieved to increase the wider usage of AHT.

Author’s share of work:

- Writing of the manuscript
- Editing of the manuscript regarding the reviewers’ comments together with Dr. Ernst and Prof. Janiak.

Reprinted with permission from the Journal Current Opinion in Chemical Engineering. Copyright 2018, with permission from Elsevier.

Available online at www.sciencedirect.com

ScienceDirect

Current Opinion in Chemical Engineering

Recent advances in adsorption heat transformation focusing on the development of adsorbent materials

Emrah Hastürk[1], Sebastian-Johannes Ernst[2] and Christoph Janiak[1]

Adsorption heat transformation (AHT) is an environmentally friendly energy-saving process applied for air conditioning purposes, that is, either for cooling (including also ice making and refrigeration), or heating. AHT is based on the cycling adsorption and desorption of a working fluid in a porous material. When the working fluid is driven to evaporation by the active empty sorbent material, the required heat of evaporation translates into useful cooling in thermally driven adsorption chillers. Driving heat regenerates the empty sorbent material through desorption of the working fluid. The heat of adsorption in the sorbent material and the heat of condensation of the working fluid can be used in the adsorption heat-pumping mode. Thus, adsorption heat transformation contributes to energy-saving technologies. Adsorbent development plays a critical role for the improvement of AHT technologies. Besides silica gel and zeolites as adsorbent materials, which are up to now used in the commercially available AHT devices; especially metal-organic frameworks (MOFs) are getting more attentions in recent years. Composite materials from salts with silica gels, zeolites and MOFs as well as activated carbons have also been researched to contribute to AHT technologies. Reduction of installation/production cost and enhancement of the efficiency of AHT devices need to be achieved to increase the wider usage of AHT.

Addresses
[1] Institut für Anorganische Chemie und Strukturchemie, Heinrich-Heine Universität, D-40204, Düsseldorf, Germany
[2] Fraunhofer Institute for Solar Energy Systems (ISE), Heidenhofstr. 2, 79110, Freiburg, Germany

Corresponding author: Janiak, Christoph (janiak@uni-duesseldorf.de)

Current Opinion in Chemical Engineering 2019, **24**:26–36

This review comes from a themed issue on **Separations engineering: advances in adsorption**

Edited by **Gennady Gor** and **Benoit Coasne**

https://doi.org/10.1016/j.coche.2018.12.011

Introduction

Increasing energy demand is one of the biggest issues for our civilizations and entails the search for alternative energy-saving technologies. Adsorption heat transformation (AHT) is a heating and cooling method, which belongs to present commercially available energy-saving and eco-friendly technologies; however, it requires further development for wider implementation. The advantages of AHT are eco-friendliness by avoiding halogenated refrigerants, silent operations by not using a compressor and the use of low temperature driving heat sources (solar, geothermal, industrial waste heat, etc.) for regeneration [1,2]. Disadvantages are large size [2,3], low efficiency, and high installation cost, and these aspects need to be improved for the development of AHT devices [4].

Working principle of AHT

AHT can be generally divided into closed and open operating systems. In the thermodynamic sense, 'closed' refers to a system with no exchange of matter but only the exchange of energy with the environment. Thus, also toxic working fluids such as methanol and ammonia can be used in such a closed system. In open AHT energy and matter are exchanged, for example, water vapor as an adsorbate is taken from and released to the environment. Furthermore, depending on the working conditions it is possible to use AHT either for cooling (including also ice making and refrigeration), or heating [5,6].

Adsorption-based heat transformation is a relatively old technology, which utilizes the thermodynamic principle to convert exothermic and endothermic processes into useable heating and cooling. The working principle of adsorption-based heat pumps and adsorption chillers is illustrated in Figure 1 [7]. During the adsorption and condensation process, heat is released as Q_{ads} and Q_{con}, which can be used for heating purposes. The liquid working fluid will be evaporated, during which heat is extracted as Q_{ev} from the environment performing the desired cooling [8,9].

The main benefit of adsorption heat transfer compared to conventional heating or compressor cooling systems is the utilization of waste heat for Q_{des} to drive the process in the regeneration step. In adsorption chillers, the heat of

Figure 1

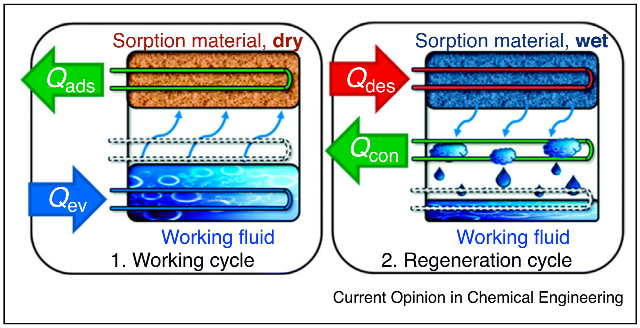

The working principle of sorption-based heat transformation consists of two switchable chambers with one of them being in the working and the other in the regeneration cycle. In the working cycle, a liquid working fluid is evaporated (under reduced pressure for water). The required heat of evaporation (Q_{ev}) is taken from the environment and leads to utilizable cooling. Heat of adsorption (Q_{ads}) is released when the dry sorption material starts to adsorb the working fluid. At sufficient loading of the sorption material, the chamber is switched to the regeneration cycle where heat of desorption (Q_{des}, also termed heat of regeneration) (from solar, geothermal, industrial waste heat etc.) is used as driving heat to desorb the working fluid from sorption material. The working fluid is condensed in the regeneration cycle, whereby heat of condensation (Q_{con}) is released.
Graphic was adapted from Ref. [7] with permission of the author, copyright the Royal Society of Chemistry 2012.

desorption Q_{des} is essentially transformed into useful cold by regenerating the wet sorption material, so that heat of evaporation Q_{ev} can be utilized. In the adsorption heat pumping mode, Q_{ads} and Q_{con} are utilized and Q_{ev} presents the additional energy gain from the environment to Q_{des} (ideally $Q_{ads} + Q_{con} = Q_{des} + Q_{ev}$).

The demands on the adsorbent can be derived from the application. Since AHT is a cyclic application, the adsorbent has to show a high hydrothermal stability under applied temperatures over thousands of cycles. The temperature boundaries are defined by the setup of the device and the specific application. An overview of the most common heat sources and sinks are listed in Table 1. A typical application is for instance a heat pump setup using an earth probe, a floor heating system and a water-based hydraulic circuit delivering desorption temperatures at slightly below 100°C. The vapor pressures at these temperatures ($p_S(T)$) can be used to calculate the relative pressure for adsorption and desorption at which the process step takes place:

$$\left(\frac{p}{p_0}\right)_{\text{ads}} = \frac{p_s(T_{evap})}{p_s(T_{ads})},\quad \left(\frac{p}{p_0}\right)_{\text{des}} = \frac{p_s(T_{cond})}{p_s(T_{des})}$$

For the described example, relative pressure is 0.22 for adsorption and 0.07 for desorption, respectively.

Table 1

Overview of temperature boundaries for AHT

	Application	Heat source	Temperature
Low temperature source	Heating	Earth probe	10°C
	Heating	Ambient air	−10 to 15°C
	Cooling	Ambience	−10 to 20°C
Mid temperature	Heating	Floor heating	35°C
	Heating	Radiator	60°C
	Cooling	Ambience	35°C
Desorption temperature		Waste heat	55–100°C
		Gas burner	>100°C

An adsorbent material should fulfill the following requirements in order to be suitable for AHT: (i) The sorption isotherm should have an S-shape (IUPAC classification Type V [10]) with a steep rise in the relative pressure range of $p/p_0 \approx 0.1–0.3$ for an effective profitable uptake in the adsorbent material [11]. The pressure range can vary depending on the desired working conditions described above. Additionally, no hysteresis is desired which reduces the usable part of the loading and causes loss of sensible heat [12,13]. The noted S-shape is advantageous because it enables a large lift of adsorption within a narrow relative pressure range [14]. (ii) The uptake or working capacity should be higher than 0.2 g/g [12], yet, for application, materials are better compared on capacity per unit volume, either a g/mL, mL/mL or kWh/m^3 [9]. The desired S-shape requirement is, however, not fulfilled by the water vapor sorption isotherm of silica gel. Despite its linear water sorption isotherm silica gel is often used in commercially available AHTs due to its comparably low price. However, adsorbents with linear water sorption require a broader temperature range to achieve a similar power output when compared with an adsorbent with S-shape sorption. (iii) Very essential is that the adsorbent is hydrothermally stable to over the desired 10-year or higher lifetime of the device, which amounts to over 100 000 adsorption–desorption cycles. (iv) Fast sorption kinetics and sufficient thermal conductivity for Q_{ads} and Q_{des} heat dissipation are also important properties, but these properties mostly rely on the whole system consisting of the adsorbent itself, eventually a binding agent, the heat transfer structure, the hydraulic circuits, the evaporator/condenser structure and so on. Especially, the form of the adsorbent and contact to the heat transfer structure are of main influence [15]. (v) Reasonable production costs of the adsorbent must be also considered for real life applications. Unfortunately, the production cost for MOFs as adsorbents are difficult to quantify in the view of the still low-scale production of many MOFs for research purposes. Such an analysis was done in the techno-economic analysis of four MOFs with possible use for natural gas storage, but not suitable for AHT, ending up with costs of around \$13/kg–\$36/kg [16]. First life-cycle assessment (LCA) calculations of two MOFs, namely CAU-10 and Alfum, revealed a higher GWP (global warming potential) and PENR (non-renewable primary energy demand) as compared to the also reported state-of-the-art materials zeolite 13X and silica gel. However, the number of cycles until brake-even will be reached is lower in case of the MOFs since these materials need either a lower desorption temperature (as compared to zeolite) or less material (as compared to silica gel) [17].

An important indicator for the energetic efficiency of the adsorption heat pump cycle is the so-called coefficient of performance (COP). This is determined as useful energy output divided by the required energy as input [9]. Below is the calculation of COP for heating (COP_H) and for cooling (COP_C) given as

$$COP_H = \frac{-(Q_{con} + Q_{ads})}{Q_{des}}, \quad COP_C = \frac{Q_{ev}}{Q_{des}}$$

The COP_C values range from zero to one and COP_H range from one to two [9]. For instance, in the screening work involving the adsorbents zeolites, silica gel, active carbon, composites and MOF materials for different adsorbates (water, methanol, ethanol, ammonia, acetone, benzene and *n*-butane) the COP_C value ranges from 0 to 0.6 with the COP_H value ranging from 1.0 to 1.2. The cycling operating conditions were given for cooling mode as 50°C (adsorption temperature), 50°C (condenser temperature), 5°C (evaporator temperature) and for heating mode 50°C (adsorption temperature), 50°C (condenser temperature), −23°C (evaporator temperature) [18••]. It is important to consider that the COP values vary with the working conditions. Working conditions depend also on the sorption properties of the adsorbent–adsorbate working pairs, which is demonstrated in Figures 3 and 4. Above mentioned working conditions were selected to demonstrate stringent conditions from the American Heating and Refrigeration Institute [18••].

It is difficult to compare conventional compressor cooling systems with AHT with respect to power density, which depends on the conditions and on the size of the systems. Energy storage capacity could also be taken into account for compression coolers but it is given for AHT based systems not for vapor compression systems. A sensible comparison to compression could be done by considering primary COP (PCOP), which is given for example for cooling as $PCOP_C$ (defined as the ratio of heat removed from the system to the total primary energy consumed), and which can be used to compare with AHT. Primary COP_C is given for typical air conditioners to less than one. The refrigeration system based on the MOF UiO-66 has $PCOP_C$ of 0.85, which is comparable with commercial vapor compression cooling systems [19].

Table 2

Selected adsorbents-adsorbate pairs with their sorption properties

Adsorbent	Adsorbate	Uptake g/g	Relative pressure p/p_0	Ref
MIL-101(Cr)	H_2O	1.60	0.50	[8]
$CaCl_2$-silica	H_2O	0.75	0.82	[27]
MIL-125(Ti)-NH_2	H_2O	0.53	0.25	[63]
BUT-46	H_2O	0.52	0.40	[65••]
Alfum	H_2O	0.35	0.35	[49]
MIL-160	H_2O	0.33	0.20	[56]
SAPO-34	H_2O	0.31	0.28	[33]
CAU-10-H	H_2O	0.30	0.20	[55]
MIL-53(Al)-TDC	H_2O	0.28	0.40	[59]
AQSOA®-FAM-Z02	H_2O	0.27	0.15	[32]
AQSOA®-FAM-Z01	H_2O	0.18	0.25	[32]
Silica gel	H_2O	0.10	0.15	[24]
MIL-101(Cr)	EtOH	0.98	0.30	[2]
KOH6-PR	EtOH	0.90	0.25	[22]
Maxsorb III	EtOH	0.84	0.25	[21]
LiCl-silica	MeOH	0.80	0.32	[28]
Silica gel	MeOH	0.15	–	[28]

This minireview focuses on very recent developments and research interests in the field of AHT, especially on the adsorbent–adsorbate working pairs, which are the centerpiece of adsorption chillers or heat pumps. While important MOFs will be discussed in more detail, zeolite, silica gel, activated carbon and some composites with salts will be also mentioned briefly. Some of the selected working pairs are listed in Table 2 with their adsorption properties. Enhancing efficiencies, shaping and a first prototype of a MOF-containing heat exchanger will be mentioned.

Activated carbon

Activated carbons are relatively low-cost hydrophobic materials with typical surface areas up between 300 and 2000 m^2/g, even if large surface areas up to 4000 m^2/g have been reported [20]. High alcohol and ammonia adsorption capacities make them interesting for AHT application.

Maxsorb III is a commercially available activated carbon with high S(BET) of around 3000 m^2/g, and indicated as one of the best candidates for AHT applications using alcohols as adsorbates with an ethanol uptake of 1.2 g/g [18••,21]. Recently, an activated carbon which was obtained from waste palm trunk and mangrove with S (BET) of nearly 3000 m^2/g showed an even significantly higher ethanol uptake with 1.8 g/g than Maxsorb III [21].

Another important example is the activated carbon KOH6-PR, which was prepared from phenol resin. KOH6-PR recorded as its highest ethanol adsorption ca. 2 g/g [22].

Silica gel

As mentioned above silica gel is one of the most used adsorbents in commercially available AHTs. Although silica gel has a quite linear water uptake curve instead of the ideal S-shaped isotherm with an overall low water uptake of 0.03–0.1 g/g for a typical AHT cycle giving a low heat storage capacity [23,24], silica gel is preferred as adsorbent mainly because of its low cost and stability. In contrast, the COP_C value can reach nearly 0.9 due to the lower affinity of silica gel to water vapor, requiring also only a low heat of desorption input [25]. Because of the low cost and availability, the development of AHTs based on silica gel focuses in recent years generally on the design and formation of composite materials. For instance, a recently developed new AHT technique, called 'Heat from Cold' (HeCol), uses LiCl-silica gel/methanol as working pairs. In the HeCol technique, depressurization is applied at low ambient temperature for regeneration instead of regeneration at a constant pressure by heating up to 80–150°C, which is the case for conventional regeneration cycles of an adsorption heat pump. This method has the advantages to be applied in colder climates for heat pumping mode [26].

Screening simulation including silica gel, zeolite and activated carbon as adsorbent and water, methanol and ethanol as adsorbate indicate LiBr-silica and $CaCl_2$-silica (water adsorption of 0.75 g/g at $p/p_0 = 0.82$ and 28°C [27]) as one of the best adsorbents with the working fluid water for air conditioning and heat pumping. COP_H and COP_C value of these composites with water are around 1.62 and 0.71, respectively. Heating and cooling enthalpy of that working pairs are around 1080 kJ/kg (300 Wh/kg) and 570 kJ/kg (158 Wh/kg). The LiCl–silica/methanol working pair (MeOH adsorption of 0.80 g/g at $p/p_0 = 0.32$ and 28°C [28]) exhibited a high performance for air conditioning cycles, with a cooling enthalpy $Q_{ev} = 640$ kJ/kg (178 Wh/kg). For refrigeration, where water cannot be used because of freezing, LiBr-silica with methanol and ethanol was indicated as the best promising working pair with COP_C in the range 0.53–0.59 having a cooling enthalpy of 180 kJ/kg (50 Wh/kg) [29•].

Zeolites

Zeolites are naturally occurring as well as synthetic porous materials based on the combination of $[SiO_4]$ and $[AlO_4]$ tetrahedrons with different ratio of Si to Al. One of the biggest disadvantageous of zeolites for AHT is their too high hydrophilicity, which requires higher desorption temperatures up to 120°C [30].

Ion exchange in the zeolites allows tuning their vapor sorption properties. In a recent example, this was achieved by stirring zeolite with magnesium nitrate solution resulting in up to 42% and 24% more water uptake, at $p/p_0 = 0.2$ and 0.9, respectively [31]. This improvement also held for the sorption performance of the ion exchanged zeolite with an adsorbate mixture of 20% MeOH and 80% H_2O. The MeOH–H_2O mixture has a lower boiling point (86°C) than water alone which means a heightened vapor pressure and lower freezing point (−18°C). Because of the depressed freezing point, the evaporator can be used at subzero temperatures, below the freezing point of water. This could be beneficial to enhance the cooling efficiency of adsorption heat pumps [31].

In the above simulations, Mitsubishi's adsorbent AQSOA®-FAM-Z02 (water uptake of 0.27 g/g at $p/p_0 = 0.15$ [32]) and the SAPO-34 zeolite (water uptake of 0.31 g/g at $p/p_0 = 0.15$ [33]) with water as adsorbate was denoted as one of the best working pair candidates for air conditioning and heat pumping similar in performance to LiBr-silica and $CaCl_2$-silica. The COP_C, COP_H, cooling enthalpy and heating enthalpy of AQSOA®-FAM-Z02 and SAPO-34 were similar to LiBr-silica and $CaCl_2$-silica (see above) [29•].

The disadvantageous large size (volume) of AHT devices was addressed by using zeolite ferroaluminophosphate (FAM-Z01 with a water uptake of 0.18 g/g at $p/p_0 = 0.25$ [32]) [34]. FAM-Z01 enabled a reduction of system size with comparable COP_C (0.59 for FAM-Z01 and 0.61 for silica gel) and larger specific cooling power (280 for FAM-Z01 and 207 for silica gel) than regular density type silica gel/water (all values at evaporation temperature of 10°C and regeneration temperature of 70°C).

MOFs

Metal-organic frameworks (MOFs) are metal-ligand coordination networks with organic ligands containing potential voids [35]. Porous MOFs are getting continuous attention because of their well-defined network structure, their variability and tunability. Besides possible use for gas storage-separation, catalysis or drug delivery [36], MOFs promise potential for heat transformation applications. Among more than 70 000 different MOFs (untill 2017) [37] only a few of them are suitable for heat transformation applications. An essential property which must be fulfilled for AHT is a very high hydrothermal stability which drastically limits the available number of MOFs as many of them are not very water stable [38]. In this minireview, we cover only the promising ones based on uptake capacity and hydrothermal stability.

MIL-101(Cr) is a hydrothermally synthesized MOF with terephthalate (benzene-1,4-dicarboxylate) as linker and a very large surface area up to 4100 m^2/g and S-type vapor sorption isotherm above 0.4 relative vapor pressure with water uptakes of up to 1.6 g/g [8]. Over 40 water sorption cycles MIL-101(Cr) showed very little loss (3.2%) on the water sorption capacity [39]. Although the steep part of the sorption isotherm does not take place in the desired relative pressure range, the highest water uptake in the field of MOF chemistry below 0.6 relative pressure make MIL-101(Cr) and its derivatives very attractive for the many research groups. The focus is to create a more hydrophilic structure preserving the fundamental skeleton of MIL-101. The effect of water sorption by even partial functionalization of the linker benzene ring with hydrophilic –NHCOCHCHCOOH, $–NH(CH_2)_3SO_3H$, –COOH, $–NO_2$ and $–NH_2$ groups showed a hydrophilic shift to lower relative pressure. However, owing to the space required by the functional groups a simultaneous reduction of the water sorption capacity relative to the parent MIL-101(Cr) was often observed [13,40].

Grafting of hydrophilic ligands, for example 3-[2-(2-aminoethylamino)ethylamino]propyl-trimethoxysilane (PAPTS), on coordinatively unsaturated chromium sites is also another approach to tune water uptake of MIL-101 (Cr) to relative low vapor pressure [41]. Although water uptake of PAPTS-grafted MIL-101(Cr) at $p/p_0 > 0.4$ is lower compared to the parent MIL-101(Cr), the grafted MIL-101(Cr) adsorbs about 25% more water than native MIL-101(Cr) at a relative pressure of 0.4 [41]. A grafting strategy was also previously applied on the still too hydrophobic MIL-100(Cr), to try to achieve enhancement of water uptake especially in the desired low relative pressure range [42].

The composite of MIL-101(Cr) with 62 wt% $CaCl_2$ salt loading [43•] has only a low remaining S(BET) of 330 m^2/g, but the water vapor uptake was not too much reduced, due to the absorption capacity of the incorporated hygroscopic salt. Thus, the $CaCl_2$@MIL-101(Cr) composite featured an improved energy storage capacity with a very high value of 450 Wh/kg [43•], compared to 87 Wh/kg of parent MIL-101(Cr) in the cycle conditions of 30°C and 1.2 kPa for adsorption and 80°C and 1.25 kPa for desorption [44•].

The usage of MIL-101(Cr) as a working pair with alcohols for adsorption chillers is controversial. The high affinity of alcohols to MIL-101(Cr) requires higher desorption temperature related to the Type-I(b) sorption isotherm up to $p/p_0 \approx 0.1$ with an uptake of about 0.46 g/g out of a total uptake of about 1.1 g/g up to $p/p_0 \approx 0.3$ [2]. Yet, this behavior may not necessarily prevent for the usage of MIL-101(Cr) in adsorption chillers and other data indicated a better performance over known activated carbons in terms of uptake of 0.51 g/g of ethanol in the operating conditions 120°C–29°C–7°C (temperature level of heat source, heat rejection/condenser, and evaporator) [45]. Furthermore, in the screening experiments for the working pairs, MIL-101(Cr) and ethanol were designated as one of the best combinations [18••]. Both for EtOH and MeOH, the maximum COP_H value of MIL-101(Cr) was slightly higher than 1.2, which is more than is given in the same work for the activated carbon AX-21/NH_3 working pair (max. $COP_H \approx 1.17$) or silica gel salt composite (SP18)/$CaCl_2$(23 wt%) and MeOH (max. $COP_H \approx 1.15$) [18••]. The cycling operating conditions were 50°C (adsorption and condenser temperature), 5°C (evaporator temperature) for the cooling mode and 50°C (adsorption and condenser temperature), −23°C (evaporator temperature) for the heating mode.

The microcrystalline MOF powders are not susceptible to be used in heat exchangers without formulation, due to dusting because of small particle size and their low thermal conductivity [46]. Shaping of MOFs is, therefore, an important issue for AHT applications. Shaping aspect can be addressed by embedding MOFs in organic polymers, for example, MIL-101(Cr) powder in resorcinol-formaldehyd (R,F) xerogels. This led to formation of stable monolithic forms with a loading of up to 77 wt% of MIL-101(Cr). The composite showed the S-shaped isotherm of the neat MOF and a water uptake of up to 0.88 g/g, which corresponds to 100% retention of pore accessibility of the embedded MOF [47].

Aluminum fumarate (Alfum, commercially also known as Basolite^{TM} A520) is one of the MOFs, which can be produced from cheap aluminum salts and fumaric acid in water at 60°C [48]. Alfum has a S(BET) of around 1000 m^2/g and an S-type water sorption isotherm with an uptake up of nearly 0.35 g/g in the narrow relative pressure range of 0.2–0.3 [49]. Theoretical calculations support the much better cooling performance for Alfum compared to silica gel and AQSOA-Z02, which are currently used in commercially available devices [50]. Alfum showed no degradation over 4500 adsorption–desorption cycles [49]. Because of its high feasibility for AHT applications, a 385 mm × 160 mm × 110 mm heat exchanger was coated with 493 g Alfum, which exhibited a gross cooling power of 2900 W (at the beginning of the adsorption cycle, Figure 2c), 1000 W for a half cycle time of t = 74 s or an average cooling power of 690 W (up to a limit of 90% equilibrium loading in 7 min) under the working conditions of a realistic adsorption chiller of 90°C–30°C–18°C (temperature level of heat source, heat rejection/condenser and evaporator) [51•]. Related to this matter, cycle duration varies depending on the working point of the devices. For instance, a recommended cycle switch time, being an essential parameter for cooling capacity, should be at least two minutes [52]. A very important figure of merit for an adsorption module is the volume specific heating/cooling power (VSHP/VSCP)

$$VSHP = \frac{Q_{ads} + Q_{cond}}{2\tau_{hc}V_{mod}}, \qquad VSCP = \frac{Q_{evap}}{2\tau_{hc}V_{mod}}$$

Wherein τ_{hc} represents the time of a half cycle and V_{mod} the volume of the module. As has been shown in the literature [53] COP and VSHP/VSCP are somehow contradictory. This can clearly be seen from Figure 2c, where the power decreases with time, whereas the amount of heat contributing to the COP increases. Consequently,

Figure 2

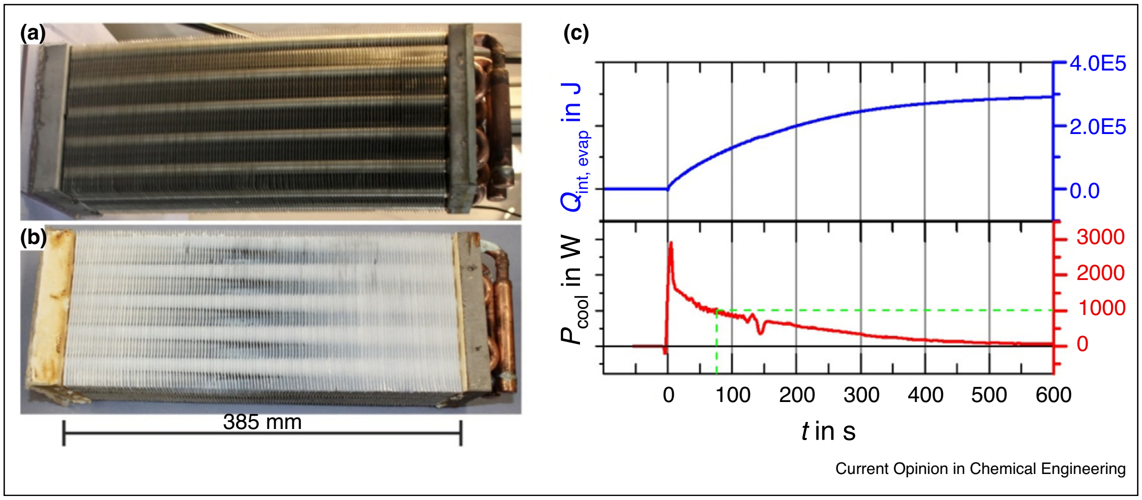

Heat-exchanger **(a)** before and **(b)** after coating with 493 g of the aluminum fumarate MOF and drying. **(c)** Gross cooling power P_{cool} of the aluminum fumarate-coated heat exchanger for operating conditions 90°C–30°C–18°C (red line, lower part; temperature level of heat source, heat rejection/condenser and evaporator), calculated from the integral heat of evaporation $Q_{\text{int,evap}}$ (blue line, upper part). The green line indicates $P_{\text{Cool}} = 1000$ W for a half cycle time of $t = 74$ s.
Figures were taken from Ref. [51•] with permission from the author, copyright the American Chemical Society 2017.

the cycle time is an optimization parameter that can be chosen with respect to either a higher COP or a higher VSHP/VSCP.

Furthermore, adding excess formic acid as a modulator to the preparation of aluminum fumarate showed that water adsorption kinetics can be improved due to the enhanced uniform micro-pore distribution [54]. Starting from the adsorbed state at $p/p_0 = 0.3$, 25°C, for instance, Alfum formed by addition of formic acid achieved the thermodynamic desorbed equilibrium state at $p/p_0 = 0.25$, 60°C in 1600 s, whereas Alfum without any additional formic acid achieved the same equilibrium in 3000 s. In that work, the modulator was applied in a problematic dimethylformamide (DMF) based synthesis, which should be modified to a water-based preparation in the interest of green chemistry.

CAU-10-H is another promising MOF for water sorption-based applications [55]. This MOF consists of aluminum metal ions, hydroxido bridges and isophthalate linkers. It possesses an S-shaped water sorption with an uptake around 0.30 g/g at a relative vapor pressure of about 0.2 [55]. The cyclic stability of CAU-10-H was tested up to 10 000 water adsorption–desorption cycles showing no loss in water loading and crystallinity. At present, CAU-10-H was denoted as the most hydrothermal stable MOF under cycling conditions between 40°C adsorption and 140°C desorption temperature [12]. Figure 3 left presents the water uptake capacity of CAU-10-H at different heat rejection and chilling (evaporating) temperature during the adsorption process (working cycle in Figure 1). The maximum water uptake (dark red region) can be reached at a chilling temperature above 12°C together with a maximum heat rejection temperature of about 32°C. Alternatively, if the heat rejection is lowered to 26°C, the chilling temperature can drop to about 6°C. Additionally, for regeneration (regeneration cycle in Figure 1) the desorption temperature is most important and can be as low as 75°C (red line in Figure 3 right) in order to achieve complete drying of the adsorbent. At the same time, the condenser temperature can vary from 28 to 35°C [12].

MIL-160 is based on Al^{3+} with the linker 2,5-furandicarboxylate [44•], isostructural to CAU-10-H, and shows promising water sorption properties with an uptake of around 0.33 g/g at $p/p_0 \approx 0.2$ [56]. Albeit not emphasized, part of the aforementioned studies with Alfum and CAU-10-H was also the shaping of the MOFs with polysiloxane binders to achieve a stable coating on the metal support (cf. Figure 2) MIL-160 was shaped into pellets via wet granulation and exhibited similar, mass-corrected sorption properties as the neat MOF. A heat-reallocation open-system reactor prototype containing MIL-160 pellets revealed one of the best performances with an energy storage density of 141 kW h/m^3, which is slightly higher than the energy storage density of Zeolite 13 X with a value 131 kW h/m^3, both after complete evacuation [44•].

MIL-53(Al)-TDC with Al^{3+} and the linker 2,5-thiophenedicarboxylate [57] was first predicted to show good water sorption properties [58]. In the follow-up experimental study, MIL-53(Al)-TDC was shown to have a

Figure 3

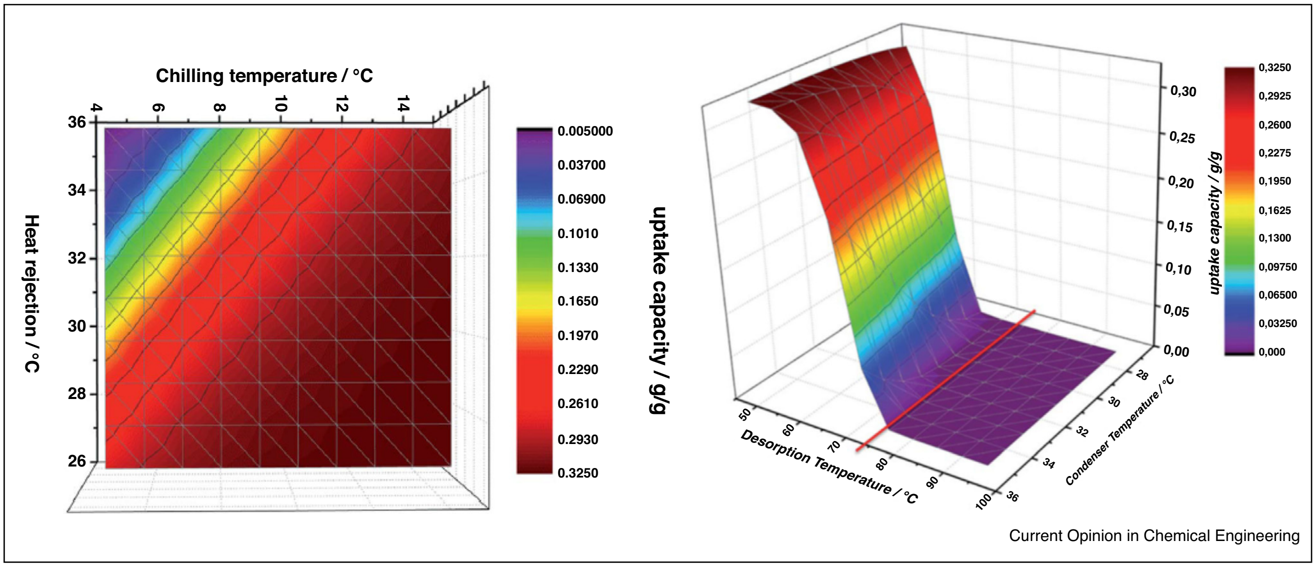

Current Opinion in Chemical Engineering

Left: water uptake capacity of CAU-10-H as a function of heat rejection temperature and evaporation (chilling) temperature. Right: Desorption temperature and condenser temperature necessary to achieve adsorbent regeneration (drying, water removal). (Note that in the original publication, the respective figure captions or figures need to be interchanged).
Figures were taken from Ref. [12] with permission from the author, copyright the Royal Society of Chemistry 2016.

higher surface area and suitable water sorption properties than was estimated before. The hydrothermal stability of MIL-53(Al)-TDC was tested to over 40 adsorption–desorption cycles with feasible water uptake of 0.28 g/g at around $p/p_0 = 0.4$ without little hysteresis and the low heat of adsorption (2.6 kJ/g = 0.72 Wh/g). These properties make MIL-53(Al)-TDC a good candidate for adsorption-based chillers [59]. In Figure 4 left, it can be seen that the maximum water uptake (dark red region) can be reached at an evaporation temperature above 15°C together with a heat rejection temperature below 25°C. Additionally, for regeneration (regeneration cycle in Figure 1) the desorption temperature can be as low as 55–60°C (Figure 4 right), with the condenser temperature above 40°C in order to achieve complete drying of the adsorbent.

Figure 4

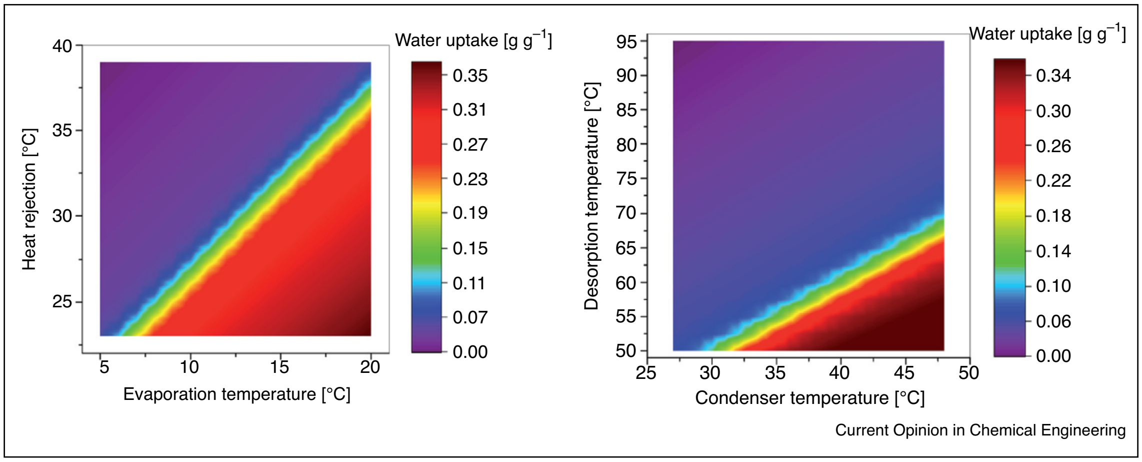

Current Opinion in Chemical Engineering

Left: water uptake capacity of MIL-53(Al)-TDC as a function of heat rejection temperature and evaporation temperature. Right: Estimation of water uptake capacity as a function of desorption temperature and condensing temperature.
Figures were taken from Ref. [59] with permission from the author, copyright the Royal Society of Chemistry 2018.

Figure 5

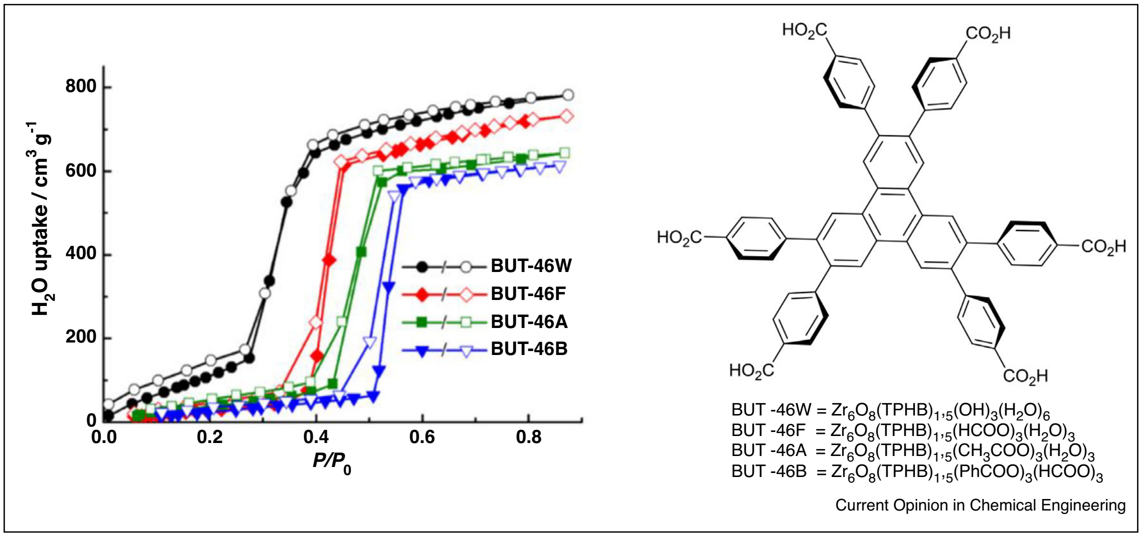

Current Opinion in Chemical Engineering

Left: water adsorption–desorption isotherms of the BUT-46 series. Right: Chemical structure of H_6TPHB ligand and molecular formulae of the BUT-46 series.
Figure 5 left was used with permission from Ref. [65••], copyright the American Chemical Society 2018.

MIL-53(Al)-TDC gave below 0.1 p/p_0 a steep uptake of ethanol, however with a very strong (unclosed) hysteresis in the desorption curve [60].

Another important candidate for AHT application is **MIL-125(Ti)-NH$_2$** [61]. As it showed promising water uptake of slightly over 0.30 g/g at 20°C with an S-shaped isotherm in the relative pressure range of 0.1 and 0.25 [62]. Over 40 adsorption–desorption cycles MIL-125(Ti)-NH$_2$ exhibited a degradation of 17%. Later on, the synthesis using Ti(BuO)$_4$ instead of Ti(*i*PrO)$_4$ as Ti sources led to improved 0.50 g/g water uptake even at 35°C in the relative pressure range of 0.1 and 0.25 [63,64]. Over 10 adsorption–desorption cycles the new MIL-125 (Ti)-NH$_2$ showed only very low decrease in water uptake. Yet, to consider this MOF further for AHT devices it must be clearly be tested for more adsorption–desorption cycles.

An isostructural **BUT-46** series, with Zr^{4+} as metal ion, $TPHB^{6-}$ (4,4′,4″,4‴,4⁗,4‴″-(triphenylene-2,3,6,7,10,11-hexayl)hexabenzoate) as linker and different terminal functional groups show promising water sorption properties at the relative pressure of 0.4 with a steep uptake of around 0.52 g/g [65••]. Although the members of the BUT-46 series have similar S(BET), changing the terminal functional groups affects hydrophilicity (p/p_0 range) and water uptake capacity of the MOFs (Figure 5). However, the multistep synthesis of the linker may make these MOFs unattractive for larger-scale applications.

Conclusion

AHT applications are receiving a strongly renewed interest in the last decades because they are economical and ecologically beneficial compared to conventional heat transformation, for example, electricity-run compressor air conditioners. However, the existing adsorbent materials such as silica gel used in the commercial available devices suffer from their low efficiency. MOFs were for about 10 years now investigated more specifically for cycling water sorption for heat transformation and gave the opportunity to enhance and tune vapor sorption through their designable pore structures. In the last years MOFs were developed with promising water sorption properties such as the desired S-shape isotherm in a low p/p_0 region, high water uptake and hydrothermal stability. However, one of the disadvantages of the MOFs is the more expensive production cost, the necessity for shaping the otherwise microcrystalline powders and the still not fully long-term proven stability. Considering the easy synthesis of MIL-160, which is prepared under reflux from aluminum salts and 2,5-furandicarboxylate (which can be derived from renewable biomass), MIL-160 could be an alternative to SAPO-34. Additionally, Alfum is easy to prepare from abundant starting materials and could be an alternative for silica for cooling purposes. On the other hand, composite materials of zeolites and silica gel with salts like LiCl or CaCl$_2$ are also gaining interest for their increased uptake and heat transformation enthalpies.

Conflict of interest statement

Nothing declared.

Acknowledgements

The authors gratefully acknowledge the financial support of the Federal German Ministry of Education and Research (BMBF) in the project Optimat under grant no. 03SF0492A/C.

References and recommended reading

Papers of particular interest, published within the period of review, have been highlighted as:

- • of special interest
- •• of outstanding interest

1. Al-Mousawi FN, Al-Dadah R, Mahmoud S: **Low grade heat driven adsorption system for cooling and power generation with small-scale radial inflow turbine**. *Appl Energy* 2016, **183**:1302-1316 http://dx.doi.org/10.1016/j.apenergy.2016.09.061.
2. de Lange MF, van Velzen BJ, Ottevanger CP, Verouden KJFM, Lin LC, Vlugt TJH, Gascon J, Kapteijn F: **Metal-organic frameworks in adsorption-driven heat pumps: the potential of alcohols as working fluids**. *Langmuir* 2015, **31**:12783-12796 http://dx.doi.org/10.1021/acs.langmuir.5b03272.
3. Meunier F: **Adsorption heat powered heat pumps**. *Appl Therm Eng* 2013, **61**:830-836 http://dx.doi.org/10.1016/j.applthermaleng.2013.04.050.
4. Settino J, Sant T, Micallef C, Farrugia M, Staines CS, Licari J, Micallef A: **Overview of solar technologies for electricity, heating and cooling production**. *Renew Sustain Energy Rev* 2018, **90**:892-909 http://dx.doi.org/10.1016/j.rser.2018.03.112.
5. Pons M, Poyelle F: **Adsorptive machines with advanced cycles for heat pumping or cooling applications**. *Int J Refrig* 1999, **22**:27-37 http://dx.doi.org/10.1016/S0140-7007(97)00042-X.
6. Ugale VD, Pitale AD: **A review on working pair used in adsorption cooling system**. *Int J Air-Cond Refrig* 2015, **23** http://dx.doi.org/10.1142/S2010132515300013 1530001(1–11).
7. Jeremias F, Khutia A, Henninger SK, Janiak C: **MIL-100(Al, Fe) as water adsorbents for heat transformation purposes a promising application**. *J Mater Chem* 2012, **22**:10148-10151 http://dx.doi.org/10.1039/C2JM15615F.
8. Jeremias F, Fröhlich D, Janiak C, Henninger S: **Water and methanol adsorption on MOFs for cycling heat transformation processes**. *New J Chem* 2014, **38**:1846-1852 http://dx.doi.org/10.1039/C3NJ01556D.
9. de Lange MF, Verouden KJFM, Vlugt TJH, Gascon J, Kapteijn F: **Adsorption-driven heat pumps: the potential of metal−organic frameworks**. *Chem Rev* 2015, **115**:12205-12250 http://dx.doi.org/10.1021/acs.chemrev.5b00059.
10. Thommes M, Kaneko K, Neimark AV, Olivier JP, Rodriguez-Reinoso F, Rouquerol J, Sing KSW: **Physisorption of gases, with special reference to the evaluation of surface area and pore size distribution (IUPAC technical report)**. *Pure Appl Chem* 2015, **87**:1051-1069 http://dx.doi.org/10.1515/pac-2014-1117.
11. Aristov YI: **Challenging offers of material science for adsorption heat transformation: a review**. *Appl Therm Eng* 2013, **50**:1610-1618 http://dx.doi.org/10.1016/j.applthermaleng.2011.09.003.
12. Fröhlich D, Pantatosaki E, Kolokathis PD, Markey K, Reinsch H, Baumgartner M, van der Veen MA, De Vos DE, Stock N, Papadopoulos GK *et al.*: **Water adsorption behaviour of CAU-10-H: a thorough investigation of its structure–property relationships**. *J Mater Chem A* 2016, **4**:11859-11869 http://dx.doi.org/10.1039/C6TA01757F.
13. Khutia A, Rammelberg HU, Schmidt T, Henninger S, Janiak C: **Water sorption cycle measurements on functionalized MIL-101Cr for heat transformation application**. *Chem Mater* 2013, **25**:790-798 http://dx.doi.org/10.1021/cm304055k.
14. Henninger SK, Jeremias F, Kummer H, Janiak C: **MOFs for use in adsorption heat pump processes**. *Eur J Inorg Chem* 2012:2625-2634 http://dx.doi.org/10.1002/ejic.201101056.
15. Kühn A, Schicktanz M, Witte KT, Füldner G, Henninger SK: **Thermally driven heat pumps for heating and cooling, Ch. 6**. *Research on Working Pairs and Apparatus Technology*. Universitätsverlag der TU Berlin; 2013:203-214 http://dx.doi.org/10.14279/depositonce-3726.
16. DeSantis D, Mason JA, James BD, Houchins C, Long JR, Veenstr M: **Techno-economic analysis of metal-organic frameworks for hydrogen and natural gas storage**. *Energy Fuels* 2017, **31**:2024-2032 http://dx.doi.org/10.1021/acs.energyfuels.6b02510.
17. Horn R, Burr M, Fröhlich D, Gschwander S, Held M, Lindner JP, Munz G, Nienborg B, Schossig P: **Life cycle assessment of innovative materials for thermal energy storage in buildings**. *Procedia* 2018, **69**:206-211 http://dx.doi.org/10.1016/j.procir.2017.11.095.
18. Boman DB, Hoysall DC, Pahinkar DG, Ponkala MKJ, Garimella S:
•• **Screening of working pairs for adsorption heat pumps based on thermodynamic and transport characteristics**. *Appl Therm Eng* 2017, **123**:422-434 http://dx.doi.org/10.1016/j.applthermaleng.2017.04.153.

This paper gives a comparative study between the important working pairs for AHT applications.

19. Bagheri MH, Schiffres Scott N: **Ideal adsorption isotherm behavior for cooling applications**. *Langmuir* 2018, **34**:1908-1915 http://dx.doi.org/10.1021/acs.langmuir.7b03989.
20. Xiao Y, Chen H, Zheng M, Dong H, Lei B, Liu Y: **Porous carbon with ultrahigh specific surface area derived from biomass rice hull**. *Mater Lett* 2014, **116**:185-187 http://dx.doi.org/10.1016/j.matlet.2013.11.007.
21. Pal A, Thu K, Mitra S, El-Sharkawy II, Saha BB, Kil H-S, Yoon S-H, Miyawaki J: **Study on biomass derived activated carbons for adsorptive heat pump application**. *Int J Heat Mass Transf* 2017, **110**:7-19 http://dx.doi.org/10.1016/j.ijheatmasstransfer.2017.02.081.
22. El-Sharkawy II, Uddin K, Miyazaki T, Saha BB, Koyama S, Kil H-S, Yoon S-H, Miyawaki J: **Adsorption of ethanol onto phenol resin based adsorbents for developing next generation cooling systems**. *Int J Heat Mass Transf* 2015, **81**:171-178 http://dx.doi.org/10.1016/j.ijheatmasstransfer.2014.10.012.
23. Vasta S, Brancato V, La Rosa D, Palomba V, Restuccia G, Sapienza A, Frazzica A: **Adsorption heat storage: state of the art and future perspectives**. *Nanomaterials* 2018, **8** http://dx.doi.org/10.3390/nano8070522 522 (1-13).
24. Chua HT, Ng KC, Chakraborty A, Oo NM, Othman MA: **Adsorption characteristics of silica gel + water systems**. *J Chem Eng Data* 2002, **47**:1177-1181 http://dx.doi.org/10.1021/je0255067.
25. Aristov Y: **Concept of adsorbent optimal for adsorptive cooling/heating**. *Appl Therm Eng* 2014, **72**:166-175 http://dx.doi.org/10.1016/j.applthermaleng.2014.04.077.
26. Voskresenskii NM, Okunev BN, Gordeeva LG: **A thermodynamic analysis of a new cycle for adsorption heat pump “Heat from Cold”: effect of the working pair on cycle efficiency**. *Therm Eng* 2018, **65**:524-530 http://dx.doi.org/10.1134/S0040601518080098}.
27. Aristov YI, Restuccia G, Cacciola G, Parmon VN: **A family of new working materials for solid sorption air conditioning systems**. *Appl Therm Eng* 2002, **22**:191-204 http://dx.doi.org/10.1016/S1359-4311(01)00072-2.
28. Gordeeva LG, Freni A, Krieger TA, Restuccia G, Aristov YI: **Composites “lithium halides in silica gel pores”: methanol sorption equilibrium**. *Microporous Mesoporous Mater* 2008, **112**:254-261 http://dx.doi.org/10.1016/j.micromeso.2007.09.040.
29. Freni A, Maggio G, Sapienza A, Frazzica A, Restuccia G, Vasta S:
• **Comparative analysis of promising adsorbent/adsorbate pairs for adsorptive heat pumping, air conditioning and refrigeration**. *Appl Therm Eng* 2016, **104**:85-95 http://dx.doi.org/10.1016/j.applthermaleng.2016.05.036.

This work presents some of the important adsorbents and composites including comparison of their COP values.

30. Henninger SK, Ernst S-J, Gordeeva L, Bendix P, Fröhlich D, Grekova AD, Bonaccorsi L, Aristov Y, Jaenchen J: **New materials**

for adsorption heat transformation and storage. *Renew Energy* 2017, **110**:59-68 http://dx.doi.org/10.1016/j.renene.2016.08.041.

31. Li X, Narayanan S, Michaelis VK, Ong T-C, Keeler EG, Kim H, McKay IS, Griffin RG, Wang EN: **Zeolite Y adsorbents with high vapor uptake capacity and robust cycling stability for potential applications in advanced adsorption heat pumps**. *Microporous Mesoporous Mater* 2015, **201**:151-159 http://dx.doi.org/10.1016/j.micromeso.2014.09.012.

32. Kakiuchi H, Shimooka S, Iwade M, Oshima K, Yamazaki M, Terada S, Watanabe H, Takewaki T: **Water Vapor Adsorbent FAM-Z02 and Its Applicability to Adsorption Heat Pump**. *Energy* 2005, **31**:273-277 http://dx.doi.org/10.1252/kakoronbunshu.31.273.

33. Luo Y, Funke HH, Falconer JL, Noble RD: **Adsorption of CO_2, CH_4, C_3H_8, and H_2O in SSZ-13, SAPO-34, and T-type zeolites**. *Ind Eng Chem Res* 2016, **55**:9749-9757 http://dx.doi.org/10.1021/acs.iecr.6b02034.

34. Hong SW, Ahn SH, Chung JD, Bae KJ, Cha DA, Kwon OK: **Characteristics of FAM-Z01 compared to silica gels in the performance of an adsorption bed**. *Appl Therm Eng* 2016, **104**:24-33 http://dx.doi.org/10.1016/j.applthermaleng.2016.05.058.

35. Batten SR, Champness NR, Chen X-M, Garcia-Martinez J, Kitagawa S, Öhrström L, O'Keeffe M, Suh MP, Reedijk J: **Terminology of metal–organic frameworks and coordination polymers (IUPAC recommendations 2013)**. *Pure Appl Chem* 2013, **85**:1715-1724 http://dx.doi.org/10.1351/PAC-REC-12-11-20.

36. Li B, Wen H-M, Cui Y, Zhou W, Qian G, Chen B: **Emerging multifunctional metal-organic framework materials**. *Adv Mater* 2016, **28**:8819-8860 http://dx.doi.org/10.1002/adma.201601133.

37. Moghadam PZ, Li A, Wiggin SB, Tao A, Maloney AGP, Wood PA, Ward SC, Fairen-Jimenez D: **Development of a Cambridge structural database subset: a collection of metal-organic frameworks for past, present, and future**. *Chem Mater* 2017, **29**:2618-2625 http://dx.doi.org/10.1021/acs.chemmater.7b00441.

38. Leus K, Bogaerts T, De Decker J, Depauw H, Hendrickx K, Vrielinck H, Van Speybroeck V, Van Der Voort P: **Systematic study of the chemical and hydrothermal stability of selected "stable" metal organic frameworks**. *Microporous Mesoporous Mater* 2016, **226**:110-116 http://dx.doi.org/10.1016/j.micromeso.2015.11.055.

39. Ehrenmann J, Henninger SK, Janiak C: **Water adsorption characteristics of MIL-101 for heat-transformation applications of MOFs**. *Eur J Inorg Chem* 2011, **4**:471-474 http://dx.doi.org/10.1002/ejic.201001156.

40. Ko N, Choi PG, Hong J, Yeo M, Sung S, Cordova KE, Park HJ, Yang JK: **Tailoring the water adsorption properties of MIL-101 metal-organic frameworks by partial functionalization**. *J Mater Chem A* 2015, **3**:2057-2064 http://dx.doi.org/10.1039/c4ta04907a.

41. Liu Z, Chen Y, Sun J, Lang H, Gao W, Chi Y: **Amine grafting on coordinatively unsaturated metal centers of MIL-101Cr for improved water absorption characteristics**. *Inorg Chim Acta* 2018, **473**:29-36 http://dx.doi.org/10.1016/j.ica.2017.12.024.

42. Wickenheisser M, Jeremias F, Henninger SK, Janiak C: **Grafting of hydrophilic ethylene glycols or ethylenediamine on coordinatively unsaturated metal sites in MIL-100(Cr) for improved water adsorption characteristics**. *Inorg Chim Acta* 2013, **407**:145-152 http://dx.doi.org/10.1016/j.ica.2013.07.024.

43. • Permyakova A, Wang SJ, Courbon E, Nouar F, Heymans N, D'Ans P, Barrier N, Billemont P, DeWeireld G, Steunou N *et al.*: **Design of salt-metal organic framework composites for seasonal heat storage applications**. *J Mater Chem A* 2017, **5**:12889-12898 http://dx.doi.org/10.1039/c7ta03069j.

In this work, the importance of composites was demonstrated for the development of adsorbents. So it was achieved significant enhancement of energy storage capacities for certain MOFs.

44. • Permyakova A, Skrylnyk O, Courbon E, Affram M, Wang S, Lee U-H, Valekar AH, Nouar F, Mouchaham G, Devic T *et al.*: **Synthesis optimization, shaping, and heat reallocation evaluation of the hydrophilic metal–organic framework MIL-160(Al)**. *ChemSusChem* 2017, **10**:1419-1426 http://dx.doi.org/10.1002/cssc.201700164.

In this work, important MOFs for the AHT applications were compared with their energy storage capacities. Additionally, shaping of MIL-160 as pellets showed nearly similar sorption properties compared to powder one.

45. Kummer H, Baumgartner M, Hügenell P, Fröhlich D, Henninger SK, Gläser R: **Thermally driven refrigeration by methanol adsorption on coatings of HKUST-1 and MIL-101(Cr)**. *Appl Therm Eng* 2017, **117**:689-697 http://dx.doi.org/10.1016/j.applthermaleng.2016.11.026.

46. Betke U, Klaus M, Eggebrecht JG, Scheffler M, Lieb A: **MOFs meet macropores: dynamic direct crystallization of the microporous aluminum isophthalate CAU-10 on reticulated open-cellular alumina foams**. *Microporous Mesoporous Mater* 2018, **265**:43-56 http://dx.doi.org/10.1016/j.micromeso.2018.01.020.

47. Wickenheisser M, Herbst A, Tannert R, Milow B, Janiak C: **Hierarchical MOF-xerogel monolith composites from embedding MIL-100(Fe,Cr) and MIL-101(Cr) in resorcinol-formaldehyde xerogels for water adsorption applications**. *Microporous Mesoporous Mater* 2015, **215**:143-153 http://dx.doi.org/10.1016/j.micromeso.2015.05.017.

48. Leung E, Müller U, Trukhan N, Mattenheimer H, Cox G, Blei S: Process for preparing porous metal-organic frameworks based on aluminum fumarate, US 2012 0082864 A1, 2012.

49. Jeremias F, Fröhlich D, Janiak C, Henninger SK: **Advancement of sorption-based heat transformation by a metal coating of highly-stable, hydrophilic aluminium fumarate MOF**. *RSC Adv* 2014, **4**:24073-24082 http://dx.doi.org/10.1039/C4RA03794D.

50. Youssef P, Mahmoud S, Al-Dadah R, Elsayed E, El-Samni O: **Numerical investigation of aluminum fumarate MOF adsorbent material for adsorption desalination/cooling application**. *Energy Procedia* 2017, **142**:1693-1698 http://dx.doi.org/10.1016/j.egypro.2017.12.551.

51. • Kummer H, Jeremias F, Warlo A, Füldner G, Fröhlich D, Janiak C, Gläser R, Henninger SK: **A functional full-scale heat exchanger coated with aluminum fumarate metal−organic framework for adsorption heat transformation**. *Ind Eng Chem Res* 2017, **56**:8393-8398 http://dx.doi.org/10.1021/acs.iecr.7b00106.

This work demonstrates the successful coating of a heat exchanger with aluminum fumarate which is one of the promising MOFs.

52. Vivekh P, Kumja M, Bui DT, Chua KJ: **Recent developments in solid desiccant coated heat exchangers – a review**. *Appl Energy* 2018, **229**:778-803 http://dx.doi.org/10.1016/j.apenergy.2018.08.041.

53. Wittstadt U, Füldner G, Laurenz E, Warlo A, Große A, Herrmann R, Schnabel L, Mittelbach W: **A novel adsorption module with fiber heat exchangers: performance analysis based on driving temperature differences**. *Renew Energy* 2017, **110**:154-161 http://dx.doi.org/10.1016/j.renene.2016.08.061.

54. Teo HWB, Chakraborty A, Kayal A: **Formic acid modulated (fam) aluminium fumarate MOF for improved isotherms and kinetics with water adsorption: cooling/heat pump applications**. *Microporous Mesoporous Mater* 2018, **272**:109-116 http://dx.doi.org/10.1016/j.micromeso.2018.06.016.

55. Reinsch H, van der Veen MA, Gil B, Marszalek B, Verbiest T, de Vos D, Norbert S: **Structures, sorption characteristics, and nonlinear optical properties of a new series of highly stable aluminum MOFs**. *Chem Mater* 2013, **25**:17-26 http://dx.doi.org/10.1021/cm3025445.

56. Cadiau A, Lee JS, Borges DD, Fabry P, Devic T, Wharmby MT, Martineau C, Foucher D, Taulelle FT, Jun C-H *et al.*: **Design of hydrophilic metal organic framework water adsorbents for heat reallocation**. *Adv Mater* 2015, **27**:4775-4780 http://dx.doi.org/10.1002/adma.201502418.

57. Tschense CBL, Reimer N, Hsu CW, Reinsch H, Siegel R, Chen WJ, Lin CH, Cadiau A, Serre C, Senker J, Stock N: **New group 13 MIL-53 derivates based on 2,5-thiophenedicarboxylic acid**. *Z Anorg*

Allg Chem 2017, **643**:1600-1608 http://dx.doi.org/10.1002/zaac.201700260.

58. Borges DD, Maurin G, Galvão DS: **Design of porous metal-organic frameworks for adsorption driven thermal batteries**. *MRS Adv* 2017, **2**:519-524 http://dx.doi.org/10.1557/adv.2017.181.

59. Tannert N, Ernst SJ, Jansen C, Bart HJ, Henninger SK, Janiak C: **Evaluation of the highly stable metal-organic framework Al-MIL-53-TDC (TDC = 2,5-thiophenedicarboxylate) as a new and promising adsorbent for heat transformation applications**. *J Mater Chem A* 2018, **6**:17706-17712 http://dx.doi.org/10.1039/c8ta04407d.

60. González-Martínez GA, Jurado-Vázquez T, Solís-Ibarra D, Vargas B, Sánchez-González E, Martínez A, Vargas R, González-Zamora E, Ibarra AI: **Confinement of H_2O and EtOH to enhance CO_2 capture in MIL-53(Al)-TDC**. *Dalton Trans* 2018, **47**:9459-9465 http://dx.doi.org/10.1039/C8DT01369A.

61. Zlotea C, Phanon D, Mazaj M, Heurtaux D, Guillerm V, Serre C, Horcajada P, Devic T, Magnier E, Cuevas F *et al.*: **Effect of NH_2 and CF_3 functionalization on the hydrogen sorption properties of MOFs**. *Dalton Trans* 2011, **40**:4879-4881 http://dx.doi.org/10.1039/C1DT10115C.

62. Jeremias F, Lozan V, Henninger SK, Janiak C: **Programming MOFs for water sorption: amino functionalized MIL-125 and UiO-66 for heat transformation and heat storage applications**. *Dalton Trans* 2013, **42**:15967-15973 http://dx.doi.org/10.1039/c3dt51471d.

63. Sohail M, Yun YN, Lee E, Kim SK, Cho K, Kim JN, Kim TW, Moon JH, Kim H: **Synthesis of highly crystalline NH_2^-MIL-125 (Ti) with S^- shaped water isotherms for adsorption heat transformation**. *Cryst Growth Des* 2017, **17**:1208-1213 http://dx.doi.org/10.1021/acs.cgd.6b01597.

64. Gordeeva LG, Solovyeva MV, Aristov YI: **NH_2-MIL-125 as a promising material for adsorptive heat transformation and storage**. *Energy* 2016, **100**:18-24 http://dx.doi.org/10.1016/j.energy.2016.01.034.

65. Zhang Y-Z, He T, Kong X-J, Lv X-L, Wu X-Q, Li J-R: **Tuning water**
•• **sorption in highly stable Zr(IV)-MOFs through local functionalization of metal-clusters**. *ACS Appl Mater Interfaces* 2018, **10**:27868-27874 http://dx.doi.org/10.1021/acsami.8b09333.

In this publication, tunability of the MOF structure was shown by functionalization of the linker. Thereby S-shapes of water sorption isotherms were achieved in different relative pressure ranges.

2 Assignment of tasks

This dissertation was prepared as a part of the OPTIMAT project (optimization of novel materials for cyclic adsorption processes, original title in German: Optimierung von neuartigen Materialien für zyklische Adsorptionsprozesse). A brief review, which is given as the introduction part, should be written about the recent developments in the field of adsorption heat transformation concerning adsorbent materials activated carbon, silica gels, zeolites and MOFs. One of the goals of the OPTIMAT project is the fabrication of MOF@polymer composites, which is also the main scope of this dissertation. A shaping procedure should be selected, in which an as high as possible MOF loading should be achieved with no or only minimal loss of the initial sorption properties of the used MOFs.

The shaping of MOFs is essential to apply MOFs in real-life applications. In most cases, MOFs are obtained as a microcrystalline powder, but the microcrystalline MOF powders are not convenient for use in heat exchangers without shaping because of dusting contingent to small particle size, their low thermal conductivity and disadvantages in handling. Shaping of MOFs is therefore an essential issue for real-life applications, inter alia, AHT applications. Shaping is a challenging method in which the textural properties of the MOFs can get lost. Not every MOF is appropriate for any shaping procedure and therefore must be tested for its compatibility with the shaping method.

By formulating MOFs, many different shapes have been achieved, such as granules, pellets, coated metal sheets, fibers, monoliths, thin films and membrane etc. From many possible shaping methods, we focused on fabrication and characterization of MOF@polymer monolith composites. In addition to maintaining the sorption properties, the monoliths should be mechanically stable and handable.

Suitable MOFs for the use in cyclic adsorption processes should be determined. The criteria of the MOFs to be used in cyclic adsorption processes are hydrothermally stability, high water vapor uptake and an S-shaped water adsorption isotherm in the desired relative pressure range. From a few suitable MOFs in the literature, the selected MOFs Alfum and MIL-160(Al) should be used for the shaping procedures. Due to its high water vapor uptake and structural modification possibilities for tuning sorption properties, MIL-101(Cr) should also be selected.

The embedding of Alfum and MIL-101(Cr) in the PVA monolith, prepared by phase separation technique, should be investigated. An alternative shaping approach should also be examined. The freeze-casting method should be used to shape Alfum, MIL-160(Al) and MIL-101(Cr). Different loading of MOFs in both techniques should be studied under consideration of the sorption properties of the monolith.

3 Published results

This chapter presents the published/submitted work of this thesis. Each of the published or submitted work is self-contained with a discrete and short introductory part and a separate list of references. The publications are presented as they appeared in the scientific, peer-reviewed journal, as full publications with their own reference lists and order for each. Figures, schemes and tables do not follow the numbering of the main text, but the numbering of the publication itself. Each publication is introduced by a short profile that contains the name of the journal, its impact factor, graphical abstract, abstract and the authors' contribution to the work. Further unpublished work is illustrated in section 4

3.1 Shaping of metal-organic frameworks into mechanically stable monoliths with poly(vinyl alcohol) by phase separation technique

Emrah Hastürk, Carsten Schlüsener, Julian Quodbach, Alexa Schmitz, Christoph Janiak

Micropor. Mesopor. Mater. 280 (2019) 277–287
https://doi.org/10.1016/j.micromeso.2019.02.011
Impact factor (2017–2019): 4.182

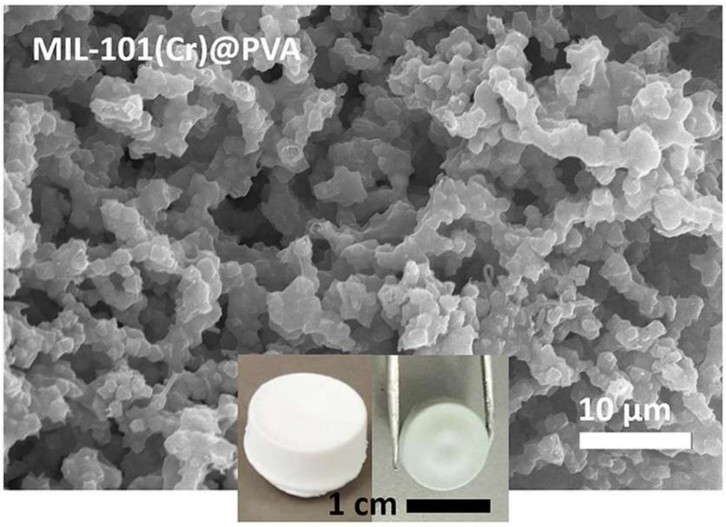

Alfum@PVA and MIL-101(Cr)@PVA Monoliths

Graphical abstract

Abstract:

The metal-organic frameworks (MOFs) Basolite^{TM} A520 (aluminum fumarate, Alfum) and MIL-101(Cr) were shaped into monoliths for the first time using a phase separation technique with the hydrophilic polymer poly(vinyl alcohol) (PVA). These composite materials (MOF@PVA) could be loaded with up to 80 wt% of MOF under retention of crystallinity (verified by powder X-ray diffractometry), porosities (from N_2 and H_2O adsorption) and morphology of MOF particles (verified by scanning electron microscopy). In the MOF@PVA monoliths, the mass-weighted apparent BET surface area from nitrogen sorption studies and the water vapor uptake capacity reproducibly reached 60 to 100% of the neat MOF values. Alfum@PVA composites with a MOF loading of 50 to 80 wt% show an increased quantitative porosity. A detailed pore analysis by the t-plot method indicates, however, that only 30 to 70% of the Alfum-micropore volume were retained during the used phase separation technique. The increased porosity is due to additional mesopores from interfacial voids which were formed

between Alfum-particles and the PVA polymer. These additional pores lead to an increase in water capacity compared to the neat/pure MOF. While the neat PVA monoliths show a primarily plastic and elastic behavior, the monoliths with 50 and 65 wt% Alfum exhibit slightly plastic properties and a high resistance against deformation. Higher stresses (up to 0.12 N/m^2, i.e. up to a force of 63 N) can be exerted together with a lower strain (< 0.2%) compared to the PVA monoliths.

Author’s share of work:

- Designing and performing of the synthetic work and evaluation of the results.
- Writing of the manuscript except for the part “Mechanical properties of Alfum@PVA2 monoliths” (done by Mr. Quodbach).
- Drawing of the figures, graphs and tables except for SEM images (taken by Mr. Schlüsener) and MOF figures (drawn with DIAMOND by Prof. Janiak).
- Editing of the manuscript regarding the reviewers’ comments together with Prof. Janiak.

Reprinted with permission from the Journal Microporous and Mesoporous Materials. Copyright 2019, with permission from Elsevier.

Microporous and Mesoporous Materials 280 (2019) 277–287

Contents lists available at ScienceDirect

Microporous and Mesoporous Materials

journal homepage: www.elsevier.com/locate/micromeso

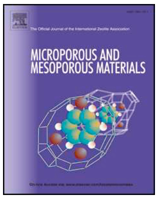

Shaping of metal-organic frameworks into mechanically stable monoliths with poly(vinyl alcohol) by phase separation technique

Emrah Hastürk[a], Carsten Schlüsener[a], Julian Quodbach[b], Alexa Schmitz[a], Christoph Janiak[a,*]

[a] Institut für Anorganische Chemie und Strukturchemie, Heinrich-Heine-Universität, D-40204, Düsseldorf, Germany
[b] Institut für Pharmazeutische Technologie und Biopharmazie, Heinrich-Heine-Universität, D-40204, Düsseldorf, Germany

ARTICLE INFO

Keywords:
Metal-organic frameworks
Shaping
Monolith
Phase separation
Poly(vinyl alcohol)

ABSTRACT

The metal-organic frameworks (MOFs) Basolite™ A520 (aluminum fumarate, Alfum) and MIL-101(Cr) were shaped into monoliths for the first time using a phase separation technique with the hydrophilic polymer poly (vinyl alcohol) (PVA). These composite materials (MOF@PVA) could be loaded with up to 80 wt% of MOF under retention of crystallinity (verified by powder X-ray diffractometry), porosities (from N_2 and H_2O adsorption) and morphology of MOF particles (verified by scanning electron microscopy). In the MOF@PVA monoliths, the mass-weighted apparent BET surface area from nitrogen sorption studies and the water vapor uptake capacity reproducibly reached 60–100% of the neat MOF values. Alfum@PVA composites with a MOF loading of 50–80 wt % show an increased quantitative porosity. A detailed pore analysis by the t-plot method indicates, however, that only 30–70% of the Alfum-micropore volume were retained during the used phase separation technique. The increased porosity is due to additional mesopores from interfacial voids which were formed between Alfum-particles and the PVA polymer. These additional pores lead to an increase in water capacity compared to the neat/pure MOF. While the neat PVA monoliths show a primarily plastic and elastic behavior, the monoliths with 50 and 65 wt% Alfum exhibit slightly plastic properties and a high resistance against deformation. Higher stresses (up to 0.12 N/m^2, i.e. up to a force of 63 N) can be exerted together with a lower strain (< 0.2%) compared to the PVA monoliths.

1. Introduction

Metal-organic frameworks (MOFs) are crystalline two- or three-dimensional metal-ligand coordination networks with potential porosity [1]. This type of microporous materials has unique properties such as high surface areas and tunability of metal center and linkers with potential applications in the field of catalysis [2–4], sensing, gas separation and storage [5,6], drug delivery [7], cyclic adsorption processes [8], etc. Adsorption heat pumps (AHPs) and thermally driven adsorption chillers (TDCs) have been reviewed recently for the integration of MOFs in these applications [9,10]. MOFs used in AHPs/TDCs must be of extraordinary stability against the cycling sorption of the adsorbate, have an appropriate S-shaped sorption isotherm [11,12] and as high as possible adsorbate loading. Aluminum fumarate (Alfum) and MIL-101(Cr) fulfill the above criteria and are possible candidates for AHPs and TDCs [13,14] (see Supp. Info. for related properties and structural details on Alfum (Fig. S3) and MIL-101(Cr) (Fig. S2)).

Still, for applications of MOFs one of the biggest current issues is to find effective methods to shape these microcrystalline, powdery materials into manageable forms such as monoliths, pellets or surface coatings with sufficient mechanical and chemical stability, maximal bulk density etc. [15] under preservation of the crucial MOF porosity properties. Different approaches have been implemented for shaping of MOFs and most important ones are granules [15], pellets and beads [16], fibers [17] and membranes [18–21]. However, in many cases, MOFs are losing access to most of their internal surface area after shaping (Table S1) [22].

The MOFs MIL-100(Fe) [23], CPO-27(Ni) [23], HKUST-1 [24], UiO-66 [24], NH_2-UiO-66 [24], UiO-67 [24], MIL-101(Cr) [25], Alfum [26] and NH_2-MIL-101(Al) [6] are selected recent examples which were shaped into pellets. With increasing pressure during the formation of the shaped MOFs, denser and mechanically stable MOF materials could be obtained, but care had to be taken not to destroy the micro-mesopores when applying pressure. In this context, the volume specific surface area (VSSA) could be increased with more dense products [27], which is also very important for industrial applications. MOF-5 powder with an apparent S(BET) of 1796 m^2 g^{-1} and VSSA (determined by multiplication of the apparent S(BET) with powder density) of

---

[*] Corresponding author.
E-mail address: janiak@uni-duesseldorf.de (C. Janiak).

https://doi.org/10.1016/j.micromeso.2019.02.011
Received 23 August 2018; Received in revised form 8 February 2019; Accepted 11 February 2019

395 $m^2 mL^{-1}$, could be formed into pellets with an apparent S(BET) of 973 $m^2 g^{-1}$ and VSSA of 823 $m^2 mL^{-1}$ and with mechanical resistance up to 29 Newton in a pressure test [27].

ZIF-8 nanofibers were prepared by electrospinning using poly(vinyl pyrrolidone) (PVP) as a binding agent containing 56 wt% ZIF-8 with an apparent S(BET) of 530 m^2/g for the composite which corresponds to no pore blocking [17]. Extrusion allowed to obtain a mechanically stable HKUST-1 monolith from a mixture of HKUST-1, binding agent and plasticizer. However, the obtained monolith with a 80 wt% MOF content had an apparent S(BET) of 484 m^2/g which is only 45% of the calculated apparent S(BET) of 1072 m^2/g for 80 wt% HKUST-1 in the monolith [apparent S(BET) of used HKUST-1 = 1340 m^2/g] [28,29]. Embedding MOFs into a shaped body can be achieved either by in-situ synthesis of MOFs in a mold or by using the synthesized MOFs directly during the fabrication of the desired form. Pre-fabricated MIL-MOFs were successfully embedded in R,F-xerogel [30] and in different polymers using high internal phase emulsion (HIPE) techniques [31,32] with up to 77% loading for MIL-101(Cr) under retention of the MIL-mass-weighted apparent BET surface area and water uptake capacity. Different MILs showed different suitability for composite formation, with MIL-100(Fe) losing more specific surface area than MIL-101(Cr) [30,31].

Phase separation is a known technique for the preparation of membranes [33]. The general working principle of monolith formation by phase separation is the addition of a 'non-solvent' to the polymer solution ('non-solvent' refers to a solvent in which the polymer is not soluble). This causes formation of a polymer-rich and a polymer-lean solution phase. At a certain amount of 'non-solvent', separation of the liquid and solid phase occurs and the formation of the monolith starts in the polymer-rich phase. During this formation, the polymer-lean phase penetrates into the forming solid structure resulting in porous channels [34,35]. Fabrication of monoliths via phase separation has the advantage that no template is needed and that the polymer can be used directly instead of the monomer. In-situ polymerization techniques such as HIPE have the disadvantageous possibility of pore blocking. The known phase separation methods are thermally induced phase separation (TIPS), 'non-solvent' induced phase separation (NIPS) and thermally impacted 'non-solvent' induced phase separation (TINIPS). In TIPS, the polymer is dissolved at an elevated temperature at which the 'non-solvent' is then added. Subsequent cooling leads to formation of the monolith. In NIPS, the addition of 'non-solvent' is performed after the cooling steps to room temperature (rt). TINIPS is a combination of NIPS and TIPS, in which the heated polymer solution has not been cooled down completely when the 'non-solvent' is added. Only after completion of the cooling procedure, formation of the monolith will start. A series of different polymers was successfully investigated for the fabrication of monolithic structures; such as cellulose via NIPS [36], poly(lactic acid) via NIPS [37] and poly(methyl methacrylate) via TIPS [38].

Poly(vinyl alcohol), PVA (Fig. S7) is a highly hydrophilic, nontoxic polymer, with high mechanical strength and an attractive material for many applications [39]. PVA is also a known binder which was successfully tested for the shaping of MOF into pellets (see Table S1) [40,41] and was recently adopted in the preparation of hierarchical porous monoliths with MOFs via a high-internal phase emulsion (HIPE) template [42]. In 3D-printing technology, PVA was investigated as plasticizer with bentonite clay to shape MOF-74(Ni) and UTSA-16(Co) (see Table S1) [43]. The 3D-printed MOF@bentonite-PVA monoliths showed very low pore blocking effects. Furthermore, ZIF-8 and HKUST-1 were shaped with PVA by extrusion with very high pore accessibility (see Table S1) [44].

Different methods have been reported for the fabrication of pure PVA monoliths such as cryo-polymerization [45] and recently water-in-oil HIPE technique [46]. Cryo-polymerization is performed by adding an appropriate cross-linker to the PVA solution, which is immediately cooled below the freezing temperature of the solvent, and polymerization is completed below the freezing point [45]. PVA can be obtained from the hydrolysis of poly(vinyl acetate) (PVAc). This hydrolysis can also be performed on poly(vinyl acetate) monoliths in a basic medium with varying reaction temperature and time to yield macroporous mixed PVA/PVAc monoliths where the hydrophilicity could be adjusted by different degrees of hydrolysis [46].

Concerning the mechanical strengths of MOF-binder composites, MOF granules, fabricated by a wet granulation technique with alumina as a binder, exhibited an average crushing strength of 6.7, 4.1, 4.7 and 2.5 N in a mechanical stability test with the MOFs MIL-100(Fe), MIL-101(Cr), UiO-66(Zr) and NH_2-UiO-66(Zr), respectively [47]. A patent on 'shaped bodies containing metal-organic frameworks' claimed mechanical stability of MOF granules in which graphite was used as binder with stability ranges from 5 N to 200 N in the crushing test [27]. The above-mentioned HKUST-1 extruded with silicone resin and methylhydroxyl propyl cellulose showed a high mechanical stability of 320 N [28].

Herein, we report phase separation as a novel method for the preparation of PVA-based MOFs composites as monoliths. This method has the advantage of using the polymer instead of monomer in order to minimize pore blocking of the embedded MOFs in the MOF@PVA monolith.

2. Experimental section

2.1. Materials and methods

Chemicals were commercially obtained from the indicated sources and used without further purification. Aluminum fumarate (Basolite™ A520) was purchased from BASF, $Cr(NO_3)_3{\cdot}9H_2O$ (99%) from Acros Organics, HNO_3 (65 wt%) from Grüssing, 1,4-benzenedicarboxylic acid (H_2BDC, > 99%) from Acros Organics, *N,N'*-dimethylformamide (DMF, p.a.) and ethanol (p.a.) from VWR, poly(vinyl alcohol) with average M_w = 124–186 kDa, 99% hydrolyzed (abbreviated as PVA1) and poly (vinyl alcohol) with average M_w = 125 kDa, 98% hydrolyzed (abbreviated as PVA2) from Sigma Aldrich and poly(vinyl alcohol) with average M_w = 22 kDa, 97.5–99.5% hydrolyzed (abbreviated as PVA3) from Fluka.

Powder X-ray diffractograms (PXRD) were obtained at ambient temperature on a Bruker D2 Phaser (300 W, 30 kV, 10 mA) using Cu-Kα radiation ($\lambda = 1.54182$ Å) between $5^\circ < 2\Theta < 50^\circ$ with a scan rate of 0.0125° s^{-1}. The diffractograms were obtained on a flat "low background sample holder", where at low angle the beam spot is strongly broadened so that only a fraction of the reflected radiation reaches the detector, hence there are low relative intensities measured at $2\theta < 7^\circ$. The analyses of the diffractograms were carried out with the "Match 3.11" software.

Nitrogen physisorption isotherm measurements were carried out on a Nova 4000e and an Autosorb-6 from Quantachrome at 77 K. Water physisorption isotherms were measured volumetrically on a Quantachrome Autosorb iQ MP at 293 K. Before each sorption measurement, the samples were activated under vacuum (1×10^{-3} mbar) at 393–423 K for 3–4 h. Brunauer-Emmett-Teller (BET) surface areas (designated as 'apparent S(BET)' for microporous materials [48]) were calculated from the nitrogen physisorption isotherms. In this work we refer to the microporous MOF surface areas from Type I isotherms as 'apparent S(BET)' based on the aforementioned reference [48], where it is noted that 'the BET-area derived from a Type I isotherm must not be treated as a realistic probe accessible surface area' but 'represents an apparent surface area, which may be regarded as a useful adsorbent "fingerprint" '. Density functional theory (DFT) calculations for the pore size distribution curves were done with the native NovaWin 11.03 software using the 'N_2 at 77 K on carbon, slit pore, non-local density functional theory (NLDFT) equilibrium' model [49–51] for MIL-101(Cr), MIL-101(Cr)@PVA composites as well as the PVA polymers. The 'N_2 at 77 K on carbon, slit pore, quench solid density functional theory (QSDFT) equilibrium' model was used for Alfum and Alfum@PVA composites. For Alfum and Alfum@PVA a comparison between two different NLDFT and the QSDFT kernel revealed the best match to the apparent S(BET) with the QSDFT model (Table S3, Supp. Info.). Again, none of the present DFT kernels for 'N_2 on carbon' does reflect the surface properties of a MOF material. Hence, the numbers can be used for comparison of similar materials but must not be taken as exact values for pore sizes or surface areas of MOFs. We just note that in the absence of MOF-specific kernels the 'N_2 on carbon' kernels with different pore types are frequently used to study the surface properties of MOFs [52] and was also previously applied for MIL-101(Cr) [30,53].

The porosity analysis of PVA monoliths was also investigated with a mercury intrusion PASCAL 140–440 porosimeter from POROTEC. The data analysis was performed with the SOLID software version of 1.6.3.

Scanning electron microscopy (SEM) images were obtained with a Jeol JSM-6510LV QSEM advanced electron microscope using a LaB_6 cathode at 5–20 keV. The microscope was equipped with a Bruker Xflash 410 silicon drift detector for energy-dispersive X-ray spectrometric (EDX) elemental analysis.

For the investigation of the mechanical properties, a texture analyzer was used (Stable Micro Systems, model TA XT2i, Fig. S10), in which a cylindrical monolith was compressed axially with a 20 mm diameter flat-faced piston. The samples were compressed up to a maximal force of 63 N (instrument limit) or up to a maximum axial compression of 3 mm depending on the dimensions of the body (Fig. S11 in Supp. Info.). When the maximum force of 63 N was achieved, the measurement stopped automatically. When the samples were deformed 3 mm before the maximum force was reached, the probe returned with the same test speed to the starting position. The force exerted on the sample during the unloading phase was also determined as indicator for elastic deformation. The applied stress was calculated by dividing the force by the average diameter of a given batch and stress-strain curves were plotted. The height/diameter range of the monolith cylinders ranged from approximately 6/13 mm to 9/17 mm (Fig. S11 in Supp. Info.) The compression length in mm was measured against the increasing force (Fig. S12 in Supp. Info.). At least four samples of a given formulation were investigated to ensure reproducibility.

FT-IR spectra were measured in ATR-mode (Platinum ATR-QL, Diamond) on a Bruker TENSOR 37 IR spectrometer in the range of $4000-550\,\mathrm{cm}^{-1}$.

Supercritical drying was carried out using an acetone-washed sample still dispersed in acetone in an automated critical point dryer (Leica EM CPD300) which was set to perform 99 exchange cycles of CO_2 at slow speed and 100% stirring.

Thermogravimetric analysis (TGA) was carried out on a Netzsch TG209 F3 Tarsus (Netzsch, Selb, Germany) device under a nitrogen atmosphere and heating at a ramp rate of $5\,\mathrm{K\,min}^{-1}$ to the target temperature (250 °C).

Freeze-drying of water washed PVA monolith samples, which were frozen in liquid nitrogen, was done overnight in an Alpha 1–2 freeze-dryer from the company Christ.

2.2. Synthesis of MIL-101(Cr)

MIL-101(Cr) was hydrothermally synthesized according to the literature [54]. $Cr(NO_3)_3{\cdot}9H_2O$ (4.0 g, 10.0 mmol), H_2BDC (1.64 g, 10.0 mmol), HNO_3 (0.45 mL, 10.0 mmol, 65 wt%) and deionized H_2O (60 mL) were placed in a 90 mL Teflon-liner and stirred for 2 h. The Teflon-liner was inserted in a steel autoclave and heated to 220 °C within 12 h, held at this temperature for 8 h and then cooled down in 6 h to rt. The green powder was centrifuged and washed consecutively with H_2O (180 mL, at rt for 2 h), DMF (150 mL, overnight at rt, followed by 110 °C overnight) and EtOH (150 mL, at rt overnight and subsequently refluxed overnight). Before each solvent change, the sample was centrifuged. The green crystalline powder was dried at 150 °C overnight under oil-pump vacuum. Yield 2.60 g (2.23 mmol, 67% for $Cr_3(\mu_3\text{-}O)(OH)(H_2O)_2(BDC)_3{\cdot}25H_2O$, $C_{24}H_{16}Cr_3O_{15}{\cdot}H_{50}O_{25}$, $1150.74\,\mathrm{g\,mol}^{-1}$). (See Fig. 5 for the powder X-ray diffractogram and Fig. S4 for SEM images of the sample. Porosity characteristics are discussed below.).

2.3. Fabrication of poly(vinyl alcohol) (PVA) monoliths

In a typical preparation, PVA (120 mg) was dissolved completely in distilled water (2 mL) above 80 °C in a 10 mL cylindrical glass vial to a homogeneous solution. This ratio can also be scaled up. Depending on the amount of PVA, a homogeneous solution was only obtained by stirring overnight above 80 °C. The solution was cooled to rt, and then acetone (1.5 mL) as a 'non-solvent' was added dropwise to the aqueous PVA solution. Slow addition prevents too rapid formation of the precipitate. The two-phase mixture was kept at rt for 48 h until phase separation was completed, forming a white monolith. The monolith was washed 10 times with 10 mL of acetone (or water for freeze-drying) by immersing the monolith for at least half an hour into the solvent during each washing cycle. We note that washing with water led to partial disintegration of the structure by splintering off small pieces. For the final product, three different drying methods were investigated. The monolith was dried in vacuum overnight at rt, by supercritical drying or by freeze-drying. The monoliths showed the least shrinkage with vacuum drying, therefore the MOF@PVA monoliths were only dried through this method (vide infra).

2.4. Fabrication of MOF@PVA monolithic composites

A stock solution of 1.2 g PVA in 20 mL of water (conc. = 60 g/L) was prepared as described above. From this PVA solution, 2 mL were placed in a 10 mL cylindrical glass vial. A chosen amount of MOF depending on the desired wt% according to (x mg MOF)/(x mg MOFs + 120 mg PVA) × 100% was added. For example, to obtain 80 wt% MOF loading in the monolith, 480 mg of MOF was added to 2 mL of PVA solution (containing 120 mg of PVA). The suspension was well stirred overnight until again a homogenous mixture was obtained. Acetone (1.5 mL) as 'non-solvent' was added dropwise to the PVA solution. The two-phase mixture was kept at rt for 48 h until the phase separation was completed with formation of a monolith. The formed monolith was washed 10 times with 10 mL of acetone or alternatively 6 times with 20 mL of acetone by immersing it for at least half an hour during each washing cycle. Finally, the monolith was dried in vacuum overnight at rt.

3. Results and discussion

3.1. Fabrication of PVA monoliths

PVA monoliths are known materials and normally prepared by using cryo-polymerization at 0 °C [45], HIPE [46] or thermally impacted 'non-solvent'-induced phase separation (TINIPS) at 55 °C [55]. Here, we realized that the desired monolith structure can be achieved by adding the 'non-solvent' after having cooled the PVA solution to rt instead of addition at 55 °C, as previously reported [55]. This has the advantage that uncontrolled evaporation of acetone is avoided. The prepared and cooled PVA solution can also be stored for later monolith preparation. After 48 h, the white monolith was separated from the supernatant solvent. The preparation procedure of PVA monoliths is depicted in Fig. 1.

In our experiments, we observed that the monolith decreased in size after the washing process with acetone and subsequent drying under vacuum. Shrinkage of the monolith can be explained by the incomplete removal of water by solvent exchange from the monolith and the subsequent capillary effect, which contracts the structure upon drying. In the literature, no shrinkage of the PVA monolith prepared via TINIPS was reported [55].

The solvent evaporation technique plays an important role in the

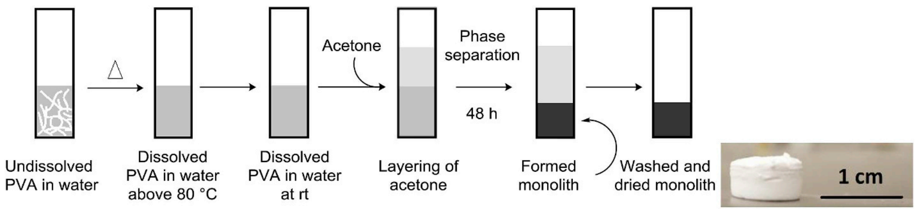

Fig. 1. Schematic fabrication procedure of PVA monolith via phase separation and photograph of an example of a PVA2 monolith.

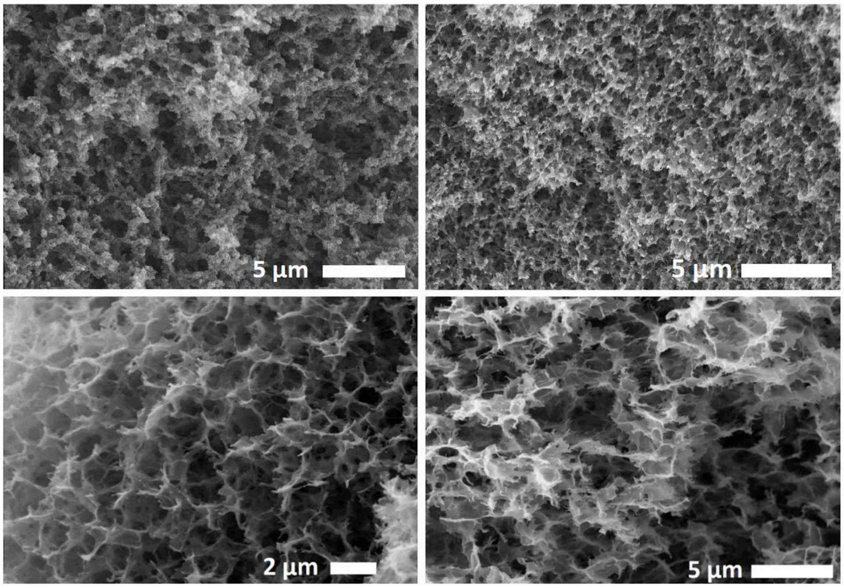

Fig. 2. SEM images of PVA2 monolith (top left) from vacuum drying and PVA1 monolith (top right) from supercritical drying, PVA1 (bottom left) and PVA2 (bottom right) monolith from freeze-drying.

preservation of the monolith structure and for the different morphologies. In this work, vacuum, supercritical and freeze-drying are compared. SEM images of PVA monoliths prepared with vacuum, supercritical and freeze-drying all indicate macroporosity (Fig. 2), which was quantified by mercury porosimetry (vide infra) (Fig. S9). However, in our hands supercritical drying was not successful to avoid shrinkage of the monolith, which is an unexpected result, compared to previous literature reports [56]. In freeze-drying, the necessary use of water in the washing procedure resulted in structural instability, leaving vacuum drying as the preferential procedure.

The macroporous properties of the PVA monoliths were analyzed by mercury porosimetry (Fig. 9). The samples show a bimodal pore size distribution with most pores in the vicinity of 0.4 and 8.4 µm from vacuum drying, 0.4 µm from supercritical drying and 1.9 and 5.2 µm from freeze-drying, (Fig. S9 in Supp. Info.). Nitrogen sorption analysis of the PVA monoliths revealed very small surface areas (Table 1) and DFT calculations (based on the non-local density functional theory (NLDFT) equilibrium' model with 'N_2 at 77 K on carbon with slit pores') confirm the existence of additional mesopores (Fig. S8 in Supp. Info).

Water sorption isotherms of the PVA1, PVA2 and PVA3 monoliths prepared by vacuum drying are displayed in Fig. 3. All PVA monoliths feature a strong hysteresis upon water desorption. The hysteresis for the water ad- and desorption of hydrogen-bond-containing polymers can be explained from the breaking of the interpolymer hydrogen bonds and formation of hydrogen bonds between the polymer and water during adsorption [57]. Such classical O—H···O hydrogen bonds have bond energies up to 40 kJ/mol. During desorption the more or less strongly hydrogen-bonded water is then only released at lower relative vapor pressure. However, the hysteresis gap is remarkably more pronounced for PVA3 such that the desorption isotherm only closes at a very low relative pressure near to zero. Obviously there is a stronger interaction of water with PVA3, which we reason by its substantially lower molecular weight (22 kDa) compared to PVA1 (124–186 kDa) and PVA2 (125 kDa). This assumption was confirmed by a comparative TGA analysis of the water-vapor loaded PVA monoliths to model the conditions prior to desorption (Fig. S15). In the case of PVA1 and PVA2 the water mass loss is completed below 100 °C. However, PVA3 losses its water content at higher temperatures and until around 180 °C.

Whereas, the water loading of the PVA1 and PVA2 monoliths are around $0.16\,\mathrm{g\,g^{-1}}$, PVA3 has a water loading of only $0.10\,\mathrm{g\,g^{-1}}$ at $p{\cdot}p_0{}^{-1} = 0.9$ (Fig. 3). The water adsorption isotherm and uptake of PVA is comparable to reported literature values [58].

3.2. MIL-101(Cr)@PVA and Alfum@PVA monolith composites

The fabrication of MOF@PVA composites containing different weight percentages of MOFs were prepared by a modified procedure of the pure PVA monolith fabrication (*cf.* Fig. 1) [55]. A typical preparation of MOF@PVA monolith is schematically depicted in Fig. 4. Since PVA is not soluble in water at rt, it was dissolved in hot water and after cooling to rt the MOF was added. Overlaying of the PVA/MOF dispersion with acetone led to formation of the two phases to give light-green monoliths for MIL-101(Cr)@PVA and white monoliths for Alfum@PVA (Fig. 4).

The monoliths were separated from the supernatant solution, washed with acetone and dried under vacuum. Vacuum drying is the drying method of choice for the preparation of MOF@PVA monoliths because of the following advantages: low shrinkage, structural stability, simplicity and possibility of applying to larger pieces of the monoliths. MIL-101(Cr) and Alfum could be embedded into the different PVA types with different mass loadings of up to 80% to yield MIL-101(Cr)*xx*@PVA*y* or Alfum*xx*@PVA*y* with *xx* referring to the wt% of MOF in the composite and *y* denoting the PVA type (see Experimental section). The phase separation took place in a sufficiently rapid time, so that no

Table 1

Results from nitrogen and water vapor sorption measurements.

Sample[a]	S(BET)[b] exp. [$m^2 \cdot g^{-1}$] (% of calc S(BET))	S(BET) calc.[c] [$m^2 \cdot g^{-1}$]	V(pore)[d] [$cm^3 \cdot g^{-1}$] (% of calc V(pore))	V(pore) calc.[c] [$cm^3 \cdot g^{-1}$]	Water loading exp. [$g \cdot g^{-1}$] (% of calc loading)	Water loading calc.[e] [$g \cdot g^{-1}$]
PVA1	36	–	0.06		0.16	-
PVA2	38	–	0.08		0.16	-
PVA3	9	–	0.01		0.10	-
MIL-101(Cr)	2731	–	1.29		1.01	-
Alfum	1038	–	0.52		0.38	-
MIL101(Cr)@PVA1						
MIL-101(Cr)33@PVA1	638 (69)	925	0.30 (65)	0.47	0.31 (71)	0.44
MIL-101(Cr)50@PVA1	914 (66)	1384	0.46 (67)	0.68	0.37 (64)	0.58
MIL101(Cr)@PVA2						
MIL-101(Cr)33@PVA2	714 (77)	927	0.34 (71)	0.48	0.34 (77)	0.44
MIL-101(Cr)40@PVA2	814 (73)	1115	0.40 (71)	0.56	0.41 (82)	0.50
MIL-101(Cr)50@PVA2	1053 (76)	1385	0.50 (73)	0.69	0.47 (80)	0.58
MIL-101(Cr)60@PVA2	1255 (76)	1654	0.61 (76)	0.81	0.56 (84)	0.67
MIL-101(Cr)70@PVA2	1521 (79)	1923	0.73 (79)	0.93	0.63 (83)	0.75
MIL-101(Cr)80@PVA2	1820 (83)	2192	0.87 (83)	1.05	0.67 (80)	0.84
Alfum@PVA2						
Alfum50@PVA2	392 (73)	538	0.25 (83)	0.30	0.30 (111)[f]	0.27
Alfum65@PVA2	639 (93)	688	0.40 (109)	0.36	0.33 (109)[f,g]	0.30
Alfum80@PVA2	786 (94)	838	0.45 (104)	0.43	0.35 (104)[f,g]	0.34
Alfum@PVA3						
Alfum50@PVA3	474 (91)	524	0.32 (123)	0.26	0.29 (120)[f,g]	0.24
Alfum65@PVA3	582 (86)	678	0.37 (108)	0.34	0.30 (106)[f,g]	0.28
Alfum80@PVA3	788 (95)	832	0.46 (112)	0.42	0.33 (102)[f,g]	0.32

[a] Nomenclature: In MIL-101(Cr)*xx*@PVA*y* or Alfum*xx*@PVA*y* *xx* refers to the wt% of MOF in the composite and *y* denotes the PVA type (see Exp. section). Thus, MIL-101(Cr)80@PVA1 has 80 wt% loading of MIL-101(Cr) in PVA1 monolith.

[b] Apparent S(BET) determined from N_2 sorption isotherm at 77 K with a standard deviation ± 20 $m^2 g^{-1}$ (calculated over 5 points in the range of $0.05 < p \cdot p_0^{-1} < 0.2$ for MIL-101 and corresponding composites, and $0.01 < p \cdot p_0^{-1} < 0.08$ for Alfum and related composites).

[c] Expected apparent S(BET) and expected micro- and small mesopore volume, *V*(pore) calculated as the sum of the mass-weighted S(BET) or V(pore) of the MOFs, PVA1 monolith, PVA2 monolith or PVA3 monolith from the following formula (Ia) or (Ib), respectively: $\text{S(BET)calc} = \frac{\text{wt\% of PVAy}}{100} \times \text{S(BET, PVAy)} + \frac{\text{wt\% of MOF}}{100} \times \text{S(BET, MOF)}$ (Ia)with apparent *S*(BET) MIL-101(Cr) = 2731 $m^2 g^{-1}$; Alfum = 1038 $m^2 g^{-1}$; PVA1 = 36 $m^2 g^{-1}$; PVA2 = 38 $m^2 g^{-1}$; PVA3 = 9 $m^2 g^{-1}$; $\text{V(pore)calc} = \frac{\text{wt\% of PVAy}}{100} \times \text{V(pore, PVAy)} + \frac{\text{wt\% of MOF}}{100} \times \text{V(pore, MOF)}$ (Ib)with *V*(pore) MIL-101(Cr) = 1.29 $cm^3 g^{-1}$; Alfum = 0.52 $cm^3 g^{-1}$; PVA1 = 0.06 $cm^3 g^{-1}$; PVA2 = 0.08 $cm^3 g^{-1}$; PVA3 = 0.01 $cm^3 g^{-1}$.

[d] Total pore volume V(pore) calculated from N_2 sorption isotherm at 77 K ($p \cdot p_0^{-1} = 0.90$) for pores ≤ 20 nm.

[e] Water adsorption value calculated (estimated) as the sum of the mass-weighted uptakes at $p \cdot p_0^{-1} = 0.9$ of the MOFs (MIL-101(Cr) = 1.01 $g\, g^{-1}$; Alfum = 0.38 $g\, g^{-1}$) and PVA monoliths (PVA1 monolith = 0.16 $g\, g^{-1}$; PVA2 monolith = 0.16 $g\, g^{-1}$; PVA3 monolith = 0.10 $g\, g^{-1}$) from the following formula (II): $\text{Water adsorption calc} = \frac{\text{wt\% of PVAy}}{100} \times \text{(uptake PVAy)} + \frac{\text{wt\% of MOF}}{100} \times \text{(uptake MOF)}$ (II) .

[f] The quantitative or even higher than 100% water uptake correlates within experimental error with the increased total pore volume of the composite, given in column 4.

[g] These water loading values were measured twice to ensure reproducibility and were reproduced within ± 0.02 $g\, g^{-1}$ of the given value.

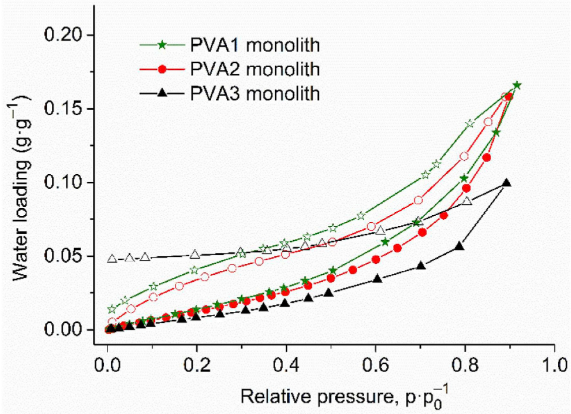

Fig. 3. Water vapor sorption isotherms of PVA1, PVA2 and PVA3 monoliths (vacuum-dried), adsorption is depicted with filled, desorption with empty symbols.

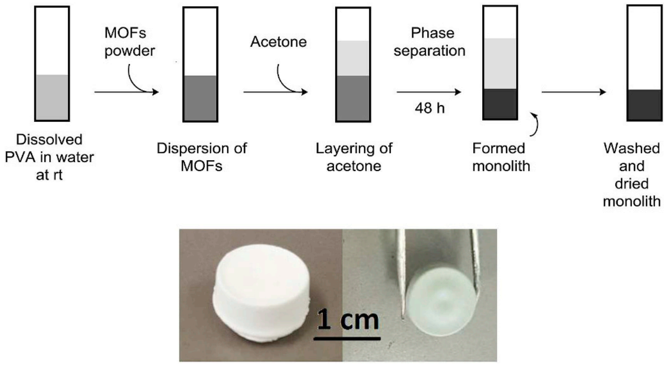

Fig. 4. Schematic fabrication procedure of MOF@PVA monoliths via phase separation (top). Photographic images of Alfum50@PVA2 (bottom-left) and MIL-101(Cr)40@PVA1 monolith (bottom-right).

significant sedimentation of the MOF particles could be visually detected. Alfum appeared more suitable than MIL-101(Cr) for the preparation of PVA composites via phase separation due to the smaller Alfum particles.

With low molecular weight polymer PVA3, phase separation for the attempted MIL-101(Cr)50@PVA3, MIL-101(Cr)65@PVA3 and MIL-101(Cr)80@PVA3 monoliths was not completed over a period of 72 h and only formed a partially monolithic structure (concentration of PVA3 was 60 g/L). The low molecular weight PVA3 (M_w = 22 kDa) could only be used for the preparation of monoliths with Alfum, presumably due its smaller particle size.

Powder X-ray diffractograms indicate the unchanged crystallinity of the MOFs after embedding in PVA (Fig. 5). Further characterization was performed with IR spectroscopy indicating no structural change either in MIL-101(Cr) or Alfum. As expected, an increase of the PVA amount is also observable with corresponding absorption bands of the PVA (see Fig. S6 in Supp. Info. for IR spectra of the monoliths).

The microstructures of the MIL-101(Cr)@PVA monoliths are very different from that of the pure PVA monoliths (compare Figs. 2–6). PVA plays a role as a binder, which can be best seen from the 1 μm-scale SEM images (Fig. 6 right). In all cases, a macroporous monolith is formed using vacuum-drying. The monolith with the embedded meso-microporous MIL particles may be described as a hierarchically macro-*meso*-microporous material. With increasing MIL wt% the monolith microstructure becomes more compact. The characteristic octahedral shape of MIL-101(Cr) (Fig. S4 in Supp. Info.) is retained upon composite formation. With 50 wt% of MIL in the MIL-101(Cr)50@PVA composites the PVA fully coats all MIL particles (Fig. 6 top and middle).

The microstructures of the high MOF-wt%, Alfum80@PVA composites (Fig. 7) resemble the SEM image of the Alfum particles itself (*cf.* Fig. S4).

3.2.1. *Nitrogen sorption studies of MIL@PVA and Alfum@PVA composites*

The nitrogen sorption isotherms of MIL-101(Cr)@PVA composites can be categorized independently from the loading amount of the MIL as Type Ib [48] (Fig. 8) and resemble the typical MIL-101(Cr) isotherm [60]. Understandably, with decreased amount of MIL in the composite the overall nitrogen adsorption decreases and the characteristic MIL-101 step before p·p$_0^{-1}$ = 0.2, which indicates the presence of micropore windows and mesoporous cavities [60], becomes less pronounced. The apparent BET surface area of the composites increases as expected with the rising amount of MIL in the composite (Table 1). The determined apparent BET surface areas in some composites are very close to the expected ones, which were calculated from the mass-percent contribution of pure MIL-101(Cr) and PVA in the composites. It can be seen that the pore accessibility is consistently well above 70% for the MIL@PVA2 monoliths, reaching even 83% for the 80 wt% sample MIL-101(Cr)80@PVA2. The pore accessibility largely rises with increasing MOF content for both MIL-101(Cr) and Alfum. This is understandable as lower relative amounts of polymer can lead to less pore blocking or surface coverage. The good pore accessibility indicates the suitability of PVA for MOF-polymer monolith fabrication. It is evident that MIL-101(Cr) with PVA1 yielded pore accessibilities of less than 70% for the two samples with different MOF loading.

As it quickly became apparent that PVA2 yields better pore accessibility than PVA1, PVA1 was not tested anymore for MIL-101(Cr) loadings to over 50 wt% and was not tested for the preparation of Alfum@PVA monoliths. On the other hand, the low molecular weight PVA3 could be successfully used with the smaller Alfum particles for the preparation of Alfum@PVA3 monoliths.

The nitrogen sorption isotherms of Alfum@PVA2 and –PVA3 composites resemble for any loading the one of pure Alfum (Fig. 9). All Alfum@PVA composites and Alfum itself exhibit Type I isotherms [48] indicating microporous materials. The increase in adsorbed volume towards p·p$_0^{-1}$ = 1 is due to meso- and macroporous interparticle volume [48]. The nitrogen uptake and concomitant surface area are

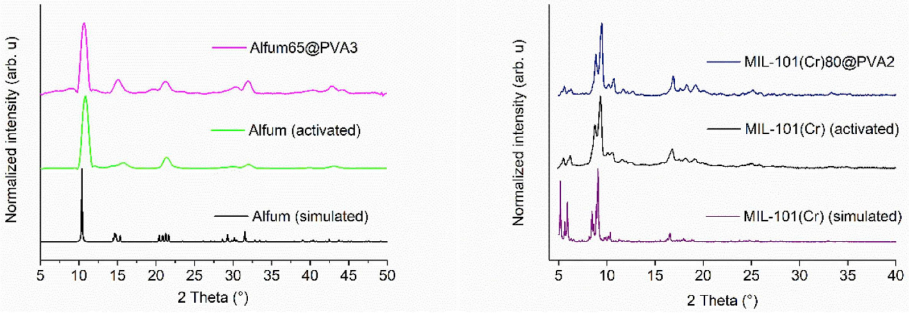

Fig. 5. Experimental powder X-ray diffraction patterns of Alfum and Alfum65@PVA3 (left) and MIL-101(Cr) and MIL-101(Cr)@PVA2 (right) (see Fig. S5 in Supp. Info. for further PXRD patterns of other monolith samples). The simulated MOF diffractograms are included for comparison (Alfum simulated from CSD-Refcode DOYBEA [59]; MIL-101Cr simulated form CSD-Refcode OCUNAK [60]).

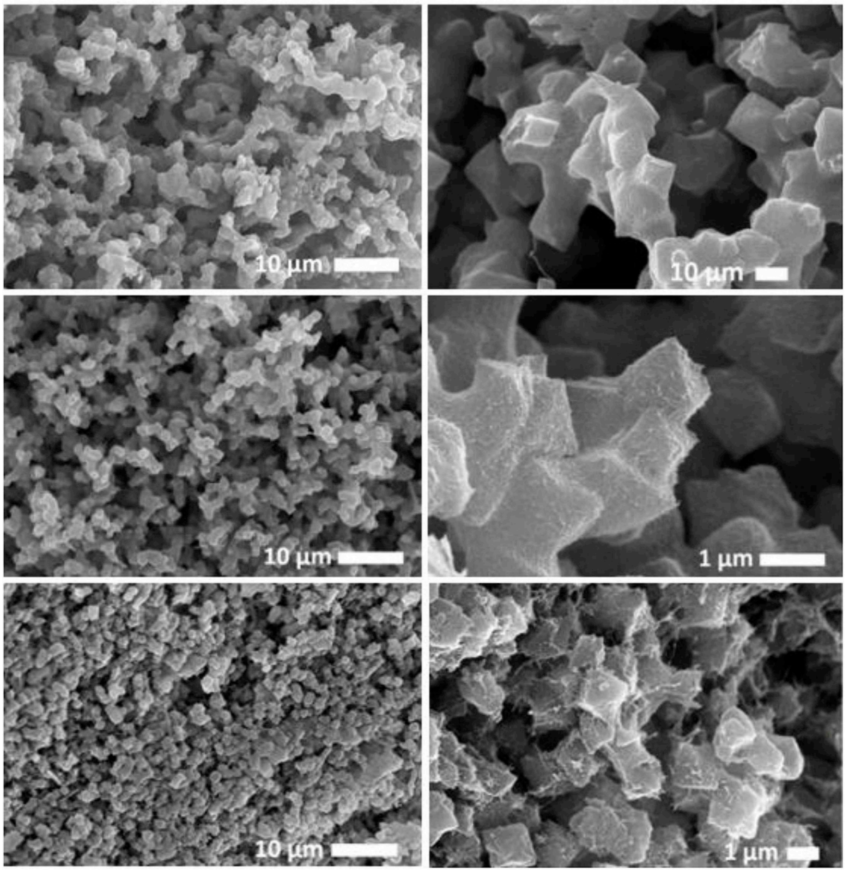

Fig. 6. Scanning electron microscopy (SEM) images of the composites MIL-101(Cr)50@PVA1 (top), MIL-101(Cr)50@PVA2 (middle), MIL-101(Cr)70@PVA2 (bottom).

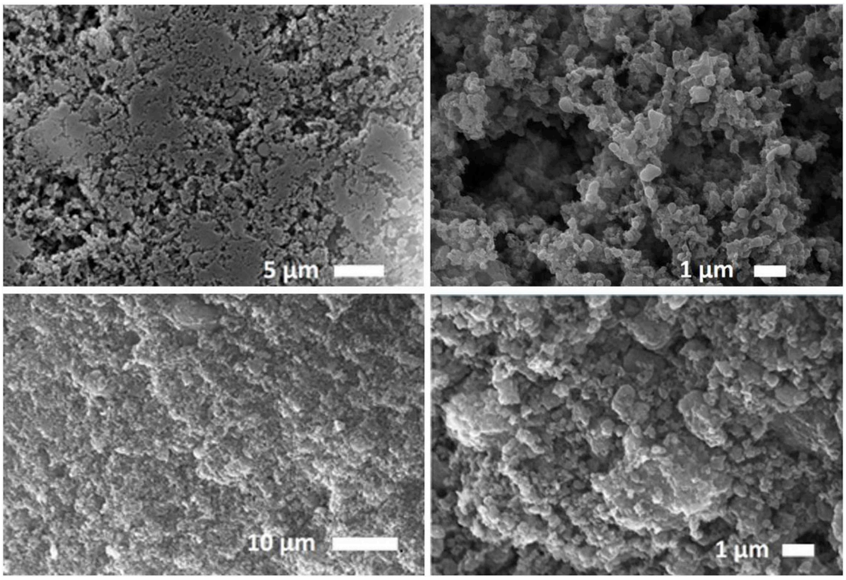

Fig. 7. Scanning electron microscopy (SEM) images of the composites Alfum80@PVA2 (top) and Alfum80@PVA3 (bottom).

increasing with the Alfum amount in the composites. Thereby, the calculated apparent S(BET) values of the Alfum composites are very close to the estimated ones, often reaching 90% and more of the expected values. In addition, for Alfum with PVA the experimentally determined total pore volume for pores smaller than 20 nm is generally slightly larger than the estimated one. This does not necessarily imply, however, retention of the original MOF porosity. A more detailed pore analysis by the t-plot method (Table S2 and Fig. S1) indicates that micropore volume of Alfum is indeed lost. Micropores are pores with less than 2 nm diameter. In the composite only 30–70% of the micropore volume of the MOF is retained. On the other hand, there is an added formation of mesopores (2–50 nm diameter) in the Alfum@PVA composites, for example, through interfacial voids between Alfum and the PVA polymer. A comparative presentation of the pore size

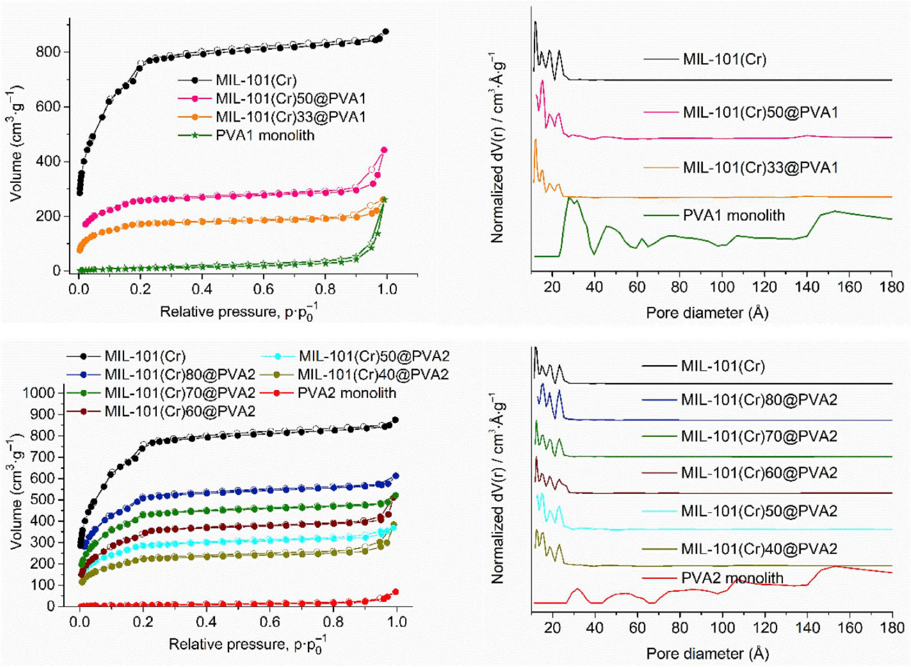

Fig. 8. N_2 sorption isotherms (left) and pore diameter distributions from DFT calculations (right) of the composites MIL-101(Cr)@PVA1 (top) and MIL-101(Cr)@PVA2 (bottom) with different MIL loadings together with the curves for neat MIL-101(Cr) and PVA monolith. See Table 1 for apparent BET surface areas. Adsorption is depicted with filled, desorption with empty symbols. The applied DFT kernels for 'N_2 on carbon' do not reflect the surface properties of a MOF material. Hence, the numbers can be used for comparison of similar materials but must not be taken as exact representation for the pore sizes of MOFs.

distributions from DFT calculations based on the nitrogen sorption measurements of the Alfum@PVA composites with pure Alfum also shows this increase in pore size around 3 nm (Fig. S14 and Table S3). These additional mesopores more than compensate for the loss in micropore volume and can be responsible for the increase in water uptake (vide infra). As the DFT kernels were not developed for MOFs, the numbers discussed here should not be taken as exact values for the pore sizes.

The benefit of the composite fabrication via the phase separation technique became evident by comparison to a composite from an aqueous Alfum dispersion in a PVA2 solution where the water was simply evaporated. A 50 and 80 wt% Alfum@PVA2 composite was prepared by simple water evaporation from such an Alfum dispersion in PVA2 solution. The composites, named Alfum50@PVA2airdried and Alfum80@PVA2airdried, gave an apparent BET surface area of 94 and 525 m^2/g, respectively. These apparent S(BET) values are substantially lower when compared with the monoliths Alfum50@PVA2 with apparent S(BET) of 392 m^2/g and Alfum80@PVA2 with apparent S(BET) of 786 m^2/g, which were prepared by phase separation.

3.2.2. *Water sorption of MIL@PVA and Alfum@PVA composites*

The water sorption isotherm of all composites, neat MOFs and polymers are depicted in Fig. 10 and the corresponding water uptake values are summarized in Table 1. Neat MIL-101(Cr) was reported to

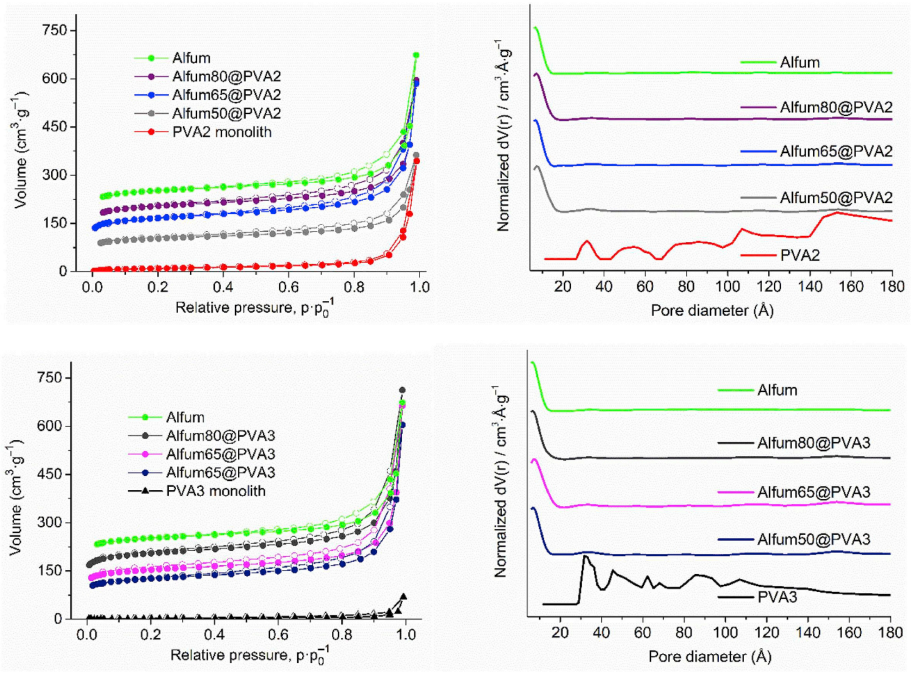

Fig. 9. N_2 sorption isotherms (left) and pore diameter distributions from DFT calculations (right) of the composites Alfum@PVA2 and Alfum@PVA3 with different Alfum loadings together with the curves for neat Alfum and PVA monolith. See Table 1 for apparent BET surface areas. Adsorption is depicted with filled, desorption with empty symbols. The applied DFT kernels for 'N_2 on carbon' do not reflect the surface properties of a MOF material. Hence, the numbers can be used for comparison of similar materials but must not be taken as exact representation for the pore sizes of MOFs.

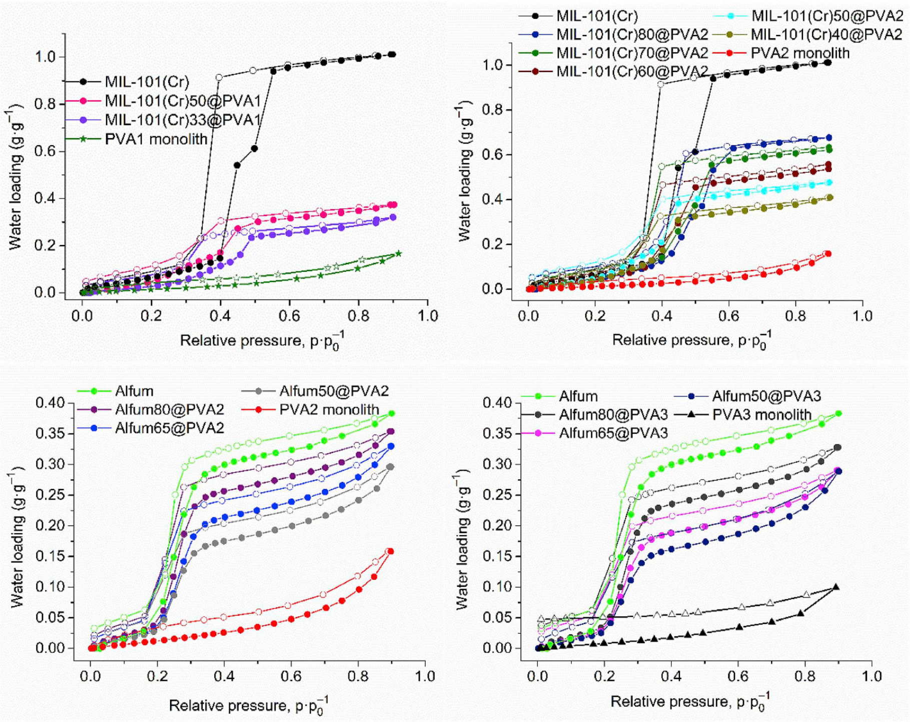

Fig. 10. Water vapor sorption isotherms of MIL-101(Cr)@PVA1 (top left), MIL-101(Cr)@PVA2 (top right), Alfum@PVA2 (bottom left) and Alfum@PVA3 (bottom right). Adsorption is depicted with filled, desorption with empty symbols.

have water loading values in the range of 1.0–1.6 g g^{-1} at p·p$_0$$^{-1}$ = 0.9 [9]. The step in the water adsorption isotherm of pure MIL-101(Cr) at nearly p·p$_0$$^{-1}$ = 0.5 is due to the two different pore sizes (Fig. S2 in Supp. Info).

The maximum water adsorption was taken at 0.9 p·p$_0$$^{-1}$ so as not to have artefacts from interparticle macropore filling. The water uptake increases with the amount of MOF in the MOF@PVA composites. Expected water loading capacities of the composites can be calculated from the contribution of MOFs and PVA due to their mass percentage in the composites (Table 1). As seen before with the apparent BET surface area PVA2 appears generally more suitable than PVA1 in combination with MIL-101(Cr), such that the former enables a higher uptake. The best water uptake of 0.67 g g^{-1} was achieved with 80 wt% MIL@PVA2 which then corresponds to 80% of the estimated water uptake of 0.84 g g^{-1}.

Neat Alfum was reported to have an S-shaped water adsorption isotherm with a steep rise around p·p$_0$$^{-1}$ ≈ 0.2 and a water loading of 0.4–0.5 g g^{-1} [13,61]. Alfum@PVA monolith composites show a similar S-shaped water sorption isotherm as neat Alfum. Towards high relative pressures of p·p$_0$$^{-1}$ > 0.8 the curvature of the water sorption isotherms resembles the neat PVA isotherm, especially for lower MOF contents. There is a slight increase in the adsorbed water amount with increasing Alfum content in the composites. In addition, the measured water loading is slightly higher than the estimated one from the mass-weighted composition. This can be explained by formation of additional interfacial mesopores in the Alfum@PVA monolith composites, which was discussed above (Table 1 and Table S2). The increased water loading for the Alfum@PVA2 and the Alfum50@PVA3 composites occurs already at lower relative pressures as is evident when comparing the water loading of the composites at relative pressure of 0.3, 0.6 and 0.9 (Fig. S13 in Supp. Info.). For these composites the measured water uptake is slightly above the estimated value over the whole pressure range. This shows that the increased uptake at p·p$_0$$^{-1}$ = 0.9 is not due to the PVA which as a neat polymer shows the major water uptake at higher p·p$_0$$^{-1}$ values.

3.2.3. Mechanical properties of Alfum@PVA2 monoliths

The mechanical properties of MOFs composites are often investigated in a simple breaking force test [27,28,47]. The breaking force is a robust value, which denotes complete material failure. However, only samples that show primarily brittle properties are suitable for a breaking force test, as any kind of plastic and elastic deformation of the samples distorts the results. A few samples manufactured in this study displayed primarily brittle behavior and, therefore, a texture analyzer was used to obtain more information on the mechanical properties. Stress-strain curves of the measurements are shown in Fig. 11 and in Fig. S12. When curves in the diagrams do not return to a stress of 0 MPa in the respective figures, the maximum applicable forces by the analytical tool were reached and the measurement was automatically stopped.

The mechanical stabilities of the monoliths were tested

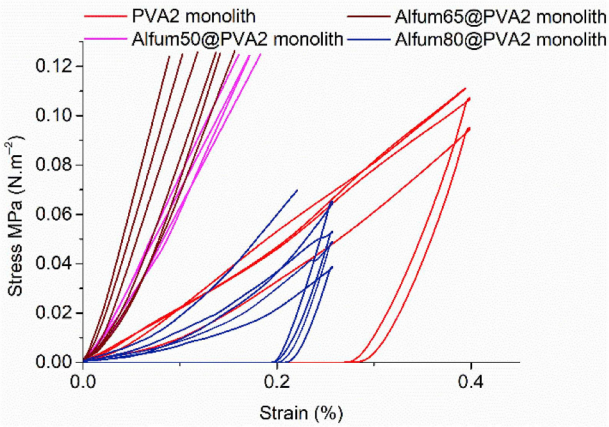

Fig. 11. Stress-strain curves of Alfum@PVA2 monoliths compressed axially. The four to six curves for each type of composite reflect the number of different samples for each composite, which were tested to ensure reproducibility.

Table 2
Density of PVA2 monolith and Alfum@PVA2 monoliths.

Sample	Average density (g/cm^{-3})
PVA2 monolith	0.10
Alfum50@PVA2	0.23
Alfum65@PVA2	0.34
Alfum80@PVA2	0.23

representatively for PVA2, Alfum50@PVA2, Alfum65@PVA2 and Alfum80@PVA2 monoliths. The data of axial compression is shown in Fig. 11. The observed variation is expected for different samples with non-identical shapes. PVA2 monoliths show a pronounced plastic and a low elastic deformation at comparably low stresses. The elastic deformation is indicated by an exerted stress on the probe during the unloading phase (return of the probe to the starting position) of two of the PVA monolith samples. The low slope at low stresses in the beginning indicates a high plastic deformation, which is supported by a remaining strain of 27–30% after unloading. The measurements of the other two samples were automatically aborted, when the maximum force was achieved, before the set absolute deformation of 3 mm was reached. Having 50 wt% Alfum in the MOF@PVA composite drastically changes the mechanical properties of the polymer (Fig. 11, pink curves). The slopes at low stresses are much higher, revealing elastic properties and a high resistance against deformation. Higher stresses have to be exerted to achieve a lower strain compared to the PVA2 monoliths. A very similar behavior is observed for a loading of 65 wt% Alfum (Fig. 11, brown curves). Concentrations of 50 and 65 wt% Alfum appear to create a rigid network that dominates the primarily plastic behavior of PVA2.

However, increasing the Alfum content to 80 wt% (Fig. 11, blue) reverses the mechanical behavior. Four out of five samples reach the set maximum deformation of 3 mm at stresses < 0.07 MPa (Fig. S12, Supp. Info.). This denotes a primarily plastic behavior. A low elastic deformation is observed again during the unloading phase.

The low elastic behavior observed for PVA2 and Alfum80@PVA2 is most likely due to an elastic expansion after an “over-pressing” of the monoliths and probably reflects the true behavior of the pure material. During compression, the porosity of the samples is continuously decreased. The further the porosity is decreased, the higher the necessary strain, as observed for PVA2 and Alfum80@PVA2. Only after most of the porous system is consumed, the elastic behavior of the material can be observed during the unloading.

Overall, Alfum65@PVA2 displays the highest mechanical resistance of all investigated MOFs. It showed only minor deformation under high loads. This correlates also with the highest detected density of all samples (Table 2). Since the test did abort automatically after the maximum loading was reached, unfortunately no information was obtained about the mode of deformation (plastic or elastic).

4. Conclusion

We present for the first-time MOF-monolith composites by using a phase-separation technique modified from the preparation technique of Sun et al. [55]. It was shown for different PVA monoliths that vacuum drying is the preferential drying procedure over supercritical and freeze-drying in order to retain the monolith shape and avoid shrinkage. The MOF@PVA composites could be reproducibly prepared. Different loading amounts of MOFs gave nearly the expected apparent mass-weighted BET surface area and water uptake capacity. Medium-molecular weight PVA2 is more suitable than high- and low-molecular weight PVA1 and PVA3, respectively for this phase-separation MOF@PVA monolith fabrication method.

For MIL-101(Cr)@PVA2 about 71–83% of the neat MIL porosity and about 77–84% of the neat MIL water uptake could be retained. For Alfum@PVAs about 86–95% of the neat Alfum surface area, about 104–123% of the neat Alfum pore volume and about 102–120% of the neat Alfum water uptake could be reached (thereby excluding Alfum50@PVA2).

It is remarkable that pore volume and water loading of Alfum@PVA monolith composites is higher than what would be estimated based on the mass-weighted composition. A plausible explanation of this result is the formation of additional mesopores at the MOF-polymer interface, which is supported from the t-plot method with the micro- and mesopore contribution. This formation of additional interfacial mesopore volume is observed in Alfum@PVA composites but not in MIL-101(Cr)@PVA composites.

Mechanical stability tests of Alfum@PVA composites reveal a maximum stability at a loading of 65 wt% of Alfum, whereas higher and lower quantities of Alfum result in mechanically less stable composite materials. For future mechanical tests, the setup of the investigations could be improved such that identical sizes of samples and different settings of the texture analyzer would lead to better data quality.

We see great potential that the technique of phase separation can be further developed and applied for other MOF@polymer monolith preparations to advance the necessary formulation of MOFs for applications. This phase-separation technique should be widely applicable to MOF@polymer monolith preparations with little tuning necessitated by differences in MOF and/or polymer.

Acknowledgments

The authors gratefully acknowledge the financial support of the Federal German Ministry of Education and Research (BMBF) in the project Optimat under grant no. 03SF0492C. We thank Anna Kira Adam from the Institute of Pharmaceutics and Biopharmaceutics at Heinrich-Heine-Universität Düsseldorf for the measurement of the mechanical stability. We also thank the Institute of Pharmaceutics and Biopharmaceutics for giving us the opportunity to measure mercury porosimetry. We thank the Institute of Organic and Macromolecular Chemistry for the usage of a freeze-drying instrument. We are indebted to Mrs. Anna Christin Kautz for measuring the IR spectra.

Appendix A. Supplementary data

Supplementary data to this article can be found online at https://doi.org/10.1016/j.micromeso.2019.02.011.

References

[1] For recent reviews on MOFs, see the editorial and issue of Chem. Soc. Rev G. Maurin, C. Serre, A. Cooper, G. Férey, The new age of MOFs and of their porous-related solids, Chem. Soc. Rev. 46 (2017) 3104–3107.
[2] J.Y. Lee, O.K. Farha, J. Roberts, K.A. Scheidt, S.T. Nguyen, J.T. Hupp, Chem. Soc. Rev. 38 (2009) 1450–1459.
[3] Y.-B. Huang, J. Liang, X.-S. Wang, R. Cao, Chem. Soc. Rev. 46 (2017) 126–157.
[4] A. Herbst, C. Janiak, CrystEngComm 19 (2017) 4092–4117.
[5] B. Li, H.-M. Wen, W. Zhou, B. Chen, J. Phys. Chem. Lett. 5 (2014) 3468–3479.
[6] P. Serra-Crespo, E.V. Ramos-Fernandez, J. Gascon, F. Kapteijn, Chem. Mater. 23 (2011) 2565–2572.
[7] P. Horcajada, R. Gref, T. Baati, P.,K. Allan, G. Maurin, P. Couvreur, G. Férey, R.E. Morris, C. Serre, Chem. Rev. 112 (2012) 1232–1268.
[8] D. Fröhlich, S.K. Henninger, C. Janiak, Dalton Trans. 43 (2014) 15300–15304.
[9] M.F. de Lange, K.J.F.M. Verouden, T.J.H. Vlugt, J. Gascon, F. Kapteijn, Chem. Rev. 115 (2015) 12205–12250.
[10] F. Jeremias, D. Fröhlich, C. Janiak, S.K. Henninger, New J. Chem. 38 (2014) 1846–1852.
[11] Y.I. Aristov, Appl. Therm. Eng. 50 (2013) 1610–1618.
[12] F. Jeremias, A. Khutia, S.K. Henninger, C. Janiak, J. Mater. Chem. 22 (2012) 10148–10151.
[13] F. Jeremias, D. Fröhlich, C. Janiak, S.K. Henninger, RSC Adv. 4 (2014) 24073–24082.
[14] J. Ehrenmann, S.K. Henninger, C. Janiak, Eur. J. Inorg. Chem. 4 (2011) 471–474.
[15] S. Kaskel, U.-H. Lee, A.H. Valekar, Y.K. Hwang, J.-S. Chang, The Chemistry of Metal-Organic Frameworks, Synthesis, Characterization, and Application, Wiley-VCH, Weinheim, 2017, pp. 551–571.
[16] L.D. O'Neill, H. Zhang, D.J. Bradshaw, J. Mater. Chem. 20 (2010) 5720–5726.

[17] R. Ostermann, J. Cravillon, C. Weidmann, M. Wiebcke, B.M. Smarsly, Chem. Commun. 47 (2011) 442–444.
[18] S. Qiu, M. Xue, G. Zhu, Chem. Soc. Rev. 43 (2014) 6116–6140.
[19] H.B.T. Jeazet, C. Staudt, C. Janiak, Dalton Trans. 41 (2012) 14003–14027.
[20] J. Dechnik, C.J. Sumby, C. Janiak, Cryst. Growth Des. 17 (2017) 4467–4488.
[21] J. Dechnik, J. Gascon, C.J. Doonan, C. Janiak, C.J. Sumby, Angew. Chem. Int. Ed. 56 (2017) 9292–9310.
[22] M. Rubio-Martinez, C. Avci-Camur, A.W. Thornton, I. Imaz, D. Maspoch, M.R. Hill, Chem. Soc. Rev. 46 (2017) 3453–3480.
[23] S. Hindocha, S. Poulston, Faraday Discuss 201 (2017) 113–125.
[24] J. Dhainaut, C. Avci-Camur, J. Troyano, A. Legrand, J. Canivet, I. Imaz, D. Maspoch, H. Reinsch, D. Farrusseng, CrystEngComm 19 (2017) 4211–4218.
[25] O. Ardelean, G. Blanita, G. Borodi, M.D. Lazar, I. Misan, I. Coldea, D. Lupu, Int. J. Hydrog. Energy 38 (2013) 7046–7055.
[26] J.A. Coelho, A.M. Ribeiro, A.F.P. Ferreira, S.M.P. Lucena, A.E. Rodrigues, D.C.S. de Azevedo, Ind. Eng. Chem. Res. 55 (2016) 2134–2143.
[27] M. Hesse, U. Müller, O.M. Yaghi, Shaped Bodies Containing Metal-Organic Frameworks, EP 1812161 A1, (2007 Aug 1).
[28] P. Küsgens, A. Zgaverdea, H.-G. Fritz, S. Siegle, S. Kaskel, J. Am. Ceram. Soc. 93 (2010) 2476–2479.
[29] P. Küsgens, Metal-organic Frameworks for Water Adsorption Application in the Automative Filtration Industry, Dissertation Dresden University of Technology, 2010.
[30] M. Wickenheisser, A. Herbst, R. Tannert, B. Milow, C. Janiak, Microporous Mesoporous Mater. 215 (2015) 143–153.
[31] M. Wickenheisser, T. Paul, C. Janiak, Microporous Mesoporous Mater. 220 (2016) 258–269.
[32] M. Wickenheisser, C. Janiak, Microporous Mesoporous Mater. 204 (2015) 242–250.
[33] P. van de Witte, P.J. Dijkstra, J.W.A. van den Berg, J. Feijen, J. Membr. Sci. 117 (1996) 1–31.
[34] X. Sun, Y. Xin, X. Wang, H. Uyama, Colloid Polym. Sci. 295 (2017) 1827–1833.
[35] Y. Xin, T. Fujimoto, H. Uyama, Polymer 53 (2012) 2847–2853.
[36] X. Sun, K. Wang, B. Zhang, F. Zou, G. Sun, W. Han, X. Wang, Chem. Lett. 46 (2017) 792–794.
[37] E. Rezabeigi, P.M. Wood-Adams, R.A.L. Drew, Polymer 55 (2014) 6743–6753.
[38] S. Yoneda, W. Han, U. Hasegawa, H. Uyama, Polymer 55 (2014) 3212–3216.
[39] J.-C. Park, T. Ito, K.-O. Kim, K.-W. Kim, B.-S. Kim, M.-S. Khil, H.-Y. Kim, I.-S. Kim, Polym. J. 42 (2010) 273–276.
[40] V. Finsy, L. Ma, L. Alaerts, D.E. De Vos, G.V. Baron, J.F.M. Denayer, Microporous Mesoporous Mater. 120 (2009) 221–227.
[41] C.A. Grande, V.I. Águeda, A. Spjelkavik, R. Blom, Chem. Eng. Sci. 124 (2015) 154–158.
[42] H. Zhu, Q. Zhang, S. Zhu, Chem. Eur J. 22 (2016) 8751–8755.
[43] H. Thakkar, S. Eastman, Q. Al-Naddaf, A.A. Rownaghi, F. Rezaei, ACS Appl. Mater. Interfaces 9 (2017) 35908–35916.
[44] J.A. Delgado, V.I. Áqueda, M.A. Uguina, P. Brea, C.A. Grande, Chem. Eng. J. 326 (2017) 117–129.
[45] F.M. Plieva, P. Ekström, I.Y. Galaev, B. Mattiasson, Soft Matter 4 (2008) 2418–2428.
[46] X. Meng, N. Zeng, J. Zhang, L. Jiang, Y. Dan, J. Colloid Interface Sci. 497 (2017) 290–297.
[47] A.H. Valekar, K.-H. Cho, U.-H. Lee, J.S. Lee, J.W. Yoon, Y.K. Hwang, S.G. Lee, S.J. Cho, J.-S. Chang, RSC Adv. 7 (2017) 55767–55777.
[48] M. Thommes, K. Kaneko, A.V. Neimark, J.P. Olivier, F. Rodriguez-Reinoso, J. Rouquerol, K.S. Sing, Pure Appl. Chem. 87 (2015) 1051–1069.
[49] A. Vishnyakov, P. Ravikovitch, A.V. Neimark, Langmuir 16 (2000) 2311–2320.
[50] L.D. Gelb, K.E. Gubbins, R. Radhakrsihan, M. Sliwinska-Bartowiak, Rep. Prog. Phys. 62 (1999) 1573–1659.
[51] N.A. Sedron, J.P.R.B. Walton, N. Quirke, Carbon 27 (1989) 853–861.
[52] J. Landers, G.Y. Gor, A.V. Neimark, Colloids Surf., A 437 (2013) 3–32.
[53] P. Karikkethu, P. Deschamps, J. Deschamps, J. Mater. Chem. A 3 (2015) 7014–7021.
[54] T. Zhao, F. Jeremias, I. Boldog, B. Nguyen, S.K. Henninger, C. Janiak, Dalton Trans. 44 (2015) 16791–16801.
[55] X. Sun, T. Fujimoto, H. Uyama, Polym. J. 45 (2013) 1101–1106.
[56] D.A. Loy, E.M. Russick, S.A. Yamanaka, B.M. Baugher, Chem. Mater. 9 (1997) 2264–2268.
[57] M. Chen, B. Coasne, R. Guyer, D. Derome, J. Carmeliet, Nat. Commun. 9 (2018) 3507.
[58] E. Marin, J. Rojas, Int. J. Pharm. Sci. Rev. Res. 30 (2015) 189–194.
[59] E. Alvarez, N. Guillou, C. Martineau, B. Bueken, B. van de Voorde, C. Le Guillouzer, P. Fabry, F. Nouar, F. Taulelle, D. de Vos, J.-S. Chang, K.H. Cho, N. Ramsahye, T. Devic, M. Daturi, G. Maurin, C. Serre, Angew. Chem. Int. Ed. 54 (2015) 3664–3668.
[60] G. Férey, C. Mellot-Draznieks, C. Serre, F. Millange, J. Dutour, S. Surblé, I. Margiolaki, Science 309 (2005) 2040–2042.
[61] E. Leung, U. Müller, N. Trukhan, H. Mattenheimer, G. Cox, S. Blei, Process for Preparing Porous Metal-Organic Frameworks Based on Aluminum Fumarate, US 201/0082864 A1, (2012 Apr 5).

Supporting Information
Shaping of metal-organic frameworks into mechanically stable monoliths with poly(vinyl alcohol) by phase separation technique

*Emrah Hastürk[a], Carsten Schlüsener[a], Julian Quodbach[b], Alexa Schmitz[a], Christoph Janiak[a]**

[a] Institut für Anorganische Chemie und Strukturchemie, Heinrich-Heine-Universität, D-40204 Düsseldorf, Germany. Email: janiak@uni-duesseldorf.de

[b] Institut für Pharmazeutische Technologie und Biopharmazie, Heinrich-Heine-Universität, D-40204 Düsseldorf, Germany

Emails:
emrah.hastuerk@hhu.de, carsten.schluesener@uni-duesseldorf.de,
julian.quodbach@uni-duesseldorf.de, alexa.schmitz@uni-duesseldorf.de

Content:

- **Results of the shaped bodies related to this work**
- **Micropore volume of samples according to the t-plot method.**
- **Structure and properties of MIL-101(Cr)**
- **Structure and properties of aluminum fumarate (Alfum)**
- **SEM (Scanning electron microscopy) images of MIL-101(Cr) and Alfum**
- **Powder X-ray diffraction (PXRD) of MIL-101(Cr), Alfum and related monoliths**
- **Infrared (IR) spectroscopy**
- **Poly(vinyl alcohol) (PVA) porosity characterization**
- **Compressive strength measurements of PVA and Alfum@PVA2 monoliths for mechanical stability test**
- **Comparison of water loading of composites at relative pressures of 0.3, 0.6 and 0.9**
- **Increase of mesopores in Alfum@PVA2 and Alfum@PVA3 composites analyzed from pore size distribution**
- **TGA (Thermogravimetric analysis) results of PVA monoliths**
- **Comparison of the different DFT methods to determine surface area for Alfum@PVA composites**

Table S2. Literature data for shaped MOF bodies

Used MOFs in the Composites	**S(BET) MOF (m^2/g)**	**Method**	**Binder**	**MOF-loading (wt%)**	**S(BET) calc (m^2/g)[a]**	**Measured S(BET) (m^2/g) of composite**
MIL-101(Cr) [1]	3060	Embedding in binder	R,F-xerogel[b]	35; 77	1140; 2380	1340; 2530
MIL-101(Cr) [2]	2860	Embedding in binder	poly(NIPAM)HIPE[c]	71; 92	2030; 2630	960; 980
Zr-MOF [3]	1360	Centrifugal granulation	Sucrose	90	1224	674
MOF-74(Ni) [4]	1180	3D-Printing	PVA[d]	80	944	737
UTSA-16(Co) [4]	727	3D-Printing	PVA[d]	85	618	568
ZIF-8 [5]	1675	Extrusion	PVA[d]	97	1626	1582
HKUST-1 [5]	1700	Extrusion	PVA[d]	97	1651	1604
MIL-101(Cr) [this work]	2731	Embedding in binder by phase separation	PVA[d]	80	2192	1820
Alfum [this work]	1031	Embedding in binder by phase separation	PVA[d]	80	832	788

[a] Apparent BET surface area S(BET) value calculated as the sum of the mass-weighted areas of the MOFs and the found or calculated binder from the following formula (I): $\mathrm{S(BET)calc} = \frac{\mathrm{wt\%\ of\ binder}}{100} \times \mathrm{S(BET, Binder)} + \frac{\mathrm{wt\%\ of\ MOF}}{100} \times \mathrm{S(BET, MOF)}$ (I)

[b] R,F-xerogel = resorcinol-formaldehyde- xerogel

[c] poly(NIPAM)HIPE = poly(N-isopropyl acrylamide) high internal phase emulsion

[d] PVA = poly(vinyl alcohol)

Table S2. Porosity analysis according to the t-plot method of de Boer [6].

Sample[a]	External and mesopore surface area [m^2/g] (% of MOF)	Micropore volume [cm^3·g^{-1}] (% of MOF)	Intercept [cm^3·g^{-1}]	Slope [cm^3·g^{-1}·Å^{-1}]	R^2
MIL-101(Cr)	303	1.054	682	19.6	0.990
MIL-101(Cr)33@PVA1	103 (34)	0.221 (21)	143	6.6	0.994
MIL-101(Cr)50@PVA1	132 (44)	0.341 (32)	220	8.5	0.992
MIL-101(Cr)33@PVA2	96 (32)	0.262 (25)	169	6.2	0.994
MIL-101(Cr)40@PVA2	152 (50)	0.277 (26)	179	9.8	0.991
MIL-101(Cr)50@PVA2	185 (61)	0.360 (34)	233	12.0	0.989
MIL-101(Cr)60@PVA2	193 (64)	0.463 (44)	299	12.5	0.989
MIL-101(Cr)70@PVA2	221 (73)	0.569 (54)	368	14.3	0.995
MIL-101(Cr)80@PVA2	178 (59)	0.718 (68)	464	11.5	0.991
Alfum	109	0.358	232	7.0	0.999
Alfum50@PVA2	92 (84)	0.120 (34)	77	5.9	0.998
Alfum65@PVA2	137 (126)	0.199 (56)	128	8.9	0.999
Alfum80@PVA2	120 (110)	0.264 (74)	171	7.8	0.999
Alfum50@PVA3	135 (124)	0.136 (38)	88	8.7	0.999
Alfum65@PVA3	123 (113)	0.184 (51)	119	8.0	0.998
Alfum80@PVA3	139 (128)	0.255 (71)	167	9.0	0.999

[a] Nomenclature: In MIL-101(Cr)*xx*@PVA*y* or Alfum*xx*@PVA*y* *xx* refers to the wt% of MOF in the composite and *y* denotes the PVA type (see Exp. section). Thus MIL-101(Cr)80@PVA1 has 80 wt% loading of MIL-101(Cr) in PVA1 monolith.

[b] The intercept of the t-plot gives the specific micropore volume, V_{MP}, by converting to a liquid volume, according to $V_{MP} = i \times 0.001547$.

[c] From the slope in the t-plot the mesopore surface area is obtained.

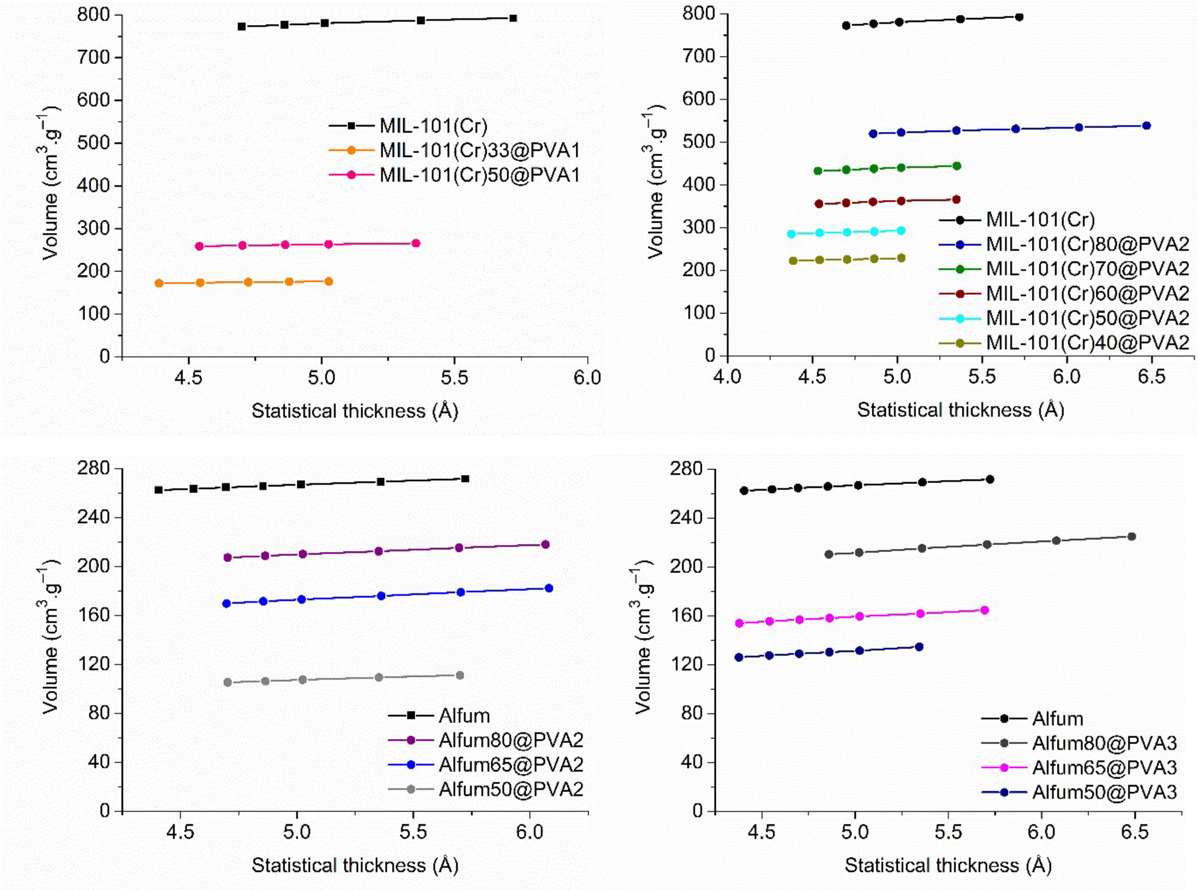

Fig. S1. t-plot curves of the MOF@PVA composites for the analysis of the micropore volume. The points for the t-plot curves were selected in the relative pressure range of 0.2 and 0.5.

Structure and properties of MIL-101(Cr)

Micro-mesoporous MIL-101(Cr), $\{Cr_3(\mu_3\text{-}O)(F,OH)(H_2O)_2(BDC)_3 \cdot {\sim}25H_2O\}_n$ (BDC = benzene-1,4-dicarboxylate, terephthalate) is built from supertetrahedra (ST) (with a free aperture of ~8.6 Å) and the connection of each ST generate two different cages with a diameter of ~29 Å and 34 Å (Fig. S2) with pentagonal windows of ~12 Å diameter and hexagonal windows of ~14.5 Å x 16 Å diameter, respectively [7]. MIL-101(Cr) has an apparent Brunauer-Emmett-Teller surface area, 'apparent S(BET)' up to 4100 $m^2 \cdot g^{-1}$ and water loading capacity in the range of 1.0 – 1.6 $g \cdot g^{-1}$ showing an S-shaped adsorption at around $p.p_0^{-1} \approx 0.5$ [7,8]. Being relatively hydrothermally stable MIL-101(Cr) is a good candidate for water sorption based applications [9]. Water cycling tests have only shown a slight degradation of approximately 3% after 40 ad-/desorption cycles [10].

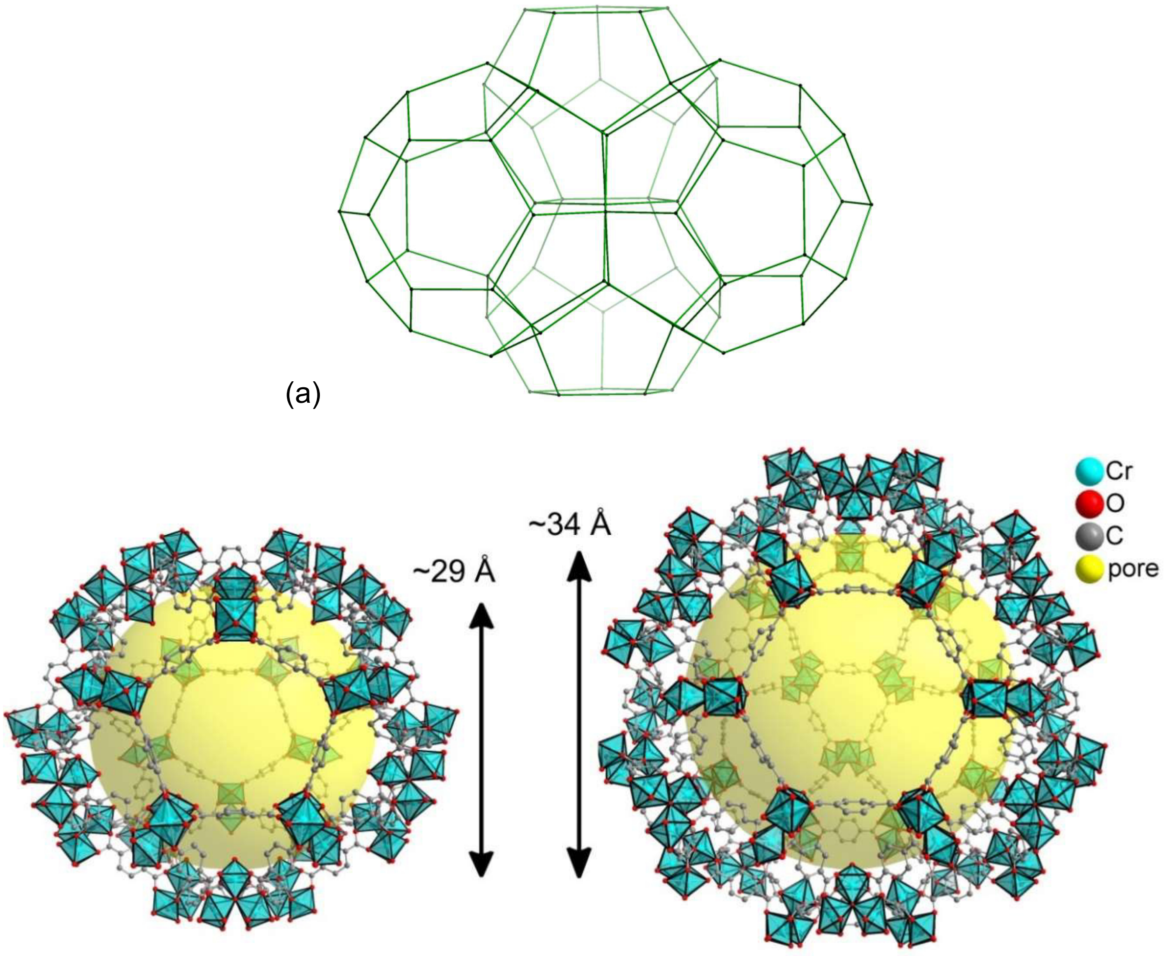

(a)

(b)

(c)

Fig. S2. MIL-101(Cr): (a) mesoporous network; (b) small cage with pentagonal windows; (c) large cage with pentagonal and hexagonal windows; Objects are not drawn to scale. The yellow spheres in the mesoporous cages with the indicated diameters take into account the van-der-Waals radii of the framework walls. Hydrogen atoms and solvent molecules of crystallization are not shown. Graphics have been drawn with DIAMOND [11] from the deposited cif-file for MIL-101(Cr) (CSD-Refcode OCUNAC) [7].

Structure and properties of aluminum fumarate

Microporous aluminum fumarate, Alfum, that is, $Al(OH)(fum)\cdot xH_2O$ (x = 3.5; fum = fumarate) is isoreticular to MIL-53(Al)-BDC or $Al(OH)(BDC)\cdot H_2O$ (BDC=1,4-benzenedicarboxylate) and also called as MIL-53(Al)-FA. The framework aluminum atoms or rather {Al(μ-OH)} chains are connected by fumarate forming infinite channels with circa 5.7 x 6.0 Å^2 free dimensions along the aluminum hydroxide chain direction [12]. Alfum was a commercially available MOF under the trade mark Basolite^{TM} A520 and can be synthesized under very mild conditions. Alfum has an apparent S(BET) above 1000 $m^2\cdot g^{-1}$ and a S-shaped water adsorptions at $p\cdot p_0^{-1} \approx 0.2$ with a water loading of 0.4–0.5 $g\cdot g^{-1}$ [13,14]. The hydrothermal stability of Alfum was tested over 4500 ad-desorption cycle resulting in no apparent decomposition [14].

Figure S3 shows the structural features of aluminum fumarate.

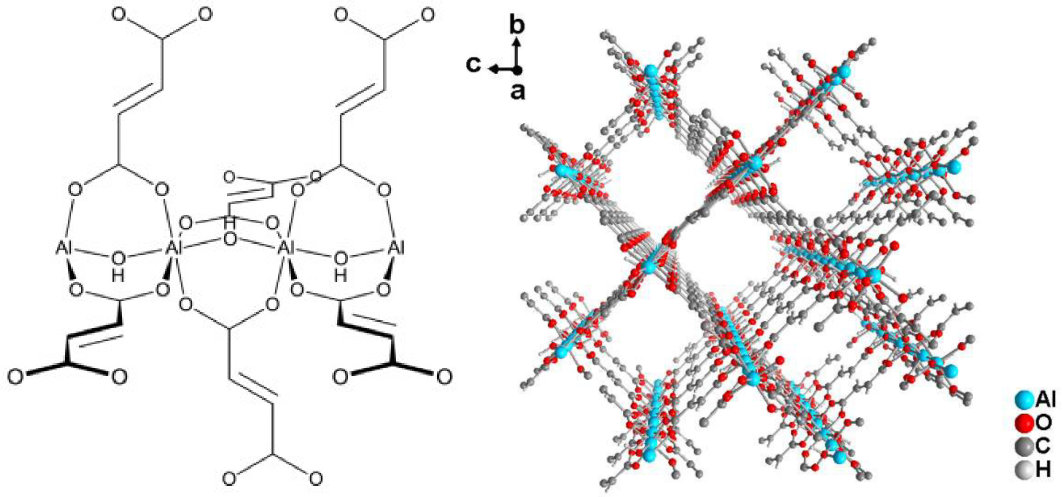

Fig. S3. Left: Building block of aluminum fumarate, in analogy to the structure of MIL-53. The Figure was taken from ref. [14]. Right: View along the a-axis of aluminum fumarate structure. Graphic produced by software Diamond [11] from cif-file for Basolite A520 (CSD-Refcode DOYBEA, CCDC no. 1051975) [12].

SEM images of MIL-101(Cr) and aluminum fumarate

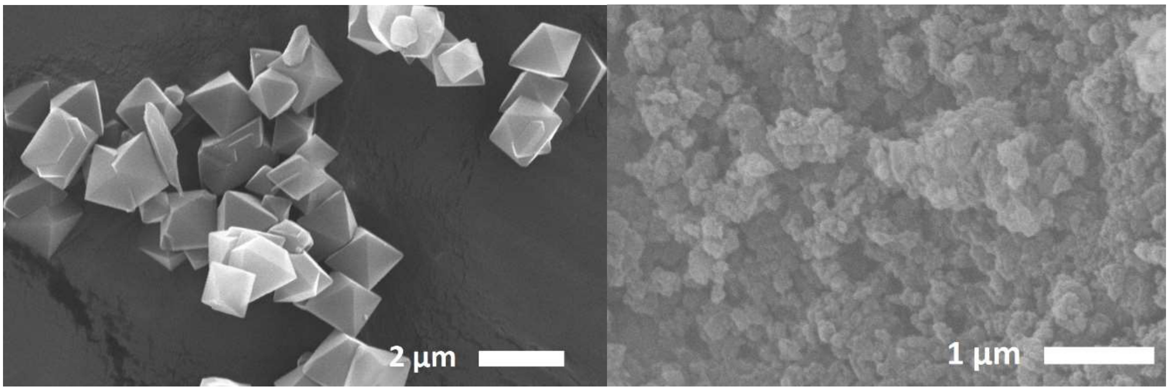

Fig. S4. Scanning electron microscopy (SEM) images of MIL-101(Cr) (left) and Alfum (right).

The morphology of MIL-101(Cr) and Alfum is shown in the SEM images in Fig. S4. MIL-101(Cr) has the characteristic octahedral morphology. The particle size of the prepared MIL-101(Cr) is around 1.5 ± 0.3 µm (determined from manually measured over 36 particles). Alfum is a very crystalline material (see PXRD in Fig. S5), but has no characteristic microcrystal morphology and tends towards aggregation so that no particle size was determined. The SEM image (Fig. S4) indicates, however, that the primary particle size is less than 1 µm [15].

Powder X-ray diffraction (PXRD) of MIL-101(Cr), aluminum fumarate and related monoliths

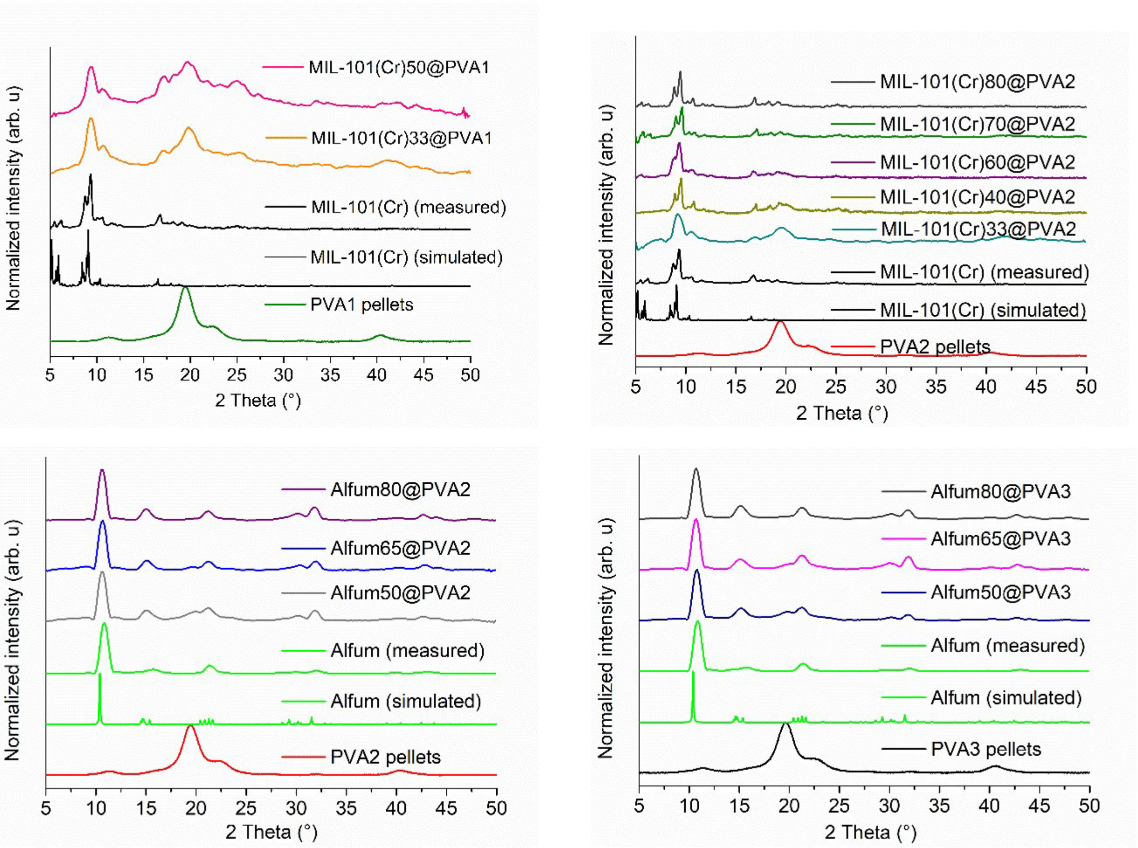

Fig. S5. Experimental powder X-ray diffraction patterns of composite pellets with the indicated composition, MIL-101(Cr)*xx*@PVA*y* (top row) or Alfum*xx*@PVA*y* (bottom row) in comparison to the simulated and experimental PXRD of the pure MOF (MIL-101(Cr) simulated from CSD-Refcode OCUNAC [7]; Alfum simulated form CSD-Refcode DOYBEA [12]).

Infrared (IR) spectroscopy

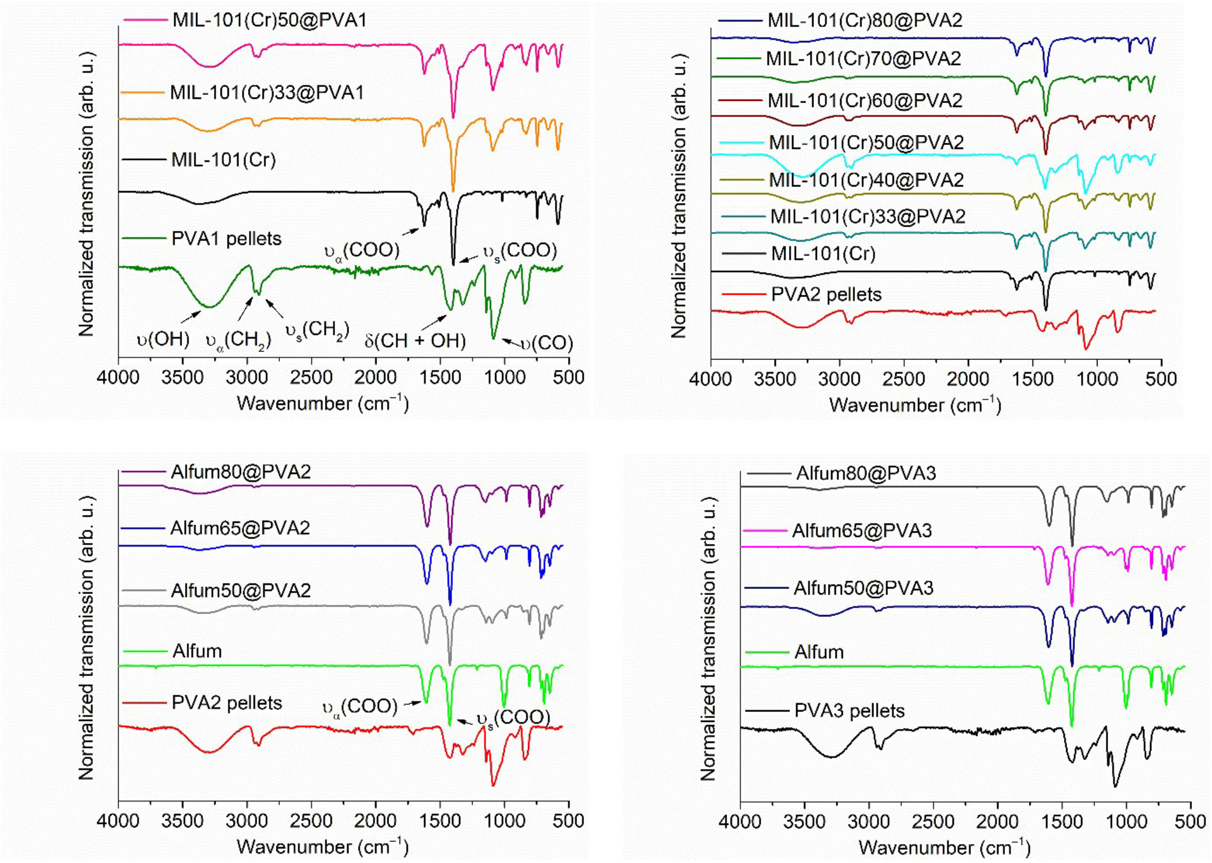

Fig. S6. IR spectra of

- PVA1 pellets, MIL-101(Cr) and MIL-101(Cr)*xx*@PVA1 (*xx* = 33; 40; 50) (top left),
- PVA2 pellets, MIL-101(Cr) and MIL-101(Cr)*xx*@PVA2 (*xx* = 33; 40; 50; 60; 70; 80) (top right),
- PVA2 pellets, Alfum and Alfum*xx*@PVA2 (*xx* = 50; 65; 80) (bottom left),
- PVA3 pellets, Alfum and Alfum*xx*@PVA3 (*xx* = 50; 65; 80) (bottom right)

Poly(vinyl alcohol) porosity characterization

Poly(vinyl alcohol) of three different degrees of polymerization that is, chain lengths or molecular weights were used:

PVA1: 124 – 186 kDa, 99% hydrolyzed (Sigma Aldrich)
PVA2: 125 kDa, 98% hydrolyzed (Sigma Aldrich)
PVA3: 22 kDa, 97.5 – 99.5% hydrolyzed (Fluka)
The repeat unit of PVA is given in Fig. S7.

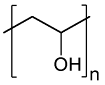

Fig. S7. Repeating unit of poly(vinyl alcohol).

By principle N_2 sorption isotherms and BET analysis cannot reveal macropores (> 50 nm) but only micropores (<2 nm) and mesopores (2-50 nm). The BET surface areas of the PVA monoliths are around 30 m^2/g, which is in the range of the outer surface areas of fine powders. The nitrogen sorption isotherms (at 77 K) of the PVA monoliths, which were dried by three different methods, are shown in Fig. S8. The isotherms can be categorized as Type II with H3 hysteresis, in line with a non-porous or macroporous material [16]. The SEM images in Fig. 2 clearly showed the existence of macropores (> 50 nm). Based on the N_2 adsorption isotherm non-linear density functional theoretical (NLDFT) analysis also shows some mesopores in the range of 2 to 20 nm (20 to 200 Å).

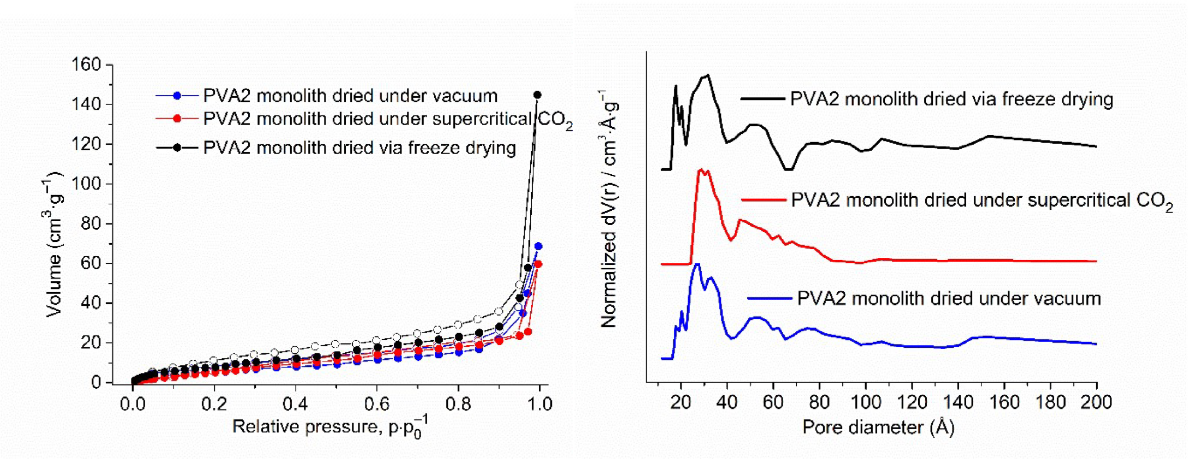

Fig. S8. N_2 sorption isotherms (77 K) of PVA2 monoliths from different drying conditions (left) and related mesopore size distribution (right). The BET surface area is 38, 28 and 33 m^2/g for the vacuum, supercritical and freeze-dried material, respectively. Pore distribution are based on the NLDFT equilibrium' model with 'N_2 at 77 K on carbon with slit pores'.

In order to evaluate the macroporosity of selected PVA monoliths, a mercury porosimetry measurement was carried out on one monolith from each drying method (Fig. S9).

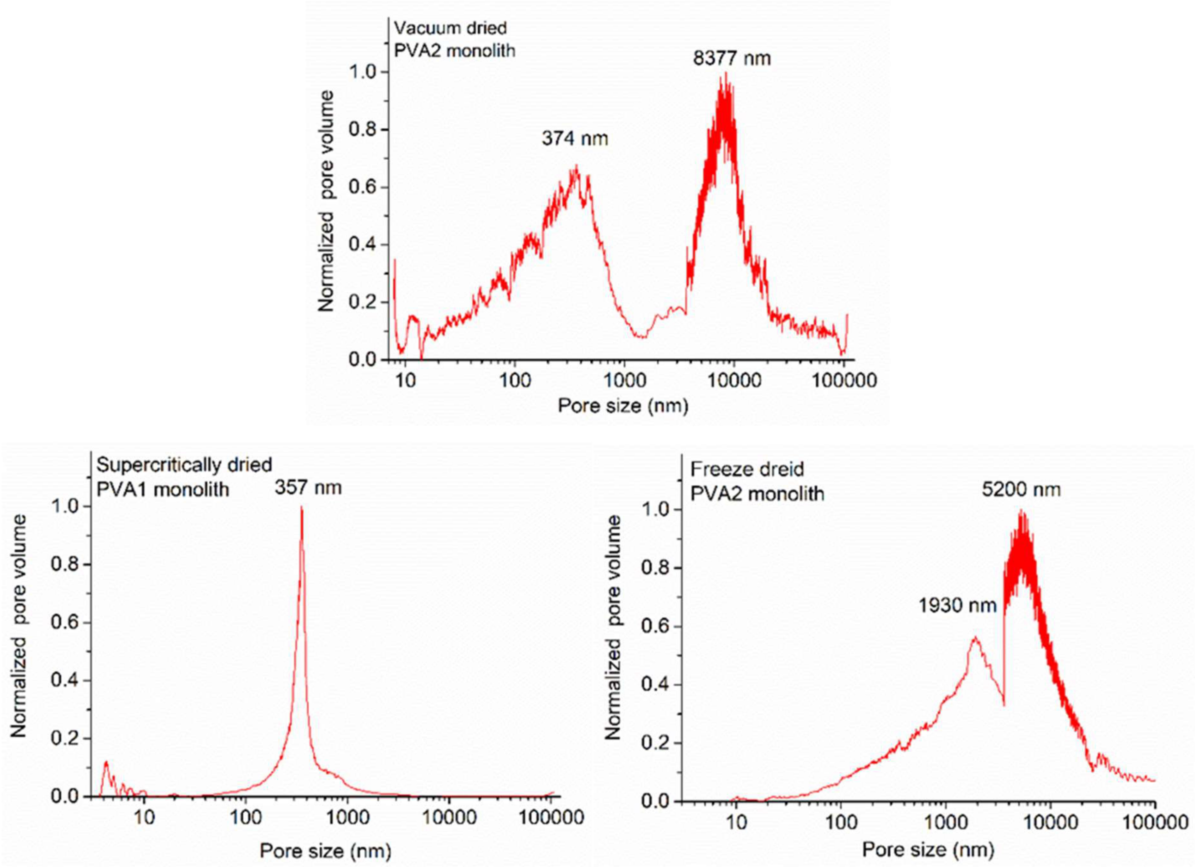

Fig. S9. Pore size distribution of vacuum dried PVA2, supercritically dried PVA1 and freeze-dried PVA2 monolith determined via Hg-porosimetry.

Compressive strength measurements of PVA and Alfum@PVA2 monoliths for mechanical stability test

Fig. S10. Images of texture analyzer (Stable Micro Systems, model TA XT2i) for the compressive strength measurement and (insert) close-up view of one example during pressing of the monolith.

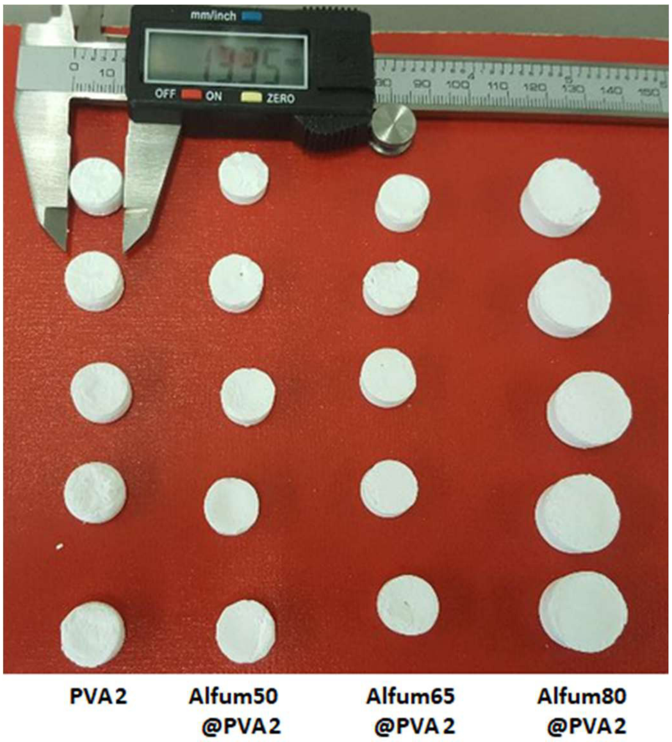

Fig. S11. Top view of the fabricated PVA and Alfum@PVA2 monoliths for the mechanical stability test.

The height/diameter range of the monolith cylinders was from about 6/13 mm to 9/17 mm.

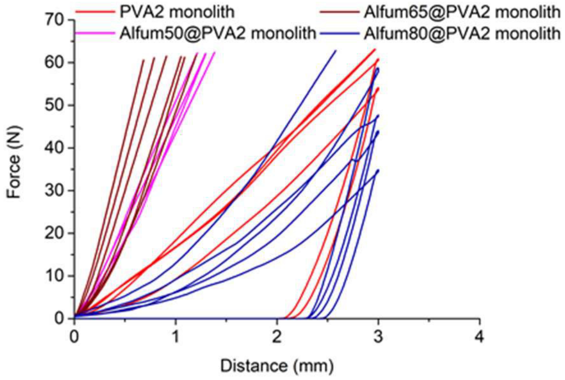

Fig. S12. Compressive strength measurements of PVA2 and Alfum@PVA2 monoliths pressed from the top. The four to six curves for each type of composite reflect the number of different samples for each composite which were tested to ensure reproducibility.

Comparison of the water loading of composites at relative pressure of 0.3, 0.6 and 0.9

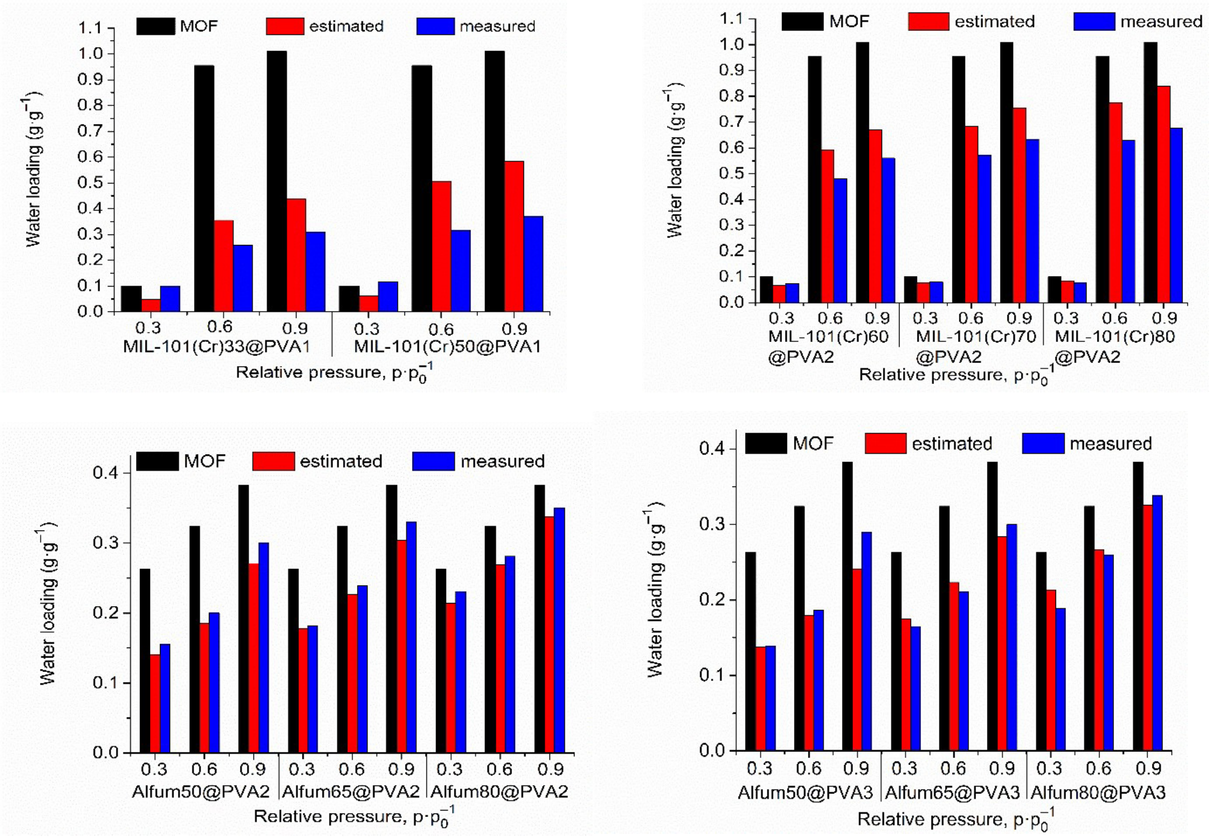

Fig. S13. Comparison of the water loading of MIL101(Cr)@PVA1 and PVA2 (top) and Alfum@PVA2 and PVA3 (bottom) at relative pressures of 0.3, 0.6 and 0.9. There is an increased measured water loading compared to the estimated values for the Alfum@PVA2 and the Alfum50@PVA3 composites over the whole pressure range.

Increase of mesopores in Alfum@PVA2 and Alfum@PVA3 composites analyzed from pore size distribution

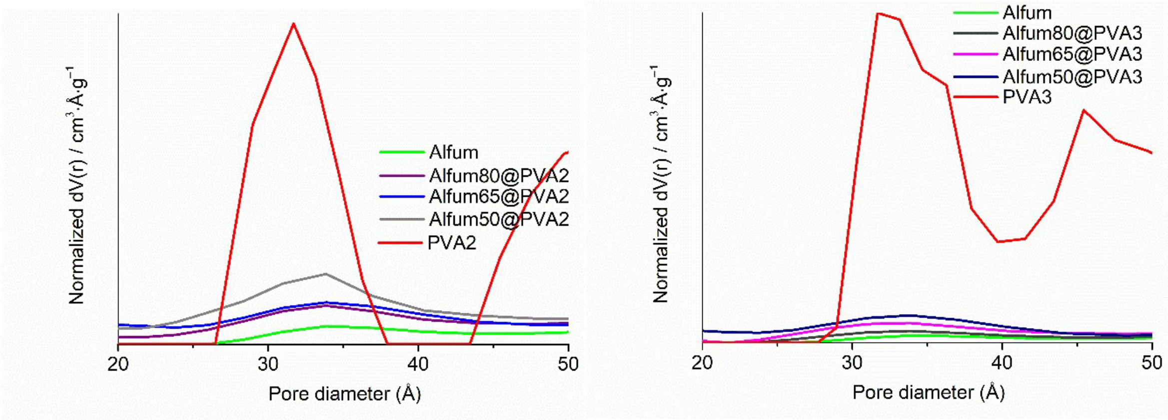

Fig. S14. Pore size distribution of Alfum@PVA2 and Alfum@PVA3 in the mesopores range around 30 Å determined using DFT calculation based on the data from nitrogen sorption measurement**.**

TGA (Thermogravimetric analysis) results of PVA monoliths

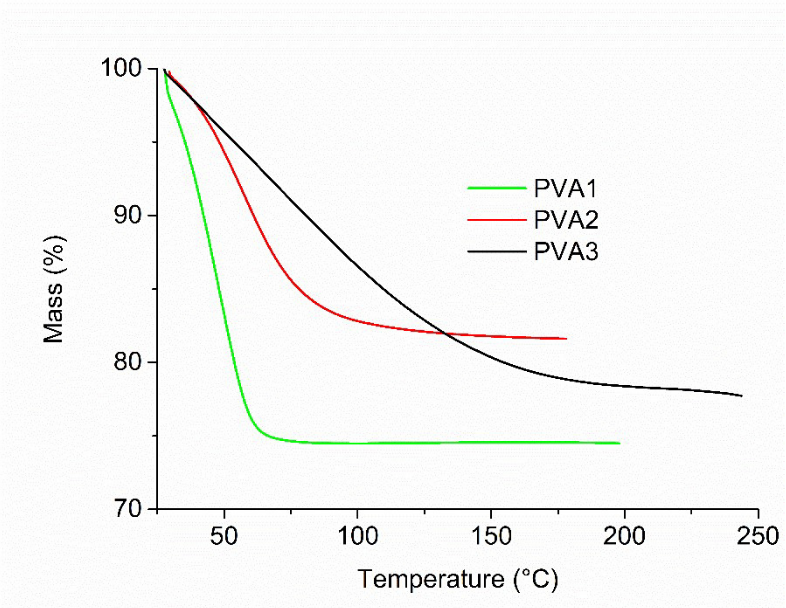

Fig. S15. Thermograms of water-vapor loaded PVA monoliths. The PVA monoliths were stored at room temperature in closed vessel under 100% relative humidity for 18 h prior to measurement in order to model the conditions prior to desorption in the volumetric vapor measurements (cf. Fig. 3).

Comparison of the different DFT methods to determine surface area for Alfum@PVA composites

In the following Table S3 are listed different DFT models to obtain surface area as well as pore size which is compared with apparent S(BET) and pore volume obtained from nitrogen sorption (and pore size according to crystal structure analysis). QSDFT gives the surface area very close to the apparent S(BET) as well as a pore size very close to the determined value from crystal structure analysis [12].

Table S3. Comparison of the apparent S(BET) and pore widths for Alfum composites with different DFT methods.

Sample	Surface area $[m^2 \cdot g^{-1}]$				Pore width [Å]			
	S(BET)[a]	NLDFT[b]	NLDFT[c]	QSDFT[d]	NLDFT[b]	NLDFT[c]	QSDFT[d]	
Alfum	1038	919	1100	1077	12.3	11.1	6.7	5.7 x 6.0[e]
Alfum50@PVA2	392	315	381	387	15.0	11.7	7.2	
Alfum65@PVA2	639	553	653	657	11.8	10.6	6.7	
Alfum80@PVA2	786	620	753	775	14.7	12.1	7.2	
Alfum50@PVA3	474	384	463	479	14.1	11.7	6.7	
Alfum65@PVA3	582	500	586	581	12.9	11.1	7.2	
Alfum80@PVA3	788	690	827	808	11.8	10.6	6.7	

[a] Apparent S(BET) determined from N_2 sorption isotherm at 77 K with a standard deviation ± 20 $m^2 \cdot g^{-1}$ (calculated over 5 points in the range of $0.05 < p \cdot p_0^{-1} < 0.2$ for MIL-101 and corresponding composites, and $0.01 < p \cdot p_0^{-1} < 0.08$ for Alfum and related composites).

[b] Density functional theory (DFT) calculations for the pore size distribution curves were done with the native NovaWin 11.03 software using the 'N_2 at 77 K on carbon, slit pore, non-local density functional theory (NLDFT) equilibrium' model.

[c] Density functional theory (DFT) calculations for the pore size distribution curves were done with the native NovaWin 11.03 software using the 'N_2 at 77 K on carbon, slit/cylindrical pore, non-local density functional theory (NLDFT) equilibrium' model.

[d] Density functional theory (DFT) calculations for the pore size distribution curves were done with the native NovaWin 11.03 software using the 'N_2 at 77 K on carbon, slit pore, quench solid density functional theory (QSDFT) equilibrium' model for Alfum and Alfum@PVA composites.

[e] Channel dimension of Alfum (5.7 x 6.0 Å^2) calculated from the crystal structure analysis (Fig. S3) [12]

[1] M. Wickenheisser, A. Herbst, R. Tannert, B. Milow, C. Janiak, Microporous Mesoporous Mater. 215 (2015) 143–153.

[2] M. Wickenheisser, T. Paul, C. Janiak, Microporous Mesoporous Mater. 220 (2016) 258–269.

[3] J. Ren, N.M. Musyoka, H. W. Langmi, A. Swartbooi, B.C. North, M. Mathe, Int. J. Hydrogen Energ. 40 (2015) 4617–4622

[4] H. Thakkar, S. Eastman, Q. Al-Naddaf, A.A. Rownaghi, F. Rezaei. ACS Appl. Mater. Interfaces 9 (2017) 35908−35916.

[5] J.A. Delgado, V.I. Águeda, M.A. Uguina, P. Brea, C.A. Grande, Chem. Eng. J. 326 (2017) 117-129.

[6] B.C. Lippens, J.H. de Boer, J. Catal. 4 (1965) 319–323.

[7] G. Férey, C. Mellot-Draznieks, C. Serre, F. Millange, J. Dutour, S. Surblé, I. Margiolaki, Science 309 (2005) 2040–2042.

[8] M.F. de Lange, K.J.F.M. Verouden, T.J H. Vlugt, J. Gascon, F. Kapteijn, Chem. Rev. 115 (2015) 12205–12250.

[9] A. Khutia, H.U. Rammelberg, T. Schmidt, S.K. Henninger, C. Janiak, Chem. Mater. 25 (2013) 790−798.

[10] J. Ehrenmann, S.K. Henninger, C. Janiak, Eur. J. Inorg. Chem. 4 (2011) 471–474.

[11] K. Brandenburg, Diamond (Version 4), Crystal and Molecular Structure Visualization, Crystal Impact – K. Brandenburg & H. Putz Gbr, Bonn (Germany), 2009-2017.

[12] E. Alvarez, N. Guillou, C. Martineau, B. Bueken, B. van de Voorde, C. Le Guillouzer, P. Fabry, F. Nouar, F. Taulelle, D. de Vos, J.-S. Chang, K. H. Cho, N. Ramsahye, T. Devic, M. Daturi, G. Maurin, C. Serre, Angew. Chem. 127 (2015) 3735–3739; Angew. Chem. Int. Ed. 54 (2015) 3664–3668.

[13] E. Leung, U. Müller, N. Trukhan, H. Mattenheimer, G. Cox, S. Blei, Process For Preparing Porous Metal-Organic Frameworks Based On Aluminum Fumarate, US 201/0082864 A1. 2012 Apr 5.

[14] F. Jeremias, D. Fröhlich, C. Janiak, S.K. Henninger, RSC Adv. 4 (2014) 24073–24082.

[15] M. Gaab, N. Trukhan, S. Maurer, R. Gummaraju, U. Müller, Microporous Mesoporous Mater. 157 (2012) 131–136.

[16] M. Thommes, K. Kaneko, A.V. Neimark, J.P. Olivier, F. Rodriguez-Reinoso, J. Rouquerol, K.S. Sing, Pure Appl. Chem. 87 (2015) 1051–1069.

3.2 Shaping of MOFs via freeze-casting method with hydrophilic polymers and their effect on textural properties

Emrah Hastürk, Simon-Patrick Höfert, Burhan Topalli, Carsten Schlüsener, Christoph Janiak

Micropor. Mesopor. Mater. (Accepted)

Impact factor (2017–2019): 4.182

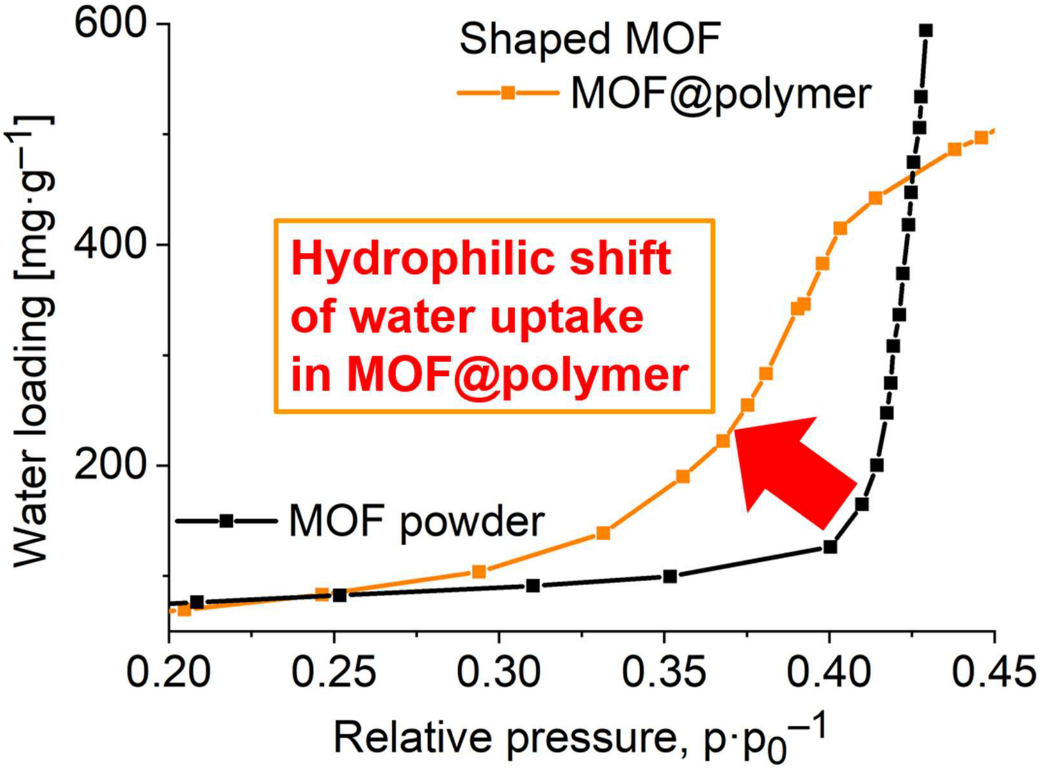

Graphical abstract

Abstract:

Shaping of metal-organic frameworks (MOFs) and tuning of their sorption properties is a very important and challenging aspect for the usage of MOFs for many applications. Both shaping and tuning can be addressed by composite preparation as an effective method. Herein, we present the shaping of the hydrothermally stable MOFs aluminum fumarate, MIL-160(Al) and MIL-101(Cr) using the freeze-casting method with the hydrophilic polymer binders polyacrylic acid (PAA), sodium polyacrylate (PAANa), polyethylene glycol (PEG), polyethylene imine (PEI), polyvinyl alcohol (PVA) and polyvinyl pyrrolidone (PVP). Furthermore, the effect of in-situ cross-linking below the freezing point (cryopolymerization) on the textural properties of monoliths was also investigated using MIL-101(Cr) and aluminum fumarate with the polymer PVA. The selected MOFs were chosen due to their outstanding stability, sorption properties

and differing hydrophilicities. In the obtained mechanically stable monoliths, each MOF showed a different compatibility with the used polymers. From 21 different MOF@polymer composites with 80 wt% loading of MOF, 12 of them exhibited negligible pore blocking effects and very high nitrogen sorption properties in correspondence with the MOF mass fraction. On the other hand, water uptake is especially in cases of MOF@PVA and MOF@PVP in good agreement with the MOF fraction and can be enhanced by the contribution of the hydrophilic polymer to the composite. In particular, most MIL-101(Cr) composites showed a hydrophilic shift to lower relative pressure $p \cdot p_0^{-1}$ compared to the rather hydrophobic neat MIL-101(Cr). IR spectroscopy indicated a clear interaction of PEI with the Al-MOFs aluminum fumarate and MIL-160(Al) resulting in MOF pore blocking. The molecular weight of the polymer is not significant for the freeze-casting method but plays an important role in the cryopolymerization.

Author’s share of work:

- Designing and performing of the synthetic work and evaluation of the results.
- Writing of the manuscript and drawing of the figures, graphs and tables except for SEM images (taken by Mr. Schlüsener) and MOF figures (drawn with DIAMOND by Prof. Janiak).
- Editing of the manuscript regarding the reviewers’ comments together with Prof. Janiak.

Shaping of MOFs via freeze-casting method with hydrophilic polymers and their effect on textural properties

*Emrah Hastürk, Simon-Patrick Höfert, Burhan Topalli, Carsten Schlüsener, Christoph Janiak**
Institut für Anorganische Chemie und Strukturchemie, Heinrich-Heine-Universität, D-40204 Düsseldorf, Germany. Email: janiak@uni-duesseldorf.de

Abstract

Shaping of metal-organic frameworks (MOFs) and tuning of their sorption properties is a very important and challenging aspect for the usage of MOFs for many applications. Both shaping and tuning can be addressed by composite preparation as an effective method. Herein, we present the shaping of the hydrothermally stable MOFs aluminum fumarate, MIL-160(Al) and MIL-101(Cr) using the freeze-casting method with the hydrophilic polymer binders polyacrylic acid (PAA), sodium polyacrylate (PAANa), polyethylene glycol (PEG), polyethylene imine (PEI), polyvinyl alcohol (PVA) and polyvinyl pyrrolidone (PVP). Furthermore, the effect of in-situ cross-linking below the freezing point (cryopolymerization) on the textural properties of monoliths was also investigated using MIL-101(Cr) and aluminum fumarate with the polymer PVA. The selected MOFs were chosen due to their outstanding stability, sorption properties and differing hydrophilicities. In the obtained mechanically stable monoliths, each MOF showed a different compatibility with the used polymers. From 21 different MOF@polymer composites with 80 wt% loading of MOF, 12 of them exhibited negligible pore blocking effects and very high nitrogen sorption properties in correspondence with the MOF mass fraction. On the other hand, water uptake is especially in cases of MOF@PVA and MOF@PVP in good agreement with the MOF fraction and can be enhanced by the contribution of the hydrophilic polymer to the composite. In particular, most MIL-101(Cr) composites showed a hydrophilic shift to lower relative pressure $p \cdot p_0^{-1}$ compared to the rather hydrophobic neat MIL-101(Cr). IR spectroscopy indicated a clear interaction of PEI with the Al-MOFs aluminum fumarate and MIL-160(Al) resulting in MOF pore blocking. The molecular weight of the polymer is not significant for the freeze-casting method but plays an important role in the cryopolymerization.

Keywords: Metal-organic frameworks, MOFs; Shaping; Monolith; Hydrophilic shift, Freeze-casting

1. Introduction

Metal-organic frameworks (MOFs) are hybrid materials, composed of metal atoms and organic linkers, possessing potential voids [1]. The high variety of metal atoms and linkers enabled, so far, more than 70 000 different MOF structures (until 2017 [2]) which were investigated for potential applications in catalysis [3,4], gas storage and gas separation [5-7], cyclic adsorption applications [8-10], etc. Among these applications, the investigation of MOFs in cyclic adsorptions chillers (ACs) and thermally driven heat pumps (TDHPs) gained considerable attention in the last decade [11,12]. ACs and TDHPs are an eco-friendly and promising technology in the field of low-electricity energy utilization [13]. The choice of adsorbent materials in the ACs and TDHPs requires, inter alia, hydrothermal stability, appropriate water sorption properties with respect to the relative pressure region, high water uptake capacity and proper operating adsorption-desorption conditions [11].

Water is the adsorbate of choice for heat transformation applications and the water adsorption-desorption behavior of the relevant adsorbents, which also includes MOFs, is very essential. Related applications based on the water adsorption-desorption of MOFs are also dehumidification [14] and water harvesting from air [15]. The most relevant MOFs for water sorption-based applications are given in the literature [11]. Among these we selected aluminum fumarate (Alfum) [16], MIL-160(Al) [17] and MIL-101(Cr) [18] for their proven hydrothermal stability and high water uptake capacity, albeit in different relative pressure regions, corresponding to different hydrophilicities. For MIL-160(Al) the steep rise of the S-shaped isotherm lies within $0.03 < p \cdot p_0^{-1} < 0.15$, while the steep rise for Alfum occurs within $0.2 < p \cdot p_0^{-1} < 0.3$ [19,20]. MIL-101(Cr) which reaches above 1 $g \cdot g^{-1}$ of water vapor uptake requires the relative pressure range of $0.4 < p \cdot p_0^{-1} < 0.6$. More information about the sorption properties of the MOFs can be found in the Supp. Info. Thus, the order of decreasing hydrophilicity is MIL-160(Al) > Alfum >> MIL-101(Cr). Clearly, the interesting rise of the S-shaped water sorption isotherm of MIL-101(Cr) [21] lies outside of the desired relative pressure range of about $0.1 < p \cdot p_0^{-1} < 0.3$ [22]. Still, its high water loading and large pores have led to various chemical modifications of MIL-101(Cr) either by functionalizing the terephthalate (BDC) linker [23,24,25] or grafting of hydrophilic groups to the metal center [26] in order to achieve a more hydrophilic MIL-101(Cr) [27], which would make this modified MIL-101(Cr) a suitable candidate for water sorption-based applications.

Additionally, one of the important requirements for most applications of MOFs is the usage of a shaped body instead of the neat-MOF powder materials. In most cases, MOFs are obtained as a microcrystalline powder material from their synthesis. Powder materials have disadvantages in handling, such as dusting and low bulk density due to the small particle size [28]. While MOFs need to be shaped for applications, at the same time shaping needs to preserve the initial porous properties of MOFs [29-31]. Shaping procedures of MOFs have been recently reviewed pointing out pelletizing, granulating, coating and monolith formation as preferred methods [32,33].

In many shaping methods, the use of a binder material is needed [32] which could cause pore-blocking of the MOF [29-31]. Because of that, each MOF must be tested and judiciously selected for a particular shaping procedure and binder and vice-versa [34,35]. In this work, we used the fabrication of MOF-polymer monoliths by the so-called freeze-casting method (ice-templating). The freezing process generates ice crystals which are removed by freeze-drying to give a stable ice-templated macroporous material [36]. A monolith has the advantages of robustness, easy handling and high density [37,38].

Application of the freeze-casting method in MOF formulation and in MOF chemistry, at large, is rare. To the best of our knowledge freeze-casting was applied to dry MOFs [39] and in the shaping of HKUST-1 to obtain hierarchically porous monoliths directly after synthesis without using any binder [37]. Additionally, a UiO-66@chitosan monolith was prepared using the freeze-casting method [40]. The UiO-66@chitosan monolith was used for the wastewater treatment and showed a high adsorption capacity of methylchlorophenoxypropionic acid (MCPP) with 34 $mg \cdot g^{-1}$ close to the MCPP adsorption of neat UiO-66 with 36 $mg \cdot g^{-1}$. However, the UiO-66@chitosan monolith composite had lost most of the apparent BET surface area, S(BET). The apparent S(BET) dropped from 1034 $m^2 \cdot g^{-1}$ for neat UiO-66 to 339 $m^2 \cdot g^{-1}$ in the UiO-66@chitosan composite which contained nearly 99 wt% UiO-66 [40]. Another example is the preparation of an ultralight hierarchically porous monolith, which was prepared by the high internal phase emulsion (HIPE) technique, combining UiO-66 and polyvinyl alcohol (PVA), followed by freeze-drying [41].

A related method to freeze-casting is cryopolymerization in which macroporous monoliths are obtained via a polymerization reaction with a cross-linker under the freezing point of the solvent, generally water [42]. This in-situ cross-linking below the freezing point is also used to obtain stable monoliths. However, this method requires a cross-linker, such as glutaraldehyde, glycerol diglycidyl ether, etc [43,44].

The polymers polyacrylic acid (PAA), sodium polyacrylate (PAANa), polyethylene glycol (PEG), polyethylene imine (PEI), polyvinyl alcohol (PVA) and polyvinyl pyrrolidone (PVP) were selected for their known hydrophilicity (see Fig. S7 in Supp. Info. for the polymer repeat unit). At $p \cdot p_0^{-1} = 0.9$ the amount of adsorbed water is 440 $mg \cdot g^{-1}$ for polyacrylic acid, 920 $mg \cdot g^{-1}$ for sodium polyacrylate, 50 $mg \cdot g^{-1}$ for polyethylene glycol, 860 $mg \cdot g^{-1}$ for polyethylene imine, 185 and 210 $mg \cdot g^{-1}$ for polyvinyl alcohol with different hydrolysis degrees and 560 $mg \cdot g^{-1}$ for polyvinyl pyrrolidone. These polymers are commercially available in bulk quantities at a relatively low price.

For the selection of MOF and polymer, it is important to consider which type of application the composite is used for. For instance, MOFs should meet some criteria for use in AHT, such as hydrothermal stability and high water uptake capacity with the S-shaped isotherm lies in the relative pressure range of about $0.01 < p \cdot p_0^{-1} < 0.3$. The choice of polymer is also important to ensure that the polymer does not compromise the desired sorption properties of the MOF and even possibly improves the sorption properties. In the example below, PEI was chosen because of its known CO_2 adsorption properties, which provided enhanced CO_2 sorption properties in MOF@PEI composite [45].

Composite materials should show similar or even enhanced material properties compared to the individual components and their weight percent. For example, a composite based on glass fibers with PEI and epoxy resin (EP) retained the water vapor uptake for PEI of around 800 $mg \cdot g^{-1}$ [46]. MIL-101(Cr)@R,F-xeorgel with 77 wt% of MIL-101(Cr) has the maximum water uptake of 0.88 $g \cdot g^{-1}$, which matches the expected value with 0.84 $g \cdot g^{-1}$ [30]. In composite materials, it is even possible to surpass the initial properties of the neat component. A MIL-101(Cr)@PEI composite with 50 wt% of MIL-101(Cr) adsorbs at 1 bar nearly 5 $mmol(CO_2) \cdot g^{-1}$(of composite), which is three times more CO_2 adsorption than MIL-101(Cr) alone [45].

In this contribution, we report 21 MOF@polymer monoliths composed of the MOFs MIL-160(Al), Alfum or MIL-101(Cr) with the polymers PAA, PAANa, PEG, PEI, PVA (two different hydrolysis degrees) and PVP using the freeze-casting method. In addition, in-situ cross-linking below the freezing point (cryopolymerization) was performed using the MOFs Alfum and MIL-101(Cr) and the polymer PVA.

2. Experimental section

2.1. Materials and methods

All used chemicals were commercially obtained from various sources and used without further purification: Aluminum fumarate (Basolite^{TM} A520, BASF, abbreviated in this work as Alfum), chromium(III) nitrate nonahydrate ($Cr(NO_3)_3 \cdot 9H_2O$, Acros Organics, 99%), nitric acid (Grüssing, 65 wt%), 1,4-benzenedicarboxylic acid (H_2BDC, Acros Organics, >99%), N,N'-dimethylformamide (DMF, VWR, p.a.), tetramethylammonium hydroxide (Alfa Aesar, 25 wt% in H_2O), basic aluminum diacetate ($Al(OH)(CH_3COO)_2$, VWR), glutaraldehyde (Alfa Aesar, 25 wt% in H_2O), ethanolamine (Chimia, 99%), hydrochloric acid (Fisher Scientific, ≥ 37%), 2,5-furandicarboxylic acid (Sigma-Aldrich, >97%), ethanol (VWR, p.a.), polyacrylic acid with an average M_w of 100 kDa (Sigma-Aldrich, 35 wt% in H_2O, abbreviated as PAA), sodium polyacrylate with an average M_w of 15 kDa (Sigma-Aldrich, 35 wt% in H_2O, abbreviated as PAANa), polyethylene glycol with an average M_w of 12 kDa (Sigma-Aldrich, abbreviated as PEG), branched polyethylene imine with an average M_w of 70 kDa (Alfa Aesar, 30 wt% in H_2O, abbreviated as PEI), polyvinyl alcohol with an average M_w of 125 kDa and 98% hydrolyzed (Sigma-Aldrich, Mowiol® 20-98, abbreviated as PVA(98)), polyvinyl alcohol with an average M_w of 10 - 26 kDa and 86-89% hydrolyzed (abbreviated as PVA(88)1), polyvinyl alcohol with an average M_w of 31 kDa and 88% hydrolyzed (Sigma-Aldrich, Mowiol® 4-88, abbreviated as PVA(88)2), polyvinyl alcohol with an average M_w of 67 kDa and 88% hydrolyzed (Sigma-Aldrich, Mowiol® 8-88, abbreviated as PVA(88)3), polyvinyl alcohol with an average M_w of 130 kDa and 88% hydrolyzed (Sigma-Aldrich, Mowiol® 18-88, abbreviated as PVA(88)4), polyvinyl alcohol with an average M_w of 205 kDa and 88% hydrolyzed (Sigma-Aldrich, Mowiol® 40-88, abbreviated as PVA(88)5) and polyvinyl pyrrolidone with an average M_w of 360 kDa (Sigma-Aldrich, abbreviated as PVP).

Powder X-ray diffractograms (PXRD) were obtained at ambient temperature on a Bruker D2 Phaser (300 W, 30 kV, 10 mA) using Cu-Kα radiation ($\lambda = 1.54182$ Å) between $5° < 2\theta < 50°$ with a scanning rate of $0.15°\ s^{-1}$ for Alfum, MIL-160(Al) and related composites and between $5° < 2\theta < 35°$ with a scanning rate of $0.0275°\ s^{-1}$ for MIL-101(Cr) and related composites. The diffractograms were obtained on a flat "low background sample holder", in which at low angle the beam spot is strongly broadened so that only a fraction of the reflected radiation reaches the detector, hence the low relative intensities measured at $2\theta < 7°$. The analyses of the diffractograms were carried out with the "Match 3.11" software.

Nitrogen physisorption measurements of MIL-160(Al), Alfum and related composites were carried out on a Nova 4000e from Quantachrome. Nitrogen physisorption isotherms of polymers, MIL-101(Cr) as well as MIL-101(Cr)@polymer composites were carried out on an Autosorb-6 from Quantachrome at 77 K. Argon physisorption isotherms were carried out on a Nova 4000e and Autosorb-6 from Quantachrome at 87 K, which was set by a Cryocooler temperature controller from Qantachrome. Water physisorption measurements of MOFs and polymer composites were measured volumetrically on a VSTAR from Quantachrome at 293 K with the following equilibrium settings: Equilibrium points number: 10; Equilibrium points Interval time of 120 s for $0.001 \leq p \cdot p_0^{-1} \leq 0.400$, 180 s 0.450 for $\leq p \cdot p_0^{-1} \leq 0.900$ during adsorption and 90 s for $0.800 \leq p \cdot p_0^{-1} \leq 0.600$, 120 s for $0.500 \leq p \cdot p_0^{-1} \leq 0.010$ during desorption. Before each sorption measurement, all probes were activated under vacuum ($< 2 \times 10^{-2}$ mbar) at 373 K for 3 hours. An exception were neat PEG monoliths, which were activated at 333 K for 3 hours because of the low melting point of 65 °C for PEG. "Brunauer-Emmett-Teller (BET) surface areas (designated as 'apparent S(BET)' for microporous materials [47]) were calculated from the nitrogen physisorption isotherms using the described conditions given in the publication by Rouquerol et al. [48].

Scanning electron microscopy (SEM) images were taken by a Jeol JSM-6510LV QSEM advanced electron microscope with a LaB_6 cathode at 5–20 keV. The microscope was equipped with a Bruker Xflash 410 silicon drift detector for energy-dispersive X-ray spectrometry (EDX).

FT-Infrared (IR) spectra were measured in ATR-mode (Platinum ATR-QL, diamond crystal) on a Bruker TENSOR 37 IR spectrometer in the range of 4000−550 cm^{-1}.

2.2. Synthesis

2.2.1. Synthesis of MIL-101(Cr) with HNO_3

MIL-101(Cr) was synthesized hydrothermally according to the literature (large scale synthesis route) [49]. $Cr(NO_3)_3 \cdot 9H_2O$ (4.8 g, 12.0 mmol), 1,4-benzenedicarboxylic acid (2.03 g, 12.2 mmol), HNO_3 (0.54 mL, 12.0 mmol, 65 wt%) and deionized H_2O (60 mL) were placed in a 90 mL Teflon-liner and stirred for 2 h. The Teflon-liner was inserted in a steel autoclave and heated to 200 °C within 8 h, held at this temperature for 15 h and then cooled down in 24 h to room temperature (rt). The precipitated green powder was centrifuged and washed consecutively with DMF (125 mL for 1 h and 125 mL for 20 h) and later on with EtOH (125 mL for 1 h). Before each solvent change, the sample was separated by centrifugation. After the final centrifugation, the green crystalline powder was dried under vacuum. Yield 2.24 g, 78% based on the "activated" product formula $Cr_3(\mu_3\text{-}O)(OH)(H_2O)_2(BDC)_3$, $C_{24}H_{17}Cr_3O_{16}$, 717.37 $g \cdot mol^{-1}$. This MIL-101(Cr) was used for the monolith preparation via the freeze-casting method.

2.2.2. Synthesis of MIL-101(Cr) with TMAOH

According to the literature [50] 1,4-benzenedicarboxylic acid (1.98 g, 11.9 mmol), tetramethylammonium hydroxide (TMAOH, 25 wt% in H_2O) (1.08 mL, 3.00 mmol) and deionized H_2O (60 mL) were placed in a 90 mL Teflon-liner and stirred for 4 h, then $Cr(NO_3)_3 \cdot 9H_2O$ (4.82 g, 12.0 mmol) was added to the solution and stirred further for 1 h. The Teflon-liner was inserted in a steel autoclave and heated to 180 °C within 12 h, held at this temperature for 48 h and then cooled down in 18 h to rt. The green powder was centrifuged and washed consecutively with the following order: deionized water (100 mL at rt), DMF (300 mL at 115 °C for 40 h), EtOH (2 x 150 mL at rt), EtOH (200 mL under reflux for 24 h), EtOH (200 mL under reflux for 72 h). Before each solvent change, the cooled-down suspension was centrifuged and the supernatant was removed. After final centrifugation, the green crystalline powder was dried under vacuum to give 2.40 g of a powdery product (84% for $Cr_3(\mu_3\text{-}O)(OH)(H_2O)_2(BDC)_3$, $C_{24}H_{17}Cr_3O_{16}$, 717.37 $g \cdot mol^{-1}$). MIL-101(Cr) obtained under basic conditions was used for the monolith preparation involving in-situ PVA cross-linking.

2.2.3. Synthesis of MIL-160(Al)

The synthesis of MIL-160(Al) was carried out by a modified method of Serre et al. [19] $Al(OH)(CH_3COO)_2$ (3.9 g, 24 mmol) and 2,5-furandicarboxylic acid (4.1 g, 26 mmol) were dispersed in a 100 mL round bottom flask in deionized water (25 mL) and refluxed at 115 °C for 24 h. The resulting white solid was recovered by subsequent centrifugation and was washed two times with 100 mL EtOH at rt (ca. 1 hour and overnight). After centrifugation and vacuum drying overnight at 100 °C a yield of 4.53 g (95% based on the framework formula $[Al(OH)(O_2C-C_4H_2O-CO_2)]$, $C_6O_6H_3Al$, 198.07 $g \cdot mol^{-1}$) was collected. MIL-160 was obtained as a white solid.

The MOFs were stored under ambient conditions under moist air. Due to their microporosity and hydrophilicity water is adsorbed into the MOFs upon storage. Directly before composite formation the MOFs were activated by drying for 3 h at 100 °C under dynamic vacuum ($2\text{-}5 \cdot 10^{-2}$ mbar).

2.2.4. Fabrication of MOF@polymer monoliths and polymer monoliths

All monoliths were prepared using a prime protocol. In the following, the preparation of 80 wt% composites is generally described for all prepared monoliths.

The amount of 60 mg polymer was dissolved in 1 mL of H_2O, if necessary (e.g. PVA) by heating to over 80 °C. After complete dissolution, the polymer solution was added to 240 mg of activated MOF and stirred for 3 h with 1000 rpm. Afterwards the suspension was filled in a disposable 1 mL syringe. Beforehand the cannula side of the syringe had been cut open (see Fig. S4 in Supp. Info.).

The filled syringe was frozen in liquid nitrogen for approximately five minutes. After freezing, the syringe allowed to warm, until the solidified monolith content could be pressed from the syringe and placed in a liquid nitrogen cooled test tube. The test tube, which was then immediately placed under dynamic vacuum (1×10^{-3} mbar) for 24 h to remove the water, giving the MOF@polymer monolith. A schematic fabrication procedure of the composite monoliths is shown in Section 3.3.

The neat polymer monoliths were prepared in the same way without the addition of MOF.

The obtained monoliths are described as MOF*xx*@polymer where *xx* refers to the wt% of MOF in the composite. For example, MIL-101(Cr)80@PAA has 80 wt% loading of MIL-101(Cr) in the monolith with the PAA polymer. wt% was calculated according to (x mg MOF)/(x mg MOFs + x mg polymer) × 100%

2.2.5. Fabrication of MOF@polymer monoliths and polymer monoliths with in-situ cross-linking of PVA by cryopolymerization

MOF@polymer cryogel monoliths were synthesized according to a method modified from the literature [51]. The polymer solutions were prepared as mentioned in Section 2.2.4 (dissolving 100 mg polymer in 2 mL of water). To this solution, finely powdered MOF was added (50 mg for 33 wt% loading and 100 mg for 50 wt% loading) and stirred vigorously for 1 h.

Two drops of HCl (5 $mol \cdot L^{-1}$) were added to this suspension which was subsequently cooled in an ice-bath. After addition of glutaraldehyde (80 µL, 10 $g \cdot L^{-1}$ final solution) at 0 °C, the viscose suspension was placed in a 5 mL cylindrical glass and kept in the freezer at –20 °C for 19 h. After thawing to rt (30 min.), the glass was broken and the obtained monolith was washed by agitation in deionized water (24 h), in ethanolamine solution to block possible free aldehyde groups (0.4 $mol \cdot L^{-1}$ in water; 1 h) and subsequently in deionized water (24 h).

The monoliths with PVA(98), PVA(88)2 and PVA(88)3 were dried by freeze-drying. MIL-101(Cr)@CP-PVA(98) and Alfum@CP-PVA(98) samples were obtained as green and white stable monoliths, respectively. The MIL-101(Cr) used here had been synthesized under basic conditions (Section 2.2.2). Composites with cross-linked (cryopolymerized) PVA were designated with “CP” in front of the polymer in the sample name, e.g., as MIL-101(Cr)50@CP-PVA(98) for 50 wt% MIL-101(Cr) loaded in cross-linked PVA(98).

The neat polymer monoliths CP-PVA(88)2 and CP-PVA(88)3 were prepared in the same way without the addition of MOF.

(CP)-PVA(98) monoliths were prepared in the same way without the addition of MOF and after addition of ethanolamine solution and deionized water, the monolith was dehydrated in ethanol for 72 h, exchanging the solvent every 24 h. Finally, the white product was dried via super critical CO_2.

3. Results and Discussion

3.1. Preparation of the MOFs

In this study, two different synthesis methods were used for the preparation of MIL-101(Cr). For the preparation of MIL-101(Cr)@polymer monoliths via the freeze-casting method, MIL-101(Cr) was synthesized with the addition of HNO_3 instead of problematic HF [49]. The measured apparent S(BET) of 3170 $m^2 \cdot g^{-1}$ is in good agreement with the literature values for this method between 3100 and 3500 $m^2 \cdot g^{-1}$ [49]. More structural details on MIL-101(Cr) are given in the Supp. Info., Section S3, PXRD in Fig. S9 and SEM images in Fig. S16.

MIL-101(Cr) synthesized with the base tetramethylammonium hydroxide TMAOH was obtained with an apparent BET surface area of 2425 $m^2 \cdot g^{-1}$ (see Fig. 8 for nitrogen sorption isotherm), somewhat lower than the literature value (3197 $m^2 \cdot g^{-1}$) [50]. The PXRD results (see Fig. S22 in Supp. Info.) are in good agreement with the simulated diffractogram of MIL-101(Cr). For the SEM-images of MIL-101(Cr) from this route, see Fig. 7. MIL-101(Cr) obtained with TMAOH was used in the monolith preparation by in-situ PVA cross-linking.

MIL-160(Al) was synthesized using 2,5-furandicarboxylic acid and basic aluminum diacetate [17]. MIL-160(Al) was obtained with an apparent BET surface area of 1100 $m^2 \cdot g^{-1}$ comparable to the reported value with an apparent BET surface area of 1070 $m^2 \cdot g^{-1}$ [17] (see Fig. 4 for the nitrogen sorption isotherm). More information on the MIL-160(Al) structure can be found in the Supp. Info., Section S2; PXRD in Fig. S9.

Alfum was obtained as a commercial product, which exhibited an apparent BET surface area of around 950 $m^2 \cdot g^{-1}$ (see Fig. 4 for nitrogen sorption isotherm) [52]. More information about the Alfum structure is given in the Supp. Info., Section S1, PXRD in Fig. S9.

The porosity properties of Alfum, MIL-160(Al) and MIL-101(Cr) are summarized in Table 5 and for MIL-101(Cr) synthesized with TMAOH in Table S4 in the Supp. Info.

3.2. Preparation of the polymer monoliths via freeze-casting method

The prepared polymer solution with a mass fraction of 5.7 wt% (this concentration was also used for the preparation of the MOF@polymer monolith) was placed in a syringe, which was cut open from the cannula side, and afterwards submerged in liquid nitrogen for 5 min. The monolith preparation with PAA, PVP, PVA(98), PVA(88), PEG and PAANa was possible, however strong shrinkage during drying caused deformation of their initial cylindrical shapes (see Fig. S5 in Supp. Info.). The strong shrinkage can be explained due to the very low polymer concentration. Furthermore, PVA monoliths were mechanically more stable in comparison to other polymer monoliths. PEI is liquid at room temperature; therefore it was not possible to obtain PEI as a monolith. Therefore, nitrogen sorption analysis of PEI was not performed but water sorption was done after activation of the liquid PEI at 373 K. According to the nitrogen sorption data, the derived BET surface areas of polymer monoliths are below 30 $m^2 \cdot g^{-1}$. The water sorption isotherms of the polymer monoliths or liquid PEI can be categorized as Type III [47] and indicate relatively high water vapor adsorption, especially for PEI and PAANa, in the late relative pressure range of around 0.9 (Fig. 1). The maximum adsorbed water vapor amount of around 900 $mg \cdot g^{-1}$ was observed here for PAANa monoliths, followed by 860 $mg \cdot g^{-1}$ for liquid PEI, both at the relative pressure of 0.9 and in agreement with the literature [46,53]. In Table 1 the amount of water uptake for all polymer monoliths and liquid PEI is compared at different relative pressure ranges. From the uptake values the order of hydrophilicity of the polymer binders would be PAANa ≈ PEI > PVP > PAA > PVA >> PEG. PAANa monoliths and liquid PEI are the best performing materials in almost each given range of the relative vapor pressure. Remarkable is the very large hysteresis of liquid PEI and PAANa monoliths, which can be explained by relatively strong hydrogen-bonding interactions of either the amino- (PEI) or carboxylate groups (PAANa) with the water molecules.

The measured water uptake of the PEG monolith at $p \cdot p_0^{-1} = 0.9$ reached only 50 $mg \cdot g^{-1}$ (determined twice to exclude measurement error) and is contrary to the reported uptake of 600 $mg \cdot g^{-1}$ [54].

A PAA monolith gave nearly 450 $mg \cdot g^{-1}$ water uptake at 20 °C and at $p \cdot p_0^{-1} = 0.9$ which is slightly higher than literature value of 350 $mg \cdot g^{-1}$ at 30° C [55]. The water sorption isotherms of PVA and PVP monoliths are comparable with the literature [56,57].

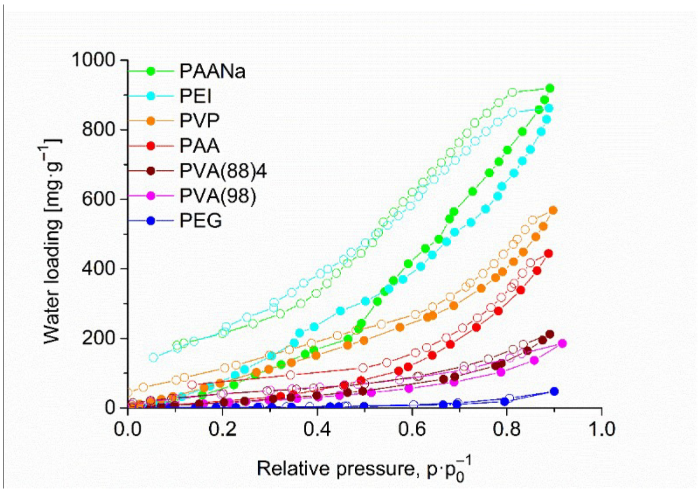

Fig. 1. Water vapor adsorption-desorption isotherms of PAA, PAANa, PEG, PVA(98), PVA(88)4 and PVP monoliths as well as liquid PEI measured at 293 K. (Adsorption is depicted with filled, desorption with empty symbols.)

Table 1. Water vapor uptake of polymer monoliths and liquid PEI (at different relative pressures).

Polymers	Water uptake [mg·g^{-1}] at p·p$_0$$^{-1}$ =						
	0.15	0.20	0.30	0.35	0.40	0.60	0.90
PAA	15	23	31	39	53	123	444
PAANa	37	67	112	140	171	414	919
PEG	1	2	2	3	3	7	48
PEI	51	79	150	187	238	390	862
PVA(98)	11	14	22	27	31	56	185
PVA(88)4	12	16	25	31	36	70	212
PVP	54	73	112	132	152	225	568

3.3. Preparation of the MOF@polymer monoliths via freeze-casting method

The freeze-casting method was tested under different freezing and drying conditions, using the Alfum80@PVA(88)4 monoliths. Freezing of the composites was either carried out in liquid nitrogen (-193 °C for 5 min) or in a freezer (-18 °C for 24 h) with subsequent drying in air or under freeze-drying conditions. Therefore, four different preparation methods are possible, which can be abbreviated as LNFD (freezing in N_2(liq) and freeze-drying), LNAD (freezing in N_2(liq) and air drying), F18FD (freezing in freezer at -18 °C and freeze-drying) and F18AD (freezing in freezer at -18 °C and air drying). Reproducibility of each method was tested three times by evaluating the obtained composite shape and surface area. Each method indicates with very low standard deviation a good reproducibility for the apparent S(BET) (see Table 2). As MOF Alfum was used for this evaluation due to good pore accessibility, simple synthesis under mild conditions and its inexpensive starting materials. Alfum was also commercially available as Basolite^{TM} A520 from BASF. PVA was selected as binder material because of a low price, larger variability of molecular weight and good mechanical stability. The MOF content was prepared up to 80 wt% in the monolith. Because of the high viscosity of the obtained suspension with 80 wt% of MOF in the MOF/polymer suspension, a higher loading amount of the MOF was not tried. Another reason is that some MOF@polymer monoliths were fragile already with 80 wt% of MOF.

Based on the superior results in shaping and slightly higher apparent S(BET), LNFD was chosen as the standard method for the preparation of the MOF@polymer composites. A schematic fabrication procedure of the composite monoliths is shown in Fig. 2.

Table 2. Comparison of different preparation methods regarding the accessible surface area and monolith-shape retention.[a]

Methods	LNFD	LNAD[b]	F18FD	F18AD
S(BET) [$m^2 \cdot g^{-1}$]	621 ± 11[a]	–	596 ± 6[a]	599 ± 10[a]
Shape retention	successful	complete deformation	successful	partial deformation

[a] Based on the preparation of an Alfum80@PVA(88)4 monolith. Average value of 6 measurements (three times from top and three times from bottom pieces of the monolith).

[b] Because of unsuccessful shaping, the sample was not analyzed further (see Fig. S6 in Supp. Info.).

It was possible with LNFD and F18FD to preserve the shape of the monolith. Interestingly, air drying was only partially successful for F18AD, in the case of LNAD complete deformation was observed (see Fig. S6). The thawing and necessary longer drying time for air-drying (AD) clearly is the cause of deformation.

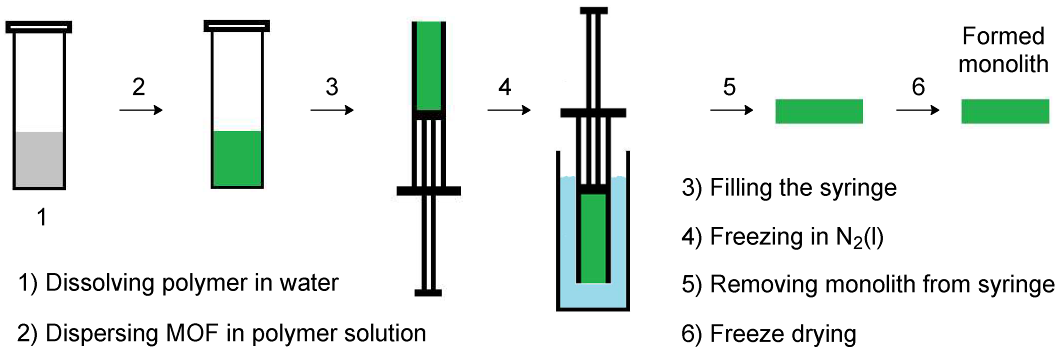

Fig. 2. Preparation of the MOF@polymer monolith via freeze-casting method.

Volume-based sorption properties instead of the more typical specific or mass-based uptake amounts are important for the usage of MOF in restricted volumes. Because of that reason, we compare the bulk density and tapped density of the neat MOFs with the density of the monoliths (see Table S2 and Table S3 in Supp. Info.). The bulk density and tapped density are explained in Supp. Info. Section S12. MIL-101(Cr) showed the smallest bulk and tapped density with 0.08 and 0.29 g·cm^{-3}, respectively. On the other hand, MIL-160(Al) has the highest bulk and tapped density among the investigated MOFs with a value of 0.25 and 0.59 g·cm^{-3}, respectively. In comparison to the neat MOFs, only the MOF@polymer composite monoliths obtained by air drying (F18AD, with partial deformation of the shape) achieved densities of up to 0.44 g·cm^{-3}, which were in the same range as the tapped density of neat Alfum (0.46 g·cm^{-3}). Whereas the freeze-drying provided monoliths with lower densities in the range of 0.30 and 0.39 g·cm^{-3} for the Alfum80@polymer monoliths and 0.28 and 0.41 g·cm^{-3} for the MIL-160(Al)80@polymer monoliths.

3.4. Effect of molecular weight of the polymer on the monoliths

The effect of the molecular weight of the polymer on the freeze-casting method was studied by using the different PVA(88) polymers with varying molecular weight of 10-26 kDa (PVA(88)1), 31 kDa (PVA(88)2), 67 kDa (PVA(88)3), 130 kDa (PVA(88)4) and 205 kDa (PVA(88)5) and by comparing monoliths with 80 wt% of Alfum MOF loading. There is a small tendency that the surface area and pore volume, that is, the pore accessibility increases with increasing molecular weight of the polymer (Table 3), which can be explained by less pore penetration or pore blocking in the case of less flexible longer chains. While the pore accessibility of PVA(88)1, PVA(88)2 and PVA(88)3 is around 70% (judged by % of calc. S(BET)), the pore accessibility can be enhanced up to 86% by using higher molecular weight PVA(88)5 .

Table 3. Porosity properties of Alfum80@PVA monoliths with different molecular weights of the polymer.

Sample[a]	M_w(PVA) [kg·mol^{-1}]	*S*(BET)[b] exp. [m^2·g^{-1}] (% of S(BET) calc.)	*S*(BET) calc.[c] [m^2·g^{-1}]	*V*(pore)[d] [cm^3·g^{-1}] (% of *V*(pore) calc.)	*V*(pore) calc.[c] [cm^3·g^{-1}]
Alfum		946	-	0.478	-
Alfum80@PVA(88)1	10 - 26	542 (72)	757	0.308 (80)	0.386
Alfum80@PVA(88)2	31	522 (69)	757	0.295 (77)	0.385
Alfum80@PVA(88)3	67	546 (72)	757	0.301 (78)	0.386
Alfum80@PVA(88)4	130	612 (80)	761	0.319 (82)	0.388
Alfum80@PVA(88)5	205	651 (86)	759	0.347 (90)	0.385

[a] Prepared by liquid nitrogen freeze-drying (LNFD)..

[b] Apparent S(BET) values were determined from N_2 sorption isotherms at 77 K with a standard deviation ± 20 m^2·g^{-1} (thereby apparent S(BET) values were calculated from the nitrogen physisorption isotherms using the described conditions in the publication by Rouquerol et al. [48] with at least 3 points. Due to the high variation of about a few hundred m^2·g^{-1}, the S(BET) of MIL-101(Cr) and corresponding composites were determined over 7 points in the relative pressure range between 0.05 and 0.2).

[c] Calculated apparent S(BET) and calculated micro- and small mesopore volume *V*(pore) in the monoliths were determined as the sum of the mass-weighted S(BET) or V(pore) of the MOFs and the respective polymer (PAA, PAANa, PEG, PEI, PVA(98), PVA(88) or PVP) monolith from the following formula (Ia) or (Ib), respectively:

$$\mathrm{S(BET)calc.} = \frac{\mathrm{wt\%\ of\ polymer}}{100} \times \mathrm{S(BET, polymer)} + \frac{\mathrm{wt\%\ of\ MOF}}{100} \times \mathrm{S(BET, MOF)} \qquad \text{(Ia)}$$

with apparent *S*(BET): Alfum = 946 m^2·g^{-1}; MIL-160(Al) = 1134 m^2·g^{-1}; MIL-101(Cr) = 3171 m^2·g^{-1}; Surface area of polymers are PAA = 5 m^2·g^{-1}; PAANa = 4 m^2·g^{-1}; PEG = 5 m^2·g^{-1}; PEI = 0 m^2·g^{-1}; PVA(98) = 26 m^2·g^{-1}; PVA(88)1 = 0 m^2·g^{-1}; PVA(88)2 = 0 m^2·g^{-1}; PVA(88)3 = 0 m^2·g^{-1}; PVA(88)4 = 19 m^2·g^{-1}; PVA(88)5 = 12 m^2·g^{-1}; PVP = 17 m^2·g^{-1};

$$\mathrm{V(pore)calc.} = \frac{\mathrm{wt\%\ of\ polymer}}{100} \times \mathrm{V(pore, polymer)} + \frac{\mathrm{wt\%\ of\ MOF}}{100} \times \mathrm{V(pore, MOF)} \qquad \text{(Ib)}$$

with *V*(pore): Alfum = 0.478 cm^3·g^{-1}; MIL-160(Al) = 0.445 cm^3·g^{-1}; MIL-101(Cr) = 1.348 cm^3·g^{-1}; PAA = 0.0135 cm^3·g^{-1}; PAANa = 0.005 cm^3·g^{-1}; PEG = 0.004 cm^3·g^{-1}; PEI = 0 cm^3·g^{-1}; PVA(98) = 0.042 cm^3·g^{-1}; PVA(88)1 = 0.018 cm^3·g^{-1}; PVA(88)2 = 0.012 cm^3·g^{-1}; PVA(88)3 = 0.016 cm^3·g^{-1}; PVA(88)4 = 0.024 cm^3·g^{-1}; PVA(88)5 = 0.011 cm^3·g^{-1}; PVP = 0.015 cm^3·g^{-1};

The values and equations are also used for Table 4 and Table 5.

[d] Total pore volumes V(pore) were determined from N_2 sorption isotherms at 77 K ($p \cdot p_0^{-1}$ = 0.90) for pores ≤ 20 nm.

3.5. Effect of MOF amount on the monoliths

The effect of increased MOF content on monoliths was also exemplarily analyzed using PVA(88) and Alfum. Different Alfum contents varying from 30 wt% to 80 wt% were prepared in the 5.7 wt% polymer solution. The porosity properties of the resulting monoliths are listed inTable 4. As expected, with increasing Alfum amount rises also its still accessible surface area and pore volume in the monolith. The best results were achieved with 80 wt% of Alfum (the highest MOF percentage in this work) in the composite, having an apparent BET surface area of 612 $m^2 \cdot g^{-1}$ and pore volume of 0.319 $cm^3 \cdot g^{-1}$, which correspond 80% and 82% of calculated values, respectively. The increasing percentage of pore accessibility with increasing Alfum amount can be explained by the lower polymer fraction leading to less polymer chains or chain ends available for pore blocking phenomena. Conversely, an increasing PVA(88) to Alfum ratio leads to the formation of thicker PVA(88) layers surrounding the Alfum particles with pore blocking.

Table 4. Porosity properties of Alfum@PVA monoliths with different Alfum content.

Sample[a]	*S*(BET)[b] exp. [$m^2 \cdot g^{-1}$] (% of calc. S(BET))	*S*(BET) calc.[c] [$m^2 \cdot g^{-1}$]	*V*(pore)[d] [$cm^3 \cdot g^{-1}$] (% of calc. *V*(pore))	*V*(pore) calc.[c] [$cm^3 \cdot g^{-1}$]
Alfum	946	-	0.482	-
Alfum30@PVA(88)4	145 (49)	297	0.110 (69)	0.161
Alfum43@PVA(88)4	215 (51)	418	0.139 (63)	0.220
Alfum45@PVA(88)4	223 (51)	436	0.149 (65)	0.229
Alfum60@PVA(88)4	353 (61)	575	0.209 (70)	0.297
Alfum69@PVA(88)4	453 (69)	659	0.244 (72)	0.338
Alfum75@PVA(88)4	490 (69)	714	0.268 (73)	0.365
Alfum78@PVA(88)4	533 (72)	742	0.281 (74)	0.378
Alfum80@PVA(88)4	612 (80)	761	0.319 (82)	0.388

[a] Prepared by liquid nitrogen freeze-drying (LNFD). [b,c,d] See Table 3 for the footnote explanations.

3.6. Powder X-ray diffraction patterns of the monoliths

The retained crystallinity of the MOFs in the prepared monoliths was ascertained with PXRD. In all MOF80@polymer composites (Alfum80@polymers, MIL-160(Al)80@polymers and MIL-101(Cr)80@polymers), the main reflexes were retained unchanged, indicating the preserved crystallinity of the MOFs upon composite formation (see Fig. 3).

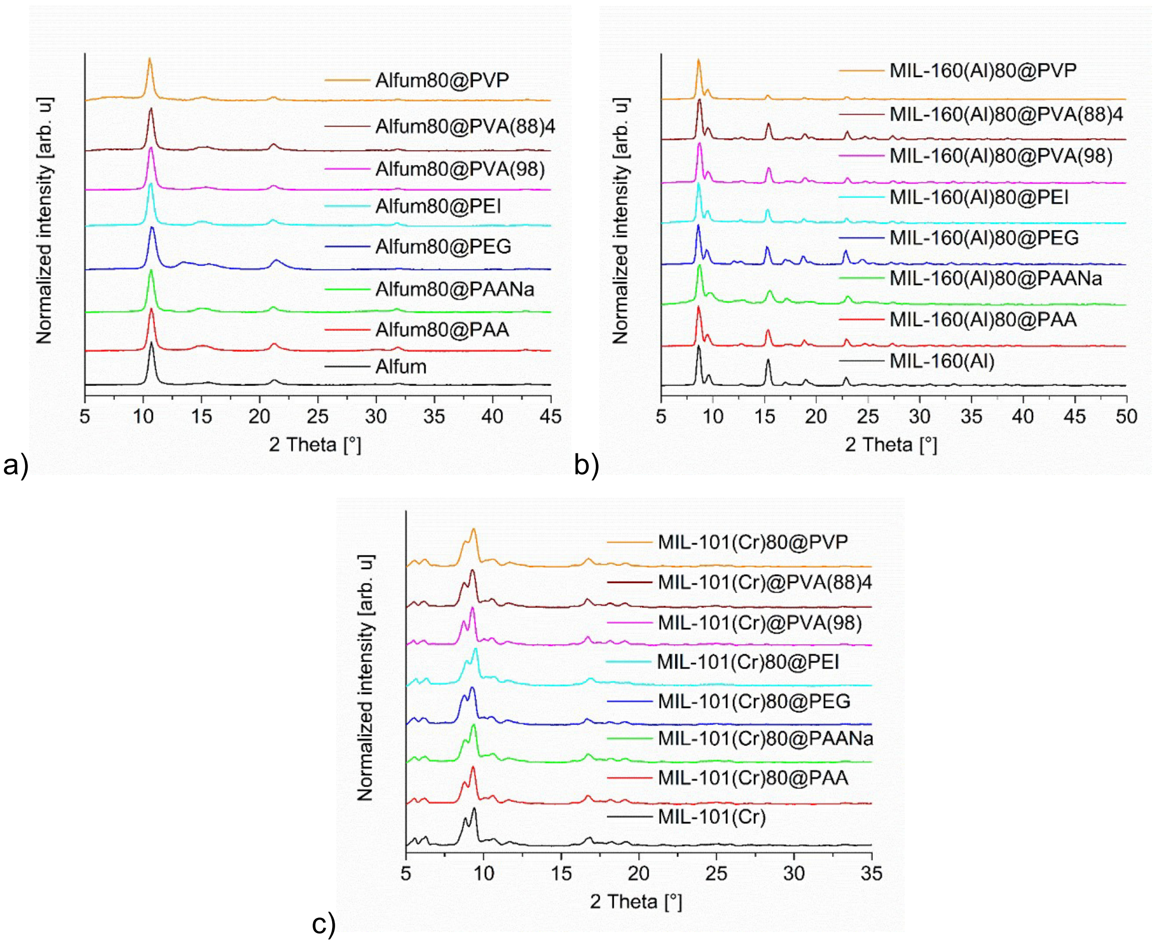

Fig. 3. Experimental powder X-ray diffraction pattern of (a) Alfum and Alfum@polymer monoliths, (b) MIL-160(Al) and MIL-160(Al)@polymer monoliths as well as (c) MIL-101(Cr) and MIL-101(Cr)80@polymer monoliths.

3.7. IR spectra of the monoliths

In general, the IR spectra of the MOF@poylmer composite were an overlay of the spectra of the pure polymer and the MOF. Even if for composites with 80wt% MOF and 20 wt% polymer, the corresponding IR absorption bands of the polymer are very weak and, in some cases, not observable. However, with increasing polymer amount the bands will clearly be seen in the IR spectra (Fig. S10a).

The IR spectra of the Alfum80@PEI composites show the disappearance of the PEI band at ~1300 cm^{-1} (Fig. S12a in Supp. Info). In the spectra of MIL-160(Al)80@PEI this band either also disappears or is shifted to about 1346 cm^{-1} (Fig. S12b in Supp. Info). This disappearance of the 1300 cm^{-1} band is also seen in the composite prepared upon mixing of $AlCl_3{\cdot}6H_2O$ with a 5.7 wt% aqueous PEI solution and freeze dried (see Fig. S13 in Supp. Info. for the IR spectra). In the literature the disappearance of this band occurs concomitant with protonation of PEI [58] and hydration of PEI [59] with the latter probably also being accompanied by proton transfer from water. Hydrated Al^{3+} metal atoms act as strong Brønsted acids through the polarization of the coordinated aqua ligands which lowers the pK_a value of H_2O from 14 to about 5 (in $[Al(H_2O)_6]^{3+}$) [60].

3.8. Nitrogen sorption of the monoliths

Nitrogen sorption studies for the determination of BET surface area and porosity show significant effects of the polymer on the pore accessibility of the MOF in the obtained monoliths (Fig. 4, Table 5).

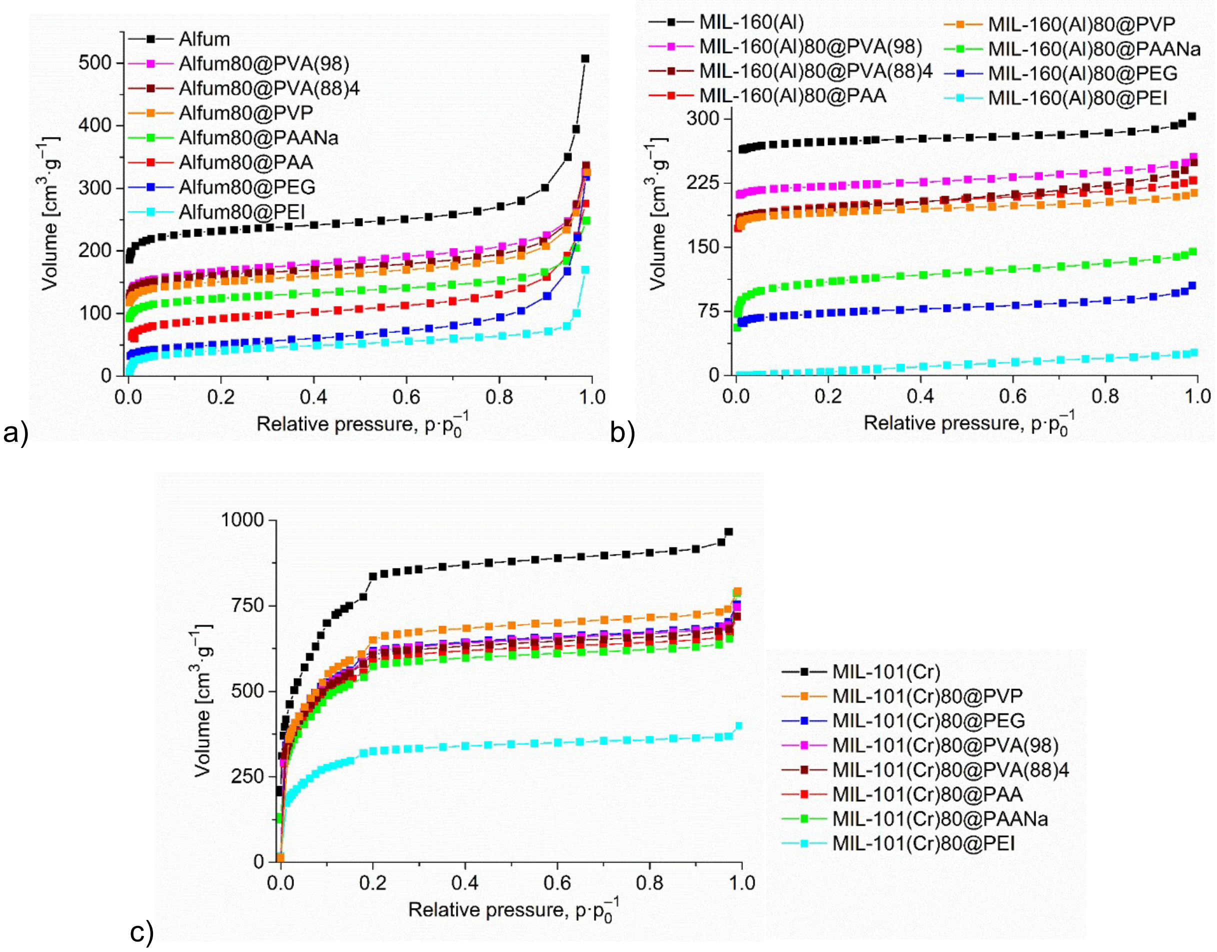

Fig. 4. Nitrogen adsorption isotherms of (a) Alfum and Alfum80@polymer monoliths (b) MIL-160(Al) and MIL-160(Al)80@polymer monoliths as well as (c) MIL-101(Cr) and MIL-101(Cr)80@polymer monoliths (For clarity, only the adsorption isotherms are shown.)

Among the Alfum80 and MIL160(Al)80@polymer composites the ones with PVA(98) revealed the best porosity results in absolute values and also with the highest percentage of the calculated mass-weighted S(BET) or V(pore), followed by PVA(88)4 and PVP. At the same time the Alfum80@polymer and MIL160(Al)80@polymer composites with PEI were lowest in pore accessibility, followed by PEG, due to the high pore blocking effects, which for PEI were discussed with the IR spectra.

To further elucidate the pore blocking, we also measured H_2 sorption of MIL-160@PEI. H_2 has a kinetic diameter of 0.29 nm, compared to N_2 with 0.36 nm [61]. The H_2 sorption (see Fig. S20 in Supp. Info.) showed similar tendency as in the case of N_2 sorption. So, the unexpected water sorption can be explained due to interaction of water with amine group of the polymers as swelling of the PEI.

MIL-101(Cr) exhibits the expected nitrogen adsorption isotherm of Type 1b [47] with the characteristic step for MIL-101 before $p \cdot p_0^{-1} = 0.2$ indicating microporous windows and mesoporous pores [18]. The shape of the nitrogen adsorption isotherms remains as Type 1b also in the composites although the amount of adsorbed nitrogen differs with the polymer (see Fig. 4c). The MIL-101(Cr)@PVP monolith shows the best results for the composite materials with an apparent S(BET) of 2470 $m^2 \cdot g^{-1}$ and pore volume of 1.120 $cm^3 \cdot g^{-1}$, which indicates no pore blocking effect. Yet, with MIL-101(Cr) all polymers, except for PEI showed comparable apparent S(BET) in the range of 2100 and 2500 $m^2 \cdot g^{-1}$ and pore volumes of 0.9 and 1.1 $cm^3 \cdot g^{-1}$ with retention of accessible porosity of over 85% compared to the mass-weighted MIL content. In earlier work, we already noted that pore blocking effects in polymer composites of MIL-101(Cr) with its large pore windows were always lowest when compared to other MOFs with smaller pore openings in MOF@polymer composites [29-31]. The stronger interaction of MIL-101(Cr) with PEI, which was discussed in the IR part, is obviously the reason for the reduction of the apparent S(BET) and pore volume in MIL-101(Cr)80@PEI monolith.

Generally, the reduction of the BET surface area and pore volume of the MOF@polymer composite is explained by blocking of the pores or pore mouths with the polymer chain ends. Enveloping of the MOF particles by polymer sheaths, acting as a thin film will also reduce accessibility to the MOF pores, even if the pore mouths remain open. Importantly and different from earlier work on MIL-100 and MIL-101 compounds [29-31], the freeze-casting method allows also to achieve little pore blockage for MOFs of lower porosity such as Alfum and MIL-160 with selected polymers.

Only PEI and PEG showed very low pore accessibility for the Alfum and MIL-160 monoliths. Both polymers have low melting points compared to the other polymers. PEI used in this work has a melting point below rt, while PEG melts at 65 °C. For this reason, the activation temperature during degassing was also lowered from 100 °C to 60 °C for MOF@PEI and MOF@PEG composites. However, the reduction of the activation temperature led to similar sorption properties and pore accessibility (see Fig. S18 in Supp. Info.).

Table 5. Results of nitrogen sorption measurements for MOFs and MOF@polymer composites.

	Sample^a	*S*(BET)^b exp. [m^2·g^{-1}] (% of calc. S(BET))	*S*(BET) calc.^{c} [m^2·g^{-1}]	*V*(pore)^d [cm^3·g^{-1}] (% of calc. *V*(pore))	*V*(pore) calc.^{c} [cm^3·g^{-1}]
	Alfum	946	-	0.478	-
Alfum	80@PAA	340 (45)	758	0.245 (64)	0.385
	80@PAANa	477 (63)	758	0.257 (67)	0.384
	80@PEG	182 (24)	758	0.198 (52)	0.384
	80@PEI	149 (20)	757	0.111 (29)	0.383
	80@PVA(98)	658 (86)	762	0.348 (89)	0.391
	80@PVA(88)4	612 (80)	761	0.319 (82)	0.388
	80@PVP	584 (77)	760	0.321 (83)	0.386
	MIL-160(Al)	1134	-	0.445	-
MIL-160(Al)	80@PAA	808 (89)	908	0.340 (95)	0.359
	80@PAANa	417 (46)	908	0.214 (60)	0.357
	80@PEG	285 (31)	908	0.142 (40)	0.357
	80@PEI	43 (5)	907	0.035 (10)	0.356
	80@PVA(98)	925 (101)	912	0.382 (105)	0.364
	80@PVA(88)4	800 (88)	911	0.357 (99)	0.361
	80@PVP	802 (88)	911	0.343 (96)	0.359
	MIL-101(Cr)	3171	-	1.348	-
MIL-101(Cr)	80@PAA	2203 (87)	2538	1.007 (93)	1.081
	80@PAANa	2152 (85)	2538	0.974 (90)	1.079
	80@PEG	2234 (88)	2538	1.056 (98)	1.079
	80@PEI	1199 (47)	2537	0.562 (52)	1.078
	80@PVA(98)	2251 (89)	2542	1.048 (96)	1.087
	80@PVA(88)4	2225 (88)	2541	1.032 (95)	1.083
	80@PVP	2470 (97)	2540	1.120 (104)	1.081

[a] Prepared by liquid nitrogen freeze-drying (LNFD). [b,c,d] See Table 3 for the footnote explanations.

For the exemplary micropore size and distribution analysis, we carried out argon sorption measurements, which are more reliable than nitrogen sorption measurement for the micropore analysis. As suggested in the literature we used for the DFT analysis the DFT kernels Ar at 87K zeolites/silica (spherical/cylindrical pores, NLDFT equilibrium) [62]. In Fig. 5 the argon sorption isotherms and pore size distribution of MIL-101(Cr) and MIL-101(Cr)80@polymers can be seen. The pore size distribution curve of bulk MIL-101(Cr) represents, with small deviation, the pore sizes, which are expected from the crystal structure analysis of MIL-101(Cr) (see Fig. S3). The pore with 7.9 Å can be related to the micropore in super tetrahedron (8.6 Å) (see Fig. 5) and the distribution in the range from 13 to 33 Å can be assigned to the pore windows of MIL-101(Cr) with 12, 14 and 16 Å as well as to the mesoporous cages with 29 and 34 Å [19]. The rather identical pore size distribution for MIL-101(Cr) and its composites suggests that there is no extra interfacial volume, that is, no MOF-polymer interface volume (so-called void volume) has formed [63]. In Fig. 5b it can be seen that primarily the pore volume due to the larger pores between 20-35 Å diameter is reduced. The polymer chains more easily penetrate these larger pores.

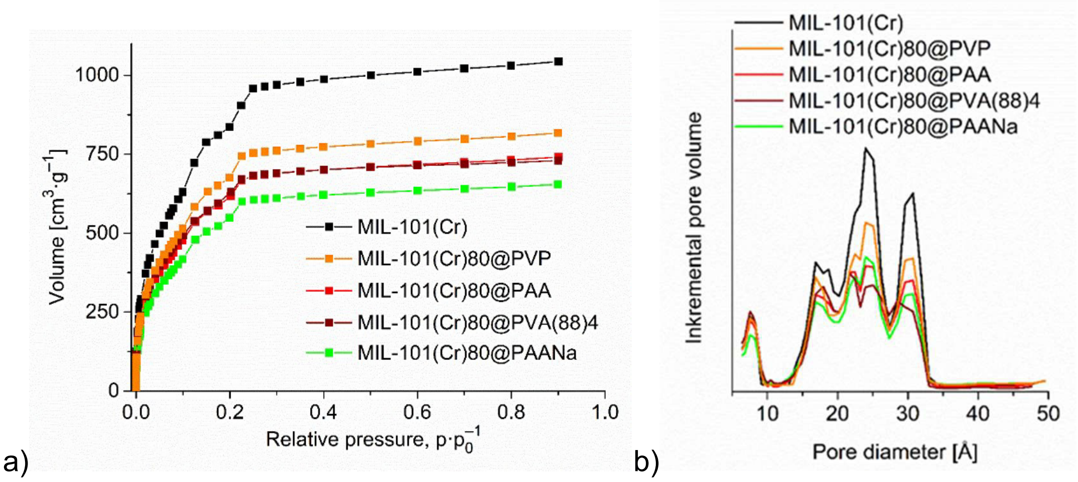

Fig. 5. (a) Argon adsorption isotherm of MIL-101(Cr) and MIL-101(Cr)80@PVP, -PAA, -PVA(88)4 and -PAANa at 87 K and (b) corresponding pore size distribution calculated with the DFT kernel “Ar at 87 K zeolites/silica” (spher./cylinder. pores, NLDFT equ.). (For clarity, only the adsorption isotherms are shown.)

3.9. Water sorption of the monoliths

The S-shape of the water sorption isotherms of the MOF@polymer monoliths remains similar to the isotherms of the neat MOF (Fig. 6). Also, at first sight, the specific water uptake of the MOF@polymer monoliths has decreased, when compared to the neat MOFs, as could be expected from the “only” 80 wt% MOF content in the monoliths (Fig. 6a,c,e, columns in Table 6 at $p \cdot p_0^{-1} = 0.9$). However, a closer view reveals a significant increase in water uptake for the monolith over the neat MOF in the lower relative pressure region which is shown enlarged in Fig. 6b,d,f. The assignment of lower relative pressure region depends on the respective MOF and is defined as the region before the steep uptake in the S-shaped adsorption isotherm. For Alfum the lower relative pressure region was set to $p \cdot p_0^{-1} \leq 0.15$, for MIL-160(Al) to $p \cdot p_0^{-1} \leq 0.05$ and for MIL-101(Cr) to $p \cdot p_0^{-1} \leq 0.4$. The water uptake at these values is listed in the grey shaded column in Table 6 together with the expected calculated water loading based on the mass-weighted uptake of the MOF and polymer at this relative pressure (as % and absolute value). It is evident that the experimental water uptake in the lower relative pressure region can surpass the calculated value by a large amount. For example, for Alfum80@PEI the measured water uptake at $p \cdot p_0^{-1} = 0.15$ is at 176% of the calculated value followed by Alfum80@PAANa with 160%. For MIL-160(Al)@PAANa the experimental water uptake is at 165% at $p \cdot p_0^{-1} = 0.05$, next to MIL-160(Al)@PAANa with 133%. Finally, for MIL-101(Cr)@PEG the water uptake is at 330% at $p \cdot p_0^{-1} = 0.40$, followed by MIL-101(Cr)@PVP with 310% MIL-101(Cr)@PAANa with 305%. Evidently for all MIL-101(Cr)@polymer monoliths at $p \cdot p_0^{-1} = 0.40$ the measured water uptake is at least almost double (>190%) then from what was calculated. That is, for MIL-101(Cr) the beginning of the steep increase S-shaped water sorption isotherm has been significantly shifted to a lower relative pressure in the monolith composites, even with the least hydrophilic PEG binder. This hydrophilic shift is comparable with the effect of the amino group in NH_2-MIL-101(Cr) compared to non-functionalized MIL-101(Cr) in the relative pressure range up to 0.4 [20]

Yet, when the whole adsorption isotherm is considered especially the PEI composites and in part also the PAANa composites do not keep up their early water uptake which appears to be clearly dominated by the polymer alone. At higher relative pressure, that is, after the steep S-increase, the water uptake of the PEI composites follows more the curvature of the pure polymer, best seen for Alfum80@PEI, with little contribution from the 80 wt% MOF content. This can be correlated to the N_2 uptake, BET surface area and porosity, which was consistently the lowest for the MOF@PEI composites (Table 5), hence, PEI led to MOF pore blocking. For MIL-160(Al)@PEI this pore blocking was also confirmed by H_2 sorption (see above and Fig. S20 in Supp. Info.). We note that the kinetic diameter of H_2 with 0.29 nm [61] is comparable to the kinetic diameter of H_2O (0.27 nm) [64].

In order to understand the exact adsorption mechanism of water sorption in each composite, it would be necessary to perform high level of theoretical calculations [65,66]. However, some general aspects can already be deduced which are important for the water sorption properties, such as the hydrophobicity/hydrophilicity of the ligand, pore size, defects (missing linkers and missing clusters), open-metal site of clusters and hydrogen-bonding capabilities of functional linker groups [67]. With respect to the above effects, changes in pore size and the addition of hydrophilic groups derived from the polymer could be responsible for the hydrophilic shift. In the literature, it was shown that, a reduced pore size distribution in the range of 15 Å and 35 Å in micro- and mesoporous silica also causes a hydrophilic shift [68]. Using the pore size distribution derived from argon sorption, we also showed a pore size reduction in the range of 20-35 Å for MIL-101(Cr)@polymer monoliths. It is also reported that hydrophilic functional groups attached to the organic ligand can supply additional nucleation sites [12], which is provided in this work by the hydrophilic polymers. This slight difference in pore size distribution and the effect of functional groups of polymers could be the result of the synergistic effect for the observed hydrophilic shift.

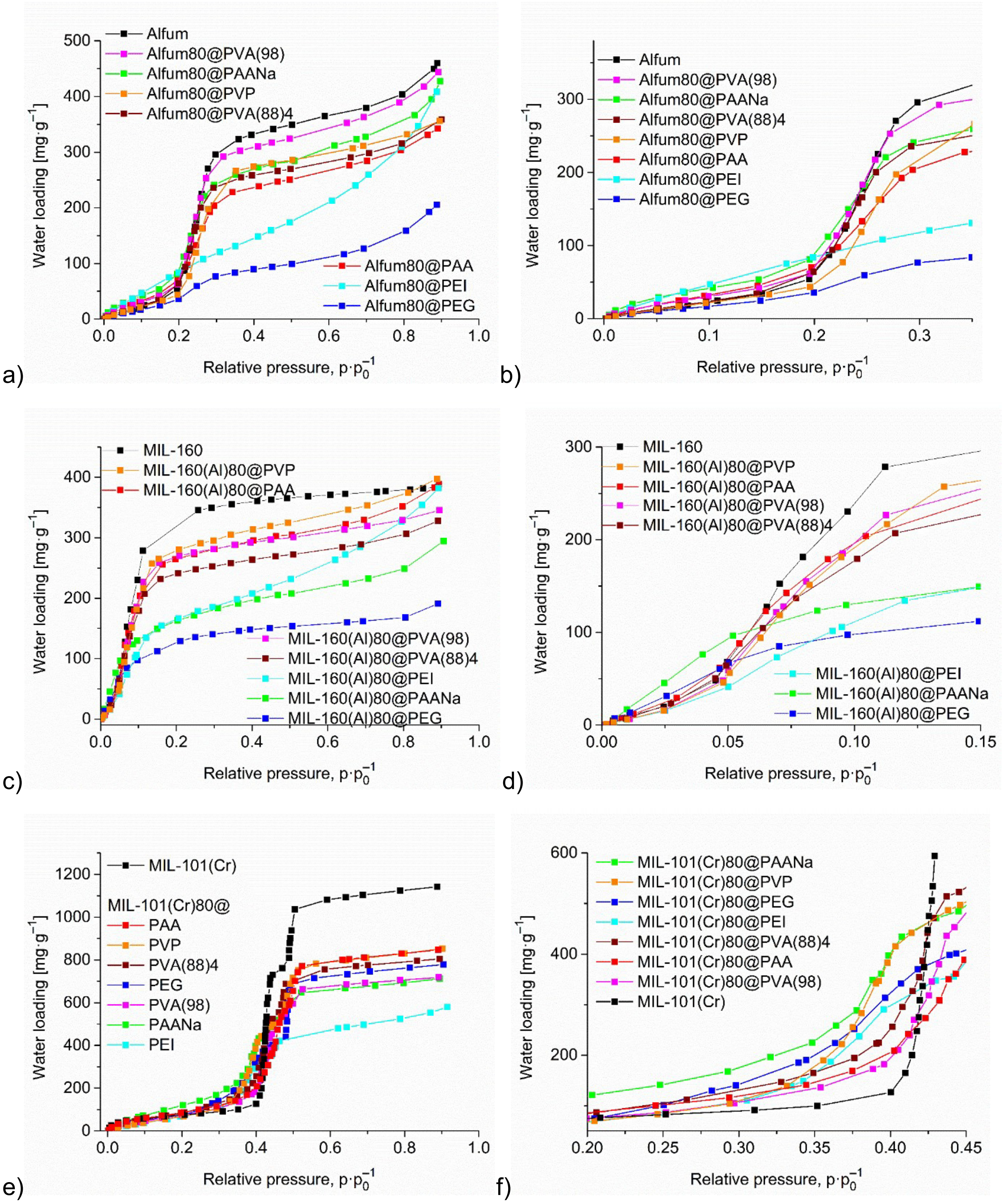

Fig. 6. Water vapor sorption isotherm of (a) Alfum and Alfum80@polymer monoliths (c) MIL-160(Al) and MIL-160(Al)80@polymer monoliths (e) MIL-101(Cr) and MIL-101(Cr)80@polymer monoliths as well as corresponding lift of samples in the relevant relative pressure range for (b) Alfum and Alfum80@polymer monoliths (d) MIL-160(Al) and MIL-160(Al)80@polymer monoliths (f) MIL-101(Cr) and MIL-101(Cr)80@polymer monoliths. (For clarity, only the adsorption isotherms are shown.)

Table 6. Results of water vapor sorption measurements.

	Sample^a	Exp. water load [mg·g^{-1}]	(% of calc. loading) at	{calc. water load ^{b}} [mg·g^{-1}]						
		$p \cdot p_0^{-1} = 0.15$			$p \cdot p_0^{-1} = 0.35$			$p \cdot p_0^{-1} = 0.90$		
	Alfum	34	(-)	{-}	321	(-)	{-}	460	(-)	{-}
Alfum	80@PAA	47	(154)	{30}	229	(87)	{264}	347	(76)	{457}
	80@PAANa	56	(160)	{35}	259	(91)	{285}	428	(77)	{552}
	80@PEG	25	(89)	{28}	83	(32)	{257}	206	(54)	{378}
	80@PEI	66	(176)	{38}	131	(45)	{294}	409	(76)	{541}
	80@PVA(98)	43	(145)	{30}	300	(114)	{262}	444	(110)	{405}
	80@PVA(88)4	37	(123)	{30}	250	(95)	{263}	359	(87)	{411}
	80@PVP	32	(83)	{38}	267	(94)	{283}	356	(74)	{482}
		$p \cdot p_0^{-1} = 0.05$			$p \cdot p_0^{-1} = 0.20$			$p \cdot p_0^{-1} = 0.90$		
	MIL-160(Al)	68	(-)	{-}	319	(-)	{-}	384	(-)	{-}
MIL-160(Al)	80@PAA	73	(133)	{55}	319	(102)	{260}	389	(98)	{396}
	80@PAANa	93	(166)	{56}	264	(61)	{268}	295	(60)	{491}
	80@PEG	67	(123)	{54}	163	(49)	{255}	191	(60)	{317}
	80@PEI	41	(72)	{57}	125	(60)	{271}	382	(80)	{480}
	80@PVA(98)	58	(105)	{55}	163	(104)	{258}	346	(100)	{344}
	80@PVA(88)4	64	(116)	{55}	269	(93)	{258}	328	(94)	{350}
	80@PVP	53	(91)	{58}	240	(103)	{270}	397	(94)	{421}
		$p \cdot p_0^{-1} = 0.40$			$p \cdot p_0^{-1} = 0.60$			$p \cdot p_0^{-1} = 0.90$		
	MIL-101(Cr)	122	(-)	{-}	1082	(-)	{-}	1142	(-)	{-}
MIL-101(Cr)	80@PAA	206	(190)	{108}	791	(89)	{890}	847	(84)	{1003}
	80@PAANa	403	(305)	{132}	660	(70)	{948}	712	(65)	{1097}
	80@PEG	325	(330)	{98}	724	(84)	{867}	778	(84)	{923}
	80@PEI	299	(206)	{145}	470	(50)	{944}	580	(53)	{1086}
	80@PVA(98)	198	(190)	{104}	677	(77)	{877}	718	(76)	{951}
	80@PVA(88)4	251	(239)	{105}	759	(86)	{880}	805	(84)	{956}
	80@PVP	397	(310)	{128}	791	(87)	{911}	853	(83)	{1027}

[a] Prepared by liquid nitrogen freeze-drying (LNFD).

[b] Calculated water uptake value as the sum of the mass-weighted uptake of the MOF and polymer at the respective relative pressure:

$$\text{Water uptake calc.} = \frac{\text{wt\% of polymer}}{100} \times (\text{water uptake polymer}) + \frac{\text{wt\% of MOF}}{100} \times (\text{water uptake MOF})$$

The value “water uptake polymer” (see Fig. 1) and “water uptake MOF” (see Fig. 6) can be taken from the adsorption isotherm of the MOF and polymer at the related relative pressure.

3.10. Preparation of MOF@polymer monoliths via cryopolymerization

Cross-linking of the polymer was tested to investigate the influence to the monolith formation and its corresponding textural properties. We used the cross-linking of PVA with glutaraldehyde. However, the cross-linked CP-PVA allowed only for a low maximum loading of 45 wt% MOF and the resulting sorption properties were not competitive to the non-cross-linked monoliths. Hence, this method is covered only superficially here. The detailed results can be found in the Supp. Info.

The IR spectra of MOF@CP-polymer composites represent MOF and PVA without any additional or missing absorption bands (see Fig. S24 and Fig. S25 in Supp. Info.).

Well-defined macropores are visible in the SEM-image of MIL-101(Cr)45@CP-PVA(88)3 monolith (Fig. 7).

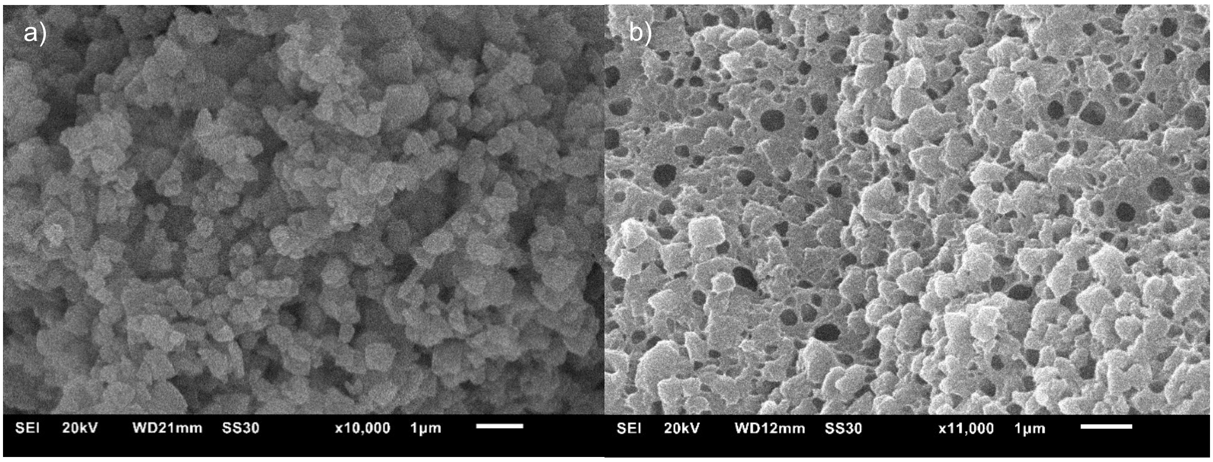

Fig. 7. Scanning electron microscopy (SEM) images of the (a) MIL-101(Cr) synthesized with TMAOH and (b) MIL-101(Cr)45@CP-PVA(88)3

Yet, only for the MIL-101(Cr)45@CP-PVA(98) monolith is the pore accessibility comparable with the monoliths obtained via freeze-casting (see Table S4, Supp. Info. for the uptake properties of the cross-linked and cryopolymerized composites). The apparent S(BET) of MIL-101(Cr)45@CP-PVA(98) is 828 $m^2 \cdot g^{-1}$ representing 74% of the calculated value. The apparent S(BET) of MIL-101(Cr)45@CP-PVA(88)2 and 3 are 137 and 133 $m^2 \cdot g^{-1}$ indicating only 13% and 12% of the calculated value, respectively. Also, Alfum45@CP-PVA(98) showed a much lower nitrogen accessibility and with decreasing molecular weight of PVA the calculated apparent S(BET) decreased dramatically. However, the loss in water uptake capacity of the cryopolymerized composites is less dramatic. Most of the MIL-101(Cr)45 and Alfum45 composites still reach about 50% of the calculated water uptake (Fig. 8). Unfortunately, it was not possible to obtain a cross-linked monolith material with a larger fraction than 45 wt% of MOF by cryopolymerization. Raising the concentration of glutaraldehyde from 10 $g \cdot L^{-1}$ to 50 $g \cdot L^{-1}$ was not successful for the monolith preparation.

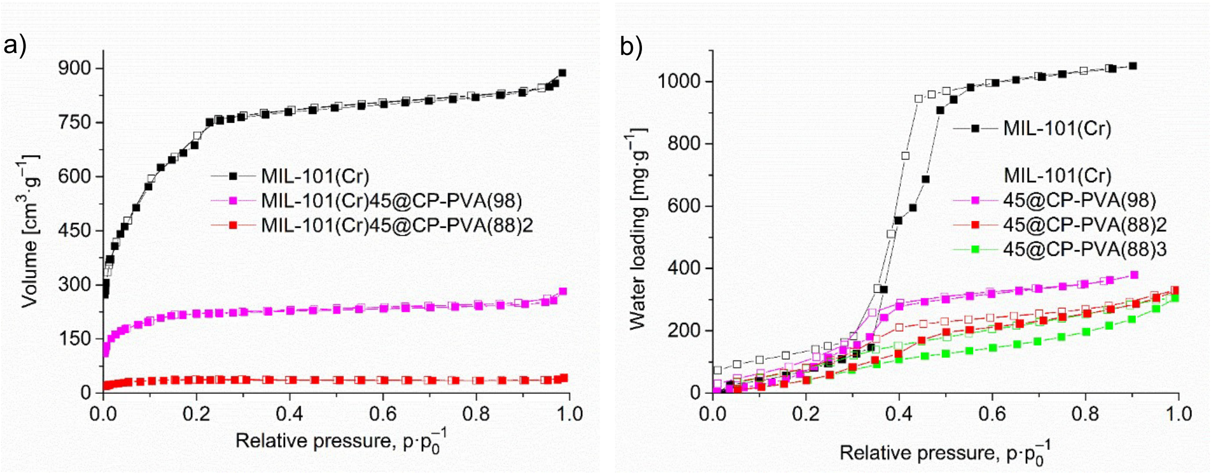

Fig. 8. (a) Water vapor adsorption-desorption isotherms of MIL-101(Cr)45@CP-PVA(98), MIL-101(Cr)45@CP-PVA(88)2, MIL-101(Cr)45@CP-PVA(88)3 and MIL-101(Cr) synthesized with TMAOH (b) nitrogen adsorption-desorption isotherms of MIL-101(Cr)45@CP-PVA(98), MIL-101(Cr)45@CP-PVA(88)2 and MIL-101(Cr) synthesized with TMAOH. (Adsorption is depicted with filled, desorption with empty symbols.)

4. Conclusions

The freeze-casting method was successfully applied to form monoliths with the polymers PAA, PAANa, PEG, PEI, PVA(98), PVA(88) or PVP and the MOFs Alfum, MIL-160(Al) or MIL-101(Cr). In all monoliths the crystallinity of the MOFs was retained. For the first time, we achieved an almost negligible pore blocking of the embedded MOFs by applying the freeze-casting method in the preparation of the MOF@polymer monoliths. Optimization experiments showed that freezing with liquid nitrogen (LN) and subsequent freeze-drying (LNFD) is the method of choice for a rapid monolith formation and its shaping together with retention of the porosity (BET surface and pore volume) of the MOFs. The molecular weight of the polymer affected the porosity properties of the monolith such that higher molecular weights induced less pore blocking of the MOFs in the monoliths.

For the MOFs Alfum and MIL-160(Al) the best porosity results concerning S(BET) and V(pore) in the monoliths were obtained with the polymers PVA and PVP. Concerning water loading with Alfum, the polymer monoliths provide highly satisfactory results from 87% to 114% of the calculated water loading at $p·p_0^{-1} = 0.35$; except for the PEI and PEG composites. With MIL-160(Al)80@PAA, PVA(98), PVA(88)4 and PVP the water loading was about 100% of the calculated water loading at $p·p_0^{-1} = 0.20$. In case of MIL-101(Cr), almost all of its polymer monoliths achieved over 85% of the calculated S(BET) and 90% of the calculated V(pore), PEI being the only exception with 47% of the calculated S(BET) and 52% of the calculated V(pore). Another remarkable result is the hydrophilic shift in the MIL-101(Cr)@polymer composites compared to neat MIL-101(Cr) such that the hydrophilic polymers induce a water uptake at lower relative pressure ($p \cdot p_0^{-1}$) than what the more hydrophobic MIL-101(Cr) would show. This hydrophilic effect was also observed in Alfum@polymer and in MIL-160(Al)@polymer monoliths in the lower relative pressure region of $p \cdot p_0^{-1} \leq 0.15$ and $p \cdot p_0^{-1} \leq 0.05$, respectively. Although the effect of molecular weight for freeze casting was negligible and showed only minor changes in the sorption properties, the effect of molecular weight plays a critical role in the monolith prepared by in-situ PVA cross-linking. Cross-linking of the PVA polymers did not lead to an improvement in the sorption properties of the composites.

We see great potential for the easy to use freeze-casting method to obtain stable polymer monolith composites with improved sorption properties for many other MOFs.

Acknowledgments

The authors gratefully acknowledge the financial support of the Federal German Ministry of Education and Research (BMBF) in the project Optimat under grant no. 03SF0492C. We thank Mr. Simon Millan for helpful discussions. We are indebted to Mrs. Birgit Tommes for measuring the IR spectra.

Supporting Information

PXRDs, TGAs, IR spectra, nitrogen sorption analyses and SEM images are available free of charge *via* the Internet at http://XXX.XX.XX

References

[1] S.R. Batten, N.R. Champness, X.-M. Chen, J. Garcia-Martinez, S. Kitagawa, L. Öhrström, M. O'Keeffe, M.P. Suh, J. Reedijk, Pure Appl. Chem. 85 (2013) 1715–1724.

[2] P.Z. Moghadam, A. Li, S.B. Wiggin, A. Tao, A.G.P. Maloney, P.A. Wood, S.C. Ward, D. Fairen-Jimenez, Chem. Mater. 29 (2017) 2618−2625.

[3] J.Y. Lee, O.K. Farha, J. Roberts, K.A. Scheidt, S.B.T. Nguyena. J.T. Hupp, Chem. Soc. Rev. 38 (2009) 1450–1459.

[4] L. Jiao, Y. Wang, H.-L. Jiang, Q. Xu, Adv. Mater. 30 (2018) 1703663 (1–23).

[5] R.-B. Lin, S. Xiang, H. Xing, W. Zhou, B. Chen, Coord. Chem. Rev. 378 (2019) 87–103.

[6] J.-R. Li, J. Sculley, H.-C. Zhou, Chem. Rev. 112 (2012) 869–932.

[7] J.A. Mason, M. Veenstra, J.R. Long. Chem. Sci. 5 (2014) 32–51.

[8] S.K. Henninger, H.A. Habib, C. Janiak, J. Am. Chem. Soc. 131 (2009) 2776–2777.

[9] S.K. Henninger, S.-J. Ernst, L. Gordeeva, P. Bendix, D. Fröhlich, A.D. Grekova, L. Bonaccorsi, Y. Aristov, J. Jaenchen, Renew. Energy 110 (2017) 59–68.

[10] M.F. de Lange, B.J. van Velzen, C.P. Ottevanger, K.J.F.M. Verouden, L.C. Lin, T.J.H. Vlugt, J. Gascon, F. Kapteijn, Langmuir 31 (2015) 12783–12796.

[11] E. Hastürk, S.-J. Ernst, C. Janiak, Curr. Opin. Chem. Eng. 24 (2019) 26–36.

[12] M.F. de Lange, K.J.F.M. Verouden, T.J.H. Vlugt, J. Gascon, F. Kapteijn, Chem. Rev. 115 (2015) 12205–12250.

[13] H. Demir, M. Mobedi, S. Ülkü, Renew. Sustain. Energy Rev. 12 (2008) 2381–2403.

[14] S. Cui, M. Qin, A. Marandi, V. Steggles, S. Wang, X. Feng, F. Nouar, C. Serre, Sci. Rep. 8 (2018) 15284 (1–9).

[15] H. Kim, S. Yang, S.R. Rao, S. Narayanan, E. A. Kapustin, H. Furukawa, A.S. Umans, O. M. Yaghi, E.N. Wang, Science 356 (2017) 430–434.

[16] E. Leung, U. Müller, N. Trukhan, H. Mattenheimer, G. Cox, S. Blei, Process For Preparing Porous Metal-Organic Frameworks Based On Aluminum Fumarate, US 201/0082864 A1. 2012 Apr 5.

[17] A. Cadiau, J.S Lee, D.D. Borges, P. Fabry, T. Devic, M.T. Wharmby, C. Martineau, D. Foucher, F.T. Taulelle, C.-H. Jun, Y.K. Hwang, N. Stock, M.F. De Lange, F. Kapteijn, J. Gascon, G. Maurin, J.-S. Chang, C. Serre, Adv. Mater. 27 (2015) 4775–4780.

[18] G. Férey, C. Mellot-Draznieks, C. Serre, F. Millange, J. Dutour, S. Surblé, I. Margiolaki, Science 309 (2005) 2040–2042.

[19] A. Permyakova, O. Skrylnyk, E. Courbon, M. Affram, S. Wang, U.-H. Lee, A.H. Valekar, F. Nouar, G. Mouchaham, T. Devic, G.D. Weireld, J.-S. Chang, N. Steunou, M. Frère, C. Serre, ChemSusChem 10 (2017) 1419–1426.

[20] F. Jeremias, D. Fröhlich, C. Janiak, S.K. Henninger, RSC Adv. 4 (2014) 24073–24082.

[21] P. Küsgens, M. Rose, I. Senkovska , H. Fröde, A. Henschel, S. Siegle, S. Kaskel, Micropor. Mesopor. Mater. 120 (2009) 325–330.

[22] Y.I. Aristov, Appl. Therm. Eng. 50 (2013) 1610–1618.

[23] N. Ko, P.G. Choi, J. Hong, M. Yeo, S. Sung, K.E. Cordova, H.J. Park, J.K. Yang, J. Kim, J. Mater. Chem. A 3 (2015) 2057–2064.

[24] G. Akiyama, R. Matsuda, H. Sato, A. Hori, M. Takata, S. Kitagawa, Micropor. Mesopor. Mater. 157 (2012) 89–93.

[25] A. Khutia, H. U. Rammelberg, T. Schmidt, S.K. Henninger, C. Janiak, Chem. Mater. 25 (2013) 790–798.

[26] M. Wickenheisser, F. Jeremias, S.K. Henninger, C. Janiak, Inorg. Chim. Acta 407 (2013) 145–152.

[27] Z. Liu, Y. Chen, J. Sun, H. Lang, W. Gao, Y. Chi, Inorg. Chim. Acta 473 (2018) 29–36.

[28] U. Betke, M. Klausa, J. G. Eggebrecht, M. Scheffler, A. Lieb, Micropor. Mesopor. Mater. 265 (2018) 43–56.

[29] M. Wickenheisser, T. Paul, C. Janiak, Micropor. Mesopor. Mater. 220 (2016) 258–269.

[30] M. Wickenheisser, A. Herbst, R. Tannert, B. Milow, C. Janiak Micropor. Mesopor. Mater. 215 (2015) 143–153.

[31] M. Wickenheisser, C. Janiak, Micropor. Mesopor. Mater. 204 (2015) 242–250.

[32] B. Valizadeh, T.N. Nguyen, K.C. Stylianou, Polyhedron 145 (2018) 1–15.

[33] M. Rubio-Martinez, C. Avci-Camur, A.W. Thornton, I. Imaz, D. Maspoch, M.R. Hill, Chem. Soc. Rev. 46 (2017) 3453–3480.

[34] P. B. Bendix, S. K. Henninger, H.-M. Henning, Ind. Eng. Chem. Res. 2016, 55, 4942−4947.

[35] P. Bendix, G. Füldner, M. Möllers, H. Kummer, L. Schnabe, S. Henninger, H.-M. Henning, Appl. Therm. Eng. 124 (2017) 83–90.

[36] L. Qian, H. Zhang, J. Chem. Technol. Biot. 86 (2011) 172–184.

[37] A. Ahmed, T. Hasell, R. Clowes, P. Myers, A.I. Cooper, H. Zhang, Chem. Commun. 51 (2015) 1717–1720.

[38] L. Huber, P. Ruch, R. Hauert, S.K. Matam, G. Saucke, S. Yoon, Y. Zhange, M. M. Koebel, RSC Adv. 6 (2016) 80729–80738.

[39] L. Ma, A. Jin, Z. Xie, W. Lin, Angew. Chem., Int. Ed. 48 (2009) 9905–9908.

[40] Q. Fu, L. Wen, L. Zhang, X. Chen, D. Pun, A. Ahmed, Y. Yang, H. Zhang, ACS Appl. Mater. Interfaces 9 (2017) 33979–33988.

[41] H. Zhu, Q. Zhang, S. Zhu, Chem. Eur.J. 22 (2016) 8751–8755.

[42] F.M. Plieva, I.Y. Galaev, W. Noppe, B. Mattiasson, Trends Microbiol. 16 (2008) 543–551.

[43] T.M. A. Henderson, K. Ladewig, D.N. Haylock, K.M. McLean, A.J. O'Connor, J. Mater. Chem. B 1 (2013) 2682–2695.

[44] N. Sahiner, S. Demirci, J. Appl. Polym. Sci. 133 (2016) 43478 (1–13).

[45] Y. Lin, Q. Yan, C. Kong, L. Chen, Sci. Rep. 3 (2013) 1859 (1–7).

[46] P. Li, S. Zhang, S. Chen, Q. Zhang, J. Pan, B. Ge, J. Appl. Polym. Sci. 108 (2008) 3851–3858.

[47] M. Thommes, K. Kaneko, A. V. Neimark, J. P. Olivier, F. Rodriguez-Reinoso, J. Rouquerol, K. S. Sing, Pure Appl. Chem. 87 (2015) 1051–1069.

[48] J. Rouquerol, P. Llewellyn, F. Rouquerol, Stud. Surf. Sci. Catal. 160 (2007) 49–56.

[49] T. Zhao, F. Jeremias, I. Boldog, B. Nguyen, S.K. Henninger, C. Janiak, Dalton Trans. 44 (2015) 16791–16801.

[50] J. Yang, Q. Zhao, J. Li, J. Dong, Micropor. Mesopor. Mater. 130 (2010) 174–179.

[51] F. M. Plieva, M. Karlsson, M.-R. Aguilar, D. Gomez, S. Mikhalovsky, I. Y. Galaev, B. Mattiasson, J. Appl. Polym. Sci. 100 (2006) 1057–1066.

[52] E. Leung, U. Muller, N. Trukhan, H. Mattenheimer, G. Cox, S. Blei, Process for preparing porous metal organic frameworks based on Aluminum fumarate. US patent (05.04.12.) 2012/0082864A1

[53] M. Bakass, J.P. Bellat, A. Mokhlisse, G. Bertrand, J. Appl. Polym. Sci. 100 (2006) 1450–1456.

[54] J.A. Baird, R. Olayo-Valles, C. Rinaldi, L. S. Taylor, J. Pharm. Sci. 99 (2010) 154–168.

[55] H.M.L. Thijs, C.R. Becer, C. Guerrero-Sanchez, D. Fournier, R. Hoogenbooma, U. S. Schubert, J. Mater. Chem. 17 (2007) 4864–4871.

[56] E. Marin, J. Rojas, Int. J. Pharm. Sci. Rev. Res. 30 (2015) 189–194.

[57] J. Teng, S. Bates, D.A Engers, K. Leach, P. Schields, Y. Yang. J. Pharm Sci. 99 (2010) 3815–3825.

[58] M.F. Daniel, B. Desbat, F. Cruege, O. Trinquet, J.C. Lassegues, Solid State Ionics 28–30 (1988) 637–641.

[59] T. Hashida, K. Tashiro, S. Aoshima, Y. Inaki, Macromolecules 35 (2002) 4330–4336.

[60] E. Riedel, C. Janiak, Anorganische Chemie, Walter de Gruyter (2015) 347.

[61] N. Mehio, S. Dai, D. Jiang, J. Phys. Chem. A 118 (2014) 1150–1154.

[62] J. Möllmer, E.B. Celer, R. Luebke, A.J. Cairns, R. Staudt, M. Eddaoudi, M. Thommes, Micropor. Mesopor. Mater. 129 (2010) 345–353.

[63] A. Nuhnen, D. Dietrich, S. Millan, C. Janiak, ACS Appl. Mater. Interfaces 10 (2018) 33589–33600.

[64] M. Zhou, P.R. Nemade, X. Lu, X. Zeng, E.S. Hatakeyama, R.D. Noble, D.L. Gin, J. Am. Chem. Soc. 129 (2007) 9574–9575.

[65] M. Wahiduzzaman, D. Lenzen, G. Maurin, N. Stock, M.T. Wharmby, Eur. J. Inorg. Chem. (2018) 3626–3632.

[66] D. Lenzen, J. Zhao, S.-J. Ernst, M. Wahiduzzaman, A.K. Inge, D. Fröhlich, H. Xu, H.-J. Bart, C. Janiak, S. Henninger, G. Maurin, X. Zou, N. Stock, Nat. Comm. 10 (2019) 3025.

[67] S. Gökpinar, S.-J. Ernst, E. Hastürk, M. Möllers, I. El Aita, R. Wiedey, N. Tannert, S. Nießing, S. Abdpour, A. Schmitz, J. Quodbach, G. Füldner, S.K. Henninger, C. Janiak, Ind. Eng. Chem. Res. (2019) in press, DOI: 10.1021/acs.iecr.9b04394.

[68] S. Saliba, P. Ruch, W. Volksen, T.P. Magbitang, G. Dubois, B. Michel, Micropor. Mesopor. Mater. 226 (2016) 221–228.

Supporting Information
Shaping of MOFs via freeze-casting method with hydrophilic polymers and their effect on textural properties

Emrah Hastürk, Simon-Patrick Höfert, Burhan Topalli, Carsten Schlüsener, Christoph Janiak*
Institut für Anorganische Chemie und Strukturchemie, Heinrich-Heine-Universität, D-40204 Düsseldorf, Germany.

Emails: emrah.hastuerk@hhu.de, simon-patrick.hoefert@uni-duesseldorf.de,
burhan.topalli@hhu.de, carsten.schluesener@uni-duesseldorf.de,
* Corresponding author: janiak@uni-duesseldorf.de

Contents

S1. Structure and properties of aluminum fumarate (Alfum), Basolite$^{\mathrm{TM}}$ A520

Microporous aluminum fumarate, $Al(OH)(fum)\cdot xH_2O$ (x = 3.5; fum = fumarate), is abbreviated in many different form such as µp-AF, AlFum, Alfum (in this work), Basolite$^{\mathrm{TM}}$ A520 and MIL-53(Al)-FA. The latter acronym is based on the MOF being isoreticular to MIL-53(Al)-BDC or $Al(OH)(BDC)\cdot H_2O$ (BDC=1,4-benzenedicarboxylate). In Alfum, the aluminum atoms are connected by hydroxide and carboxylate bridges to an infinite chain. Neighboring chains are connected by the fumarate linkers forming infinite channels with a free dimension of about 5.7 x 6.0 $Å^2$ [1] (see Fig. S1). The apparent S(BET) of Alfum is around 1000 $m^2\cdot g^{-1}$ and the S-shaped water adsorption isotherm has a maximum water uptake of 400–500 $mg\cdot g^{-1}$ [2,3]. Alfum is hydrothermally stable for over 4500 adsorption-desorption cycles [3].

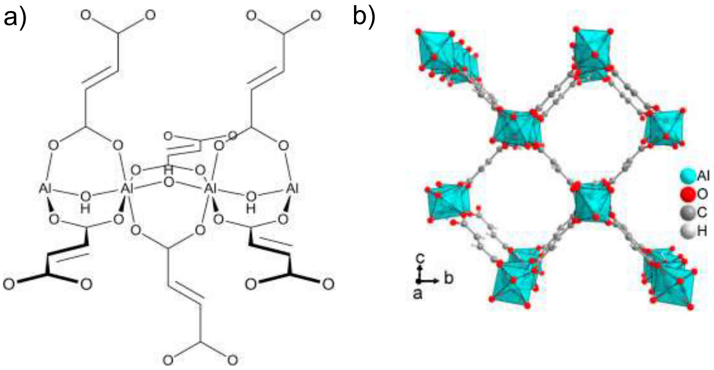

Fig. S1. (a) The building block of Alfum is analogous to the structure of MIL-53. The Figure was taken from ref. [3] with permission of the author, copyright the Royal Society of Chemistry 2014. (b) View along the a-axis of the aluminum fumarate structure. The crystal structure graphic was produced with the software Diamond [4] from the cif-file for Basolite A520 (CSD-Refcode DOYBEA, CCDC no. 1051975) [1].

S2. Structure and properties of MIL-160(Al)

MIL-160(Al) [5] is isoreticular to CAU-10-H. The structure of MIL-160(Al) is constructed by vertex-sharing {AlO_6} octahedral forming helical chains linked by 2,5-furandicarboxylate. Adjacent {AlO_6} octahedra in the same chain are in addition bound to each other over a cis-μ-OH-connection (see Fig. S2). The resulting infinite channels have a dimension of 4-6 Å [5,6]. The surface area of MIL-160(Al) is around 1150 $m^2 \cdot g^{-1}$ [7]. MIL-160(Al) is a relatively hydrophilic MOF possessing a water uptake of nearly 300 $mg \cdot g^{-1}$ in the relative pressure range of 0.1 [5].

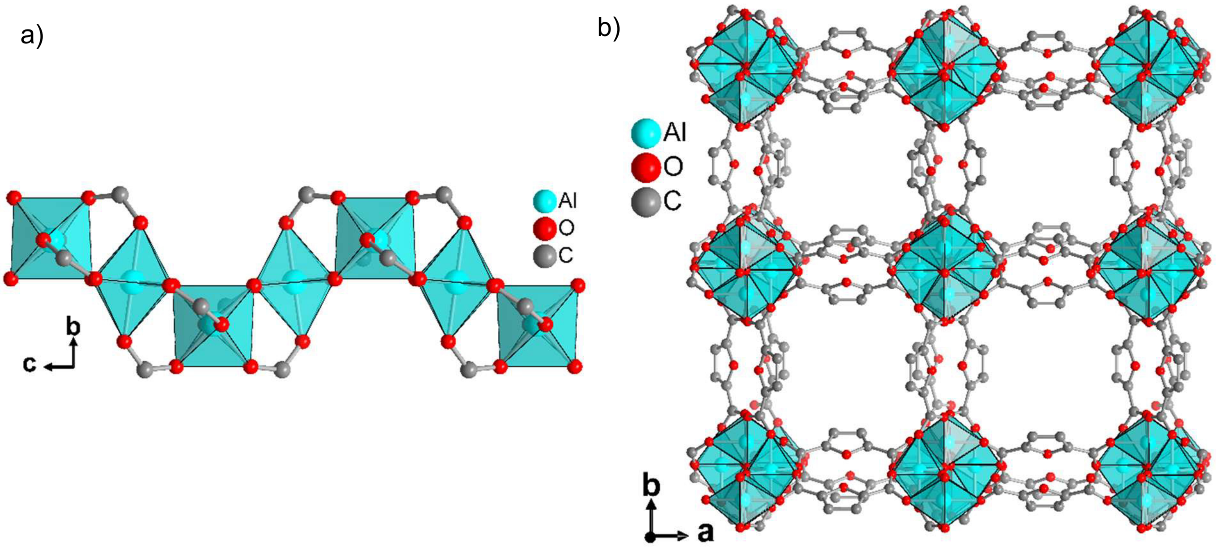

Fig. S2. Structure details of MIL-160: (a) Helical chains of cis vertex-bridged {AlO_6}-polyhedra and (b) connectivity of neighboring parallel chains to square-shaped channels. The graphics were produced with the software Diamond [4] from the cif-file for MIL-160 (CSD-Refcode PIBZOS) [8].

S3. Structure and properties of MIL-101(Cr)

MIL-101(Cr) has three different pores. The so-called super tetrahedra (ST) enclose micropores with ~8.6 Å diameter pore size. More significant are the two mesoporous cages with a diameter of ~29 Å and 34 Å. The mesopore with ~29 Å has pentagonal windows with a size of ~12 Å, which are also found in the mesopore with ~34 Å pore size (see Fig. S3). In addition, the mesopore with ~34 Å pore size has hexagonal windows of ~14.5 Å x 16 Å cross-section [9]. These three pores are connected to each other. MIL-101(Cr) has a relatively high surface area with an apparent S(BET) of up to 4100 $m^2 \cdot g^{-1}$. The water loading of MIL-101(Cr) ranges from 1.0 $g \cdot g^{-1}$ to 1.4 $g \cdot g^{-1}$ showing an S-shaped adsorption isotherm at around $p \cdot p_0^{-1} \approx 0.5$ [9,10]. Because of its hydrothermal stability with low degradation of 3% after 40 adsorption-desorption cycles and tunability of its structure, MIL-101(Cr) is an interesting candidate for water sorption-based applications [11,12].

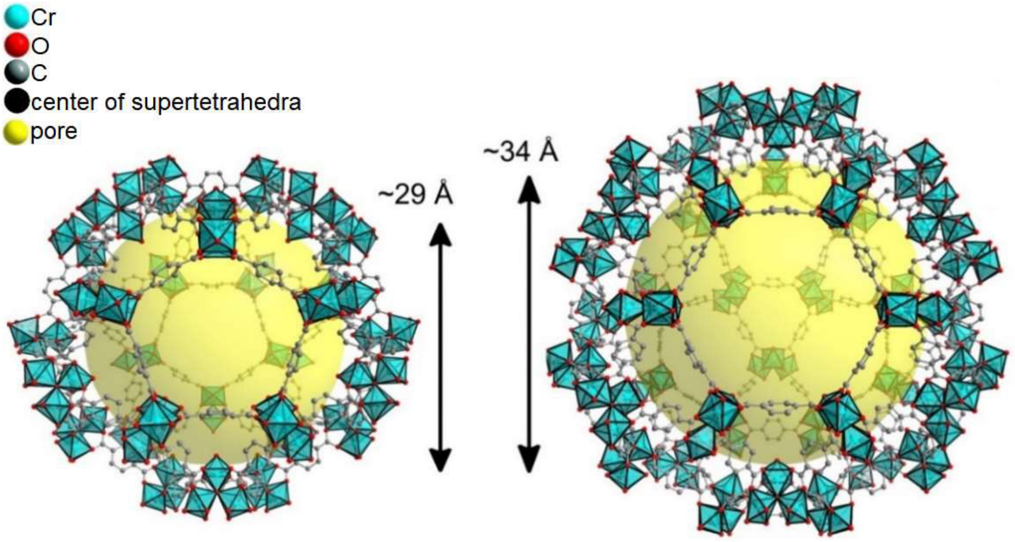

Fig. S3. The two types of mesoporous cages in MIL-101(Cr): At left, the small cage with pentagonal windows only. At right, the large cage with pentagonal and hexagonal windows. The yellow spheres in the mesoporous cages with the indicated diameters take into account the van-der-Waals surface of the framework walls. Hydrogen atoms and solvent molecules of crystallization are not shown. Graphics have been drawn with Diamond [4] from the deposited cif-file for MIL-101(Cr) (CSD-Refcode OCUNAC) [9].

S4. Shaped monolith and used syringe for freeze-casting method

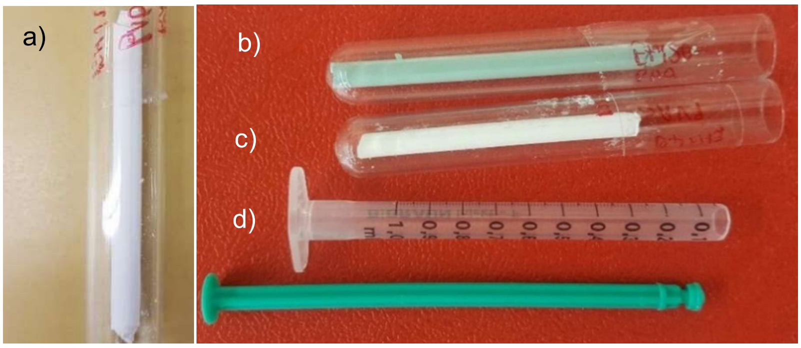

Fig. S4. (a) MIL-160(Al)80@PVP monolith (b) MIL-101(Cr)80@PAA monolith (c) Alfum80@PVA(88)4 monolith and (d) cut syringe.

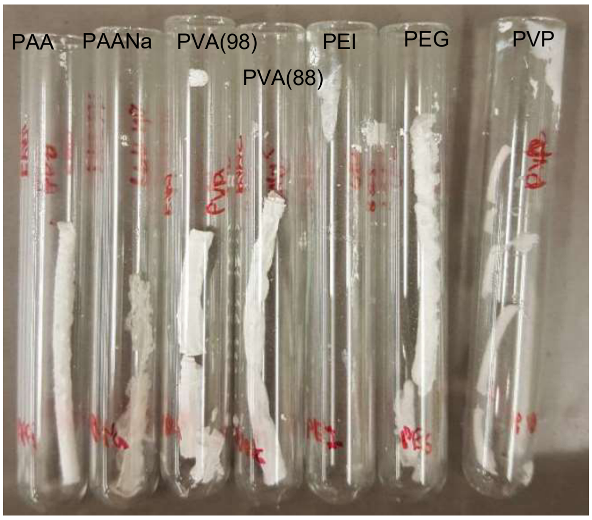

Fig. S5. Polymer monoliths prepared by the freeze-casting method, from left to right: polyacrylic acid (PAA), sodium polyacrylate (PAANa), polyvinyl alcohol 98% hydrolyzed (PVA(98)), polyvinyl alcohol 88% hydrolyzed (PVA(88)), polyethylene imine (PEI, liquid, no monolith formation), polyethylene glycol (PEG) and polyvinyl pyrrolidone (PVP).

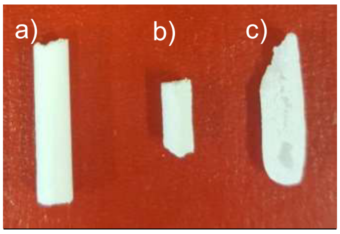

Fig. S6. Shape of monoliths obtained by different preparation methods: (a) freeze-drying (b) air-drying after freezing at -18 °C and (c) air-drying after freezing in liquid nitrogen.

5. Repeat units of the used polymers

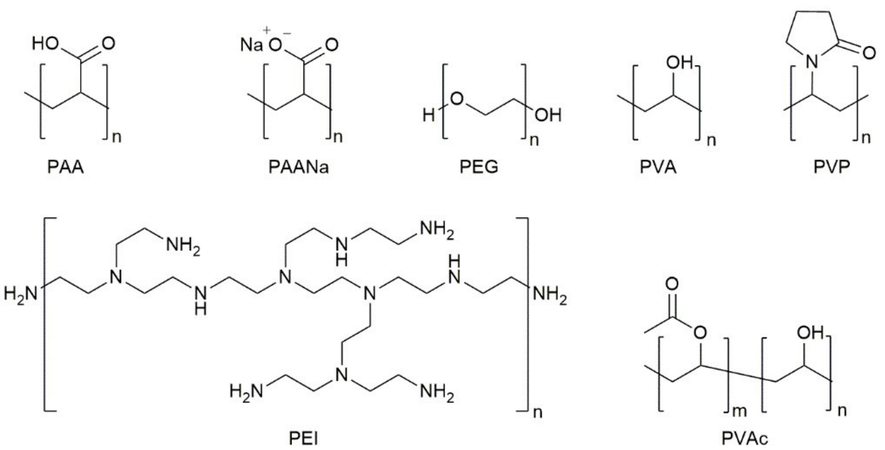

Fig. S7. Repeat units of the polymers: polyacrylic acid (PAA), sodium polyacrylate (PAANa), polyethylene glycol (PEG), polyethylene imine (PEI), polyvinyl alcohol (PVA, as PVA(98) when essentially fully hydrolyzed, or PVA(88) when only about 88% hydrolyzed from the starting polyvinyl acetate, PVAc) and polyvinyl pyrrolidone (PVP).

S6. Powder X-ray diffractometry (PXRD)

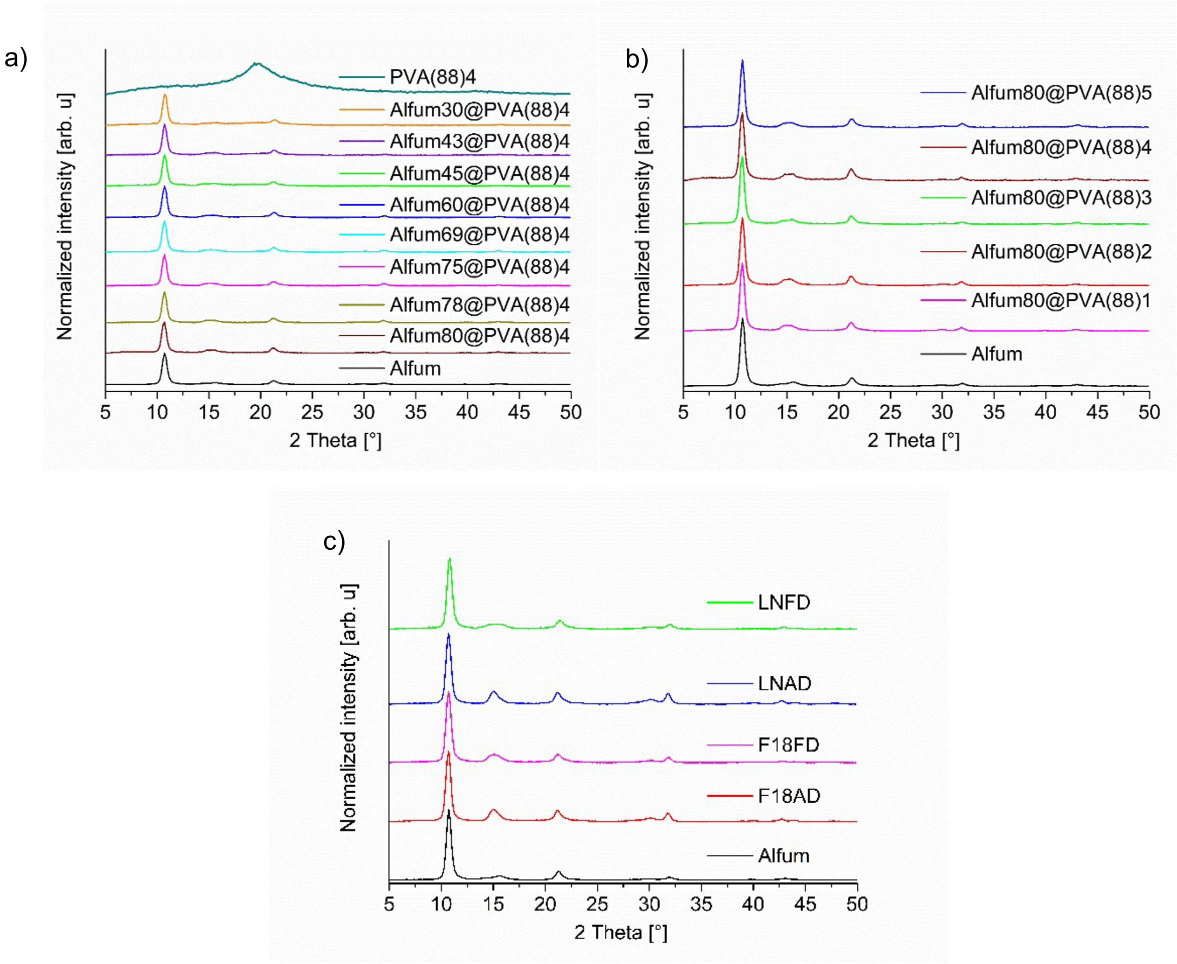

Fig. S8. Powder X-ray diffraction patterns of Alfum and (a) Alfum@PVA(88) monoliths with different loading amount of Alfum, (b) Alfum80@PVA(88)4 monoliths with different molecular weight of polymers and (c) different preparation methods of Alfum80@PVA(88)4 monoliths.

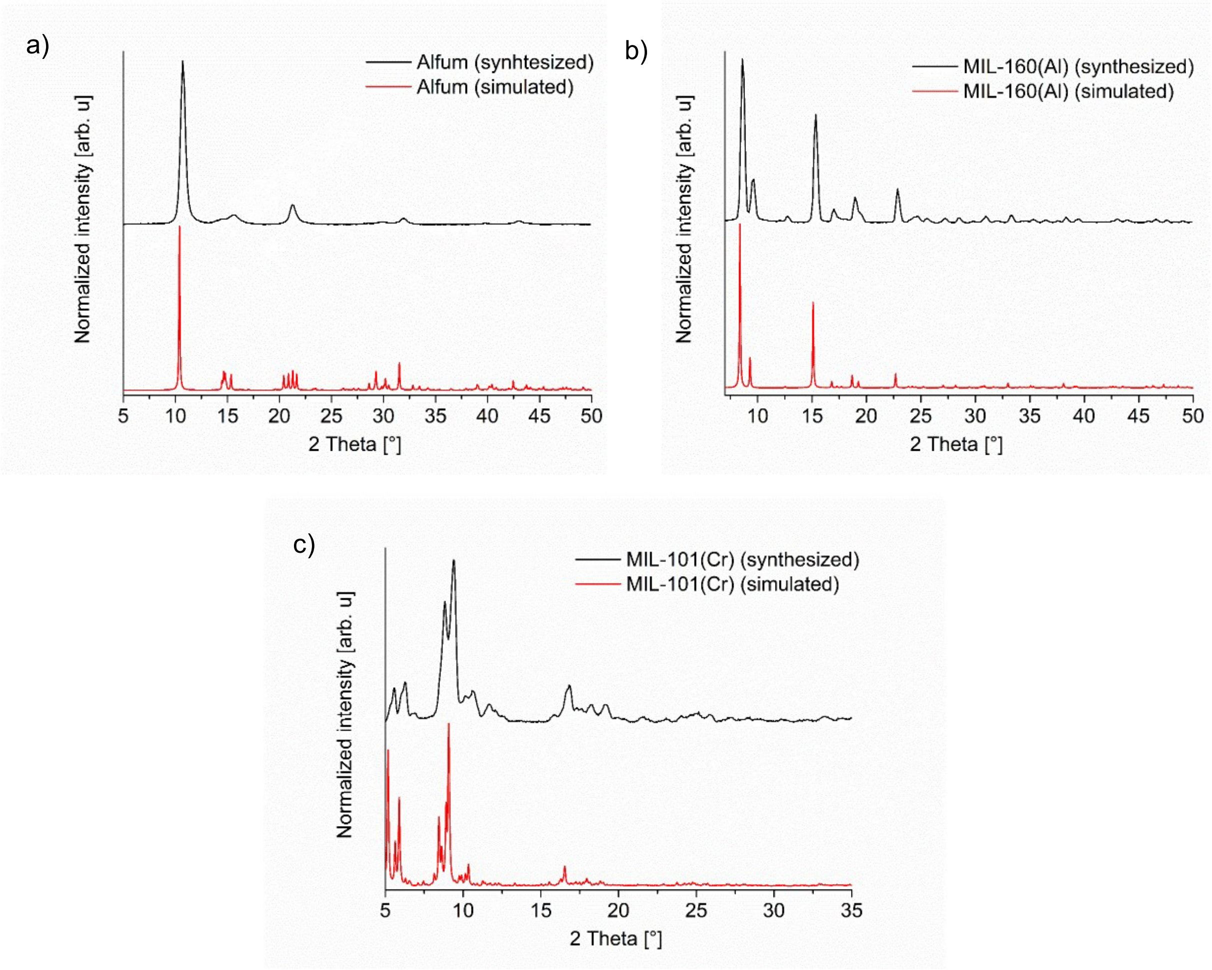

Fig. S9. Powder X-ray diffraction patterns of simulated (in red) and synthesized (in black) (a) Alfum, (b) MIL-160(Al) and (c) MIL-101(Cr).

S7. Infrared (IR) spectra

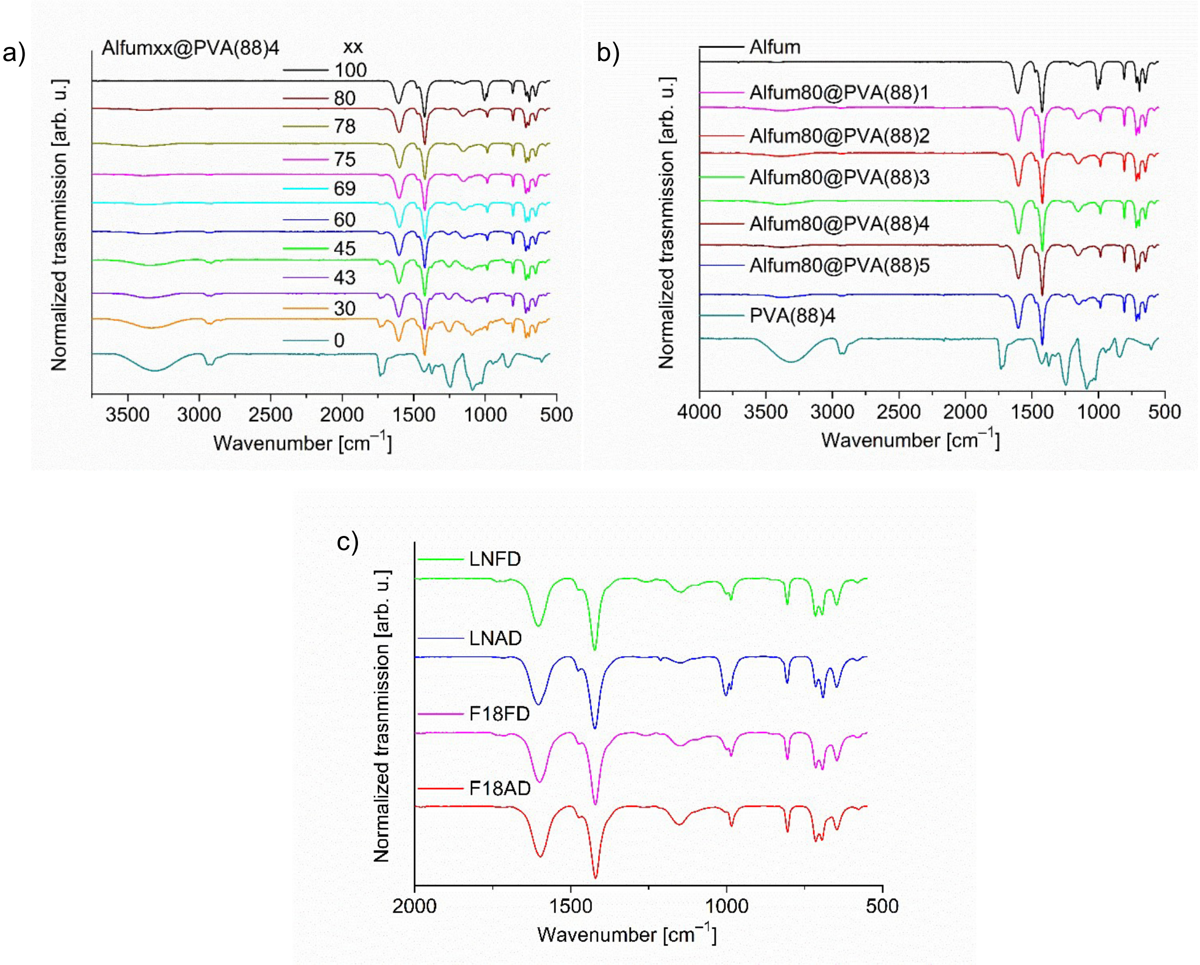

Fig. S10. IR spectra of Alfum and (a) Alfum@PVA(88) monoliths with different loading amounts of Alfum, (b) Alfum80@PVA(88)4 monoliths with different molecular weight of polymers and (c) different preparation methods of Alfum80@PVA(88)4 monolith. The C=O vibration at 1733 cm^{-1} (from the not-hydrolyzed acetate group) is characteristic for PVA(88).

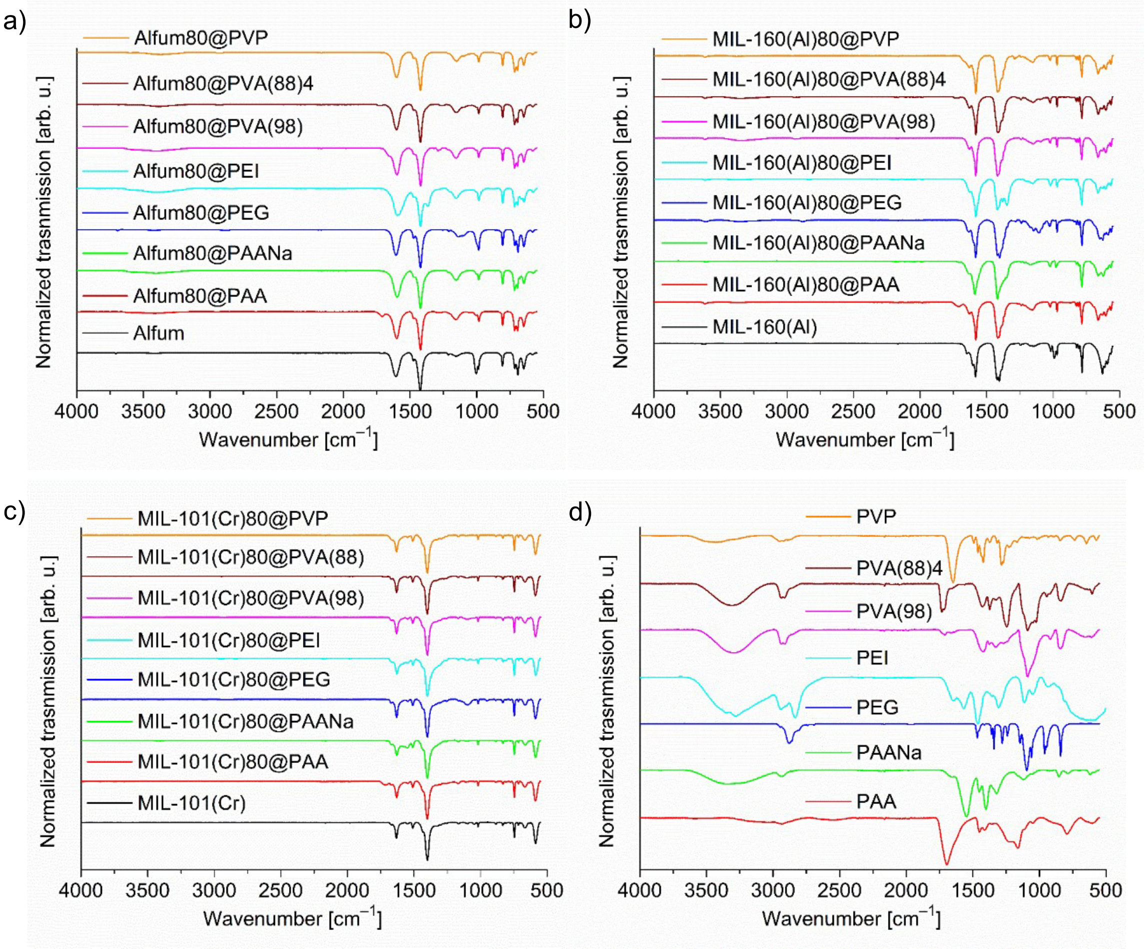

Fig. S11. IR spectra of (a) Alfum and Alfum@polymer monoliths (b) MIL-160(Al) and MIL-160(Al)@polymer monoliths (c) MIL-101(Cr) and MIL-101(Cr)@polymer monoliths (d) polymers.

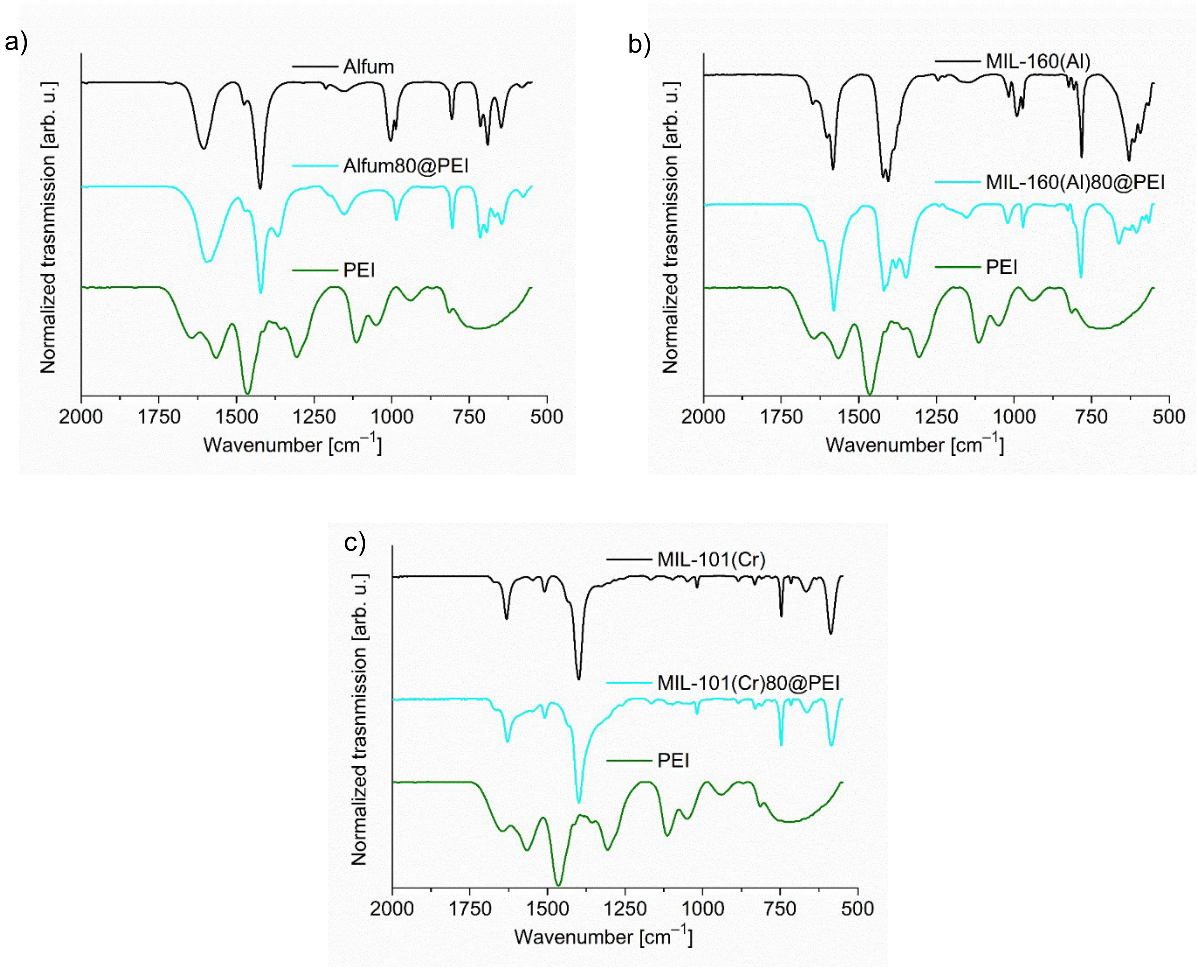

Fig. S12. IR spectra of (a) Alfum, Alfum80@PEI monolith and PEI (b) MIL-160(Al), MIL-160(Al)80@PEI monolith and PEI (c) MIL-101(Cr), MIL-101(Cr)80@PEI monolith and PEI.

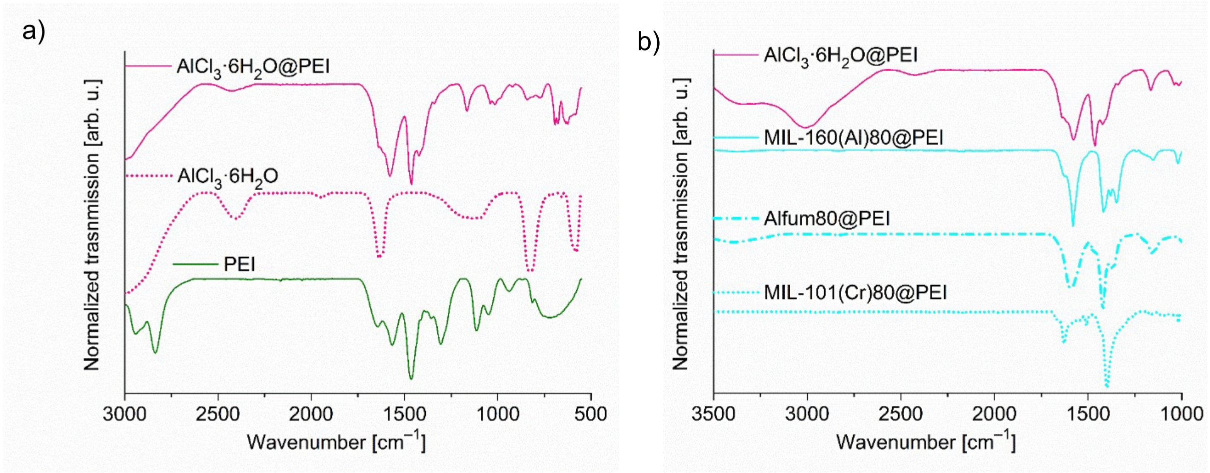

Fig. S13. IR spectra of (a) $AlCl_3 \cdot 6H_2O$@PEI, $AlCl_3 \cdot 6H_2O$ and PEI (b) $AlCl_3 \cdot 6H_2O$@PEI and MOF@PEI monoliths.

S8. Scanning electron microscopy (SEM) images

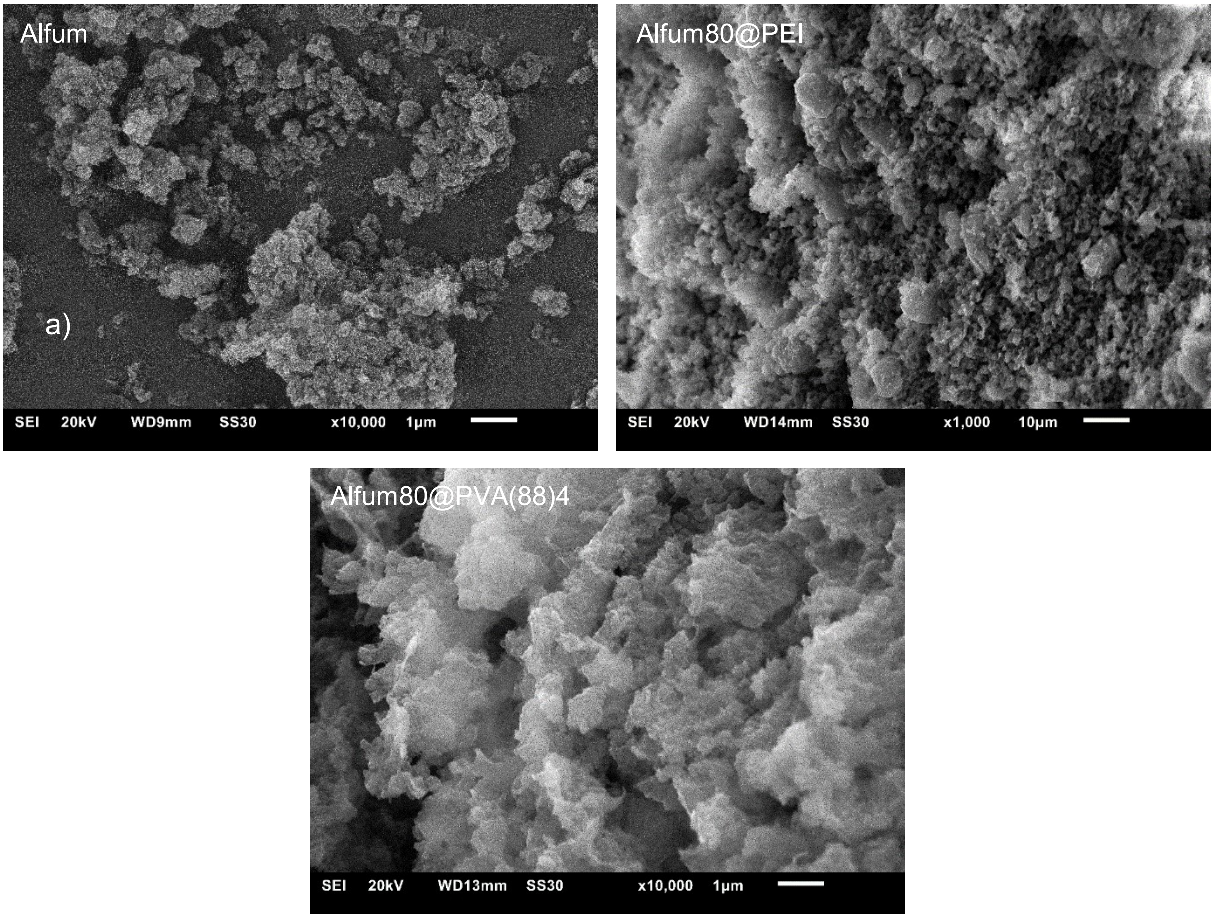

Fig. S14. Scanning electron microscopy (SEM) images of Alfum, Alfum80@PEI and Alfum80@PVA(88)4.

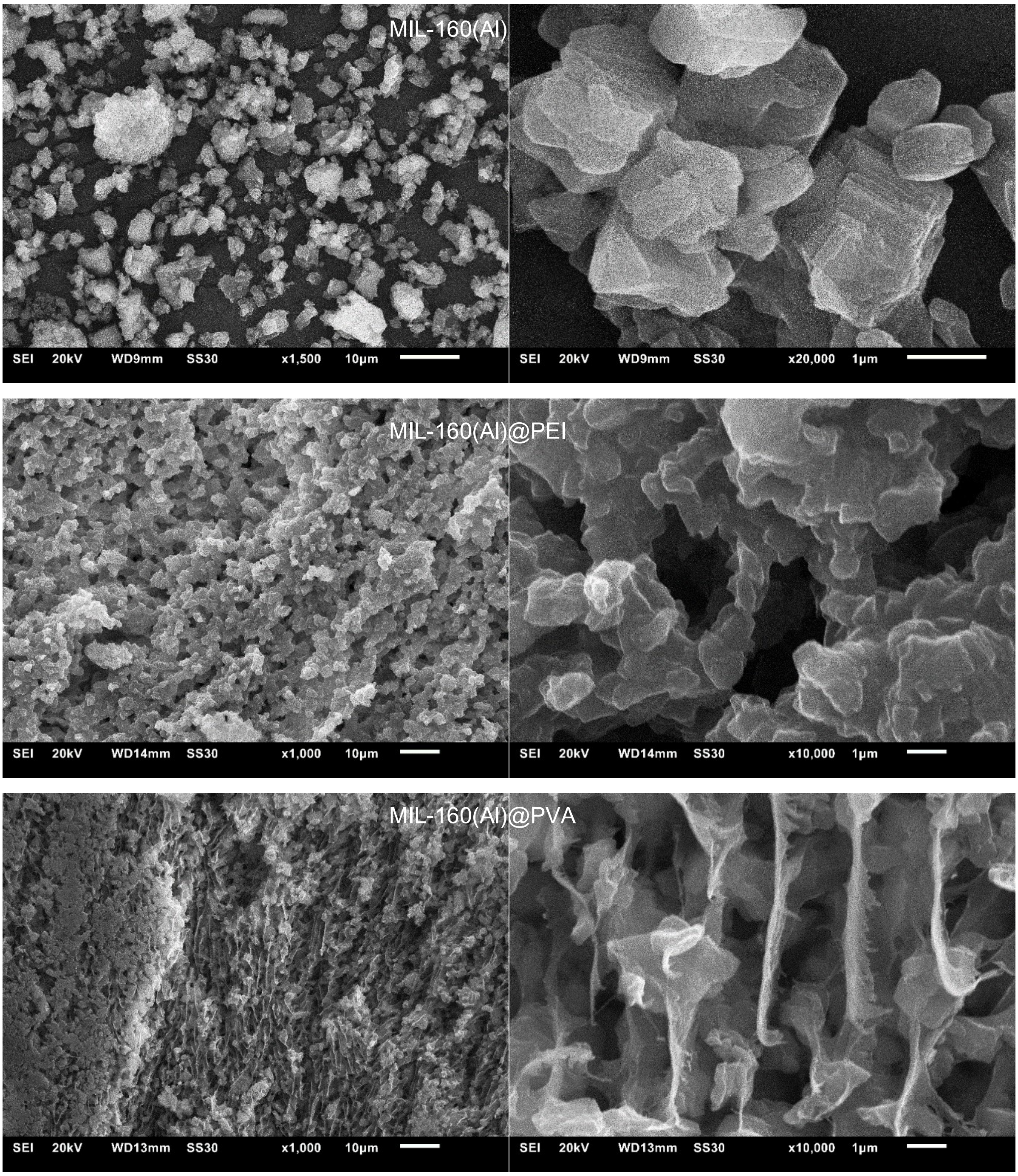

Fig. S15. Scanning electron microscopy (SEM) images of MIL-160(Al), MIL-160(Al)80@PEI and MIL-160(Al)80@PVA(98) with different magnification.

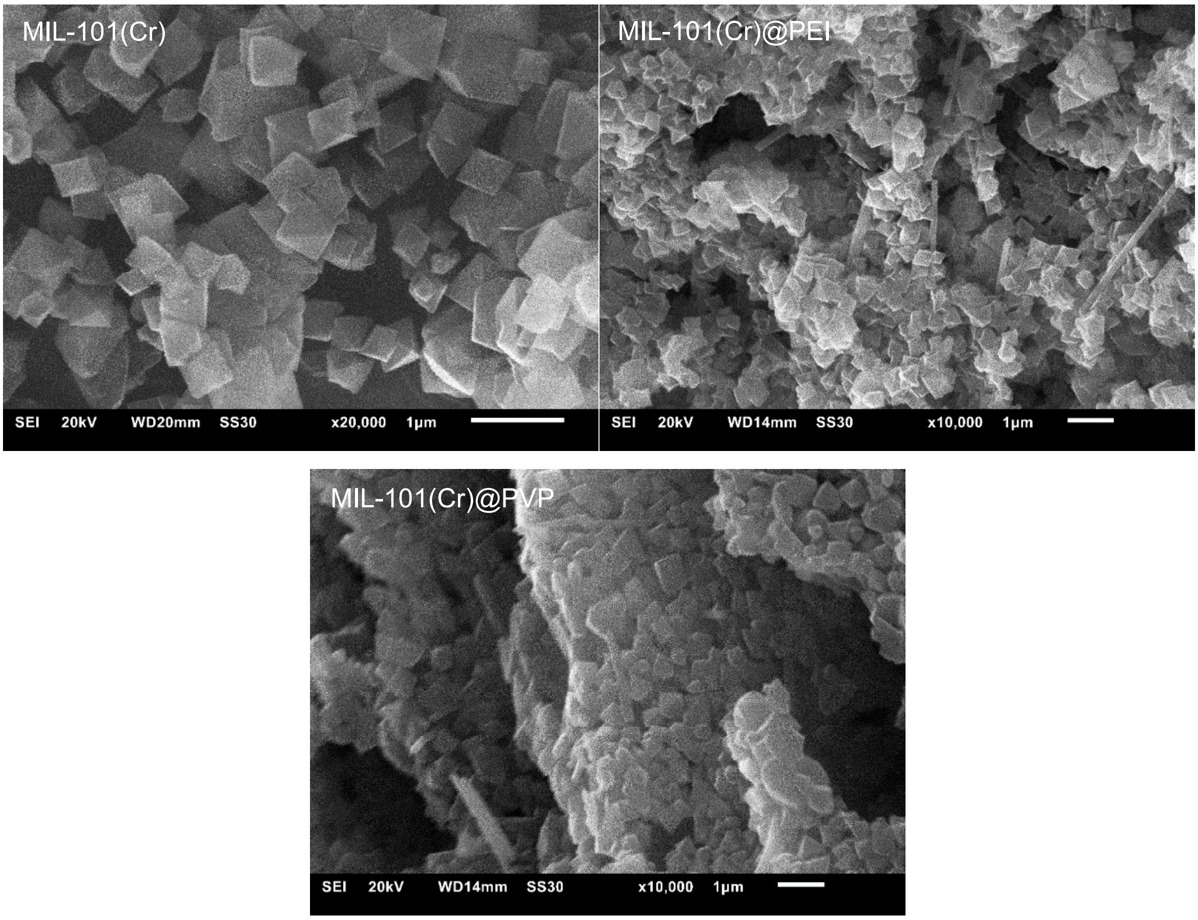

Fig. S16. Scanning electron microscopy (SEM) images of MIL-101(Cr), MIL-101(Cr)80@PEI and MIL-101(Cr)80@PVP.

S9. Nitrogen sorption isotherms

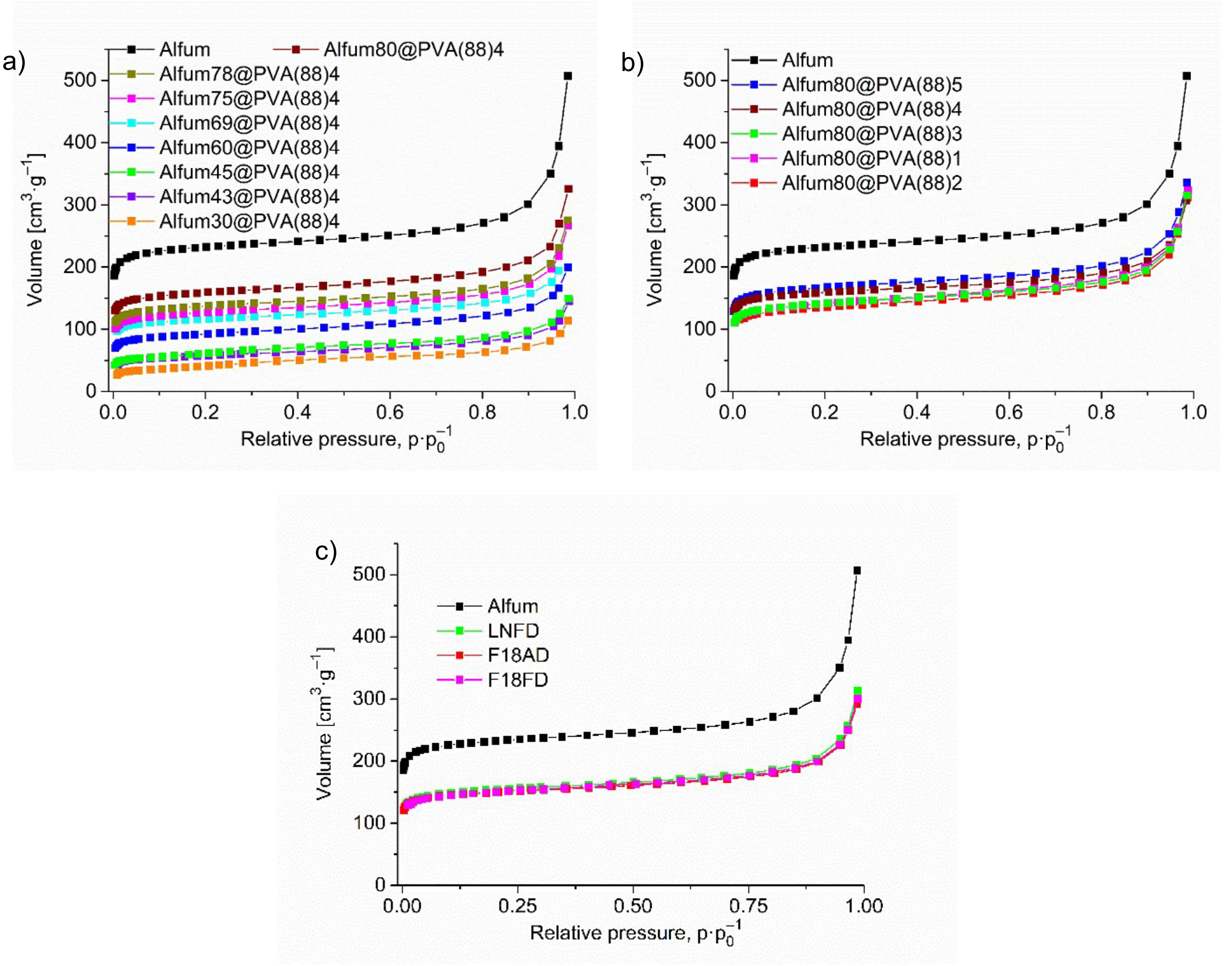

Fig. S17. Nitrogen adsorption isotherms of Alfum and (a) Alfum@PVA(88) with different loading amount of Alfum, (b) Alfum80@PVA(88)4 with different molecular weight of polymers and (c) different preparation methods of Alfum80@PVA(88)4 monolith. For clarity only the adsorption isotherms are depicted. For the given Type I branch of the isotherms up to about $p \cdot p_0^{-1} = 0.6$ the desorption isotherms are, however, almost superimposed with negligible hysteresis (cf. Fig. S18a).

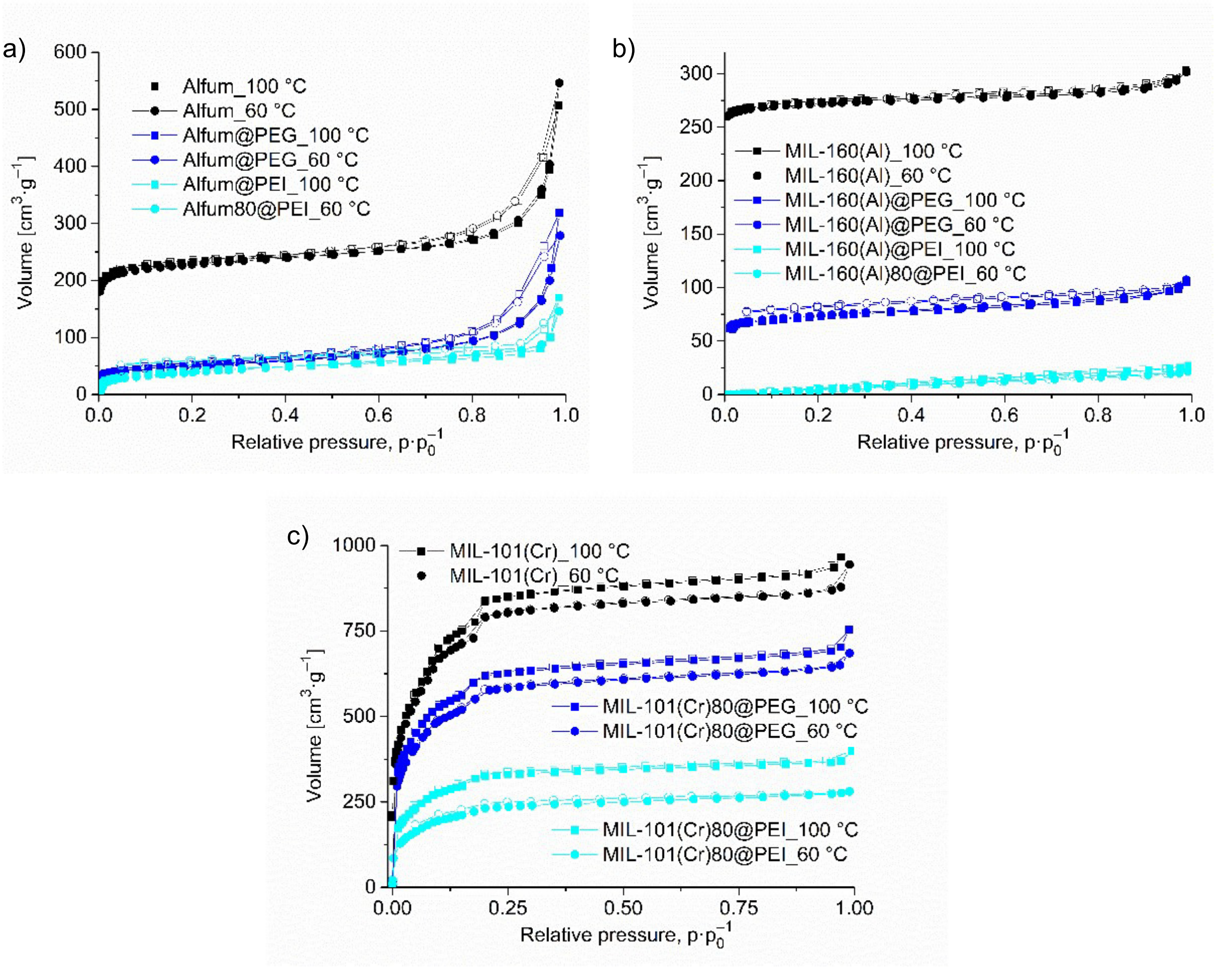

Fig. S18. Nitrogen adsorption-desorption isotherms of (a) Alfum, Alfum@PEG and Alfum@PEI (b) MIL-160(Al), MIL-160(Al)@PEG and MIL-160(Al)@PEI and (c) MIL-101(Cr), MIL-101(Cr)@PEG and MIL-101(Cr)@PEI activated either at 60 °C or 100 °C. (Adsorption is depicted with filled, desorption with empty symbols.)

Table S1. Comparison of S(BET) and pore volume of Alfum, Alfum@PEG, Alfum@PEI, MIL-160(Al), MIL-160(Al)@PEG, MIL-160(Al)@PEI, MIL-101(Cr), MIL-101(Cr)@PEG and MIL-101(Cr)@PEI depending on the activation condition (60 °C or 100 °C).

Sample[a] [Activation temp. in °C]		*S*(BET)[b] exp. [m^2·g^{-1}] (% of S(BET) calc.)	*S*(BET) calc.[c] [m^2·g^{-1}]	*V*(pore)[d] [cm^3·g^{-1}] (% of *V*(pore) calc.)	*V*(pore) calc.[c] [cm^3·g^{-1}]
Alfum [100]		946	-	0.478	-
Alfum [60]		893	-	0.473	-
Alfum	80@PEG [100]	182 (24)	758	0.198 (52)	0.384
	80@PEG [60]	174 (24)	715	0.192 (51)	0.379
	80@PEI [100]	149 (20)	757	0.111 (29)	0.383
	80@PEI [60]	144 (20)	714	0.120 (32)	0.378
MIL-160(Al) [100]		1134	-	0.445	-
MIL-160(Al) [60]		1130	-	0.424	-
MIL-160(Al)	80@PEG [100]	285 (31)	908	0.142 (40)	0.357
	80@PEG [60]	281 (31)	905	0.144 (42)	0.340
	80@PEI [100]	43 (5)	907	0.035 (10)	0.356
	80@PEI [60]	44 (5)	904	0.028 (8)	0.339
MIL-101(Cr) [100]		3171	-	1.348	-
MIL-101(Cr) [60]		2983	-	1.330	-
MIL-101(Cr)	80@PEG [100]	2234 (88)	2539	1.056 (98)	1.079
	80@PEG [60]	2087 (87)	2387	0.984 (92)	1.065
	80@PEI [100]	1199 (47)	2537	0.562 (52)	1.078
	80@PEI [60]	865 (36)	2386	0.418 (39)	1.064

[a] Nomenclature: In MOF*xx*@polymer *xx* refers to the wt% of corresponding MOF in the composite. Thus, MIL-101(Cr)80@PAA has 80 wt% loading of MIL-101(Cr) in the monolith.

[b] Apparent S(BET) values were determined from N_2 sorption isotherms at 77 K with a standard deviation ± 20 m^2·g^{-1} (thereby, the apparent S(BET) values were calculated from the nitrogen physisorption isotherms using the described condition in the publication by Rouquerol et al. [13] with at least 3 points. Due to the high variation of about a few hundred m^2·g^{-1}, the S(BET) of MIL-101(Cr) and corresponding composites were determined over 7 points in the relative pressure range of 0.05 and 0.2).

[c] Calculated apparent S(BET) and calculated micro- and small mesopore volume *V*(pore) in the monoliths were determined as the sum of the mass-weighted S(BET) or V(pore) of the MOFs and the respective polymer (PAA, PAANa, PEG, PEI, PVA(98), PVA(88) or PVP) monolith from the following formula (Ia) or (Ib), respectively:

$$\mathrm{S(BET)calc.} = \frac{\mathrm{wt\%\ of\ polymer}}{100} \times \mathrm{S(BET, polymer)} + \frac{\mathrm{wt\%\ of\ MOF}}{100} \times \mathrm{S(BET, MOF)} \qquad \text{(Ia)}$$

with apparent *S*(BET) after activation at 100 °C: Alfum = 946 $m^2 \cdot g^{-1}$; MIL-160(Al) = 1134 $m^2 \cdot g^{-1}$; MIL-101(Cr) = 3171 $m^2 \cdot g^{-1}$ and activation at 60 °C: Alfum = 893 $m^2 \cdot g^{-1}$; MIL-160(Al) = 1130 $m^2 \cdot g^{-1}$; MIL-101(Cr) = 2983 $m^2 \cdot g^{-1}$.

Because PEI is a liquid and PEG has a melting point of 65 °C, PEG was only activated at 60 °C and the resulting S(BET) of PEG was 5 $m^2 \cdot g^{-1}$.

$$\mathrm{V(pore)calc.} = \frac{\mathrm{wt\%\ of\ polymer}}{100} \times \mathrm{V(pore, polymer)} + \frac{\mathrm{wt\%\ of\ MOF}}{100} \times \mathrm{V(pore, MOF)} \qquad \text{(Ib)}$$

with *V*(pore) after activation at 100 °C: Alfum = 0.478 $cm^3 \cdot g^{-1}$; MIL-160(Al) = 0.445 $cm^3 \cdot g^{-1}$; MIL-101(Cr) = 1.348 $cm^3 \cdot g^{-1}$; and activation at 60 °C: Alfum = 0.473 $cm^3 \cdot g^{-1}$; MIL-160(Al) = 0.424 $cm^3 \cdot g^{-1}$; MIL-101(Cr) = 1.330 $cm^3 \cdot g^{-1}$; PEG = 0.004 $cm^3 \cdot g^{-1}$.

[d] Total pore volumes V(pore) were determined from N_2 sorption isotherms at 77 K ($p \cdot p_0^{-1} = 0.90$) for pores ≤ 20 nm.

S10. Water sorption isotherms

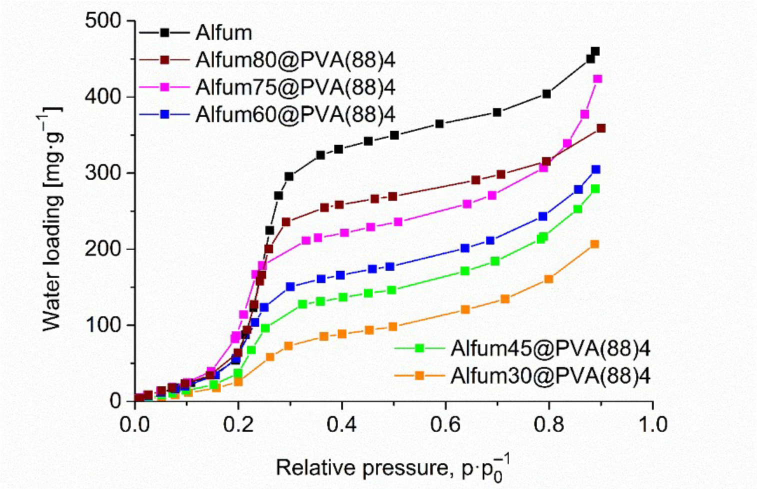

Fig. S19. Effect of MOF amount in the monolith for water sorption.

S11. Hydrogen sorption isotherms

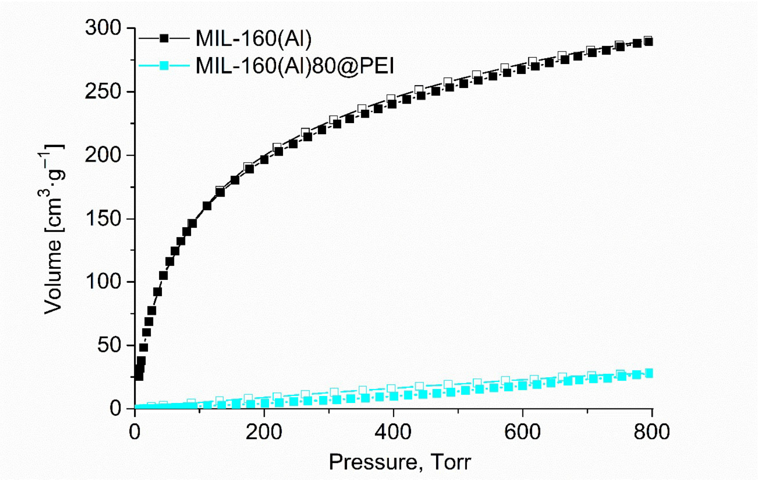

Fig. S20 Hydrogen ad-desorption isotherm of MIL-160(Al) and MIL-160(Al)@PEI at 77 K.

S12. Bulk and tapped density

For the determination of tapped density a large amount of material of around 100 g is needed or a sufficient amount to nearly fill a 250 mL graduated cylinder would be desirable [14]. In the case of less substance, a 100 mL graduated cylinder can be also used. Because of the usually small scale synthesis in MOF chemistry, yielding often around only 1 gram of product, we determined the bulk and tapped density in a simple way according to a falling experiment which is described below. To make a comparison, two powder materials available in larger amount were tested according to the description given in the European Pharmacopeia (8.0 volume I 01/2014; Method 1) and with the falling experiment. European Pharmacopeia describes determination of bulk density by filling a 250 mL graduated cylinder with 100 g material or for the material with low density to fill as much as possible in the graduated cylinder. Bulk density is determined from the initial mass and bulk volume (V_0) as well as V_{10}, V_{500}, V_{1250} after 10 taps, 500 taps and 1250 taps, respectively. If the volume change is more than 2 mL after 500 and 1250 taps, the measurement is repeated for 1250 times until less than 2 mL change observed. Tapped density can be determined from the corresponding tapped volume. In our method (to distinguish from Method 1 in the European Pharmacopeia we call it Method A), the bulk density was determined by filling the powdered material in a 1 mL syringe (prepared as in the Fig. S21b) with the help of a suitable glass funnel (with a tip length of ca. 5 cm). About 1 mL of the sample, which was carefully weighted before, was filled in the syringe and during the filling any touch to the syringe must be avoided so as not to compact the sample. After determination of the bulk density, the filled syringe with the sample was closed from the top with the stopper (Fig. S21b) which should not contact the sample. After each fall, the stopper was moved back to the initial position. A small cleft on the stopper prevented that the sample sucked up when pulling stopper back to the initial position. The tapped density was determined by letting the 1 mL filled syringe fall from a height of 1135 mm through a glass pipe with an inner diameter of 7.5 mm. Falling was repeated until no visible change was observed in the tapped volume over 100 falls. Then the tapped density was calculated from tapped volume and the known mass of the sample.

To make a comparison, we selected a sample with low density (Aerosil) and high density (Mannitol). Bulk density and tapped density determined by both Method 1 and Method A are very close to each other. While the bulk density by Method A is slightly denser, the tapped density, which was obtained from Method A is slightly lower than from Method 1. The results of the comparison are given in the Table S2.

Table S2. Comparison of Method 1 in the European Pharmacopeia with Method A.

Method	Sample	Bulk density [g·cm^{-3}]	Tapped density [g·cm^{-3}]
Method A	Aerosil	0.12	0.15
Method 1[a]	Aerosil	0.09	0.19
Method A	Mannitol	0.53	0.59
Method 1[a]	Mannitol	0.52	0.64
Method A	Alfum[b]	0.19	0.46
Method A	MIL-101(Cr)[b]	0.08	0.29
Method A	MIL-160(Al)[b]	0.25	0.59

[a] Determined according to the European Pharmacopeia (8.0 volume I 01/2014; Method 1)

[b] MOFs were tested only with Method A because of little amount of material available.

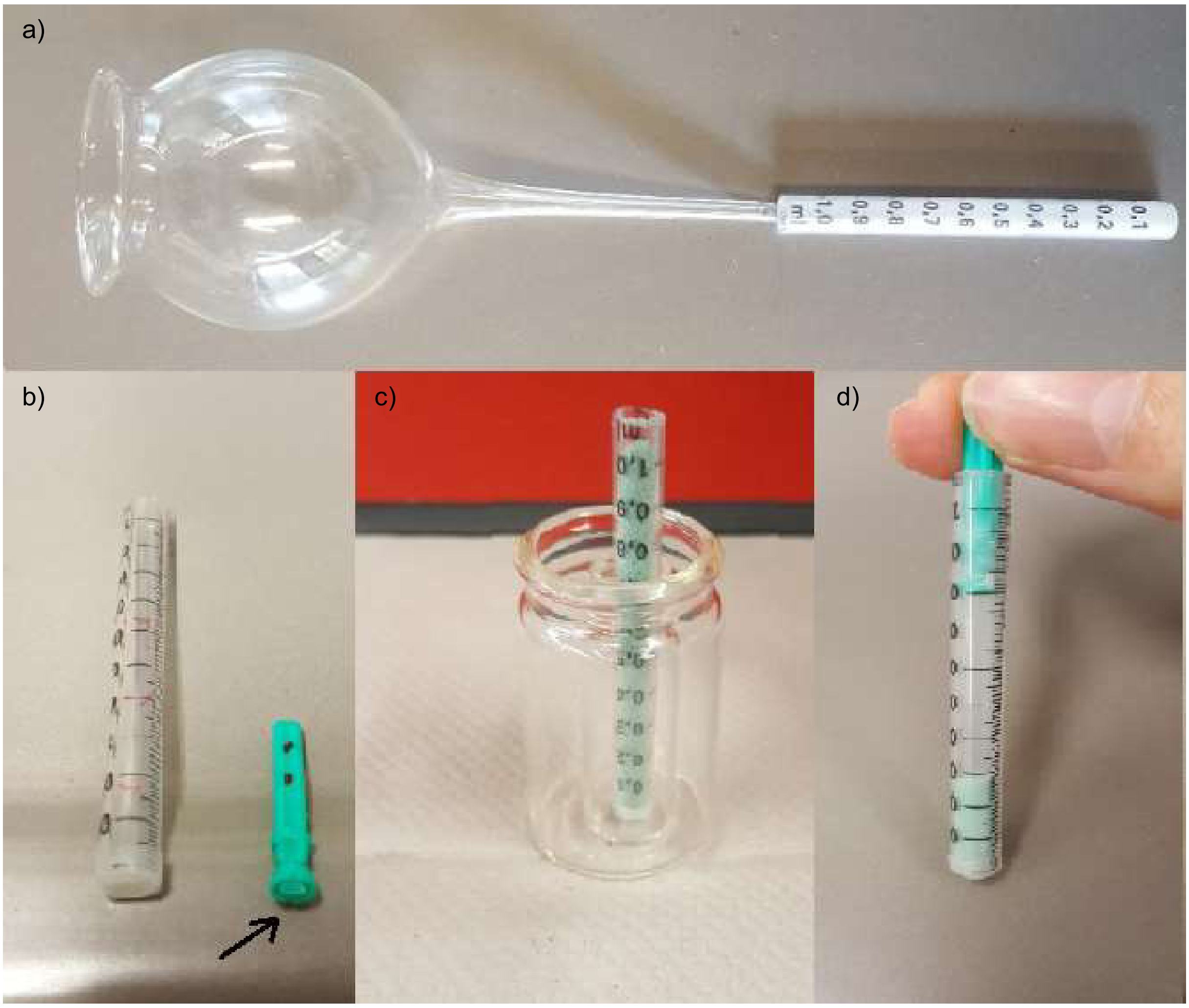

Fig. S21. (a) Glass funnel. (b) 1 mL syringe, which is filled with the sample and closed with a green stopper. The green stopper is cut at the tip to get a small cleft, which is shown with the arrow. (c) MIL-101(Cr) filled in the syringe for the determination of bulk density and (d) tapped volume.

Estimation of the density of the monoliths

The volume of the MOF, v_{MOF} for a given mass can be calculated from the crystal density of the MOF. The crystal density of MOFs (d_{MOF}) is given as 1.54 g·cm^{-3} for Alfum (taken from the cif-file for Basolite A520 (CSD-Refcode DOYBEA, CCDC no. 1051975 [1]), 1.57 g·cm^{-3} for MIL-160(Al) (taken from the cif-file for MIL-160 (CSD-Refcode PIBZOS) [8]) and 0.44 g·cm^{-3} for MIL-101(Cr) [15].

$$v_{MOF} = \frac{m_{MOF}}{d_{MOF}}$$

The following exemplary calculation is done for the density of the Alfum80@PVP monolith:
The MOF mass, m_{MOF} was 0.240 g and the above corresponding crystal density of MOF then gives the volume for the MOF v_{Alfum} = 0.16 cm^3.
Addition of this MOF volume of 0.16 cm^3 to the 1.00 cm^3 (1 mL) of the polymer solution should in a good approximation give the volume of the monolith as 1.16 cm^3.
To the mass of MOF (0.240 g) plus polymer (0.060 g) or in total 0.300 g we must also consider the water vapor, which is adsorbed from the air by the monolith as the monolith was stored and handled under ambient air of about 50% humidity ($p \cdot p_0^{-1} = 0.5$).
This adsorbed amount of water at $p \cdot p_0^{-1} = 0.5$ can be read from Fig. 6 in manuscript. For the Alfum80@PVP monolith, the water vapor adsorption is 0.28 g·g^{-1}at $p \cdot p_0^{-1} = 0.5$.

Thus, for 0.300 g Alfum80@PVP monolith then 0.084 g water needs to be added to the mass and divided by the volume of 1.16 cm^3 of the monolith to give an estimated density of the Alfum80@PVP monolith with a value of 0.33 g·cm^{-3}. This value is only slightly lower than measured one with a value of 0.36 g·cm^{-3}.

Table S3. Density of the MOF@polymer monoliths.*

		Sample	Density $[\mathrm{g \cdot cm^{-3}}]$			Sample	Density $[\mathrm{g \cdot cm^{-3}}]$
Optimization experiments	**a**	Alfum80@PVA(88)1	0.32	**MOFs@Polymer**	**e**	Alfum80@PAA	0.38
		Alfum80@PVA(88)2	0.32			Alfum80@PAANa	0.38
		Alfum80@PVA(88)3	0.25			Alfum80@PEG	-[i]
		Alfum80@PVA(88)4	0.29			Alfum80@PEI	0.39
		Alfum80@PVA(88)5	0.38			Alfum80@PVA(98)	0.35
	b	Alfum30@PVA(88)4	0.16			Alfum80@PVA(88)4	0.30
		Alfum43@PVA(88)4	0.19			Alfum80@PVP	0.36
		Alfum45@PVA(88)4	0.18		**f**	MIL-160(Al)80@PAA	0.32
		Alfum60@PVA(88)4	0.21			MIL-160(Al)80@PAANa	0.36
		Alfum69@PVA(88)4	0.25			MIL-160(Al)80@PEG	0.30
		Alfum75@PVA(88)4	0.21			MIL-160(Al)80@PEI	0.39
		Alfum78@PVA(88)4	0.34			MIL-160(Al)80@PVA(98)	0.33
		Alfum80@PVA(88)4	0.29			MIL-160(Al)80@PVA(88)4	0.28
	c	LNFD	0.30			MIL-160(Al)80@PVP	0.41
		LNAD	-[h]		**g**	MIL-101(Cr)80@PAA	0.28
		F18FD	0.29			MIL-101(Cr)80@PAANa	0.33
		F18AD	0.44			MIL-101(Cr)80@PEG	0.29
	d	PEG	1.32			MIL-101(Cr)80@PEI	0.38
		PVA(98)	1.47			MIL-101(Cr)80@PVA(98)	0.28
		PVA(88)4	1.53			MIL-101(Cr)80@PVA(88)4	0.29
		PVP	1.53			MIL-101(Cr)80@PVP	0.26

* Length and width of each monolith was measured with a caliper.

[a] Alfum@PVA(88)4 with different molecular weight of polymers.

[b] Alfum@PVA(88) with different loading amount of Alfum.

[c] Different preparation methods of Alfum80@PVA(88)4 monolit.

[d] Density of the polymer powders.

[e] Alfum80@polymer.

[f] MIL-160(Al)80@polymer.

[g] MIL-101(Cr)80@polymer.

[h] Because of a not uniform shape of the monolith, the density could not be determined.

[i] Alfum80@PEG was too fragile to measure its length and width with the caliper.

S13. Cryopolymerized (CP)-monoliths

S13.1. Powder X-ray diffractometry (PXRD) of CP-monoliths

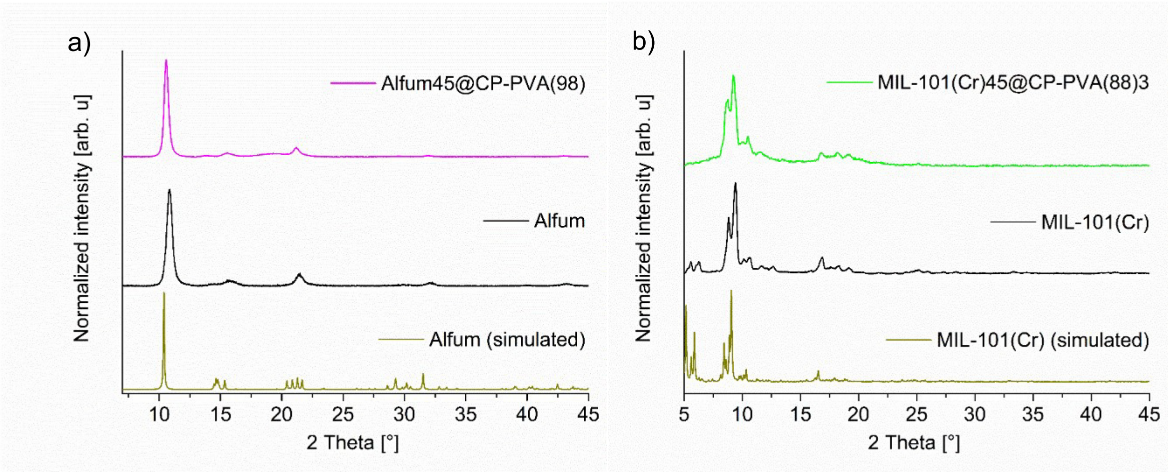

Fig. S22. Powder X-ray diffratograms of (a) Alfum45@CP-PVA(98) and Alfum, (b) MIL-101(Cr)45@CP-PVA(98) and MIL-101(Cr) synthesized with TMAOH and simulated.

S13.2. Scanning electron microscopy (SEM) images of CP-monoliths

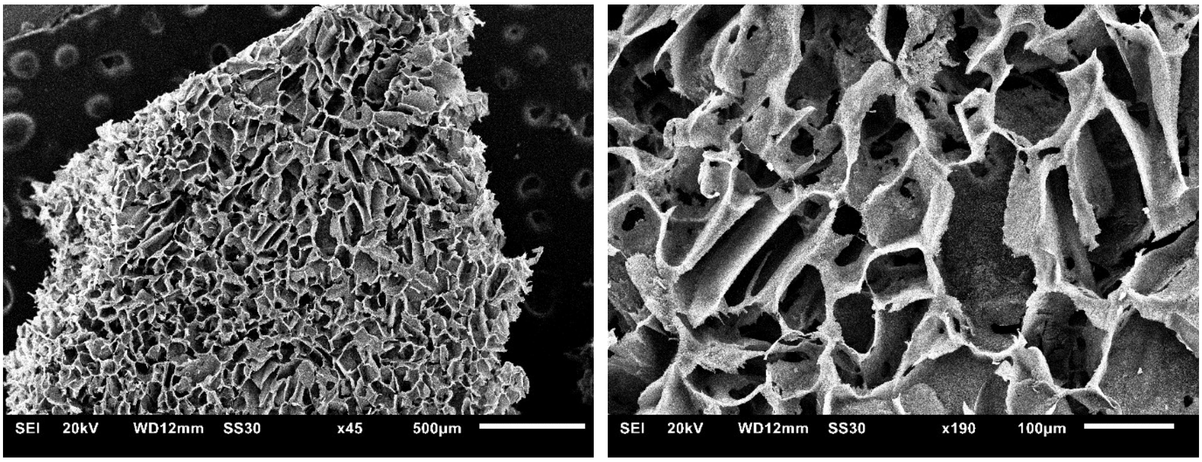

Fig. S23. SEM images of MIL-101(Cr)45@CP-PVA(88)3 with different magnification.

S13.3. IR spectra of CP-monoliths

The IR spectra of MOF@CP-polymer composites represent the features of MOF and PVA(88) without any additional or missing absorption bands (see Fig. S24 and Fig. S25).

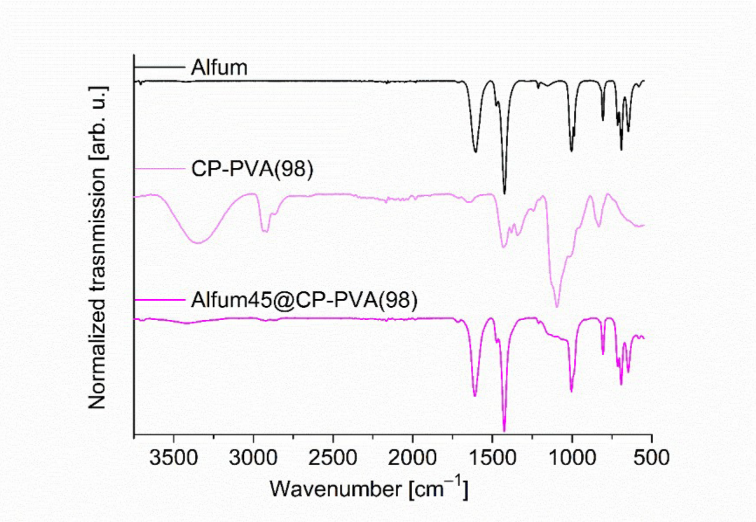

Fig. S24. IR spectra of Alfum45@CP-PVA(98), CP-PVA(98) and Alfum.

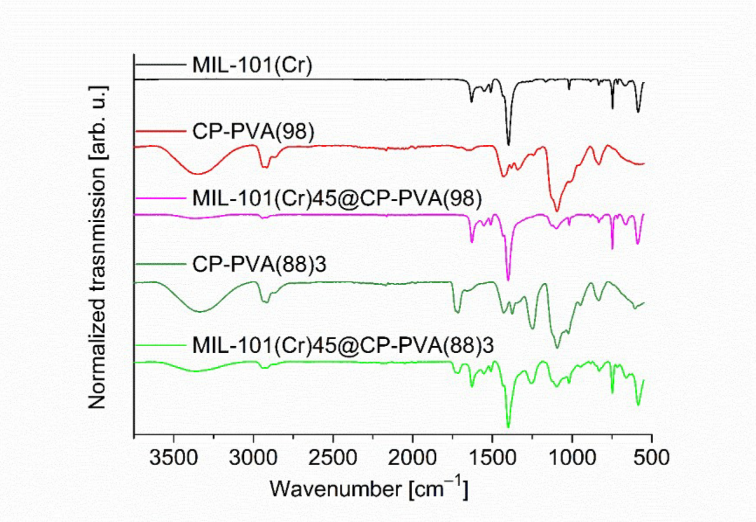

Fig. S25. IR spectra of MIL-101(Cr)45@CP-PVA(98), MIL-101(Cr)45@CP-PVA(88)3, CP-PVA(98), CP-PVA(88)3 and MIL-101(Cr) synthesized with TMAOH.

S13.4. Water sorption isotherms of CP monoliths

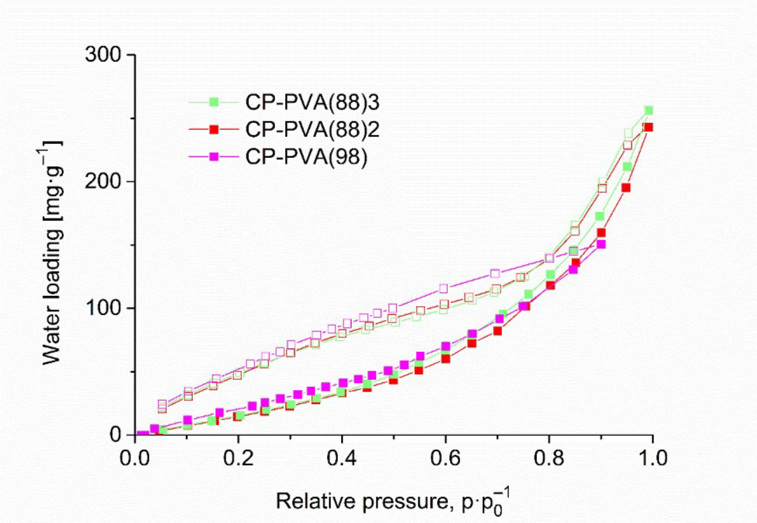

Fig. S26. Water vapor adsorption-desorption isotherms of CP-PVA(98), CP-PVA(88)2 and CP-PVA(88)3.

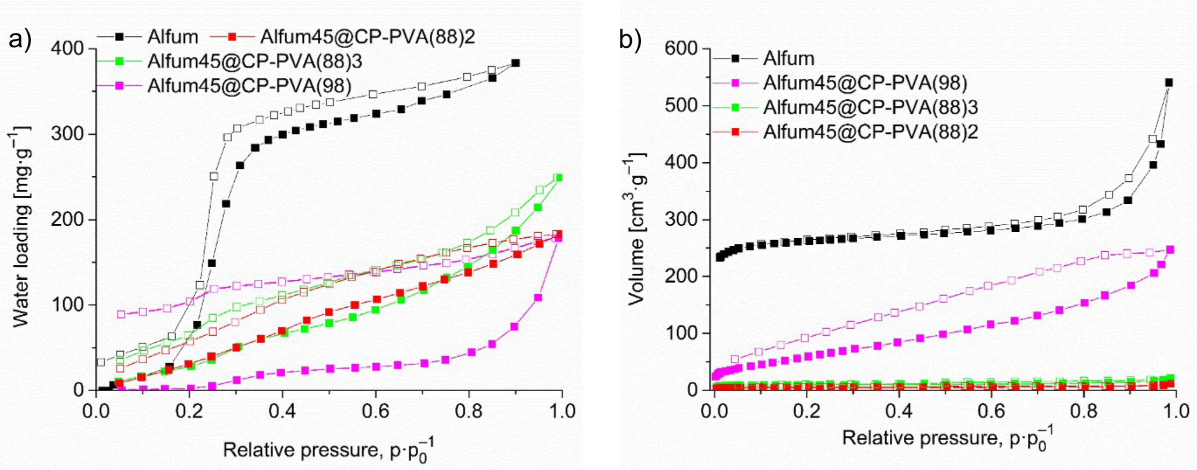

Fig. S27. (a) Water vapor adsorption-desorption isotherms of Alfum45@CP-PVA, Alfum45@CP-PVA(88)2, Alfum@CP-PVA(88)3 and Alfum, (b) nitrogen adsorption-desorption isotherms of Alfum45@CP-PVA(98), Alfum45@CP-PVA(88)2, Alfum@CP-PVA(88)3 and Alfum. (Adsorption is depicted with filled, desorption with empty symbols.)

Table S4. Results of nitrogen sorption measurements and water sorption measurements of MOFs and CP-monoliths.

Samples[a]	**S(BET)[b] exp. [$m^2 \cdot g^{-1}$] (% of S(BET) calc.)[b] {S(BET) calc. [$mg \cdot g^{-1}$]}**	**Water loading exp.·[$mg \cdot g^{-1}$] (% of Water loadng calc.)[d] {Water loading calc.[b] [$mg \cdot g^{-1}$]} at**	
		0.55 $p \cdot p_0^{-1}$	0.90 $p \cdot p_0^{-1}$
MIL-101(Cr)[e]	2425 (-) {-}	0.980 (-) {-}	1.050 (-) {-}
MIL-101(Cr)45@CP-PVA(98)	828 (**74**) {1113}	310 (**66**) {470}	380 (**68**) {560}
MIL-101(Cr)45@CP-PVA(88)3	133 (**12**) {1091}	210 (**45**) {470}	310 (**56**) {550}
MIL-101(Cr)45@CP-PVA(88)2	137 (**13**) {1091}	200 (**43**) {470}	290 (**52**) {560}
Alfum	1030 (-) {-}	320 (-) {-}	380 (-) {-}
Alfum45@CP-PVA(98)	154 (**32**) {486}	30 (**17**) {180}	70 (**28**) {250}
Alfum45@CP-PVA(88)3	37 (**8**) {464}	90 (**50**) {180}	190 (**76**) {250}
Alfum45@CP-PVA(88)2	15 (**3**) {464}	100 (**59**) {170}	160 (**62**) {260}

[a] Nomenclature: In MOF*xx*@polymer *xx* refers to the wt% of corresponding MOF in the composite. Thus, MIL-101(Cr)80@PAA has 80 wt% loading of MIL-101(Cr) in the monolith.

[b] Expected apparent S(BET) is calculated as the sum of the mass-weighted S(BET) of the MOFs and PVA(98), PVA(88)2 or PVA(88)3 polymer according to the following formula (I):

$$\mathrm{S(BET)calc.} = \frac{\mathrm{wt\%\ of\ PVAy}}{100} \times \mathrm{S(BET, PVAy)} + \frac{\mathrm{wt\%\ of\ MOF}}{100} \times \mathrm{S(BET, MOF)} \qquad \text{(I)}$$

with apparent *S*(BET) MIL-101(Cr) = 2425 $m^2 \cdot g^{-1}$; Alfum = 1030 $m^2 \cdot g^{-1}$; PVA(98) = 40 $m^2 \cdot g^{-1}$; PVA(88)2 = 0 $m^2 \cdot g^{-1}$; PVA(88)3 = 0 $m^2 \cdot g^{-1}$;

[c] Apparent S(BET) values determined from N_2 sorption isotherm at 77 K with a standard deviation ± 20 $m^2 \cdot g^{-1}$ (calculated over 5 points in the range of $0.05 < p \cdot p_0^{-1} < 0.2$ for MIL-101 and corresponding composites, and $0.01 < p \cdot p_0^{-1} < 0.08$ for Alfum and related composites).

[d] Calculated water adsorption value is the sum of the mass-weighted uptakes of the MOF and the polymer at the respective relative pressure as given by the following formula (II):

$$\mathrm{Water\ uptake\ calc.} = \frac{\mathrm{wt\%\ of\ polymer}}{100} \times (\mathrm{water\ uptake\ polymer}) + \frac{\mathrm{wt\%\ of\ MOF}}{100} \times (\mathrm{water\ uptake\ MOF}) \qquad \text{(II)}$$

The values “water uptake polymer” (see Fig. S26) and “water uptake MOF” (see Fig. 9 and Fig. 10 in the publication) can be taken from the water vapor adsorption isotherm of the MOF and polymer at the respective relative pressure.

[e] MIL-101(Cr) was synthesized with TMAOH.

S14. References

[1] E. Alvarez, N. Guillou, C. Martineau, B. Bueken, B. van de Voorde, C. Le Guillouzer, P. Fabry, F. Nouar, F. Taulelle, D. de Vos, J.-S. Chang, K.H. Cho, N. Ramsahye, T. Devic, M. Daturi, G. Maurin, C. Serre, Angew. Chem. Int. Ed. 54 (2015) 3664–3668.

[2] E. Leung, U. Müller, N. Trukhan, H. Mattenheimer, G. Cox, S. Blei, Process For Preparing Porous Metal-Organic Frameworks Based On Aluminum Fumarate, US 201/0082864 A1. 2012 Apr 5.

[3] F. Jeremias, D. Fröhlich, C. Janiak, S.K. Henninger, RSC Adv. 4 (2014) 24073–24082.

[4] K. Brandenburg, Diamond (Version 4), Crystal and Molecular Structure Visualization, Crystal Impact – K. Brandenburg & H. Putz Gbr, Bonn (Germany), 2009-2017.

[5] A. Cadiau, J.S Lee, D.D. Borges, P. Fabry, T. Devic, M.T. Wharmby, C. Martineau, D. Foucher, F.T. Taulelle, C.-H. Jun, Y.K. Hwang, N. Stock, M.F. De Lange, F. Kapteijn, J. Gascon, G. Maurin, J.-S. Chang, C. Serre, Adv. Mater. 27 (2015) 4775–4780.

[6] D.D. Borges, P. Normand, A. Permiakova, R. Babarao, N. Heymans, D.S. Galvao, C. Serre, G. De Weireld, G. Maurin, J. Phys. Chem. C 121 (2017) 26822−26832.

[7] A. Permyakova, O. Skrylnyk, E. Courbon, M. Affram, S. Wang, U.-H. Lee, A.H. Valekar, F. Nouar, G. Mouchaham, T. Devic, G.D. Weireld, J.-S. Chang, N. Steunou, M. Frère, C. Serre, ChemSusChem. 10 (2017) 1419–1426.

[8] M. Wahiduzzaman, D. Lenzen, G. Maurin, N. Stock, M.T. Wharmby, Eur. J. Inorg. Chem. 2018 (2018) 3626-3632.

[9] G. Férey, C. Mellot-Draznieks, C. Serre, F. Millange, J. Dutour, S. Surblé, I. Margiolaki, Science 309 (2005) 2040–2042.

[10] M.F. de Lange, K.J.F.M. Verouden, T.J.H. Vlugt, J. Gascon, F. Kapteijn, Chem. Rev. 115 (2015) 12205–12250.

[11] A. Khutia, H.U. Rammelberg, T. Schmidt, S.K. Henninger, C. Janiak, Chem. Mater. 25 (2013) 790−798.

[12] J. Ehrenmann, S.K. Henninger, C. Janiak, Eur. J. Inorg. Chem. 4 (2011) 471–474.

[13] J. Rouquerol, P. Llewellyn, F. Rouquerol, Stud. Surf. Sci. Catal. 160 (2007) 49–56.

[14] Ph. Eur 8.0, 1 (01/2014) 345–346.

[15] P.L. Llewellyn, S. Bourrelly, C. Serre, A. Vimont, M. Daturi, L. Hamon, G. De Weireld, J.S. Chang, D.Y. Hong, Y.K. Hwang, S.H. Jhung, G. Férey, Langmuir 24 (2008) 7245–7250.

4 Unpublished results

The unpublished part also dealt with the shaping of MOFs (section 4.1 and 4.2) and additionally with synthesis of MOFs to modify their sorption properties (section 4.3 and 4.4). The Shaping of MOFs as well as modification of sorption properties of MOFs were also objectives of OPTIMAT project, which was mentioned in the section “assignment of tasks”. Related experimental part and literature on unpublished results are given in section 4.5 and Section 4.6, respectively.

4.1 Alfum@R,F-xerogel monolith composites

Wickenheisser et al. reported MOF@R.F-xerogel composites that gave promising properties with negligible pore blocking effects [1]. In that work, MIL-100(Fe), MIL-100(Cr) and MIL-101(Cr) were used for monolith preparation. Alfum, which is in the field of interest of this thesis, has many advantages, since it is hydrothermal stable and has an appropriate S-shaped water sorption isotherms for AHT at $p \cdot p_0^{-1} \approx 0.2$ with a water vapor uptake of about 450 $mg \cdot g^{-1}$ [2]. Due to the fact that each MOF in the composite behaves characteristically, Alfum should also be tested in R,F-xerogel composites with promising properties.

Various amounts of MOF in the R,F-xerogel were analyzed and tested for their sorption properties (see Table 4.1). The effect of adding additional water after pre-polymerization to the MOF@R,F-xerogel properties was tested. This additional water showed an improvement BET surface area and water loading in the MIL-101(Cr)@R,F-xerogel compared to the expected value [1]. In the Alfum@R,F-xerogel composite, however, the positive effect of additional water was not observed. Nevertheless, Alfum@R,F-xerogel showed satisfactory results compared to the expected value. The best result was achieved with Alfum57@R,F-xerogel with an apparent S(BET) of 539 $m^2.g^{-1}$, which corresponds to the 89% of the expected value. The water sorption results of the composites indicated nearly 100% of the expected value. The other results are summarized in Table 4.1.

Table 4.1. Results from nitrogen and water vapor sorption.

Sample[a]	S(BET) exp.[b] $[m^2 \cdot g^{-1}]$	S(BET) calc.[c] $[m^2 \cdot g^{-1}]$	Water loading[d] exp. $[g \cdot g^{-1}]$ (% of calc loading)	Water loading calc.[e] $[g \cdot g^{-1}]$
Alfum	1038	–	0.38	–
R,F-xerogel	40	–	0.10[f]	–
Compites[g]	Standard		Standard	
Alfum40@R,F-xerogel	308	439	0.21	0.21
Alfum50@R,F-xerogel	470	539	0.23	0.24
Alfum56@R,F-xerogel	539	599	0.25	0.26
	with water added		with water added	
Alfum42@R,F-xerogel	358	459	n.d.[h]	0.22
Alfum52@R,F-xerogel	399	559	0.25	0.25
Alfum58@R,F-xerogel	509	618	n.d.[h]	0.26

[a] In the Alfumxx@R,F-xerogel, xx refers to Alfum amount in the composites.

[b] Apparent S(BET) determined from N_2 sorption isotherm at 77 K with a standard deviation ± 20 $m^2 \cdot g^{-1}$ (calculated over 5 points in the range of $0.01 < p \cdot p_0^{-1} < 0.08$ for Alfum and Alfum@R,F-xerogel composites).

[c] Expected apparent S(BET) as the sum of the mass-weighted S(BET) of the MOF and R,F-xerogel monolith from the following formula:

$$\mathrm{S(BET)calc} = \frac{\mathrm{wt\%\ of\ R,F-xerogel}}{100} \times \mathrm{S(BET, R, F-xerogel)} + \frac{\mathrm{wt\%\ of\ Alfum}}{100} \times \mathrm{S(BET, Alfum)}$$

with apparent *S*(BET) Alfum = 1038 $m^2 \cdot g^{-1}$; R,F-xerogel = 40 $m^2 \cdot g^{-1}$

[d] Water vapor uptake value measured from water sorption isotherm at 293 K ($p \cdot p_0^{-1} = 0.9$)

[e] Water adsorption value calculated (estimated) as the sum of the mass-weighted uptakes at $p \cdot p_0^{-1} = 0.9$ of Alfum = 0.38 $g \cdot g^{-1}$ and R,F-xerogel = 0.10 $g \cdot g^{-1}$:

$$\mathrm{Water\ adsorption\ calc} = \frac{\mathrm{wt\%\ of\ R,F-xerogel}}{100} \times (\mathrm{uptake\ R, F-xerogel}) + \frac{\mathrm{wt\%\ of\ Alfum}}{100} \times (\mathrm{uptake\ Alfum}) \quad \mathrm{(II)}$$

[f] This value was taken from the literature [1].

[g] "Standard" refers the value, which was obtained from the sample obtained by the standard syntheses of Alfum@R,F-xerogel; "with added water" refers the value, which was obtained from the sample obtained by the syntheses of Alfum@R,F-xerogel with adding additional water.

[h] n.d. = not determined.

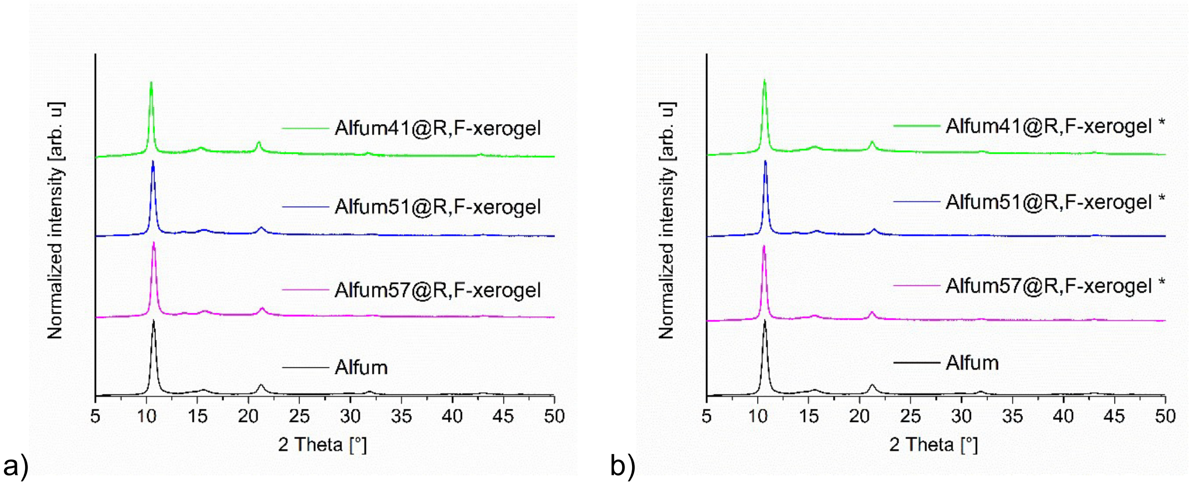

Fig. 4.1. Experimental powder X-ray diffraction pattern of (a) Alfum and Alfum@R,F-xerogel composites obtained from the standard syntheses and (b) Alfum and Alfum@R,F-xerogel composites obtained from syntheses with adding additional water (star means adding additional water).

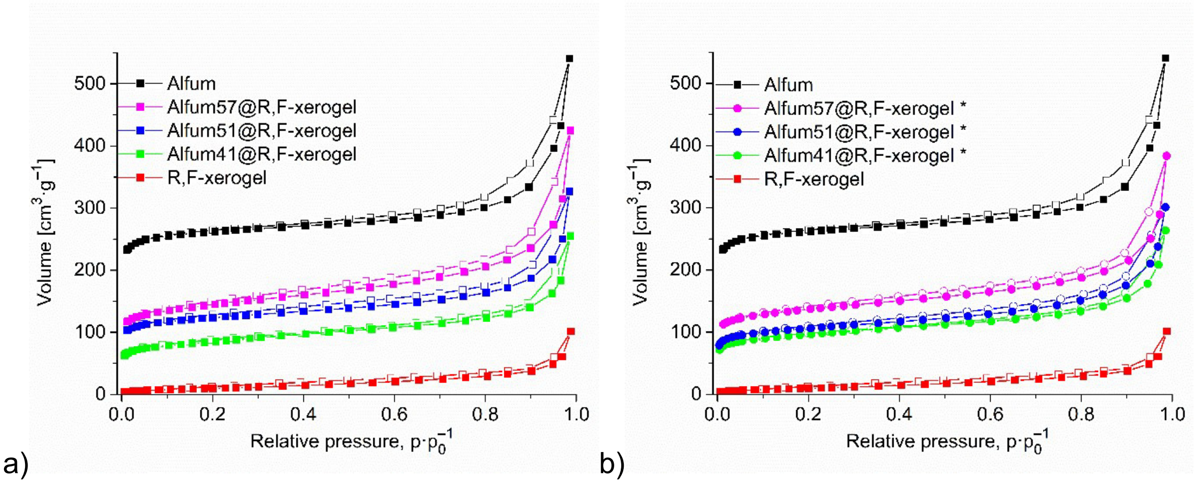

Fig. 4.2. Nitrogen adsorption isotherms of (a) Alfum and Alfum@R,F-xerogel composites obtained from the standard syntheses and (b) Alfum and Alfum@R,F-xerogel composites obtained from syntheses with adding additional water (star means adding additional water).

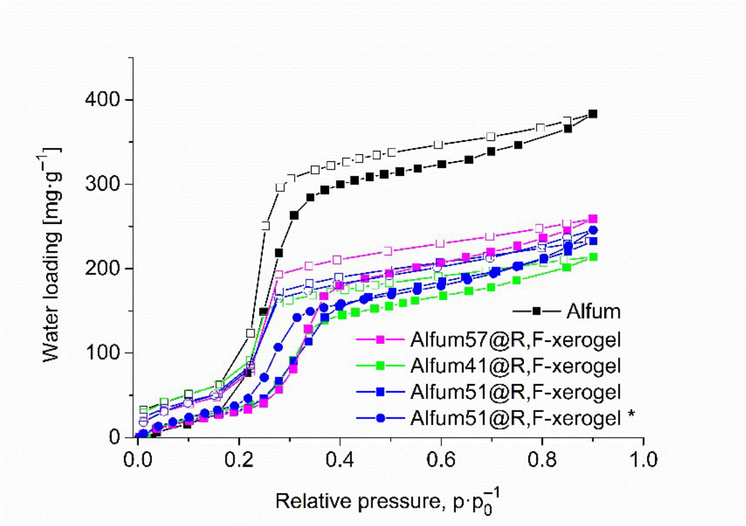

Fig. 4.3. Water vapor sorption isotherm of Alfum and Alfum@R,F-xerogel composites obtained from the standard syntheses and Alfum@R,F-xerogel composite obtained from syntheses with adding additional water (star means adding additional water).

4.2 MOF@PEI composites

In this part, hydrophilic PEI polymer was used to obtain a monolith with Alfum. The formation of the monolith was carried out by an epoxy-amine reaction by means of cryopolymerization technique [3]. It was possible to obtain a stable Alfum@PEI monolith with only 36 wt% Alfum. The other loading amount of Alfum with 51% and 66% showed partially formation of monolithic structure. At 81 wt% Alfum was not possible to get any monolith. According to the nitrogen sorption, the BET surface area of composite with 36 wt% Alfum indicated complete pore blocking with an S(BET) of 5 $m^2 \cdot g^{-1}$. SEM image of Alfum@PEI composites presented formation of macropores. The EDX mapping of Alfum@PEI with 36 wt% showed 50 wt% Alfum. This unexpected high fraction of Alfum can be explained by the fact that during washing process of the Alfum@PEI composite with water, some of the non-cross-linked PEI could be washed away.

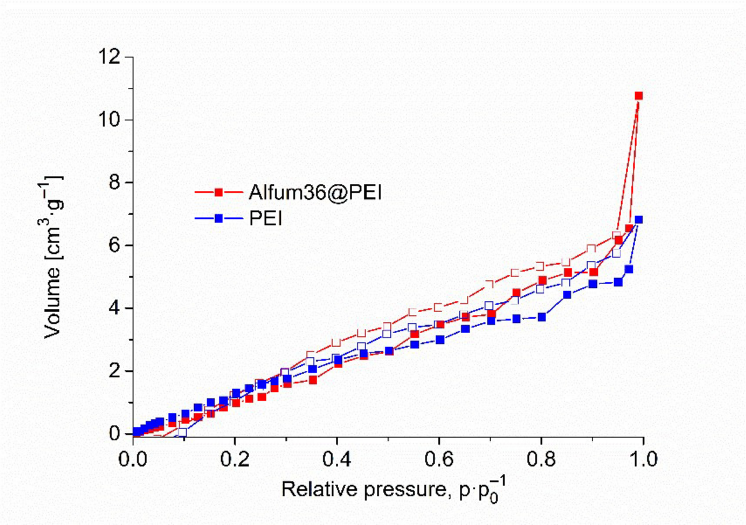

Fig. 4. 4. Nitrogen adsorption-desorption isotherms of PEI and Alfum36@PEI monolith.

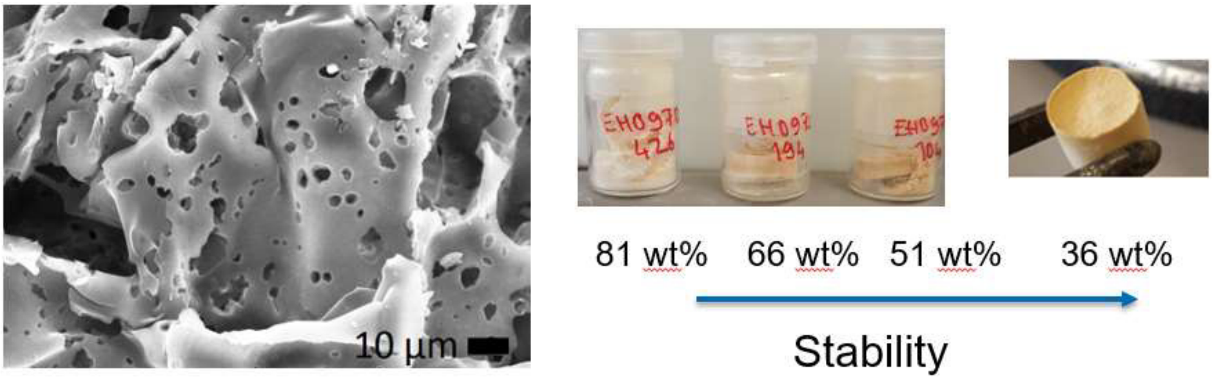

Fig. 4. 5. SEM image of Alfum36@PEI and increasing stability of Alfum@PEI composites with decreasing Alfum amount.

4.3 Reactions between different metal salts and linker with target MOFs: MIL-101(Fe), H_2N-MIL-101(Al) und H_2N-MIL-101(Fe)

The development of new adsorbent materials is essential for adsorption heat transformation AHT applications. MIL-101(Cr) is one of the interesting adsorbent materials. Although MIL-101(Cr) is not enough hydrophilic material for water based adsorption heat transformation, its high water uptake capacity with 1 $g \cdot g^{-1}$ and tunability properties make MIL-101(Cr) an attractive material for AHT research. Another important point is that, MIL-101(Cr) contains Cr(III) cation, which is classified as a low toxic material. MIL-101(Cr) could be criticized being of a source of toxic and carcinogenic sample Cr(VI) [4]. Considering this aspect, alternative materials to the Cr compound are the Al, and Fe compounds. MIL-101(Cr) and H_2N-MIL-101(Cr) are more hydrolytically stable compounds compared to the isostructural MIL-101(Fe), H_2N-MIL-101(Fe) and H_2N-MIL-101(Al). The alternative structure MIL-101(Al) is not yet known. The hydrothermal instability of the MIL-101(Fe), NH_2-MIL-101(Fe) und NH_2-MIL-101(Al) was postulated depending on the terminal bounded chlorine atom to the metal center [5]. This argument attributed to the hydrothermal stability of the MIL-100 with various metal centers Al, Fe and Cr, which were synthesized with chlorine free metal sources. Terminal ligand fluoride or hydroxide appears to be responsible for the improved water stability of MIL-100(Al), MIL-100(Cr) and MIL-100(Fe) as well as MIL-101 (Cr) structures. However, to the best of our knowledge, no literature has been reported for the synthesis of MIL-101(Fe), H_2N-MIL-101(Fe) and H_2N-MIL-101(Al). For this purposes, it can be attempted to synthesis MIL-101(Fe), H_2N-MIL-101(Fe) and H_2N-MIL-101(Al) with chlorine-free metal sources to vary the terminal ligand (Cl, F, OH). Table 4.2 shows the reaction of different metal sources that do not contain a chlorine atom. The amorphous product of these reactions was not further analyzed, correspondingly the nitrogen sorption measurement was not carried out. None of the reactions were successful to obtain the desired MOF. The PXRD and nitrogen sorption isotherms of the samples are given below and the results are listed in Table 4.2. Two interesting results from these experiments are given below.

The reaction of $Al(NO)_{3.}9H_2O$ with H_2N-BDC under solvothermal conditions gave H_2N-MIL(53) as the product [6]. The same starting materials were tried to obtain H_2N-MIL-101(Al) using a different method from the literature [7]. In this method, however using $AlCl_3 \cdot 6H_2O$, H_2N-MIL-101(Al) was synthesized under reflux with an improved BET surface area of 3100 $m^2 \cdot g^{-1}$, which was previously reported as 2100 $m^2 \cdot g^{-1}$ under solvothermal conditions. We used also this method under reflux with $Al(NO)_{3.}9H_2O$. The sample was obtained with a BET surface area of 250 $m^2 \cdot g^{-1}$ (entry 7, see Table 4.2). The resulting nitrogen sorption isotherm (see Fig. 4.15) can be classified as type I isotherm with hysteresis type H2(b) [8].

Promising results were obtained using $Al(acac)_3$ (entry 8, see Table 4.2) with a BET surface area of 1195 $m^2 \cdot g^{-1}$. The product was semi-crystalline and broad reflections were observed, where the reflection of the H_2N-MIL-101(Al) can be found (see Fig. 4.16). The reaction was performed under solvothermal conditions. The reaction condition can also be optimized to obtain H_2N-MIL-101(Al). However, hydrothermal treatment of this product (holding a sample in a steam room at 70 °C for 24 h) showed a decrease in S(BET) from 1195 to 517 $m^2 \cdot g^{-1}$.

A possible approach to obtain above mentioned MOFs could be to use the synthesis pathway of MIL-100(Cr) according to the literature [9]. In this approach Cr metal was used as metal source and the terminal ligand F, Cl or SO_4 originated from the used acid HF, HCl and H_2SO_4, respectively. The same strategy can be used with Al, Fe and related ligands with addition of HF, H_2SO_4 and HNO_3 to obtain MIL-101(Fe), NH_2-MIL-101(Fe) or), NH_2-MIL-101(Al). HCl can also be tested to analyze the effect of Cl in the reaction.

Final approach could be to wash the obtained MIL-101(Fe), H_2N-MIL-101(Fe) and H_2N-MIL-101(Al) from chlorine containing metal sources for ligand exchange with fluorine salts such as ammonium fluoride [5].

Table 4.2. Results of the reactions between different metal salts and ligands with target MOFs: MIL-101(Fe), H_2N-MIL-101(Al) und H_2N-MIL-101(Fe).

Entry	Metal salt	Ligand	Method	PXRD	S(BET) ($m^2 \cdot g^{-1}$)
Target MOF: MIL-101(Fe)					
1	$Fe(NO_3)_3 \cdot 9H_2O$	BDC	sts	am	n.d.
2	$Fe(SO_4)_3 \cdot xH_2O$	BDC	sts	am	n.d.
3	$Fe(acac)_3$	BDC	sts	am & cr	**94**
Target MOF: H_2N-MIL-101(Fe)					
4	$Fe(acac)_3$	H_2N-BDC	sts	am	n.d.
5	$Fe(SO_4)_3 \cdot xH_2O$	H_2N-BDC	sts	am	n.d.
Target MOF: H_2N-MIL-101(Al)					
6	$Al_2(SO_4)_3 \cdot 18H_2O$	H_2N-BDC	sts	cr	**10**
7	$Al(NO_3)_3 \cdot 9H_2O$	H_2N-BDC	ref	am & cr	**252**
8	$Al(acac)_3$	H_2N-BDC	sts	am & cr	**1195**

sts: Solvothermal synthesis; ref: under reflux; amorphous material; cr: crystalline material; n.d. = not determined.

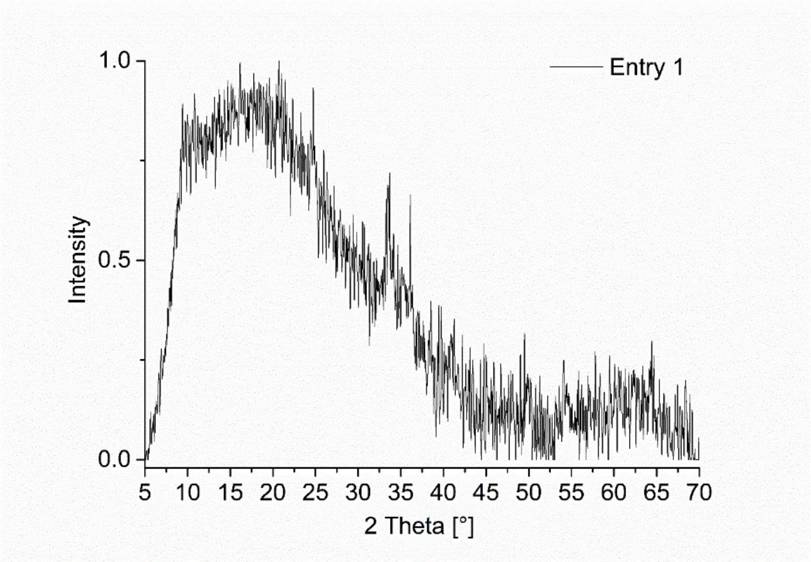

Fig. 4.6. Experimental powder X-ray diffraction patterns of the entry 1 (the product of the reaction between $Fe(NO_3)_3 \cdot 9H_2O$ and BDC).

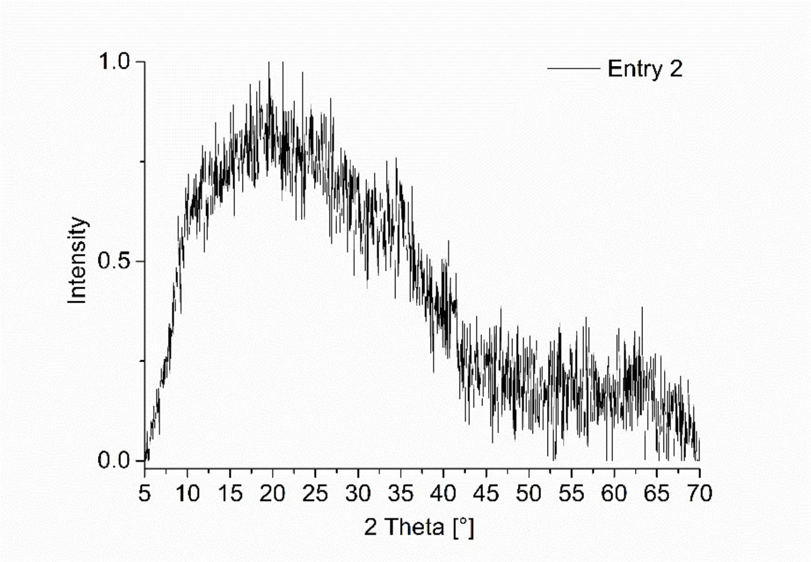

Fig. 4.7. Experimental powder X-ray diffraction patterns of the entry 2 (the product of the reaction between $Fe(SO_4)_3 \cdot xH_2O$ and BDC).

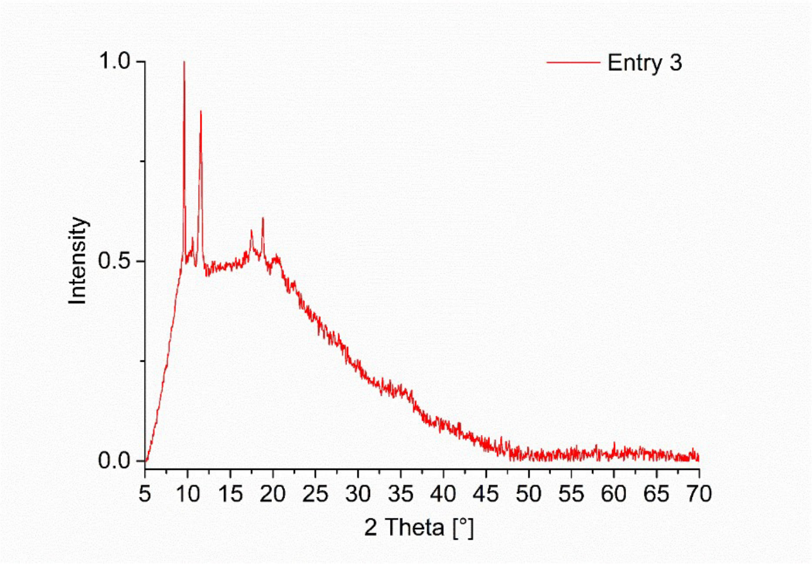

Fig. 4.8. Experimental powder X-ray diffraction patterns of the entry 3 (the product of the reaction between $Fe(acac)_3$ and BDC).

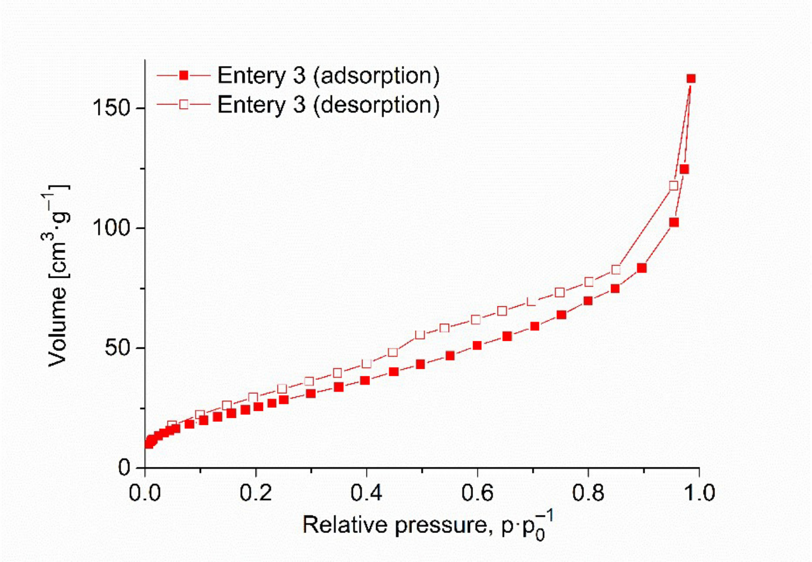

Fig. 4.9. Nitrogen adsorption-desorption isotherms of the entry 3 (the product of the reaction between $Fe(acac)_3$ and BDC).

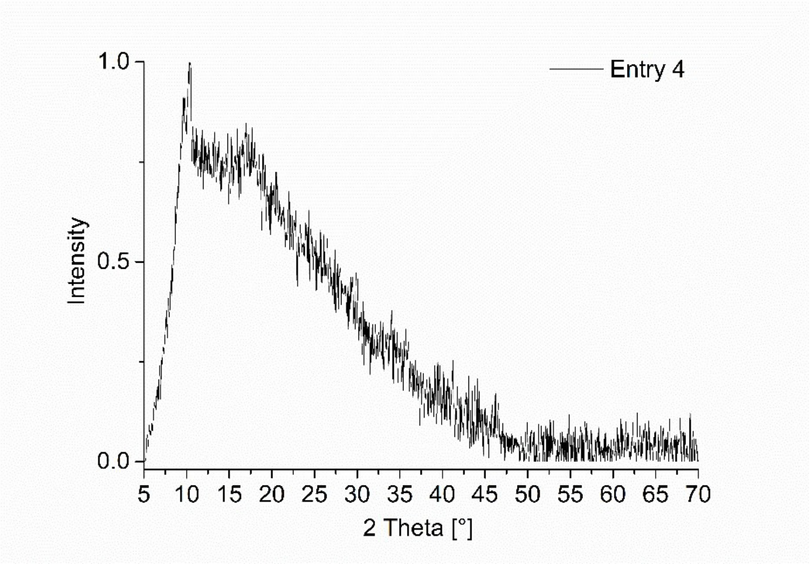

Fig. 4.10. Experimental powder X-ray diffraction patterns of the entry 4 (the product of the reaction between $Fe(acac)_3$ and H_2N-BDC).

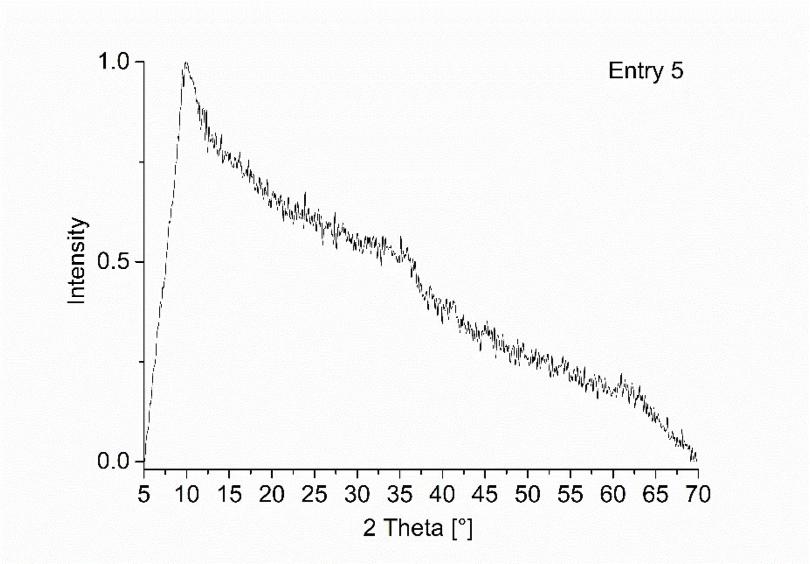

Fig. 4.11. Experimental powder X-ray diffraction patterns of the entry 5 (the product of the reaction between $Fe(SO_4)_3 \cdot xH_2O$ and H_2N-BDC).

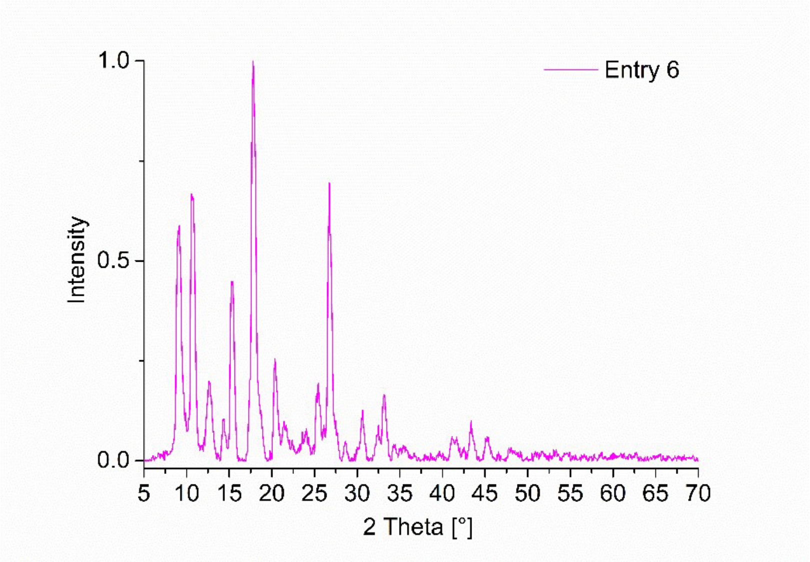

Fig. 4.12. Experimental powder X-ray diffraction patterns of the entry 6 (the product of the reaction between $Al_2(SO_4)_3 \cdot 18H_2O$ and H_2N-BDC).

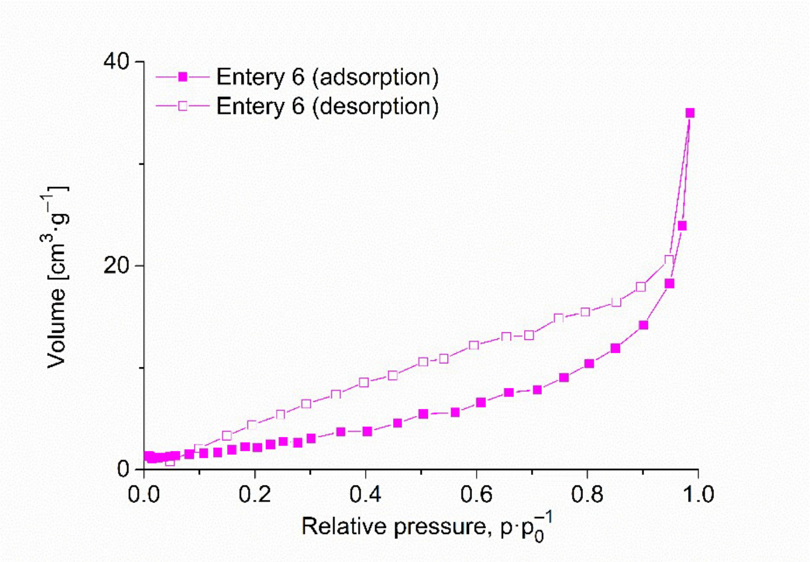

Fig. 4.13. Nitrogen adsorption-desorption isotherms of the entry 6 (the product of the reaction between $Al_2(SO_4)_3 \cdot 18H_2O$ and H_2N-BDC).

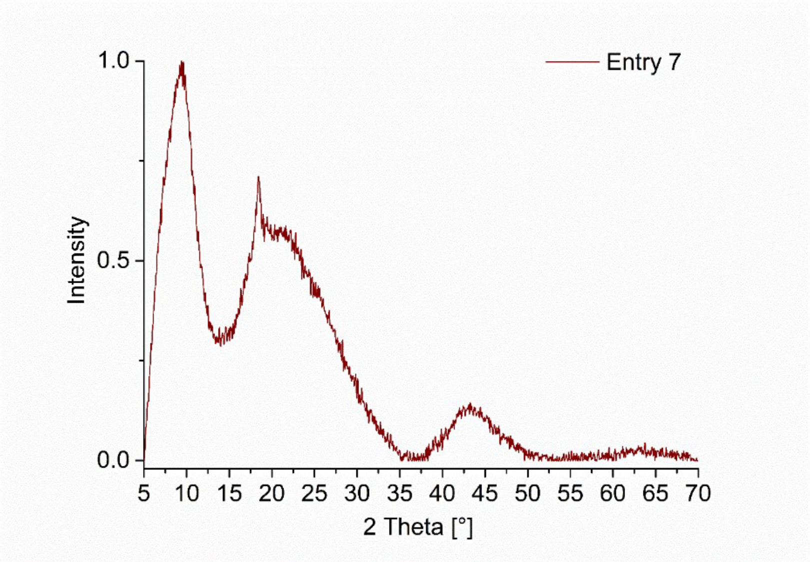

Fig. 4.14. Experimental powder X-ray diffraction patterns of the entry 7 (the product of the reaction between $Al(NO_3)_3 \cdot 9H_2O$ and H_2N-BDC).

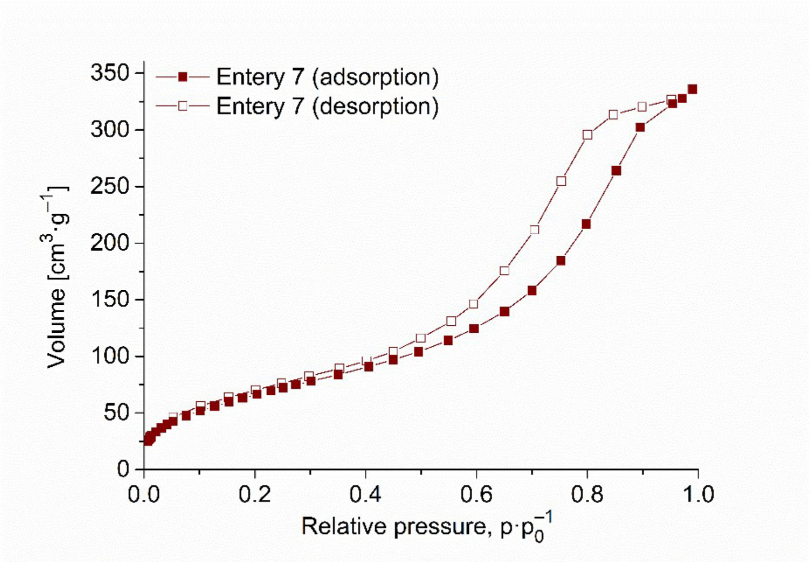

Fig. 4.15. Nitrogen adsorption-desorption isotherms of the entry 7 (the product of the reaction between $Al(NO_3)_3 \cdot 9H_2O$ and H_2N-BDC).

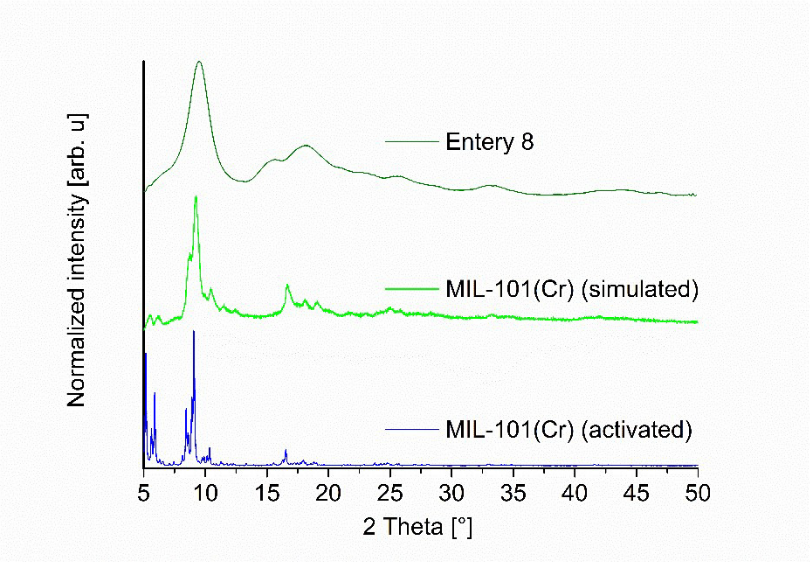

Fig. 4.16. Experimental powder X-ray diffraction patterns of the entry 8 (the product of the reaction between Al(acac)$_3$ and H$_2$N-BDC). compared with synthesized MIL-101(Cr) and MIL-101(Cr) simulated from CSD-Refcode OCUNAC [10].

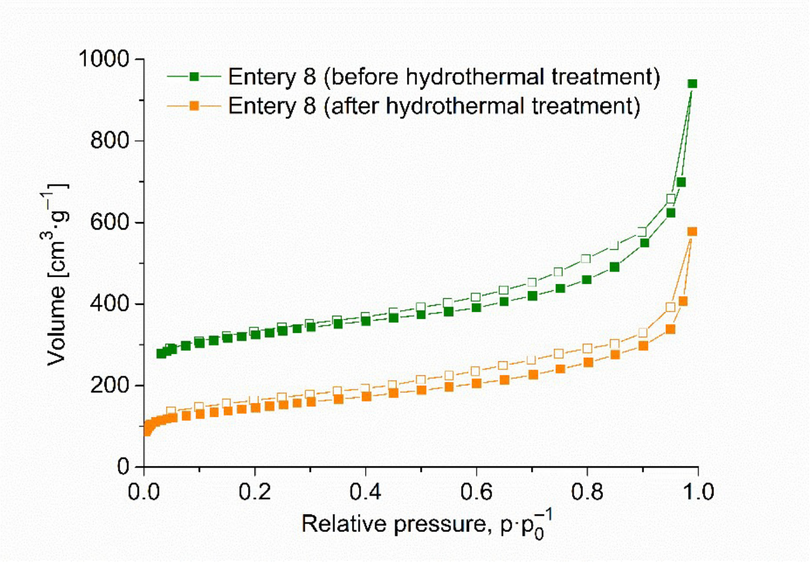

Fig. 4.17. Nitrogen adsorption-desorption isotherms of the entry 8 (the product of the reaction between Al(acac)$_3$ and H$_2$N-BDC) before and after hydrothermal treatment.

4.4 Alfum/MIL-101(Cr) composite

The goal of this project was to synthesize MOF with smaller pores in another MOF with larger pores. Alfum and MIL-101(Cr) were selected as MOFs with small pores and larger pores, respectively. Alfum has a pore size of with approximately 5.7 x 6.0 Å^2 [11] and MIL-101(Cr) has one micropore with a pore size of ~8.6 Å, two mesopores with a pore size of ~29 Å (with a window size of ~12 Å) and ~34 Å (with a window size of ~12 Å and ~15 Å) [10]. Alfum has an S-shaped water adsorption isotherm at the relative pressure range of 0.2–0.3 with a water loading of 400 –500 mg·g^{-1} [12]. MIL-101(Cr) has a water vapor uptake over 1 g·g^{-1}, but the steep rise uptake occurs in the relative pressure range of $0.4 < p \cdot p_0^{-1} < 0.6$, which is slightly hydrophobic compared to the desired range of $0.1 < p \cdot p_0^{-1} < 0.3$ for AHT applications [13]. Interpenetration of Alfum causing formation of small pores in MIL-101(Cr) could shift MIL-101(Cr) into the hydrophilic range.

The synthesis of Alfum does not have to be performed in very basic conditions, due to the instability of MIL-101(Cr) in basic conditions [14]. Considering this, instead of the typical synthesis method of Alfum, which is based on the use of NaOH, the synthesis pathway of Alfum in DMF was used to obtain Alfum/MIL-101(Cr) composite [15,16]. PXRD indicated formation of the Alfum and the broadening of the MIL-101(Cr) reflection could indicate the partial formation of the Alfum in the MIL-101(Cr) pores (see Fig. 4.18). Nitrogen adsorption of MIL-101(Cr) and Alfum/MIL-101(Cr) was carried out only to determine S(BET) (see Fig. 4.19a). In this work MIL-101(Cr) with a BET surface area of 2872 m^2·g^{-1}was used. The BET surface area of Alfum/MIL-101(Cr) was obtained as 2223 m^2·g^{-1}.

There is a good correlation between water vapor uptake of Alfum/MIL-101(Cr) and EDX mapping. EDX mapping was performed on agglomerated Alfum/MIL-101(Cr) and one or two Alfum/MIL-101(Cr) particles (in SEM images, the particle amount is not very well distinguishable, see Fig. 4.20c). The weight percentages of Alfum obtained by EDX were very close to each other in agglomerated Alfum/MIL-101(Cr) and Alfum/MIL-101(Cr) particles, which is 46% and 43%, respectively. For example, the water uptake of Alfum/MIL-101(Cr) at $p \cdot p_0^{-1} = 0.35$ is 170 mg·g^{-1}, which necessitate 42 wt% Alfum, which is very closed to the value obtained from EDX. The effect of Alfum in Alfum/MIL-101(Cr) can be clearly seen in the water sorption isotherm of Alfum/MIL-101(Cr) (see Fig. 4.19b).

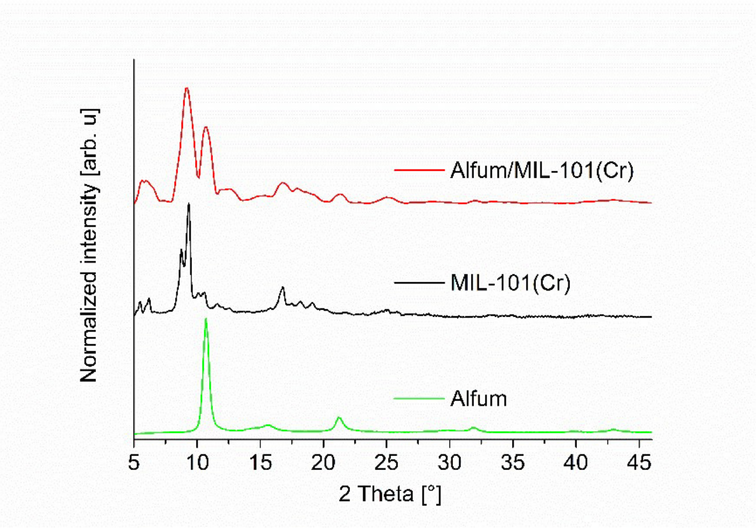

Fig. 4.18. Experimental powder X-ray diffraction patterns of the Alfum, MIL-101(Cr) and Alfum/MIL-101(Cr) composite.

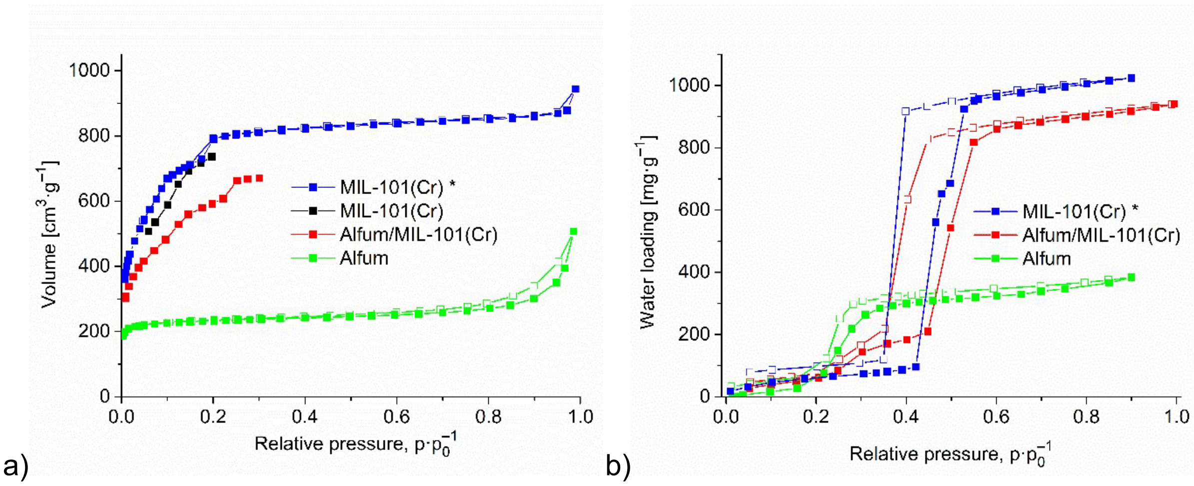

Fig. 4.19. (a) Nitrogen adsorption isotherms of MIL-101(Cr) and Alfum/MIL-101(Cr) composite, and nitrogen adsorption-desorption isotherms of MIL-101(Cr)* and Alfum (Nitrogen adsorption of MIL-101(Cr) and Alfum/MIL-101(Cr) was carried out only to determine the S(BET). (b) Water adsorption-desorption isotherms of MIL-101(Cr), Alfum/MIL-101(Cr) composite and MIL-101(Cr)* (Alfum is shown for the compression and because the complete isotherm MIL-101(Cr) was not measure, MIL-101(Cr)* was shown with similar S(BET) 3005 $m^2 \cdot g^{-1}$)

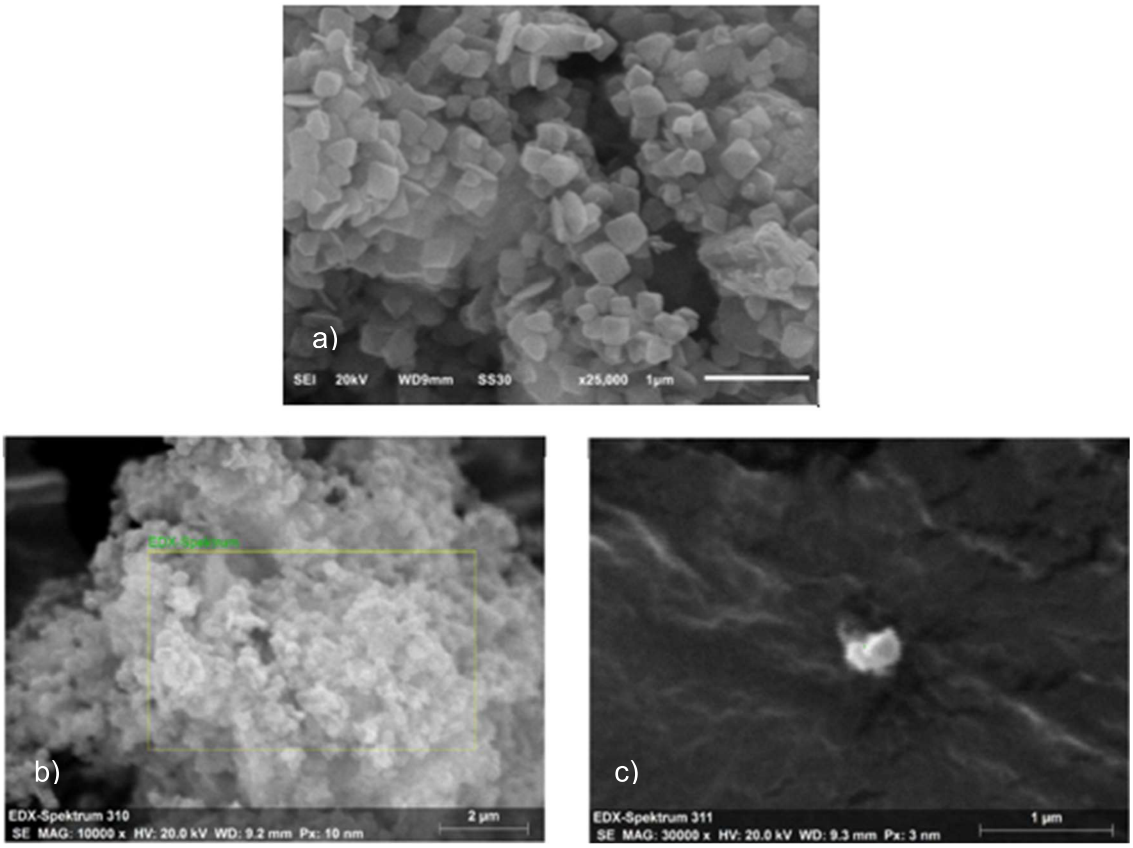

Fig. 4.20. (a) SEM images of Alfum/MIL-101(Cr) (b) mapping area of Alfum/MIL-101(Cr) with yellow rectangel EDX (c) Alfum/MIL-101(Cr) particle used by the EDX mapping.

4.5 Experimental part

4.5.1 General section

All experiments were carried out with exposure to air. All glassware was cleaned by storage in a KOH/isopropanol bath overnight followed by storage in a diluted HCl bath at least for one hour. Between both baths and after the HCl bath, the glassware where rinsed with deionized water and finally dried overnight in an oven at 353 K. Centrifugation and filtration steps were carried out on centrifuges EBA 3S and Rotina 46 from Hettich as well as on high performance centrifuge Allegra 64R, Beckmann Coulter. For the hydrothermal and solvothermal synthesis, a Memmert oven with programmable temperature ramps was used.

Chemicals and solvents (p.a. grade) were commercially obtained from the indicated sources and used without further purification and listed in Table 4.3.

This section refers to the section unpublished results. The each published part in the section published results contains its own experimental part.

Table 4.3. Chemicals and solvents

Chemicals/Solvents	**Source**	**Purity**
Acetic acid	VWR	p.a., 99.9%
Acetone	VWR	p.a., 99.9%
$AlCl_3 \cdot 6H_2O$	Sigma-Aldrich	99.0%
Alfum (Basolite™ A520)	BASF	-
$Al(NO_3)_3 \cdot 9H_2O$	Alfa Aesar	98.0%
$Al_2(SO_4)_3 \cdot 18H_2O$	Sigma-Aldrich	≥ 98.00%
2-Aminoterephthalic acid	Acros Organics	≥ 99%
1,4-Benzenedicarboxylic acid	Acros Organics	≥ 99%
Dimethylformamide	Fisher Chemicals	p.a. ≥ 99.0%
Ethylene glycol diglycidyl ether	Tokyo Chemical Industry	-
Ethanol	VWR Chemicals	p.a., 99.9%
$Fe(NO_3)_3 \cdot 9H_2O$	Alfa Aesar	≥ 98.0%
Formaldehyde	VWR	24% in H_2O, not buffered
Fumaric acid	Alfa Aesar	≥ 99.0%
Na_2CO_3	Riedel-de Haën	≥ 99.8%
Polyacrylic acid	Sigma-Aldrich	35 wt% in H_2O, branched
Polyethylene imine	Alfa Aesar	30 wt% in H_2O, branched
Resorcinol	Acros Organics	98.0%

4.5.2 Analytical methods

4.5.2.1 Powder X-ray diffraction (PXRD)

Powder X-ray diffractograms (PXRD) were obtained at ambient temperature on a Bruker D2 Phaser (300 W, 30 kV, 10 mA) using Cu-Kα radiation ($\lambda = 1.54182$ Å) between $5° < 2\theta < 70°$ with a scanning rate of $0.15° \ s^{-1}$ and between $5° < 2\theta < 50°$ with a scanning rate of $0.0275° \ s^{-1}$.

4.5.2.2 Nitrogen and water sorption analyses

Nitrogen physisorption measurements of MIL-160(Al), Alfum and related composites were carried out on a Nova 4000e from Quantachrome. Water physisorption isotherms were measured volumetrically on a Quantachrome Autosorb iQ MP at 293 K. Brunauer-Emmett-Teller (BET) surface areas (designated as 'apparent S(BET)' for microporous materials [8]) were calculated from the nitrogen physisorption isotherms. Before each sorption measurement all probes were activated under vacuum ($< 2 \times 10^{-2}$ mbar) at 373 K for 3 hours.

4.5.2.3 Scanning electron microscopy

Scanning electron microscopy (SEM) images were taken by a Jeol JSM-6510LV QSEM advanced electron microscope with a LaB_6 cathode at 5–20 keV. The microscope was equipped with a Bruker Xflash 410 silicon drift detector for energy-dispersive X-ray spectrometry (EDX).

4.5.3 Syntheses

4.5.3.1 Syntheses of samples in the section 4.1

Alfum was purchased from BASF under the product name Basolite™ A520 and used also in this section. Here is given a syntheses procedure of Alfum, which was performed in this work in laboratory scale by a procedure from the literature [

Soduim hydroxide (0.285 g, 7,14 mmol) and fumaric acid (0.387 g, 3.33 mmol) in 5.7 mL deionized water. A solution of aluminium sulfate octadecahydrate (1.113 g, 1.670 mmol) in 4.8 mL deionized water was dissolved at 60 °C. After that, solution containing the ligand, was added with a dropping funnel to the solution of aluminium sulfate a period of one hour and the complete solution was stirred for further two hours at 60 °C. The formed suspension was centrifuged. The precipitate was washed two times with deonized water and then overnight in deionized water in a 50 mL round bottom flask. The white precipitate was separated again by centrifugation and dried overnight at 130 °C in a vacuum drying oven.

S(BET) = 1061 $m^2 \cdot g^{-1}$

R,F-xerogel

The synthesis was prepared by a modified procedure from the literature [1].

Resorcinol (6.88 g, 62.5 mmol) was dissolved in an aqueous Na_2CO_3 solution (29.6 g, $2.1 \cdot 10^{-3}$ $mol \cdot L^{-1}$; 0.063 mmol Na_2CO_3). Then a formaldehyde solution (10.71 g, 85.5 mmol; $\rho = 1.06$ $g \cdot mL^{-1}$; 24 wt% in H_2O) was added and the solution was stirred for 5 min. The molar ratios of the starting materials were: resorcinol/formaldehyde = 0.73, resorcinol/Na_2CO_3 = 1000, resorcinol/water = 0.031. From this clear solution was filled 1.01 g into a plastic syringe, which was cut open from the cannula side, sealed by several layers of polyethylene- and aluminum foil and cured for 7 days at 60 °C. The brown monolith was stored in 50 mL of acetic acid (10 wt% in water) for 20 h, followed by storing it in EtOH (3 x 50 mL, min. 7 h each washing step) and dried with following order: 21 h at 40 °C, 71 at 60 °C, 24 h at 80 °C. 820 mg of a brown monolith was isolated.

Alfum@ R,F-Xerogel without water

The synthesis was prepared by a modified procedure from the literature [1].

Resorcinol (6.88 g, 62.5 mmol) was dissolved in an aqueous Na_2CO_3 solution (29.6 g, $2.1\cdot10^{-3}$ mol·L^{-1}; 0.063 mmol Na_2CO_3). Then a formaldehyde solution (10.71 g, 85.5 mmol; $\rho = 1.06$ g·mL^{-1}; 24 wt% in H_2O) was added and the solution was stirred for 5 min. The molar ratios of the starting materials were: resorcinol/formaldehyde = 0.73, resorcinol/Na_2CO_3 = 1000, resorcinol/water = 0.031. From this clear solution was filled 1.01 g into a plastic syringe, which was cut open from the cannula side, sealed by several layers of polyethylene- and aluminum foil and cured for 5 h at 70 °C which leads a formation of a highly viscous solution. 100, 150 and 180 mg of Alfum powders were added into the syringes (In the case of preparation with additional water, 0.6 mL water was added), stirred well by a spatula until homogenous appearance is reached, and cured for 7 days at 60 °C. The brown monolith was stored in 50 mL of acetic acid (10 wt% in water) for 20 h, followed by storing it in EtOH (3 x 50 mL, min. 7 h each washing step) and dried with following order: 21 h at 40 °C, 71 at 60 °C, 24 h at 80 °C. 820 mg of a brown monolith was isolated.

Because the amount of Alfum is known, mass percentage of Alfum in R,F-xerogel was calculated by weighing Alfum@R,F-xerogel after preparation. Addition of 100, 150 and 180 mg led the formation of wt% 40, 50 and 56, respectively. Addition of 100, 150 and 180 mg with 0.6 mL led the formation of wt% 42, 52 and 58, respectively.

4.5.3.2 Syntheses of samples in the section 4.2

MOF@PEI composites

This reaction was prepared by a modified procedure from the literature [3]
334 mg of PEI (30 wt% in H_2O) were dissolved in 2 mL water in a 5 mL vial. Alfum (56 mg, 104 mg, 194 mg and 426 mg) was added to the 2 mL PEI solution and stirred overnight at rt. To this suspension was added 60 mL ethylene glycol diglycidyl ether (EGDE) 0 °C and this mixture was vortexed and kept for 21 h at -18 °C to complete cryoplymerization. The prepared MOF@PEI composites were washed by agitation 6 times with acetone. Stable monoliths were taken out by breaking the vials and dried in an oven at 50 °C. Pure PEI monoliths were prepared as described above without addition of MOF. The amount of Alfum with 56 mg, 104 mg, 194 mg and 426 mg led in 100 mg PEI a wt% of Alfum 36, 51, 66 and 81, respectively.

4.5.3.3 Syntheses of samples in the section 4.3

Reactions between different metal salts and linkers with target MOFs: MIL-101(Fe), H_2N-MIL-101(Al) und H_2N-MIL-101(Fe)

Preparation of the entry 1 (reaction between $Fe(NO_3)_3{\cdot}9H_2O$ and BDC)

This reaction was prepared by a modified procedure from the literature [17].

1,4-Benzenedicarboxylic acid (0.104 g, 0.625 mmol), $Fe(NO_3)_3{\cdot}9H_2O$ (0.505 g, 1.25 mmol) and DMF (7.5 mL) were placed in a 15 mL Teflon-liner and stirred well. The Teflon-liner was inserted in a steel autoclave and heated to 110 °C within 1 h, held at this temperature for 20 h and then cooled down in 6 h to rt. The product was centrifuged and washed consecutively with the following order: EtOH (3 x 10 mL at rt), DMF (2 x 10 mL at rt) and EtOH (3 x 10 mL at rt). Before each solvent change, suspension was centrifuged and the supernatant was removed. After final centrifugation, the dark brown powder was dried at 80 °C to give 0.105 g of a powdery product.

Preparation of the entry 2 (reaction between $Fe(SO_4)_3{\cdot}xH_2O$ and BDC)

This reaction was prepared by a modified procedure from the literature [18].

1,4-Benzenedicarboxylic acid (0.104 g, 0.625 mmol), $Fe(SO_4)_3{\cdot}xH_2O$ (0.453 g, 1.25 mmol), deionized H_2O (0.041 g, 2.25 mmol) and DMF (25 mL) were placed in a Teflon-liner and stirred for 2 h. Deionized H_2O (2.5 mL) was added to this suspension. The Teflon-liner was inserted in a steel autoclave and heated to 110 °C within 1 h, held at this temperature for 24 h and then cooled down in 20 h to rt. The product was centrifuged and washed consecutively with the following order: DMF (3 x 10 mL at rt) and EtOH (10 mL, 2 x 7.5 mL at rt). Before each solvent change, suspension was centrifuged and the supernatant was removed. After final centrifugation, the black powder was dried at 80 °C to give 0.043 g of a powdery product.

Preparation of the entry 3 (reaction between $Fe(acac)_3$ and BDC)

This reaction was prepared by a modified procedure from the literature [18].

1,4-Benzenedicarboxylic acid (0.104 g, 0.625 mmol), $Fe(acac)_3$ (0.442 g, 1.25 mmol), deionized H_2O (0.068 g, 3.75 mmol) and DMF (25 mL) were placed in a Teflon-liner and stirred well. The Teflon-liner was inserted in a steel autoclave and heated to 110 °C within 1 h, held at this temperature for 24 h and then cooled down in 20 h to rt. The product was centrifuged and washed consecutively with the following order: DMF (3 x 10 mL at rt) and EtOH (2 x 10 mL at rt). Before each solvent change, suspension was centrifuged and the supernatant was removed. After final centrifugation, the powdery product was dried at 80 °C and obtained as 103 mg.

Preparation of the entry 4 (reaction between $Fe(acac)_3$ and H_2N-BDC)

This reaction was prepared by a modified procedure from the literature [18].

2-Amino-1,4-benzenedicarboxylic acid (0.113 g, 0.625 mmol), $Fe(acac)_3$ (0.442 g, 1.25 mmol), deionized H_2O (0.068 g, 3.75 mmol) and DMF (25 mL) were placed in a Teflon-liner and stirred for 80 min. The Teflon-liner was inserted in a steel autoclave and heated to 110 °C within 20 h, held at this temperature for 24 h and then cooled down in 6 h to rt. The product was centrifuged and washed consecutively with the following order: DMF (2 x 7.5 mL at rt). Before each solvent change, suspension was centrifuged and the supernatant was removed. After final centrifugation, the powdery product was dried.

Preparation of the entry 5 (reaction between $Fe(SO_4)_3 \cdot xH_2O$ and H_2N-BDC)

This reaction was prepared by a modified procedure from the literature [18].

2-Amino-1,4-benzenedicarboxylic acid (0.113 g, 0.625 mmol), $Fe(SO_4)_3 \cdot xH_2O$ (0.453 g, 1.25 mmol), deionized H_2O (0.041 g, 2.25 mmol) and DMF (25 mL) were placed in a Teflon-liner and stirred well. The Teflon-liner was inserted in a steel autoclave and heated to 110 °C within 20 h, held at this temperature for 24 h and then cooled down in 6 h to rt. The product was centrifuged and washed consecutively with the following order: DMF (2 x 7.5 mL at rt), DMF (25 mL, hold in ultrasound for 1 h, subsequently stirred for 18 h) and EtOH (2 x 10 mL at rt). Before each solvent change, suspension was centrifuged and the supernatant was removed. After final centrifugation, the powdery product was dried at 100 °C.

Preparation of the entry 6 (reaction between $Al_2(SO_4)_3 \cdot 18H_2O$ and H_2N-BDC)

This reaction was prepared by a modified procedure from the literature [6]

2-Amino-1,4-benzenedicarboxylic acid (0.540 g, 2.98 mmol), $Al_2(SO_4)_3 \cdot 18H_2O$ (0.666 g, 1.00 mmol) and deionized H_2O (30 mL) were placed in a Teflon-liner. The Teflon-liner was inserted in a steel autoclave and heated to 130 °C within 1.5 h, held at this temperature for 45 h and then cooled down in 1.5 h to rt. The product was centrifuged and washed consecutively with the following order: DMF (2 x 10 mL at rt) and MeOH (40 mL under reflux). Before each solvent change, suspension was centrifuged and the supernatant was removed. After final centrifugation, the yellow powdery product was dried at 60 °C.

Preparation of the entry 7 (reaction between $Al(NO_3)_3 \cdot 9H_2O$ and H_2N-BDC)

This reaction was prepared by a modified procedure from the literature [7]

2-Amino-1,4-benzenedicarboxylic acid (0.136 g, 0.75 mmol) was dissolved in DMF (30 mL) placed in a 50-mL two-neck round-bottom flask under stirring with a magnetic stirrer at 110 °C.

To this solution, $Al(NO_3)_3{\cdot}9H_2O$ (0.563 g, 1.5 mmol) was added in 7 equal portions with a time delay of 15 min between each two additions. After the last portion was added, the temperature was kept at 110 °C for 3 h under stirring and for 16 h without stirring. The yellow product was centrifuged and washed consecutively with the following order: DMF (12 mL at rt), EtOH (12 mL at rt) and EtOH (50 mL under reflux). After final centrifugation, the yellow powder was dried at 90 °C to give 0.095 g of a powdery product.

Preparation of the entry 8 (reaction between $Al(acac)_3$ and H_2N-BDC)

2-Amino-1,4-benzenedicarboxylic acid (0.018 g, 0.1 mmol) and $Al(acac)_3$ (0.065 g, 0.2 mmol) were dissolved in DMF (4 mL) placed in a 10 mL Pyrex tube. The Pyrex tube was heated to 130 °C within 6 h, held at this temperature for 40 h and then taken from the oven and cooled down to rt. The product was centrifuged and washed with acetone (4 x 5 mL). Before each solvent change, suspension was centrifuged and the supernatant was removed. After final centrifugation, the yellow powdery product was dried under air.

4.5.3.4 Syntheses of Alfum/MIL-101(Cr) composite in the section 4.4

MIL-101(Cr) (0.1 g), $AlCl_3{\cdot}6H_2O$ (0.054 g, 0.22 mmol) and fumaric acid (0.042 g, 0.36 mmol) were stirred in water for 18 h. DMF (5 mL) was added and stirred at 120 °C for 48 h. The reaction mixture was cooled down to rt. The product was centrifuged and washed consecutively with the following order: Acetone (3 x 5 mL at rt) and MeOH (3 x 5 mL at rt). After drying rt under air, 111 mg green powder was obtained.

4.6 References

[1] M. Wickenheisser, A. Herbst, R. Tannert, B. Milow, C. Janiak, Microporous Mesoporous Mater. 215 (2015) 143–153.

[2] F. Jeremias, D. Fröhlich, C. Janiak, S.K. Henninger, RSC Adv. 4 (2014) 24073–24082.

[3] N. Sahiner, S. Demirci, J. Appl. Polym. Sci. 133 (2016) 43478 (1–13).

[4] D.G. Barceloux, D. Barceloux, J Toxicol. Clin. Toxicol. 37 (1999) 173–94.

[5] F. Jeremias, Synthesis and Characterization of Metal-Organic Frameworks for Heat Transformation Applications, Dissertation, Heinrich-Heine-Universität Düsseldorf (2015).

[6] P. Serra-Crespo, E.V. Ramos-Fernandez, J. Gascon, F. Kapteijn, Chem. Mater. 23 (2011) 2565–2572.

[7] M. Hartmann, M. Fischer, Microporous Mesoporous Mater. 164 (2012) 38–43

[8] M. Thommes, K. Kaneko, A. V. Neimark, J. P. Olivier, F. Rodriguez-Reinoso, J. Rouquerol, K. S. Sing, Pure Appl. Chem. 87 (2015) 1051–1069.

[9] G. Akiyama, R. Matsuda, S. Kitagawa, Chem. Lett. 39 (2010) 360–361.

[10] G. Férey, C. Mellot-Draznieks, C. Serre, F. Millange, J. Dutour, S. Surblé, I. Margiolaki, Science 309 (2005) 2040–2042.

[11] E. Alvarez, N. Guillou, C. Martineau, B. Bueken, B. van de Voorde, C. Le Guillouzer, P. Fabry, F. Nouar, F. Taulelle, D. de Vos, J.-S. Chang, K. H. Cho, N. Ramsahye, T. Devic, M. Daturi, G. Maurin, C. Serre, Angew. Chem. 127 (2015) 3735–3739; Angew. Chem. Int. Ed. 54 (2015) 3664–3668.

[12] F. Jeremias, D. Fröhlich, C. Janiak, S.K. Henninger, RSC Adv. 4 (2014) 24073–24082.

[13] Y.I. Aristov, Challenging offers of material science for adsorption heat transformation: A review, Appl. Therm. Eng. 50 (2013) 1610–1618.

[14] N. Ko, P. G. Choi, J. Hong, M. Yeo, S. Sung, K.E. Cordova, H.J. Park, J.K. Yang, J. Kim, J. Mater. Chem. A 3 (2015) 2057–2064

[15] E. Leung, U. Müller, N. Trukhan, H. Mattenheimer, G. Cox, S. Blei, Process For Preparing Porous Metal-Organic Frameworks Based On Aluminum Fumarate, US 201/0082864 A1. 2012 Apr 5.

[16] C. Kiener, U. Muller, M. Schubert, Organametallic aluminum fumarate backbone material, US 2009/0092818 A1. 2009 Apr. 9.

[17] N.V. Maksimchuk, K.A. Kovalenko, V.P. Fedin, O.A. Kholdeeva, Chem. Commun. 48 (2012) 6812–6814.

[18] S. Bauer, C. Serre, T. Devic, P. Horcajada, J. Marrot, G. Férey, N. Stock, Inorg. Chem. 47 (2008) 7568–7576.

5 Conclusions and Outlook

Adsorption heat transformation (AHT) applications are an important technology to address energy demand as they are eco-friendly energy saving process with less greenhouse effect for air condition purposes, heating and cooling including ice making and refrigeration. However, development is required to improve the efficiency of the commercial available adsorbent materials. Important classes of adsorbents are activated carbons, silica gel, zeolites and MOFs. Composite materials based on the zeolites and silica gels with salt are in the focus of research because of their increased uptake and heat transformation enthalpies. Integration of MOFs into AHT applications are also getting more attention in the last years, because of the tunability of their vapor sorption properties through their tunable pore structures, their desired S-shape isotherm in a low $p \cdot p_0^{-1}$ region, high water uptake and hydrothermal stability. Beside this, MOFs have also some disadvantages such as high production cost and still not fully proven long-term stability as well as additional process is needed to shape MOF microcrystalline powders. However, there are only a few MOFs in the literature that are potential candidates for AHT applications. From these MOFs, Alfum and MIL-160(Al) were chosen for the shaping process in this work. Preparation of Alfum is easy and can be performed in large scale. The sorption properties of Alfum make it an alternative to silica for cooling in AHT. The preparation of MIL-160 is also simple and prepared under reflux with aluminum salts and 2,5-furandicarboxylate. The one of the best energy storage density of MIL-160(Al) make it a promising materials for AHT.

In addition, MIL-101(Cr) was also used in this work, although the water sorption isotherm of MIL-101(Cr) is slightly hydrophobic and is not within the desired relative pressure range for AHT applications, it is an interesting adsorbent with a very high water adsorption above 1 $g \cdot g^{-1}$ and with the possibility of hydrophilic modification.

The shaping of MOFs was extensively studied in this dissertation, and two different methods to monolithic composites, phase separation and freeze-casting, was systematically investigated.

Phase separation is a well-known technique for the fabrication of monolithic structures. In this work, this technique was used for the first time to obtain shaped MOFs in the form of MOF@PVA monoliths. For optimization, different drying methods were tested on PVA monoliths, which resulted in vacuum drying being the preferred drying method to maintain the monolithic shape and avoid shrinkage. Alfum and MIL-101(Cr) were used for shaping and different loading amounts of MOF up to 80 wt% was successfully achieved. The reproducibility was also shown with a different loading amount of MOFs in the MOF@PVA monolith by nearly same expected apparent mass-weighted BET surface area and water vapor uptake. Three different PVAs with different molecular weight were used: high-, medium- and low-molecular weight PVA1, PVA2 and PVA3, respectively. MIL-101(Cr)@PVA2 monoliths showed better results than the MIL-101(Cr)@PVA1 monoliths, so PVA1 was not used for the shaping of Alfum. In the MIL-101(Cr)@PVA2, a porosity of up to 83% of the neat MIL-101(Cr) and water uptake of up to 84% of the neat MIL-101(Cr) was achieved. For Alfum@PVA, a surface area of up to 95%, pore volume of up to 123% and water uptake of up to 120% of the neat Alfum were obtained. The remarkably higher pore volume and water loading of Alfum@PVA, which is more than 100% of the estimated value, was attributed to the additional mesopores at the MOF-polymer interface. These additional mesopores at the MOF-polymer interface were determined by using the t-plot method. While in the Alfum@PVA additional interfacial mesopore volume was observed, this phenomenon was not observable in MIL-101(Cr)@PVA. The mechanical stability of MOF@PVA monolith prepared by phase separation was also studied representatively by means of Alfum@PVA2 monoliths. Interestingly, 65 wt% Alfum in the monolithic composite revealed a maximum stability compared to the monolithic composites with the lower and higher Alfum quantities.

The freeze-casting method was selected as another method to form MOFs as monoliths. First of all, optimization experiments were carried out with Alfum and PVA. Alfum has good pore accessibility, can easily be synthesized under mild conditions and is a cheap material. PVA is also a cheap material with larger variability of molecular weight and has good mechanical stability. The optimization experiments showed that freezing in liquid nitrogen and subsequent freeze-drying provided the best results considering rapid monolith formation, retention of the BET surface area and pore volume of the MOF in the monolithic composites. In addition, polymers with higher molecular weight block the pores of the MOF less compared to polymers with lower molecular weight. The effect of different MOF loading percentages on the pore blocking was also investigated, showing that the MOF@polymer monolith with increased MOF content corresponds to least blocked the pores. Even 80 wt% of MOF in the MOF/polymer suspension resulted in high viscosity, which means that a higher MOF content would give an inhomogeneous mixture. In addition, some MOF@polymer monoliths were already mechanically fragile with 80 wt% MOF. For these reasons, 80 wt% MOF was selected for the preparation of the other MOF@poylmer composites with the MOFs Alfum, MIL-160(Al), MIL-101(Cr) and polymers PAA, PAANa, PEG, PEI, PVA(98), PVA(88) and PVP. The crystallinity of the MOFs was maintained in all monolith composites. With this work, it was reported for the first time, that shaped MOFs obtained by the freeze-casting method exhibit nearly negligible pore blocking. In the Alfum@polymer and MIL-160(Al)@polymer composites, the best results in terms of S(BET) and V(pore) were achieved with PVA and PVP. All MIL-101(Cr)@polymer composites yielded over 85% of the calculated S(BET) and 90% of the calculated V(pore) (excluding MIL-101(Cr)@PEI with 47% of the calculated S(BET) and 52% of the calculated V(pore)). In general, there is a good correlation with the pore volume and maximum water uptake of MOF@poylmer composites at the relative pressure of 0.9. It is interesting to note that a detailed analysis of the water sorption isotherm of the MOF@polymer composites indicate an additional hydrophilic shift in the relative pressure range before the starting point of the S-shaped water uptake of the corresponding MOFs. For example, with MIL-101(Cr)@PEG a water vapor uptake of 330% of the calculated value was obtained at the relative pressure of 0.4.

In both works, different MOF@polymer monolith composites were systematically investigated and the desired monolithic structure with negligible pore blocking and improved water sorption properties was successfully obtained.

Further composite materials can be produced with other MOF and polymer combinations using the above two techniques. Other gas sorption properties of the composites could also be interesting such as methane and CO_2.